2019 R&D 100 Joint Entry

Los Alamos National Laboratory, Lawrence Livermore National Laboratory, and Sandia National Laboratories

MC-15 PORTABLE NEUTRON MULTIPLICITY DETECTOR

- Records neutron detections with 100-nanosecond precision
- Uses a Feynman excess-variance method to look for correlated neutrons in real time
- Designed to be smaller, lighter and faster than any other detector on the market today
- Operates easily either from an onboard touch-screen or remotely from a computer connected to local Ethernet

Los Alamos NATIONAL LABORATORY EST. 1943

Lawrence Livermore National Laboratory

Sandia National Laboratories

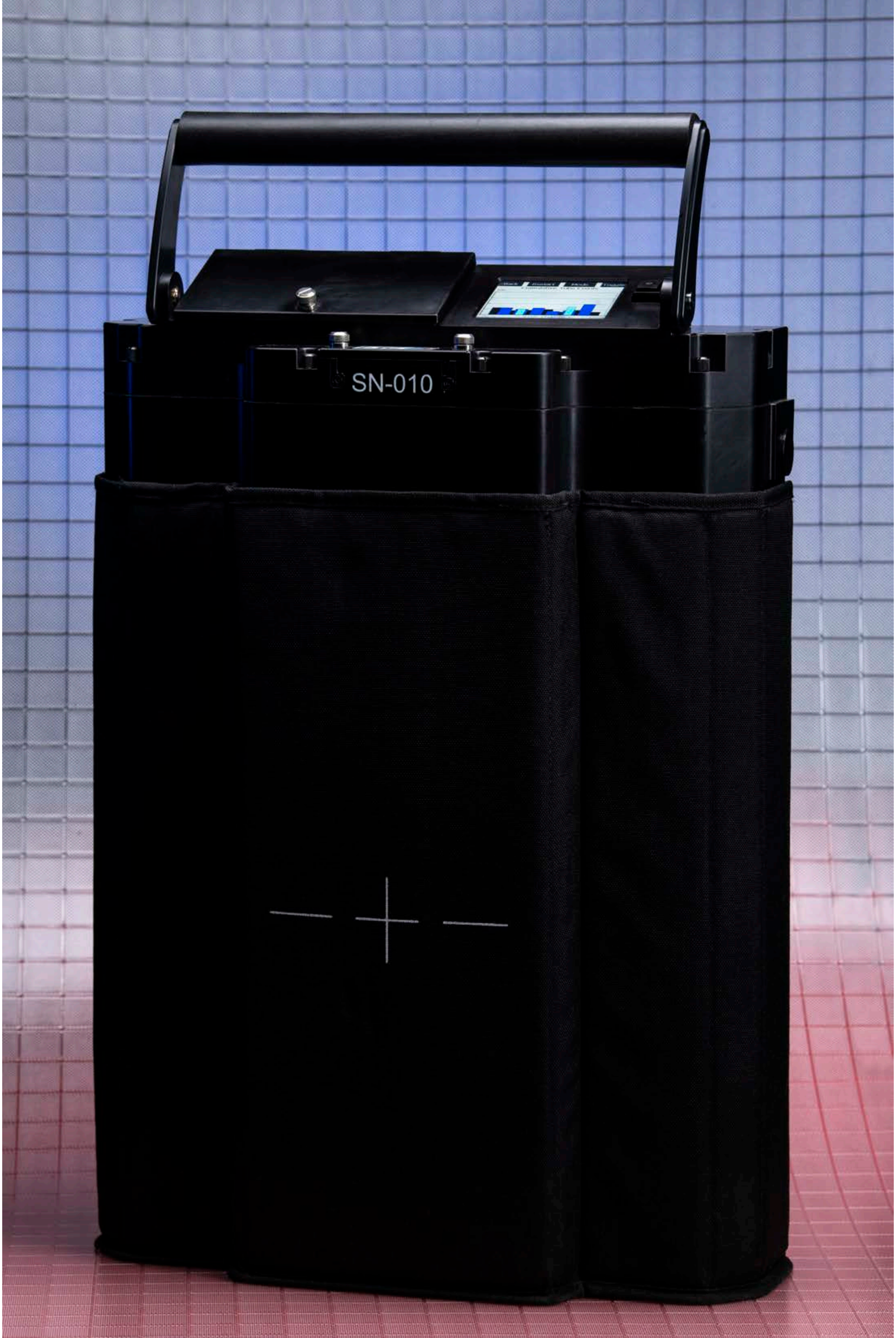
SN-010

2019 R&D 100 Awards template

MC-15 Portable Neutron Multiplicity Detector
Helping emergency response teams quickly identify and assess nuclear-based threats

LA-UR-19-24933

Categories

☒ Analytical/Test	☐ Special recognition: Corporate Social Responsibility
☒ IT/Electrical	☐ Special recognition: Green Tech
☐ Mechanical/Materials	☐ Special recognition: Market Disruptor - Products
☐ Process/Prototyping	☐ Special recognition: Market Disruptor - Services
☒ Software/Services	
☐ Other	

Note: There is a $450 entry fee per category

Name of primary submitting organization

Los Alamos National Laboratory

Names of co-developing organizations

Lawrence Livermore National Laboratory
Sandia National Laboratories

Product/service brand name

MC-15—Next-Generation Portable Neutron Multiplicity Detector

Was the product/service introduced to the market between January 1, 2018, and March 31, 2019?

☒ Yes
☐ No

If your submission is subject to regulatory approval, has the product been approved?

☐ Yes
☐ No
☒ Not applicable to this product

Price of product/service (U.S. dollars)

Estimated price of $150,000–$250,000 per detector.

Product description

The MC-15 detects neutrons to within 100-nanosecond resolution, enabling emergency response teams to quickly identify and assess nuclear-based threats. The MC-15 processes data in real time, requires little training to operate, and is portable, lighter, and faster than any neutron multiplicity detector on the market.

Indicate the type of institution you represent

Government Laboratory

Submitter's relation to entered product/service

Product Developer

Product Photos

2019 R&D 100 Cover for MC-15 Portable Neutron Multiplicity Detector
MC-15 1
MC-15 2
MC-15 3

Video Files

N/A

What does the product or technology do? Describe the principal applications of this product.

In the United States, agencies such as the Department of Energy and Department of Justice use highly trained teams to respond, assess, and resolve nuclear and radiological threats worldwide. Threats range from illegal nuclear development and testing to the illegal proliferation of nuclear materials to outright attempts at nuclear terrorism.

In addition to having specialized training and experience, these teams rely on the latest technology in nuclear detection instrumentation to quickly evaluate whether a potential nuclear threat is nuclear in nature or just a deception. If the item is truly nuclear, then it is equally important to estimate the magnitude of the danger. One of the parameters that can be used to identify and assess the size of a threat is neutron multiplication. Neutron multiplication is a useful parameter to quantify Special Nuclear Material (SNM), such as plutonium and uranium. Neutron multiplication is based on the fact that when spontaneous fission occurs in special nuclear material (SNM), multiple neutrons may be emitted (see Figure 1) and these neutron emissions are correlated in time.

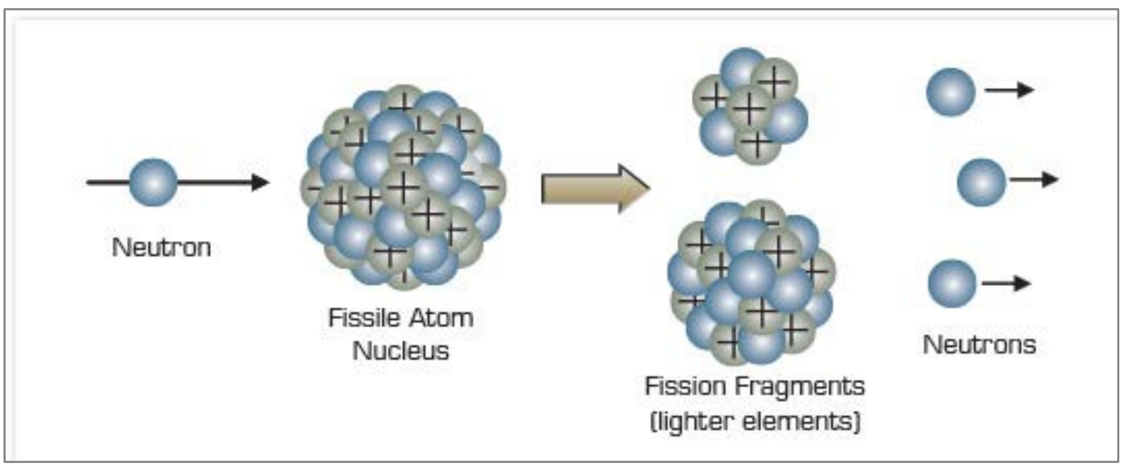

Figure 1. Neutron multiplication happens in a fission event of special nuclear material (SNM). A neutron colliding with a fissile SNM nucleus results in fission fragments plus additional neutrons emitted, that is, the number of neutrons multiply in a fission event. These neutrons can then initiate more fission reactions.

These initial neutrons then propagate through the material and induce more fissions, which then release more neutrons which then may induce more fissions. This process repeats itself until either the neutrons leak out and terminate the chain reaction or the SNM itself heats up and disassembles. The number of neutrons created during this process is called the chain length and this process occurs within 100's of nanoseconds. This chain-reaction process occurs in SNM and is one indication of the presence of nuclear material. This information can be used to determine the total mass of the SNM.

The neutrons in these chains are all created in clusters that last 100s to 1,000s of nanoseconds. The way this clustering is detected is by recording when the neutrons are detected and determining if there are more than the expected number of neutrons in a short-time. The time scales that are used to look for correlated neutrons range from a few microseconds to 1,000s of microseconds. The presence of a fission chain indicates the presence of a threat, and the length of the fission chain can be used to determine the magnitude of the threat.

Developed by scientists at Los Alamos, Lawrence Livermore, and Sandia national laboratories, the MC-15 Portable Neutron Multiplicity Detector is an innovative, lightweight, portable, and easy-to-use detector that identifies and assess nuclear-based threats by detecting the time-correlated neutrons emitted from SNM. The MC-15 is small and weighs only 47 pounds. The detector has its own power source that lasts for 12 hours. Copyrighted software provides unique features. The detector is operated easily using an onboard touchscreen or works remotely via a computer connected to a local Ethernet.

The MC-15 has been designed to detect a neutron within 100 nanoseconds, the average time a neutron burst lasts. The events are recorded with 100 nanosecond precision. The MC-15 has a large dynamic range for data collection. It can record count rates of less than a few counts per second to approximately a million counts per second.

The MC-15 contains 15 helium-3 filled tubes each with their own preamplifier designed specifically for this detector. The signal from these preamplifiers is sent to a field programmable gate array (FPGA) that tags the event with the time of detection and in which tube the detection occurred. The ability to record when and where a neutron is detected in the detector allows for the data from the MC-15 to estimate the chain-length and the rate at which the chains occur, which are the parameters that are required in order to determine if an object is a threat and how much of a threat.

The recorded data is the most versatile of formats. The benefit of this is that it can be processed any number of ways multiple times. This allows for the data to be used in traditional algorithms and yet the same data is available to be analyzed by new methods that have yet to be conceived.

However, post-processing data is not ideal when an immediate answer is needed. The MC-15 also processes data in real time using the Feynman excess-variance method. This method counts how many events occur in a short time-gate-width (on the order of a 100s of microseconds) and then bins such data into a histogram (see Figure 2). If a neutron burst comes from a nonthreat object, the neutron chain-length is short, enabling the resultant histograms to be modeled using a Poisson distribution. However, if the neutron chain-length is long, the resultant histograms are broader than a Poisson distribution, with the excess variance in the histogram correlating to the neutron chain-length and the average number of neutrons per gate correlates to the rate the chains are created.

The data shown in Figure 2 were taken with an MC-15 and processed in real time onboard the detector. Overlaying a Poisson distribution over the data shows that the histogram's width is much greater than that of the Poisson distribution indicating that the average chain-length is long.

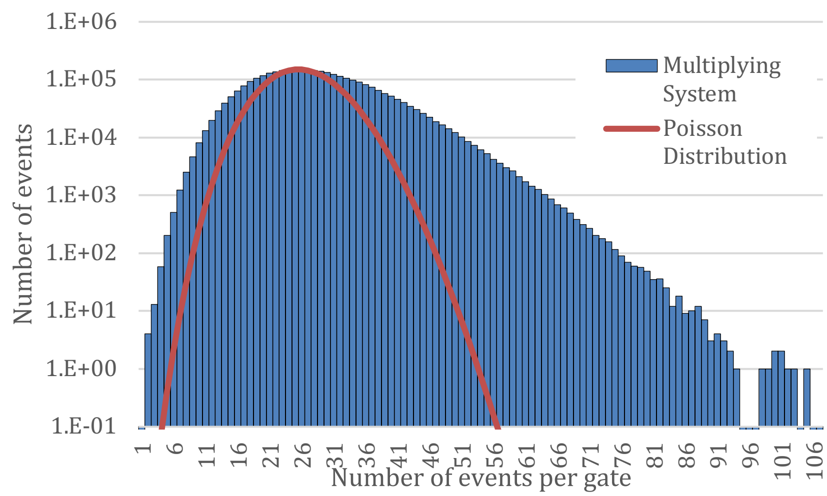

Figure 2. Measurements of a plutonium source. The MC-15 neutron detector creates 15 of these histograms in real time. The difference in the width of this histogram when compared to a Poisson distribution (red curve) is correlated to the length of a neutron chain. The histogram is much wider than what would be modeled by a Poisson distribution. This indicates that the measured object is producing long neutron chains, which are only created by SNM. The data were created by opening a time gate of width 256 microseconds (μs) multiple times and counting how many neutrons were detected. This counting is repeated multiple times and was on the order of 10^6 times.

In addition to information gleaned from neutron detection times, it is important to observe the distribution of detection locations when SNM may be present. Such distribution is important because neutrons from nuclear material must slow down to be detected to an energy of around 0.025 electron Volts (eV). This slowing-down process, or moderation, occurs when a neutron strikes the nucleus of an atom, thus transferring part of its energy. The atom that most effectively slows down neutrons is hydrogen, which is the reason for the high-density polyethylene in the MC-15. The energy of a neutron being emitted from SNM is around 2 mega electron Volts (MeV), and the neutrons need to bounce from a hydrogen atom to another atom around 26 times before they slow down to 0.025 eV. The neutrons from bare SNM are energetic enough that they will penetrate into the MC-15 and will be detected primarily by the second row of tubes.

However, hydrogenous material may also be present in nuclear threats and will slow down neutrons before they reach the MC-15. Neutrons transiting through this additional hydrogenous material will undergo collisions and will lose energy in the process. Because these neutrons have lost some energy before they reach the MC-15, they will not penetrate as far into the detector before they reach 0.025 eV, and they will be predominantly detected in the front tubes.

Hence, the distribution of detections in the MC-15 changes depending on how much hydrogenous material is around a neutron-emitting object. The more hydrogenous material that surrounds SNM, the more efficient the front tubes become at detecting escaping neutrons, and the more the relative count rate increases. This correlation can be reversed in order to estimate how much hydrogenous material is surrounding neutron-emitting material by evaluating which tubes detected most of the neutrons.

Figure 3 shows the relative efficiencies of the He-3 tubes for a series of measurements taken of a 4.5-kilogram (kg) sphere of plutonium with multiple thicknesses of a moderator surrounding it. Note that when there is no moderator around the plutonium that most of the detections occur in the detector's middle tubes. As more moderator material is placed around the plutonium, more of the detections occur in the front tubes. Data from experiments like this have been and will be used in versions of the *International Criticality Safety Benchmark Evaluation Project* handbook. (See website for the DOE National Criticality Safety Program and a related article on the program, "National Criticality Experiments Research Center," in the Appendix.)

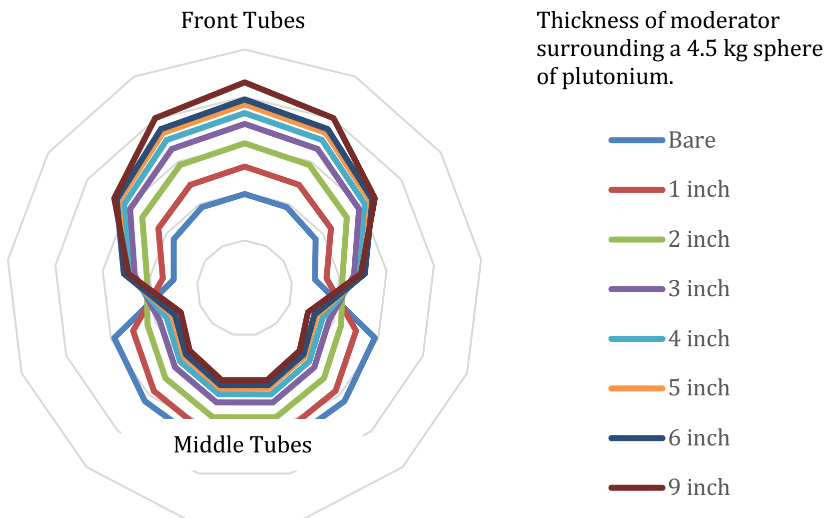

Figure 3. Measurement of a plutonium source surrounded by hydrogenous material. The distribution of neutron detections is correlated to how much hydrogenous material surrounds nuclear material. The more hydrogenous material that surrounds the nuclear material, the greater the detection efficiency of the front tubes on the MC-15. This correlation can be reversed by evaluating the ratio of the tube count rates in the front tubes over the middles tubes to the thickness of hydrogenous material around nuclear material.

Neutron multiplicity analysis began at Los Alamos National Laboratory during the Manhattan Project; during this time, scientists started to work on estimating neutron chain-length. Such estimates required the precise recording of the detection times of the neutrons from these chains. The timeframe for recording such times is on the order of 100s of nanoseconds to a few microseconds. To understand just how fast these times are, consider one flash of a strobe light, which takes one microsecond.

Detecting time-correlated neutrons is typically performed in well-controlled environments, such as research laboratories or at nuclear reactors. Typical research setups perform such measurements using multiple and independent neutron detectors connected to a central data recorder via cables. The recorder is in turn connected to an external computer via another cable. Such setups are so cumbersome that they are not practical for field measurements and in many cases could not be battery-operated.

In contrast to this, the MC-15 is an ideal field instrument for neutron detection. Measurements are performed quickly, often in harsh environments by personnel who may not be experts in multiplicity measurements (see Figure 4).

Figure 4. Field-testing the MC-15 at the Nevada National Security Site: The worker is using the touchscreen on the MC-15 detector, which will measure the special nuclear material inside the container.

The MC-15 is compact enough and light enough (47 pounds) to be transported by a single person. (The single-person lift limit, according to the Occupational Safety and Health Administration [OSHA] is 50 lbs.) The detector works in unforgiving environments because it is self-contained and can be controlled remotely from a computer via an Ethernet connection. It even includes its own power source that lasts for more than 12 hours. The MC-15 uses hot-swappable rechargeable batteries, ensuring continuous operation. It was designed to be easy to use through its onboard touchscreen, and it requires minimal training for personnel who can collect the data but who may not be experts in interpreting the data.

In addition to its principal use in Department of Energy and Department of Justice applications for nuclear and radiological threats, the MC-15 is being used in ongoing research in fields associated with nuclear data and radiation transport validation. This research requires taking precise and accurate measurements of subcritical and critical assemblies that contain SNM.

These validations involve taking measurements of known configurations containing nuclear material and comparing these measurements with calculations. These calculations are typically performed using a stochastic code, such as the Los Alamos National Laboratory Monte-Carlo N-Particle (MCNP®) (https://mcnp.lanl.gov) or a discrete computational code, such as PARallel, TIme-Dependent SN (PARTISN), a Los Alamos-developed code (https://rsicc.ornl.gov/codes/ccc/ccc7/ccc-760.html). Although over the years the accuracy and precision of the calculations have increased, measurements have not. If the measurements do not match the results from the models, then the models are adjusted to ensure consistency. Adjustments to the models may include changing parameters that are easily justified, such as dimensions of materials, all the way to modifying more fundamental parameters, such as nuclear constants. The nuclear constants are incorporated into MCNP®, which are used as part of the design and modeling of nuclear power reactors and their operational safety. The precision of MC-15 has been beneficial in justifying refinements to these nuclear data constants, and thus aids in improving the design and modeling of nuclear power reactors.

The MC-15 has been used to improve upon the resolution and quality of the measured data by taking correlated neutron data. Measurements to support this research have included measuring plutonium surrounded by copper and polyethylene. (For documentation of the evaluations of these nuclear measurements and the associated nuclear data, see "Validating the performance of correlated fission multiplicity implementation in radiation transport codes with subcritical neutron multiplication benchmark experiments," in the Appendix) Additionally, two of these detectors were submerged in the research reactor pool at Rensselaer Polytechnic Institute to compare multiplicity calculations. (See the journal article, "Development of a Research Reactor Protocol for Neutron Multiplication Measurements," in Appendix.)

Figure 5 shows a photo of the measurement configurations using the MC-15 detector at Rensselaer Polytechnic Institute.

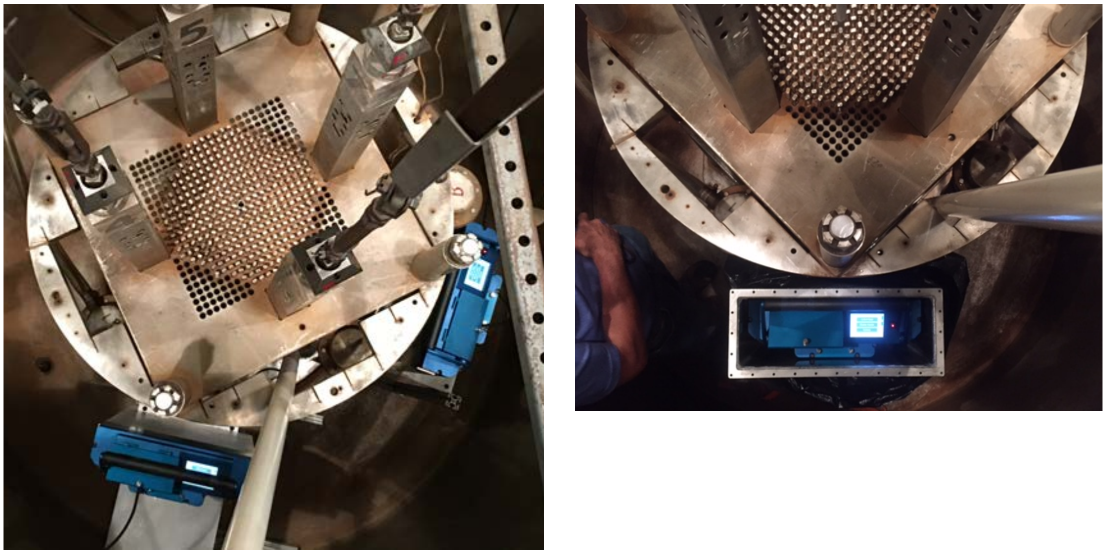

Figure 5. Left: Photo shows of a measurement configuration of two MC-15s (blue) around the reactor core during a measurement at the Reactor Critical Facility (RCF) at Rensselaer Polytechnic Institute (RPI). The measurement was taken of the fuel source (in the middle) when the reactor pool was empty. Right: Measurements were also taken with the pool filled with water; for these measurements, the MC-15s were placed inside water-tight aluminum containers (one MC-15 in container shown here).

Another example of using MC-15 for neutron multiplicity measurements consists of campaigns for the Department of Energy Nuclear Criticality Safety Program, which is dedicated in part to preventing nuclear and radiation accidents resulting from an inadvertent, self-sustaining nuclear chain reaction.

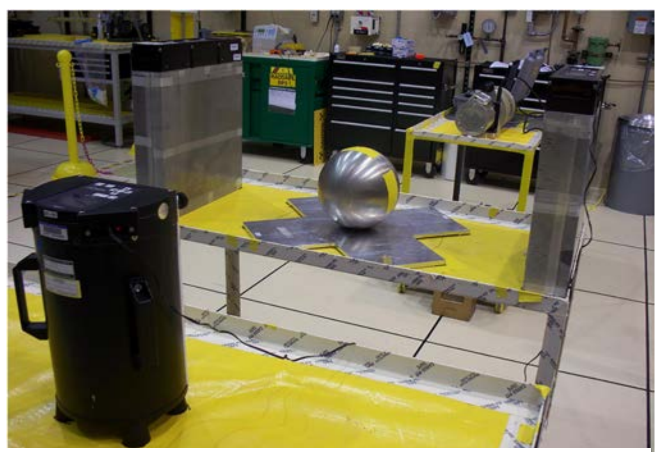

Figure 6. The MC-15 was used in a benchmark experiment at the National Criticality Experiments Research Center (NCERC) at the Nevada National Security Site. The MC-15 was used to investigate intermediate energy neutron cross-sections of a plutonium sphere surrounded by copper, polyethylene, and steel.

Figure 6 shows a benchmark experiment using the MC-15 at the National Criticality Experiments Research Center (NCERC) at the Nevada National Security Site. This experiment, conducted on subcritical experimental configurations, was supported by the Nuclear Criticality Safety Program. (See article describing the experiment, “Subcritical Copper-Reflected α-phase Plutonium (SCRαP) Measurements and Simulations,” in the Appendix.)

For criticality safety purposes, it is extremely important to be able to accurately predict the multiplication of systems for various processes and experiments. This type of accident prevention is also important when it comes to safely operating nuclear power plants.

Other potential applications of this technology include:

- Educational benefits: training for emergency response, international safeguards, and basic nuclear engineering personnel
- International safeguards, including material verification
- Nuclear waste assessment for the nuclear power reactors
- Field search applications, such as rapidly deployable radiation portal monitors, used for screening illicit radioactive materials in vehicles and people and to secure borders

For an overview of the MC-15 neutron detector, see “The Next Generation Neutron Multiplicity Counter for Counterterrorism” in the Appendix.

See Appendix for a “List of sites and organizations where the MC-15 Neutron Multiplicity Detector has been tested or used.”

The following support letters (see Appendix) address the MC-15’s features and applications:

- Patrick Brettell, DOE National Nuclear Security Administration
- D. Mackenzie C. Odell, Gideon Technical Consulting, LLC

How does the product operate? Describe the mechanism of action, theories, materials, composition, or construction.

The MC-15 is comprised of commercially available components; the design and the copyrighted software provides the unique features of the invention.

The MC-15 consists of 15 neutron detectors filled with helium-3 (see Figure 7). All 15 detectors are embedded in a high-density polyethylene block that, through a series of scatters, reduces the energy of neutrons released from fission to maximize detection efficiency. An embedded field-programmable gate array (FPGA) monitors the output from the He-3 tubes, recording each individual detection in a computer file. These data contain the time of each detection with a resolution of 100 nanoseconds, in addition to which tube detected the neutron. Commonly known as list-mode, the most basic data structure enables the collected data to be analyzed by multiple methods, making this information widely accessible to multiple analytical systems.

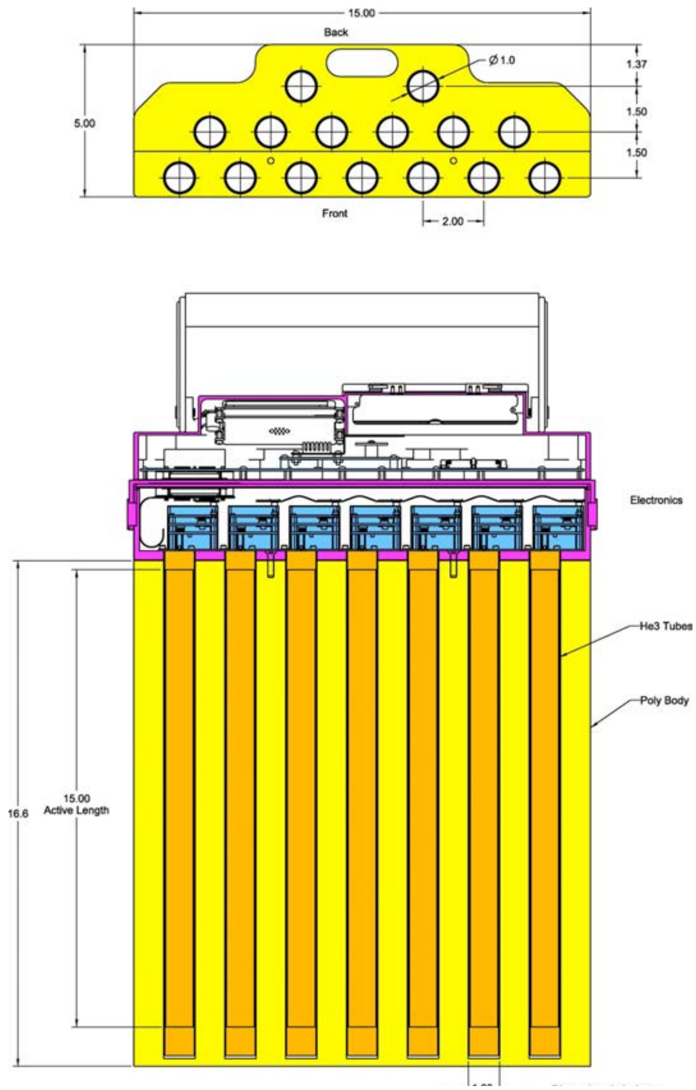

Figure 7. Schematic of the MC-15: 15 helium-3 tubes are embedded in a high-density polyethylene block. These tubes are arranged in three rows. The response of each row depends on the energy spectrum of incoming neutrons. And this can be used to estimate the amount of material around a fission source.

Self-contained, the MC-15 is easy to operate. A user simply interacts with an onboard touchscreen. In particularly hazardous environments (hot, cold, dusty), the MC-15 can be operated via a computer connected to a local Ethernet. Copyrighted MC-15 user application software controls all aspects of the system takes input from the LCD touchscreen or over the local network (see Figure 8). Electrical signals from the He-3 tubes are processed in the copyrighted programmable logic firmware, passed to the data pipeline, then eventually moved to onboard storage or shipped out via the network connection. We intentionally split the processing up among the individual elements (User Interface, CPU, and Programmable Logic) to keep the workload at any one element low while maintaining high overall throughput at low power. The software running on the CPU has direct access to the real-time data being calculated in the firmware, which is updated once each second. This enables the option for real-time data analysis (an important benefit of the MC-15 for emergency responders). That data is passed over to the LCD or can be sent out the network connection.

MC-15 Control and Data Flow Architecture

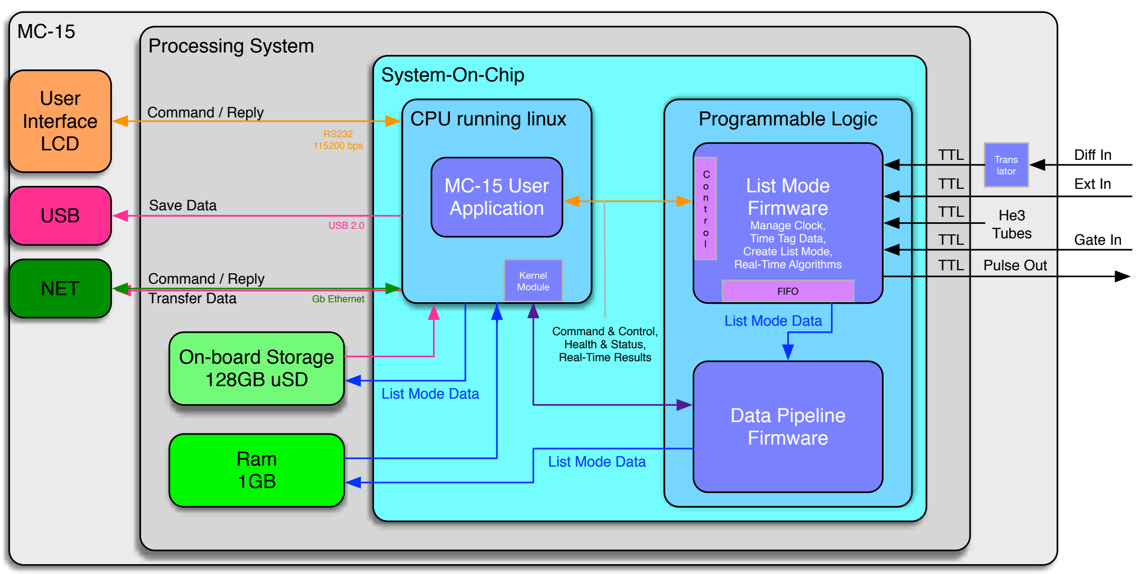

Figure 8. The MC-15 control and data flow architecture (block diagram) showing the electrical signals being processed in the List Mode firmware and being passed to the data pipeline firmware for storage in the onboard memory or transmitted via the network connection.

In a neutron multiplicity detector, after an He-3 tube collects neutrons, it resets, resulting in a "dead-time" when it can't collect neutrons. The MC-15's dead-time is shorter than other competitive detectors. The MC-15's short dead-time allows for more of the neutrons contributing to the singles and doubles rates to be collected. (The singles rate is the rate of detection of single neutron in a fission chain; the doubles rate is the rate of detection of two neutrons from a fission chain.) While a decrease from 4.0 μs to 2.5 μs results in a small decrease in the singles rate, this decrease in dead-time results in a 3% decrease in the doubles rate, which provides better precision for nuclear data evaluation. The accuracy of the singles and doubles rates is even greater when the dead-time is reduced from 5.0 μs to 2.5μs.

The MC-15 has similar detector efficiency per unit as competitive units, but it is smaller, lighter, and faster than the competition. We have designed the MC-15 to work as a single unit or paired with a second MC-15 (see Figure 9). When working in unison, two MC-15s automatically function as a single detector that records which tube in the attached unit had a detection within 100 nanoseconds. Connecting the two MC-15 units can double the detection efficiency of the units. When it comes to neutron multiplicity analysis, scientists are looking for how many times two neutrons are detected from a fission chain. The probability of detecting one neutron is proportional to the efficiency. The probability of detecting two neutrons is proportional to the efficiency squared and the doubles rate can loosely be thought of as a quality factor relating to multiplicity data. (The doubles rate is the detection of two neutrons from the same fission chain.) When the efficiency is doubled, the rate is quadrupled, along with the quality of data. Connecting two MC-15s allows this to happen, improving the detection efficiency as well as the quality of the data.

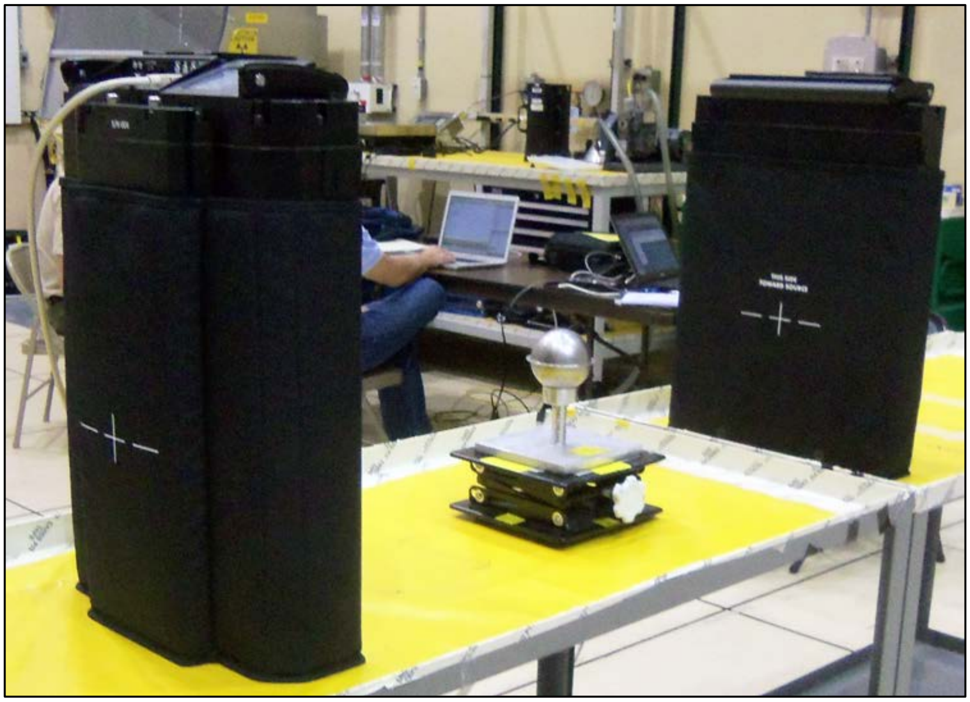

Figure 9. Two MC-15s collecting data on a 4.5-kg sphere of alpha-phase plutonium. This experiment was conducted at the National Criticality Experiments Research Center (NCERC) at the Nevada National Security Site.

To optimize detection efficiency, we used the Monte Carlo N-Particle (MCNP®) computer code for the layout of the He-3 tubes in the MC-15. Los Alamos National Laboratory created and maintains this code.

We have successfully subjected the MC-15 to extensive environmental testing. (See "MC-15 Next Generation Multiplicity Counter Test & Evaluation Report" in Appendix.) Such tests include vibrational testing and simulating transport by passenger vehicle, commercial truck, aircraft, helicopter, and forklift. Other environmental testing included storing the MC-15 in extreme cold and hot environments, as well as misty and dusty environments. The MC-15 passed all these and other tests including the NIST Testing and Evaluation Protocol for Radiation Detection Portal Monitors for Use in Homeland Security. The detection unit even passed drop-testing inside of its shipping case from 1 meter above a concrete surface. These successfully tests demonstrated that the MC-15 can fulfill its designed mission: field use in severe environments.

In another feature on the MC-15, the detector was designed for use with active interrogation. Active interrogation is the process of injecting neutrons into a system that has a low neutron emission rate and may or may not contain nuclear material. To prevent saturation of neutrons from a neutron generator, the MC-15 will suspend data collection when a digital signal from a neutron generator is detected.

For more details about the MC-15, see the following articles in the Appendix:

- "Validating the Performance of Correlated Fission Multiplicity Implementation in Radiation Transport Codes with Subcritical Neutron Multiplication Benchmark Experiments"
- "Development of a Research Reactor Protocol for Neutron Multiplication Measurements"
- "Validation of Statistical Uncertainties in Subcritical Benchmark Measurements: Part II – Measured Data"
- "Comparison of Methods for Determining Multiplication in Subcritical Configurations of a Plutonium System" [*Note: This paper refers to MC-15 by its previous name, NoMAD (Neutron Multiplicity* ^{3}*He Array Detector)*]
- "Comparison of Predicted and Measured Subcritical Benchmark Uncertainties as a Function of Counting Time"

To read more research related to the neutron multiplicity measurements of the MC-15, see the following articles in the Appendix:

- "2-Exponential PDF and Analytic Uncertainty Approximations for Rossi-alpha Histograms"
- "Eliminating Detector Response in Neutron Multiplicity Measurements for Model Evaluation"

Comparison Matrix

Parameter	MC-15	Fission Meter	nPod
Time resolution	**100 ns**	**1 μs**	**1 μs**
Comments: The MC-15 records when a detection occurs with 10 times more precision than the other detectors.			
Was designed for use with active interrogation	**Yes**	**No**	**No**
Comments: Active interrogation is the process of injecting neutrons into a system that has a low neutron emission rate and may or may not contain nuclear material. A neutron generator creates millions of neutrons that bombard a container within a short time. Because there are so many neutrons present in the environment, any detector nearby will become saturated. During this saturation period, it is disadvantageous to keep recording data because such data will need to be stripped from the analysis at a later time and will unnecessarily increase the size of a data file. The MC-15 was designed to suspend data collection when a digital signal from a neutron generator is detected. The other units for comparison do not have this ability.			
Provides onboard and remote operation	**Yes**	**No**	**No**
Comments: Only the MC-15 provides both onboard and remote operation. All control options are available regardless which interface is controlling the MC-15. The Fission Meter requires an additional computer to run and the nPod supports only onboard operation. Onboard processing allows for a real-time calculation of neutron multiplicity, whereas post-processing of the data allows for flexibility by allowing for multiple methods to be used on the data.			
Processes data in real time and has List Mode	**Yes**	**No**	**No**
Comments: Real-time processing means faster analytical times, which are key when action must be taken as quickly as possible. In low count rate measurements, MC-15 reliabily reproduces consistent data. However, the Fission Meter is less consistent due to the way it bins the measurement data. The MC-15 has resources to accommodate additional algorithms available without affecting performance level.			

Parameter	MC-15	Fission Meter	nPod
Synchronizes two units	**Yes**	**No**	**No**
Comments: Only the MC-15 can synchronize two units. Connecting two MC-15s can double the detection efficiency of the units. This doubling of detection efficiency quadruples the “quality” of the multiplicity data. Adding the second unit does not increase the size of the onboard-processed data file stored by the MC-15.			
Maximum count rate	**Approximately 1 million counts per second**	**About 200,000 counts per second (no list-mode data)**	**About 35,000 counts per second**
Comments: The large dynamic range of the MC-15 increases the variety of situations where this detector can be used. High count rates can be experienced with experimental reactors and with nuclear waste assessment.			
Dead-time	**About 2.5 microseconds**	**About 4.0 microseconds**	**About 5.0 microseconds**
Comments: In a neutron multiplicity detector, after an He-3 tube collects neutrons, it resets, resulting in a “dead-time” when it can’t collect neutrons. The MC-15’s dead-time is shorter than the other detectors. Its short dead-time allows for more of the neutrons contributing to the singles and doubles rates to be collected. (The singles rate is the rate of detection of single neutron in a fission chain; the doubles rate is the rate of detection of two neutrons from a fission chain.) While a decrease from 4.0 µs to 2.5 µs results in a small decrease in the singles rate, this decrease in dead-time results in a 3% decrease in the doubles rate, which provides better precision for nuclear data evaluation. The accuracy of the singles and doubles rates is even greater when the dead-time is reduced from 5.0 µs to 2.5µs. This can be seen in the graph and chart below.			

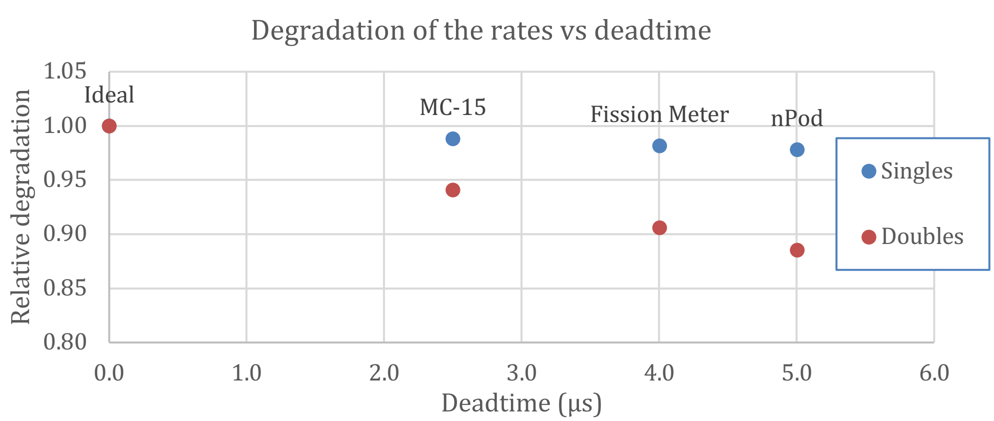

Dead-Time (µs)	Detector	Singles	Doubles
0.0	Ideal	1.00	1.00
2.5	MC-15	0.99	0.94
4.0	Fission Meter	0.98	0.91
5.0	nPod	0.98	0.89

Parameter	MC-15	Fission Meter	nPod
Portability	**Yes**	Partial	Partial

Comments: The MC-15 is the most portable and easiest to operate of the three detectors. The MC-15 is the lightest. In their carrying cases, the MC-15 is 47 lbs, the nPod is 52.5 lbs, and the Fission Meter is 59 lbs. (The single-person lift limit, according to the Occupational Safety and Health Administration [OSHA] is 50 lbs.) The MC-15 is self-contained, has a touchscreen, and can be remotely operated via a Local Area Network. By comparison, the Fission Meter requires an external computer connected to the detector via an RS-232 cable to operate. And although the nPod is self-contained, it does not have a touchscreen.

Describe how your product/service improves upon competitive products or technologies.

Easier to use because of touch-screen LCD. The MC-15 uses an onboard LCD touch-screen for control. This touch-screen makes the detector easier to use than the Fission Meter and the nPod. The Fission Meter requires an external computer to be connected to the unit via an RS-232 cable. By not having an external controller, the MC-15 is quicker to set up, experiences fewer failure modes, and has no chance of losing a critical item for operation. The nPod's interface is a series of push-buttons that require the user to be trained in what buttons control the detector's various operations. The MC-15's touch screen is much more intuitive than either of the competition's interface systems.

The touch screen is a single board computer running Microsoft Windows CE. The user interface software can be customized easily with standard Microsoft software development tools.

Provides onboard and remote operation. Only the MC-15 has the ability to be operated both locally by using the onboard LCD screen and remotely via an Ethernet cable. The ability to remotely operate the MC-15 via an Ethernet cable makes it simple to connect this detector to a local area network in one room and use a computer in a completely different location to control it.

While controlling the MC-15 remotely, the user has the option to store data internally to the MC-15 and retrieve it at a later time, or stream the data over the network connection and store it on the remote computer.

This remote operation capability allows for the MC-15 to be used in environments where it is prohibitive to have personnel present, as was demonstrated when taking measurements in the filled reactor pool at the Walthousen Reactor Critical Facility at Rensselaer Polytechnic Institute. (See the article, "*Development of a Research Reactor Protocol for Neutron Multiplication Measurements*," in Appendix.) Such measurements would have been much more difficult to execute, if they were possible at all, with the other multiplicity detectors because it requires combined local and remote capabilities in one detector; neither of the competitors have that combination.

Processes data in real time. The ability to process the neutron data in real-time allows for immediate feedback to a user as to whether an object is creating neutron chains, which are created only in special nuclear material. This ability is native to the onboard easy-to-use system embedded in the MC-15.

Algorithms are loaded into the programmable logic of the FPGA and run in real-time. Ample resources are available to expand on-board analysis methods as they are developed. Implementing the analyses in firmware removes computational load from the on-board processor allowing it to act in a supervisory mode, thus allowing for significantly higher data collection rates.

In contrast, the Fission Meter requires an external computer to connect to and evaluate the data, and the nPod has no such capability.

Synchronizes two units for the first time. The ability to synchronize two units can double the efficiency of the detector, which quadruples the "quality" of the data. Figures 10 and 11 show plots of the singles and doubles rates recorded by one and two MC-15.

A doubling of the efficiency results in a doubling of the singles rate, the number of times that we detected two neutrons from a fission-chain increased by a factor of four. No other portable neutron multiplicity detector has this capability.

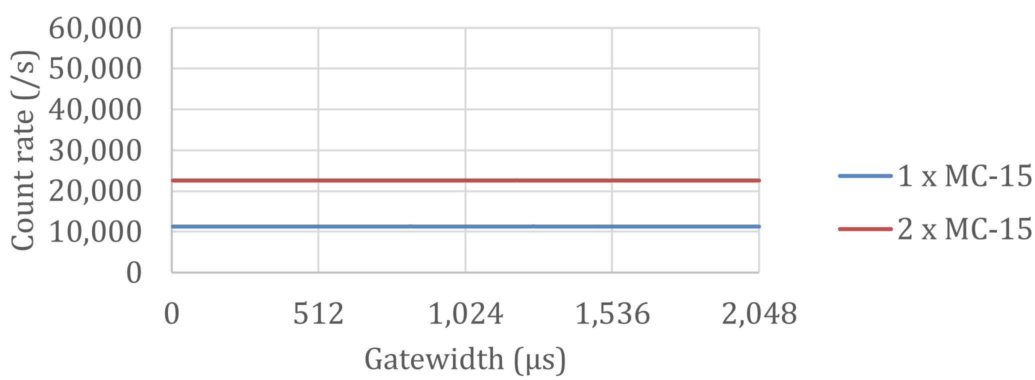

Figure 10. The plot above shows the count rate of an MC-15 for various Feynman-Variance histograms. The count rated doubled when two MC-15s were used.

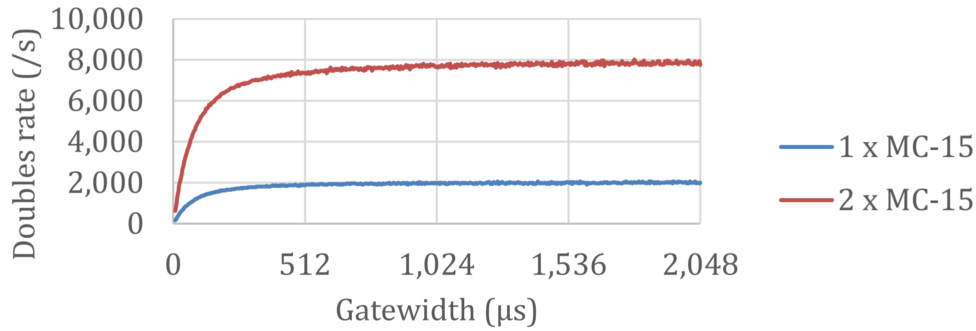

Figure 11. The plot above shows that the doubles rate (which can loosely be correlated to the quality of data) increases by a factor of four when two MC-15s are used to collect data.

Provides maximum count rate. The large dynamic range of the MC-15 increases the variety of situations where this detector can be used.

Due to the unique implementation of data movement from the programmable logic, through a dedicated pipeline into processor memory and then into storage, data collection rates covering 7 orders of magnitude are easily attained.

High count rates can be experienced with experimental reactors and with nuclear waste assessment.

Environmental testing demonstrates that the MC-15 will survive and perform properly in any environment in which it is deployed or stored, during any method of transportation, and during any drops that may occur from handling the detector. The MC-15 sets a new standard for field portable nuclear instrumentation. The MC-15 has passed military specifications for radiation emission sensitivity.

Describe the limitations of your product/service.

The MC-15 is currently lacking a robust onboard chain-length evaluation. To improve this limitation, research is currently underway to evaluate and validate potential threat algorithms for implementation onto the MC-15. Any threat algorithm that is implemented on the MC-15 will be tested before it is programmed onto the MC-15.

Summary

Los Alamos, Lawrence Livermore, and Sandia national laboratories developed the MC-15 neutron multiplicity detector, which is capable of recording neutrons to within 100-nanosecond resolution. MC-15 processes data in real time and can operate either from an easy-to-use onboard touchscreen or remotely from a computer connected to a local Ethernet.

MC-15 is portable, lighter, and faster than any other detector in use today. MC-15 is being used by American highly trained teams at agencies such as the Department of Energy and Department of Justice to resolve radiological threats ranging from illegal nuclear development to illegal nuclear material proliferation to nuclear terrorism attempts.

MC-15 can also be used for research in nuclear data and radiation transport validation. Such research involves taking accurate measurements of subcritical assemblies that contain special nuclear material. The measurements contribute to the precision of nuclear constants, important to nuclear reactor design and modeling, and thus to their safe operation.

Nuclear energy and nuclear-based weaponry canvas the globe. With the MC-15, agencies can continue to ensure that the world remains a safer place.

Support Letters

- Patrick Brettell, DOE National Nuclear Security Administration
- D. Mackenzie C. Odell, Sr., Gideon Technical Consulting LLC

Appendix: Supporting Information

- "The Next Generation Neutron Multiplicity Counter for Counterterrorism: MC-15" (PDF poster).
- "Validating the performance of correlated fission multiplicity implementation in radiation transport codes with subcritical neutron multiplication benchmark experiments," *Annals of Nuclear Energy* **120** (2018), 348–366.
- "Development of a research reactor protocol for neutron multiplication measurements," *Progress in Nuclear Energy* **106** (2018), 120–139.
- "Validation of statistical uncertainties in subcritical benchmark measurements: Part II – Measured data," *Annals of Nuclear Energy* **125** (2019), 342–359.
- "Subcritical Copper-Reflected α-phase Plutonium (SCRαP) Measurements and Simulations," presented at the International Conference on Mathematics & Computational Methods Applied to Nuclear Science & Engineering (Jeju, Korea, April 16–20, 2017).
- "Comparison of Methods for Determining Multiplication in Subcritical Configurations of a Plutonium System," *Proceedings of the PHYSOR 2018* (Cancun, Mexico, April 22–26, 2018). [Note: This paper refers to MC-15 by its previous name, NoMAD (Neutron Multiplicity ^{3}He Array Detector)]
- "Comparison of Predicted and Measured Subcritical Benchmark Uncertainties as a Function of Counting Time," in *Transactions of the American Nuclear Society*, **119** (Orlando, Fla., Nov. 11–15, 2018).
- "2-Exponential PDF and Analytic Uncertainty Approximations for Rossi-alpha Histograms," in *Transactions of the American Nuclear Society,* **119** (Orlando, Fla., Nov. 11–15, 2018).
- Eliminating Detector Response in Neutron Multiplicity Measurements for Model Evaluation," in *Transactions of the American Nuclear Society,* **117** (Washington, D.C., Oct. 29–Nov. 2, 2017).
- "MC-15 Next Generation Multiplicity Counter Test & Evaluation Report," Department of Energy, LLNL-TR-772718 (2019).
- DOE National Criticality Safety Program website, https://ncsp.llnl.gov (April 2019).

- “National Criticality Experiments Research Center,” Los Alamos National Laboratory news release (Sept. 5, 2018), https://www.lanl.gov/discover/news-stories-archive/2018/September/0905-national-criticality-experiments.php
- List of sites or organizations where the MC-15 Neutron Multiplicity Detector has been tested or used (PDF document).

Principal investigators from each of the submitting organizations

PI name: Mark Andrew Nelson
Title: Scientist
Organization: Los Alamos National Laboratory
Email: manelson@lanl.gov
Phone: (505) 500-5132

PI name: Sean Walston
Title: Scientist
Organization: Lawrence Livermore National Laboratory
Email: walston2@llnl.gov
Phone: (925) 423-7364

PI name: Scott Kiff
Title: Scientist
Organization: Sandia National Laboratories
Email: skiff@sandia.gov
Phone: (925) 337-1548

Full development team members

Team member name: Eric Sorenson
Title: R&D Engineer
Organization: Los Alamos National Laboratory
Email: esorensen@lanl.gov
Phone: (505) 665-3630

Team member name: Brian Rooney
Title: R&D Manager
Organization: Los Alamos National Laboratory
Email: rooney@lanl.gov
Phone: (505) 667-5372

Team member name: Richard Rothrock
Title: Guest Scientist
Organization: Los Alamos National Laboratory
Email: rothrock@lanl.gov
Phone: (505) 670-4944

Team member name: Kiril Ianakiev
Title: R&D Engineer
Organization: Los Alamos National Laboratory
Email: iankiev@lanl.gov
Phone: (505) 667-6483

Team member name: Metodi Iliev
Title: R&D Engineer
Organization: Los Alamos National Laboratory
Email: metodi@lanl.gov
Phone: (505) 665-6657

Team member name: Samual Salazar
Title: Electrical Technician
Organization: Los Alamos National Laboratory
Email: samsal@lanl.gov
Phone: (505) 665-3621

Team member name: Chris Romero
Title: Designer-Drafter
Organization: Los Alamos National Laboratory
Email: cdromero@lanl.gov
Phone: (505) 667-3141

Team member name: David Jones
Title: R&D Engineer
Organization: Los Alamos National Laboratory
Email: dcjones@lanl.gov
Phone: (505) 667-0438

Team member name: Jesson Hutchinson
Title: R&D Engineer
Organization: Los Alamos National Laboratory
Email: jesson@lanl.gov
Phone: (505) 667-5411

Team member name: Matthew Newell
Title: R&D Manager
Organization: Los Alamos National Laboratory
Email: mnewell@lanl.gov
Phone: (505) 665-1327

Team member name: Daniel Dietrich
Title: Project Manager (retired)
Organization: Lawrence Livermore National Laboratories
Email: dietrich1@llnl.gov
Phone: (925) 423-7364

Team member name: John Mattingly
Title: Associate Professor
Organization: North Carolina State University – Formerly at Sandia National Laboratories during design of the MC-15
Email: john_mattingly@ncsu.edu
Phone: (919) 515-0224

Marketing and media information

Contact person to handle all arrangements on exhibits, banquet, and publicity.

First name: Janet
Last name: Mercer-Smith
Title: R&D 100 Coordinator
Organization: Los Alamos National Laboratory
Email: mercer-smith_janet@lanl.gov
Phone: 505-665-9574

Contact person for media and editorial inquiries.

First name: Mark
Last name: Nelson
Title: Scientist
Organization: Los Alamos National Laboratory
Email: manelson@lanl.gov
Phone: (505) 500-5132

Company logo

Los Alamos
NATIONAL LABORATORY
EST. 1943

LANL LinkedIn profile URL

https://www.linkedin.com/company/los-alamos-national-laboratory

LANL Twitter handle

https://twitter.com/LosAlamosNatLab

LANL Facebook page URL

https://www.facebook.com/LosAlamosNationalLab

National Nuclear Security Administration

28 March 2019

Subject: Letter of support for MC-15 R&D 100 Award Application

Dear R&D 100 Committee,

I would like to offer my support for the MC-15, the Next Generation Neutron Multiplicity Detector, being granted an R&D 100 award. The MC-15 is the result of years of cooperative effort between Los Alamos National Laboratory, Lawrence Livermore National Laboratory, Sandia National Laboratories, and the National Security Campus in Kansas City. This new detector is quickly becoming a vital part in the Department of Energy's National Nuclear Security Administration's (NNSA) nuclear counter-proliferation mission.

This project was started in order to update and replace aging emergency response (ER) equipment first developed in the 1990s. Some of the capabilities added in the design included easily synchronizing multiple detectors to increase efficiency, adding a native capability to allow active interrogation, and the ability to be easily reconfigured to optimize its effectiveness depending upon situational considerations.

The enhanced versatility of the MC-15 as compared to previous detectors allowed an expansion of the mission space in which it can be used and an increase in the number of intergovernmental partners who can make use of it. This expansion of the number of teams with a portable neutron multiplicity detector greatly increases NNSA's ability to quickly respond to emergencies.

Because of the need to operate across a spectrum of environmental conditions, the MC-15 has undergone and passed extensive environmental resiliency testing. This is an important aspect of the project in that we have a high confidence that this detector will be able to survive the rigors of field deployments.

In addition to being valuable to the ER community this detector is desired for basic research. The design team is moving forward with transferring this technology to a commercial manufacturer so that non-governmental organizations can procure and use the tool for studies of nuclear related investigations.

In summary, the MC-15 is a great step forward in improving the NNSA's capability to responding to nuclear threats and to further investigations into nuclear research. I highly recommend that the MC-15 receive an R&D 100 award. If you have any questions, please contact me at Patrick.Brettell@nnsa.doe.gov or (202) 586-2397.

Patrick Brettell
NA-84 Capability Assurance Program Manager
National Nuclear Security Administration

Gideon
Technical Consulting LLC

Letter of unqualified support for the MC-15 R&D 100 submission

As an electronics, computing, and instrumentation development engineer for over 40 years, I heartily support the submission of the MC-15 neutron multiplicity counter for an R&D 100 award. The features and capabilities of this instrument are a testament to the teamwork and the determination of the NNSA's scientists and engineers to produce the best field deployable instrument of its kind in the world. A short list of its technical highlights will suffice to confirm their success in building not only a highly capable instrument, but also an enduring one:

Outstanding detector performance and stability -- Precision, proprietary, yet inexpensive, amplifiers combine with proven 3He tubes to provide unmatched consistency in performance over time and across a broad range of environmental conditions.

Extensive, highly efficient, on-board computational resources – The combination of a main processor built for high resolution, real time video processing, ample memory for both program storage and computation, and generous, high speed FPGA resources enable rapid development and implementation of on-board, real time data analysis. Code development is straightforward using C++ and a real time Linux OS, resulting in high performance, real time computations running in parallel with loss-free neutron data collection at rates well in excess of 500,000 counts per second. At the same time, twin lithium battery packs provide over eight hours of continuous operation which can be extended indefinitely by hot swapping.

Data collection and connectivity -- List mode data acquisition with 100 nanosecond time resolution enables multi-scale time analyses of data, a first for neutron multiplicity field measurements. Ethernet connectivity provides remote operation and data retrieval anywhere a network connection can be made. With its server mode interface, data retrieval is as simple as accessing a web page for either batch downloads or continuous data streaming.

Rugged and adaptive to changing technologies over its long, intended service life -- The MC-15 has been designed and tested to MIL-SPEC standards for shock, vibration, temperature and humidity, setting a new standard for field portable nuclear instrumentation. With an expected service life of well over a decade under field conditions, the MC-15's electronics backbone is designed to adapt to advances in commercially available user I/O and computational capabilities without redesign and replacement of major components.

D Mackenzie C Odell, Sr. 4 April 2019

D. Mackenzie C. Odell, Sr.
Principal, Gideon Technical Consulting LLC

Los Alamos NATIONAL LABORATORY EST. 1943

The Next Generation Neutron Multiplicity Counter For Counterterrorism MC-15

M. Nelson, E. Sorensen, B. Rooney, S. Salazar, R. Rothrock: NEN-2
C. Romero: AET-1
D. Jones, M. Newell, K. Ianakiev: NEN-1

LA-UR-18-26988

Abstract

- The MC-15 is the next generation of portable neutron multiplicity counters.
- Work was sponsored by NA-84 (Office of Nuclear Incident Response TI Program).
- This is a tri-lab project between LANL, LLNL, and SNL.

Design Highlights

- Design was optimized for efficiency for a variety of sources by using MCNP.
- Modern design practices allowed for rapid prototype changes.
- 16 channels per system.
- 2 systems can easily be synchronized.
- Sunlight readable LCD touch screen interface.
- "Hot swappable" rechargeable batteries.
- Remote Operation by Ethernet.
- Easily Reconfigurable.
- Designed to be used for passive diagnostics as well as with active interrogation systems.
- Records arrival times with 100 ns precision.
- 128 GByte onboard storage.
- Maximum count rate is > 500 kcps.
- Onboard creation of Feynman histograms in real-time.
- Nominated for the 2015 Richard P. Feynman Innovation Prize.

FCI

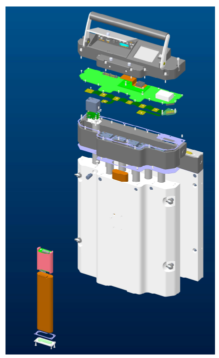

KM-100 Preamp

The preamp was designed by NEN-1 specifically for the MC-15. This preamp has a shorter dead-time than commercially available preamps, which is demonstrated by the plot below of the time-interval between pulses. The commercial preamp used in previous multiplicity counters has a dead-time of approximately 5 to 6 μs while the KM-100 has a dead-time of 2 to 3 μs.

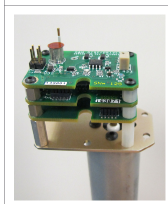

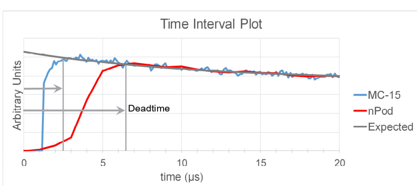

Extensive Environmental Testing

Extensive environmental testing has been performed by LLNL. This testing included a variety of vibrational tests that simulate various modes of transportations. Additional tests included damp environments and temperature extremes. This testing did identify some failure modes which resulted in some design changes.

Multiple rows of He-3 tubes

Fifteen He-3 tubes are embedded in a high density polyethylene block. These tubes are arranged in three rows, which is illustrated in the schematic below.

The response of each row depends upon the energy spectrum of incoming neutrons and this can be used to estimate the amount of material around a fission source. This is demonstrated by the radar plot below which plots the row distribution as a function of moderator thickness around a 4.5 kg plutonium sphere.

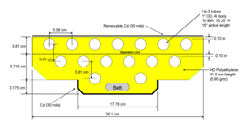

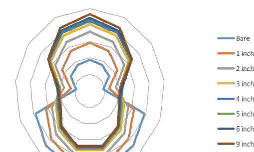

Synchronizing two MC-15's

Two MC-15's can be connected by a synchronization cable, which can double the detection efficiency. A doubling of the efficiency results in twice the count rate, but it also increases the chance of detecting correlated neutrons by a factor of four.

Below shows two MC-15's collecting data on a 4.5 kg sphere of alpha-phase plutonium. The plots below also show the difference in the singles rates when one MC-15 is used versus when two MC-15's are used.

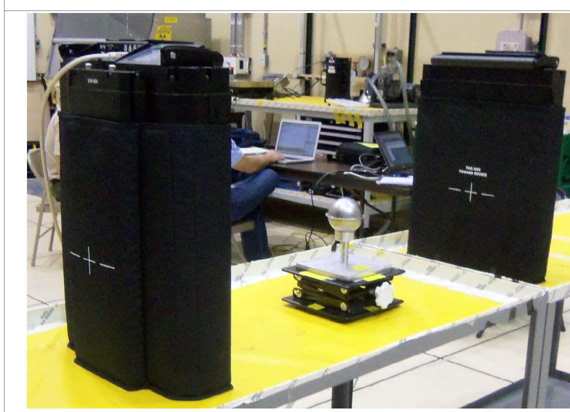

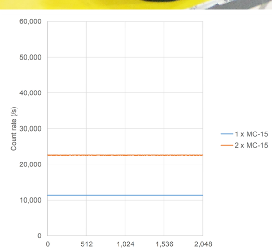

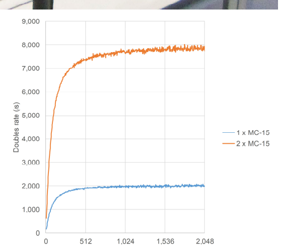

List Mode Data

The MC-15 records when a detection is made and in which tube. Below is a printout of the events recorded in an MC-15. Even if multiple tubes detect a neutron at the same time this information is captured.

Index	Time Tick	Channel	Flag	# Events
974,556	391,645,666	0000 0000 0000 0000 0000 0100 0000 0000		1
974,557	391,645,689	0000 0000 0000 0001 0000 0000 0000 0000		1
974,558	391,645,703	0000 0000 0000 0000 0000 0000 0001 0000		1
974,559	391,646,659	0001 0000 0001 0100 0000 0000 0000 0000		3
974,560	391,648,280	0000 0001 0000 0000 0000 0000 0000 0000		1
974,561	391,649,005	0000 0000 0000 1000 0000 0000 0000 0000		1

List mode allows for multiple methods to be used for analysis on the same data set.

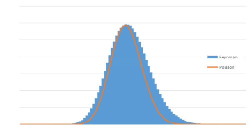

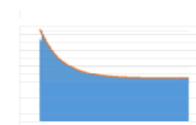

Current Work

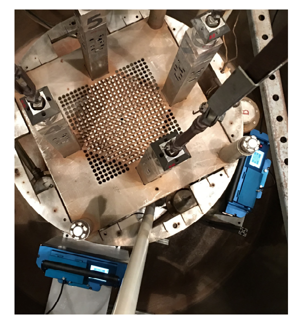

- Field-tested during various measurement campaigns.
- Multiple measurement campaigns, including a series of measurements at the Rensselaer Polytechnic Institute's Reactor Critical Facility (RCF), and measurements at the National Criticality Experiments Research Center (NCERC). The measurements at NCERC have included international partners in support of subcritical benchmarks and other measurements have been in support of the emergency response community.
- The photo to the left shows two MC-15's setup around the reactor core of the RCF.
- The photo to the right shows the MC-15 during field-testing at the Nevada National Security Site (NNSS).

Path Forward

- The MC-15 will continue to be used in future sub-critical nuclear benchmarks.
- The MC-15 is being deployed to the emergency response community.
- Technology transfer to a private company for production and commercialization.

MC15

Annals of Nuclear Energy 120 (2018) 348–366

Contents lists available at ScienceDirect

Annals of Nuclear Energy

journal homepage: www.elsevier.com/locate/anucene

Validating the performance of correlated fission multiplicity implementation in radiation transport codes with subcritical neutron multiplication benchmark experiments

Jennifer Arthur [a,b,*], Rian Bahran [a], Jesson Hutchinson [a], Avneet Sood [a], Michael Rising [a], Sara A. Pozzi [b]

[a] Los Alamos National Laboratory, Los Alamos, NM 87545, United States
[b] University of Michigan Department of Nuclear Engineering and Radiological Sciences, Ann Arbor, MI 48109, United States

ARTICLE INFO

Article history:
Received 20 March 2018
Received in revised form 25 May 2018
Accepted 28 May 2018

Keywords:
Fission multiplicity
Radiation transport
Subcritical benchmark
Neutron multiplication

ABSTRACT

Historically, radiation transport codes have uncorrelated fission emissions. In reality, the particles emitted by both spontaneous and induced fissions are correlated in time, energy, angle, and multiplicity. This work validates the performance of various current Monte Carlo codes that take into account the underlying correlated physics of fission neutrons, specifically neutron multiplicity distributions. The performance of 4 Monte Carlo codes - MCNP®6.2, MCNP®6.2/FREYA, MCNP®6.2/CGMF, and PoliMi - was assessed using neutron multiplicity benchmark experiments. In addition, MCNP®6.2 simulations were run using JEFF-3.2 and JENDL-4.0, rather than ENDF/B-VII.1, data for ^{239}Pu and ^{240}Pu. The sensitive benchmark parameters that in this work represent the performance of each correlated fission multiplicity Monte Carlo code include the singles rate, the doubles rate, leakage multiplication, and Feynman histograms. Although it is difficult to determine which radiation transport code shows the best overall performance in simulating subcritical neutron multiplication inference benchmark measurements, it is clear that correlations exist between the underlying nuclear data utilized by (or generated by) the various codes, and the correlated neutron observables of interest. This could prove useful in nuclear data validation and evaluation applications, in which a particular moment of the neutron multiplicity distribution is of more interest than the other moments. It is also quite clear that, because transport is handled by MCNP®6.2 in 3 of the 4 codes, with the 4th code (PoliMi) being based on an older version of MCNP®, the differences in correlated neutron observables of interest are most likely due to the treatment of fission event generation in each of the different codes, as opposed to the radiation transport.

1. Introduction

Experts in the fields of nuclear nonproliferation, safeguards, and criticality safety have been continually performing subcritical special nuclear material (SNM) measurements since the 1940s. The results of these experiments have provided data used for simulations of SNM systems. Improvements in nuclear detection instrumentation and SNM availability in the 1950s and 1960s lead to increased research activity in both the theory and practice of multiplication and reactivity measurements. Neutron multiplication is an extremely important parameter in SNM systems, as it can give information about the type, enrichment, and risk level of the SNM being investigated for nuclear security reasons. In addition, for criticality safety purposes, it is extremely important to be able to accurately predict the multiplication of systems for various processes and experiments. Neutron multiplication inference measurements take advantage of the fact that neutrons emitted during fission are correlated in time and can be used to gain knowledge about the system being measured. Multiplying system parameters of interest include neutron leakage multiplication M_L, total neutron multiplication M_T, the neutron multiplication factor k_{eff}, and the prompt neutron multiplication factor k_p. M_L represents the average number of prompt neutrons escaping a system for every neutron injected into the system, while M_T represents the number of prompt neutrons created on average by a single neutron in the multiplying system. k_{eff} is a measure of the ratio of the total number of neutrons in the current fission generation to the total number of neutrons in the previous generation. k_p is a measure of the ratio of the number of prompt neutrons in the current fission generation to the number of prompt neutrons in the previous

* Corresponding author at: Los Alamos National Laboratory, Los Alamos, NM 87545, United States.
E-mail address: jennifera@lanl.gov (J. Arthur).

https://doi.org/10.1016/j.anucene.2018.05.051
0306-4549/© 2018 The Authors. Published by Elsevier Ltd.

generation. Some subcritical inferred neutron multiplication parameters of interest are sensitive to the distribution of the number of neutrons emitted per fission. Comparisons between subcritical neutron multiplication inference measurements and simulations have been used to validate multiplication inference techniques and radiation particle transport codes, and to identify and correct deficiencies in underlying nuclear data quantities such as $\bar{\nu}$ (average number of prompt neutrons emitted per fission) (Arthur et al., 2016; Bahran et al., 2014; Sood et al., 2014; Bolding and Solomon, 2013; Miller et al., 2010; Mattingly et al., 2009; Bahran et al., 2014; Boldeman and Hines, 1985). Most notably, recent (1990s and 2000s) methods of obtaining list mode data (time stamps of neutron events registered in a detector) from both measurements and simulations have also been developed and allow for a more detailed comparison between the two (Hutchinson et al., 2016).

More recently, there has been significant progress on the design and execution of benchmark quality subcritical neutron multiplication measurements for radiation transport code and nuclear data validation. The majority of these experiments have involved a 4.5 kg alpha-phase plutonium sphere (BeRP ball) surrounded by copper (Bahran and Hutchinson, 2016), tungsten (Richard et al., 2016), and nickel (Richard et al., 2016). The International Criticality Safety Benchmark Evaluation Project (ICSBEP) Handbook (Briggs, 2014) includes accepted evaluations of both the nickel and tungsten measurements. The ICSBEP handbook contains thousands of critical and subcritical measurement benchmark evaluations. The purpose of the handbook is to provide trusted benchmarks for validation and improvement of nuclear databases and radiation transport codes. The nickel benchmark was the first ICSBEP-accepted evaluation of measurements analyzed with the Hage-Cifarelli formalism based on the Feynman Variance-to-Mean method (Cifarelli and Hage, 1986), and was the culmination of many years of collaborative subcritical experiment research (Arthur et al., 2016; Bahran et al., 2014; Sood et al., 2014; Bolding and Solomon, 2013; Miller et al., 2010; Mattingly et al., 2009; Hutchinson et al., 2016; Richard et al., 2016; Richard et al., 2016; Hutchinson et al., 2013; Hutchinson et al., 2014; Hutchinson et al., 2013; Hutchinson et al., 2015).

This work investigates the performance of various current Monte Carlo codes that take into account at least some of the correlated physics of fission neutrons (i.e. correlations in time, energy, angle, or some combination of the three). Historically, radiation transport codes have uncorrelated fission emissions. In reality, both spontaneous and induced fissions release particles that are correlated in time, energy, angle, and multiplicity. The fission process can be either spontaneous or initiated by an interacting neutron. In the case of spontaneous fission, the nucleus is inherently unstable and randomly decays by fission. In the case of neutron-induced fission, an unstable compound nucleus forms after an incident neutron collides with the original nucleus. In either case, the nucleus scissions into two fission fragments, which receive some of the energy liberated from the rearrangement of mass as kinetic energy. The fission fragments release the remaining energy in the form of prompt neutron emission, prompt gamma ray emission, and delayed β or electron conversion decay. Because the particles are emitted from moving fission fragments, the multiplicities, energies, and angles of emission of prompt neutrons and gamma rays are dependent upon both each other and the initial masses and kinetic energies of the fission fragments (Wagemans, 1991). For this work, only prompt fission neutrons are of interest and the authors do not consider the physics of gamma production in fission. Because of their large impact on correlated neutron results, this work also compares underlying fission neutron multiplicity distributions utilized by the different codes.

2. Correlated fission multplicity

2.1. Nuclear data

For the purposes of this paper we will be focusing on the nuclear reaction database utilized by the general purpose Monte Carlo code MCNP®6.2[1], namely the Evaluated Nuclear Data File (ENDF) (Chadwick et al., 2011), although results will also be obtained using the Joint Evaluated Fission and Fusion File (JEFF) (Santamarina et al., 2009) and the Japanese Evaluated Nuclear Data Library (JENDL) (Shibata et al., 2011). ENDF contains information related to the types and probabilities of the different possible reactions between radiation particles and various isotopes. Evaluators use data from high-quality differential measurements to evaluate nuclear data libraries such as ENDF, and comparisons of simulated and measured data from benchmark-quality integral measurements to validate the libraries. Fig. 1 summarizes the process. Included in the information provided by ENDF are data summarizing both the probability of fission occurring and the average number of neutrons released per fission of each fissionable isotope, represented as $\bar{\nu}$, as functions of incident neutron energy. The multiplicity distribution $P(\nu)$ represents the probability for ν neutrons to be emitted per fission. Complete multiplicity distributions, $P(\nu)$, are not included in ENDF/B-VII.1; correlations in angle and energy are also not included.

Overall, the ENDF evaluation process focuses on complying as closely as possible with differential experimental data contained in the CSISRS (or EXFOR) database (NRDC-Network, 2017), while simultaneously showing general agreement with critical benchmark measured data. Evaluators did not make any changes to $\bar{\nu}$ between the previous evaluation (ENDF/B-VII.0) and the current evaluation (ENDF/B-VII.1) (Chadwick, 2006). Therefore, the evaluation process of the ENDF/B-VII.0 version will be described with regard to $\bar{\nu}$. For the ENDF/B-VII.0 evaluation, the experimental database from the ENDF/B-VI evaluation was used, with corrections to the normalization of the $\bar{\nu}$ nuclear data. This resulted in evaluations that match well with the corrected experimental database for ^{235}U, ^{238}U and ^{239}Pu. Appreciable deviation from experimental data occurs in the energy range below 1.5 MeV for ^{239}Pu, and this is partially due to the desire to match JEZEBEL (a LANL fast critical benchmark experiment) results in particular (Chadwick, 2006).

One of the main parameters of interest that is used to validate ENDF is the effective multiplication factor k_{eff}, which is sensitive to $\bar{\nu}$ but not to the other moments of the $P(\nu)$ distribution. The effective multiplication factor is in general insensitive to changes in the correlated physics of fission and depends only on averages. This can be illustrated by examining the neutron transport equation, which consists of terms representing the loss of neutrons due to leakage out of the system, the loss of neutrons due to all interactions, the addition of neutrons due to in-scattering from another energy group, and the production of neutrons due to fission. Only the average quantity $\bar{\nu}(E)$ is required to calculate neutron transport and the effective multiplication factor of a system. However, by looking at the Hage-Cifarelli equation for the leakage multiplication of a system, in Eqs. (11) and (12), which are presented and explained later in this work, it is clear that other moments of the multiplicity distribution (ν_{s2}, ν_{I2}) are also important.

The average number of neutrons released per fission is a specific measured observable of some of the differential measurements of fission product yields, masses, and fission neutron energy spectra contained in EXFOR. Because of the contribution of neutrons from

[1] MCNP® and Monte Carlo N-Particle® are registered trademarks owned by Los Alamos National Security, LLC, manager and operator of Los Alamos National Laboratory.

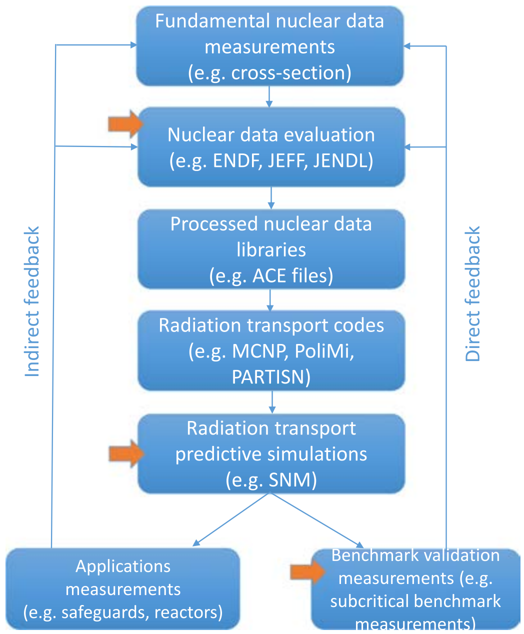

Fig. 1. The nuclear data evaluation and validation process. Arrows indicate the steps in the process that this work focuses on.

interactions other than fission, it is difficult to measure characteristics of the fission neutrons only, such as the spectra or the number released per fission, especially at high incident neutron energies. In addition, some actinides are not readily available in a very pure isotopic concentration, and impurities affect the observed yields. Methods such as time-of-flight, multiplicative transmission through a fissionable target, and gamma-ray spectroscopic techniques have been used to measure fission yields, but overall few measurements of this type have been conducted. As a result of the lack of reliable differential fission yield measurements, semi-empirical calculations and systematic fission models have been used by nuclear data evaluators (Barnard et al., 1965; Flerov and Talyzin, 1960; Iyer et al., 2000; Naika et al., 2013; Howerton, 1977; Madland and Nix, 1982; Holden and Zucker, 1988; Rising, 2013). Thus, integral measurements that are sensitive to the nuclear data corresponding to fission yields, such as $\bar{\nu}$ and fission neutron energy spectra, are very important for fission yield nuclear data validation and evaluation.

The goal of this work is to apply subcritical ICSBEP benchmarks to comparisons of measured correlated neutron observables, and simulated observables generated by various Monte Carlo (MC) radiation transport codes that take into account various parts of the correlated physics of fission neutrons. Such comparisons will offer a type of validation that has never before been considered in nuclear data evaluation. In addition, this work investigates the effects of the different multiplicity distributions used by various MC codes on correlated neutron observables of interest.

2.2. Implementation in transport codes

The Monte Carlo radiation transport codes that this work currently compares include MCNP (Goorely, 2012), MCNP/FREYA (Rising et al., 2014; Hagmann, 2013), MCNP/CGMF (Talou, 2013), and PoliMi (Pozzi, 2012; Pozzi et al., 2003). The first few of these codes are specific releases of or options contained in the Monte Carlo N-Particle (MCNP) code, the precursors of which were originally developed during the Manhattan Project era to simulate neutron diffusion and multiplication in fissioning systems (Goorely, 2012). Diffusion and multiplication depend on average quantities only, and do not require modeling of the correlated physics of fission. Therefore, the correlated physics of fission was irrelevant for the Monte Carlo transport code developers at that time, and average parameters such as $\bar{\nu}$ were sufficient to simulate the fission process. However, with the increasing interest in nuclear security, safeguards, and nonproliferation, experimenters are desiring extremely accurate predictive modeling of SNM measurements. SNM has correlated fission emissions, and therefore average event treatment is not always sufficient for these applications. This work investigates various codes that are able to handle correlated fission quantities of interest, such as spontaneous and induced fission multiplicity distributions.

By default, MCNP uses a bounded integer treatment and the $\bar{\nu}$ data from ENDF to sample the number of neutrons emitted from each simulated fission event. In the bounded integer treatment, the two integers bounding $\bar{\nu}$ are the only values of ν that are sampled, instead of a complete multiplicity distribution. The FMULT card, an optional input in MCNP that allows for user definition of spontaneous and induced fission parameters, can be utilized to call either built-in or user-specified multiplicities to replace the bounded integer treatment (MCNP6, 2013). The user can also use the FMULT card to call either the Fission Reaction Event Yield Algorithm (FREYA) or the Cascading Gamma-Ray Multiplicity with Fission (CGMF) fission event generating codes to handle fission. The FREYA fission event generator determines the number, energy, and direction of particles emitted for each fission event and gives the results to MCNP for transport. The fission event generator uses fission fragment mass and kinetic energy distributions, unbounded statistical evaporation models, and conservation of energy and momentum to generate the number, energy, and direction of neutrons released by each fission event using the Monte Carlo Weisskopf approach. The Weisskopf approach repeatedly samples emitted neutron parameters from the Weisskopf distribution, until the remaining fission fragment excitation energy is below a specified threshold. This fission fragment then releases the remaining excitation energy in the form of fission gamma rays. Eqs. (1)–(3) describe the sampling process of emitted neutrons. Eq. (1) is used to calculate the maximum temperature of the evaporated neutron from the Q-value for neutron emission (Q_n) and the level-density parameter of the fission fragment nucleus (a_d). The neutron kinetic energy in the center of mass frame (ϵ_n) is then sampled from Eq. (2). Finally, the new excitation energy of the fission fragment is recalculated using Eq. (3), and the process repeats until E_d^* falls below the specified excitation energy threshold (Hagmann, 2013; Rising et al., 2014; Verbeke et al., 2015; Verbeke et al., 2016).

$$a_d T_{max}^2 = Q_n \tag{1}$$

$$f_n(\epsilon_n) \sim \epsilon_n exp\left(\frac{-\epsilon_n}{T_{max}}\right) \tag{2}$$

$$E_d^* = Q_n - \epsilon_n \tag{3}$$

CGMF generates prompt fission neutrons using the statistical Hauser-Feshbach formalism (Hauser and Feshbach, 1952; Talou, 2013), which is the primary difference between FREYA and CGMF, and gives results to MCNP for transport. The Hauser-Feshbach approach accounts for the competition between neutrons and gamma rays emitted during the fission process. It is therefore technically a more complete fission model, but significantly increases computational time. Eq. (4) is used to sample the emitted neutron kinetic energies, and makes use of transmission coefficients (T_n) calculated using optical models. In this equation $\rho(Z, A-1, E-\epsilon_n-S_n)$ is the level density of the fission fragment nucleus after the neutron is emitted (Z is the atomic number, and $A-1$ is the new atomic mass), using the remaining available excitation energy (the original excitation energy E, minus the emitted neutron kinetic energy ϵ_n and the neutron separation energy S_n) (Talou, 2013; Rising et al., 2014).

$$P(\epsilon_n)dE \propto T_n(\epsilon_n)\rho(Z, A-1, E-\epsilon_n-S_n) \tag{4}$$

PoliMi utilizes a few different built-in multiplicity sets, and also models both the angular anisotropy and multiplicity-dependent energy spectra of neutrons emitted in spontaneous fission. The user is able to choose which spontaneous and induced fission built-in multiplicity distributions to use, and whether or not to turn on the modeling of angular anisotropy in spontaneous fission sources (Padovani et al., 2012; Santi and Miller, 2008; Terrell, 1957).

3. Benchmark experiments

3.1. Inferred multiplication benchmarks

Historically, criticality safety has always been a concern for those working with systems containing nuclear material. In the early years of the nuclear industry, physical experiments were used to answer questions pertaining to criticality safety. Then, analytic calculations were performed using computers. Finally, Monte Carlo radiation transport simulation techniques were developed that allowed for accurate modeling of complex multi-dimensional systems. Because of this, validation of radiation transport codes and associated basic nuclear data through comparisons with integral experimental data became an issue of importance to the criticality safety field. Experimenters executed many measurements, but these measurements lacked quality assurance and sufficient documentation. ICSBEP was created by the United States Department of Energy in 1992 to satisfy this need for systematic evaluation and documentation of integral experimental data, and the Organisation for Economic Cooperation and Development (OECD) - Nuclear Energy Agency (NEA) took on the project as one of its official duties in 1995 (Briggs, 2014; Briggs, 2003). The ICSBEP handbook contains thousands of benchmark quality critical and subcritical measurement evaluations from Argentina, Brazil, Canada, China, the Czech Republic, France, Germany, Hungary, India, Japan, Kazakhstan, Poland, Russia, Serbia, Slovenia, Spain, Sweden, the United Kingdom, and the United States. The purpose of the handbook is to provide peer-reviewed benchmark quality data for validation and improvement of nuclear databases and radiation transport codes, specifically codes that calculate the effective neutron multiplication factor (Briggs, 2014; Briggs, 2003). Several of the included measurements involve inferred multiplication measurements, wherein list-mode data is used to calculate leakage multiplication from the sample of interest. The result can then be compared to both criticality and fixed source Monte Carlo calculations for validation purposes. Raw list-mode data and other parameters of interest can also be compared.

3.2. Reflected plutonium benchmark series

In recent years Los Alamos National Laboratory (LANL) has performed several reflected plutonium benchmark experiments (Hutchinson and Loaiza, 2007; Richard et al., 2016; Richard et al., 2016; Hutchinson et al., 2017). In this study, performance of the different codes is compared using various plutonium metal benchmark cases. The growing database of subcritical neutron multiplication inference benchmark experiments includes recent benchmark experiments with a 4.5 kg α-phase plutonium sphere (BeRP ball) surrounded by copper (Hutchinson et al., 2017), tungsten (Richard et al., 2016), and nickel (Richard et al., 2016). Evaluations of the measurements were the first ICSBEP-accepted evaluations of measurements using the Feynman Variance-to-Mean method. This was the culmination of many years of subcritical experiment research, including measurements in 2009 by Sandia National Laboratory (Mattingly et al., 2009; Miller, 2012) which showed a marked sensitivity of subcritical leakage multiplication to the full ^{239}Pu induced fission multiplicity distribution, and indicated the possible existence of nuclear data deficiencies (Hutchinson et al., 2016).

The available BeRP benchmark MCNP models have been adjusted to be compatible with the other codes while maintaining the original measurement geometries. The measured benchmark results are also available for comparison. The typical reflected plutonium subcritical benchmark measurement setup involves the BeRP ball surrounded by various thickness of metal reflectors, with multiplicity detectors 50 cm on either side, as shown in Fig. 2. The BeRP-Ni benchmark geometry consists of the BeRP ball surrounded by various thicknesses of nickel reflectors, ranging from 0 in. to 3.0 in., with a LANL ^{3}He multiplicity detector (NPOD) 50 cm away on either side, as shown in Fig. 3. The BeRP-W benchmark consists of the BeRP ball surrounded by various thicknesses of tungsten reflectors, ranging from 0 in. to 3.0 in., with an NPOD 50 cm away on either side, as shown in Fig. 4. The NPOD consists of 15 ^{3}He neutron detectors inside a polyethylene moderator, and is a predecessor to the currently used NoMAD (Moss et al., 2016; Richard et al., 2016; Richard et al., 2016).

4. Data analysis method

4.1. Multiplicity distributions

The ^{239}Pu neutron induced fission and ^{240}Pu spontaneous fission multiplicity distributions $P(\nu)$ used by all of the codes are investigated for comparison purposes. Because this work focuses on BeRP ball experiments, all induced fissions are assumed to be of ^{239}Pu, and all spontaneous fissions of ^{240}Pu. This is because, at the time of both the BeRP-Ni and BeRP-W experiments, the ^{239}Pu and ^{240}Pu atomic fractions in the BeRP ball were 9.260E-01 and 5.838E-02, respectively, with the next largest actinide atomic fraction being 2.527E-03 (^{241}Am). In addition, the percentage of spontaneous fission neutrons coming from ^{240}Pu was calculated to be 98.5% (Richard et al., 2016; Richard et al., 2016). The singles, doubles, and Feynman histogram results are expected to be sensitive to differences in the underlying multiplicity distributions. User-defined MCNP and PoliMi distributions are obtained from Lestone (Lestone, 2005), Santi (Santi and Miller, 2008), and Terrell (Terrell, 1957). Multiplicity distributions are specified as either a cumulative distribution function (CDF) or as a Gaussian mean ($\bar{\nu}$) and width (σ). If the distribution is given as a CDF, the probability distribution function (PDF) and mean and width are solved for. If the distribution is given as a Gaussian mean and width, the PDF is calculated. In the case of induced fission multiplicity distributions for MCNP and PoliMi, the means are obtained as a function of incident neutron energy from the nuclear data library ENDF/B-VII.1 and only the widths come from the above references. MCNP/FREYA and MCNP/CGMF $P(\nu)$, which are produced by the fission event generator of the code rather than being pulled from a pre-existing multiplicity distribution, are extracted from the particle track (PTRAC) file. The PTRAC file gives the individual ν for each fission, from which a frequency distribution is formed. The Gaussian mean and width are calculated from the frequency distribution, which is treated as a PDF.

The spontaneous and neutron induced fission (at 2 MeV incident neutron energy) multiplicity distributions for each code were obtained from Lestone, Santi, and Terrell (Lestone, 2005; Santi and Miller, 2008; Terrell, 1957), as well as the ENDF/B-VII.1 library and

Fig. 2. CAD image of a typical reflected plutonium setup (left), and picture of the BeRP ball within metal reflector shells (right).

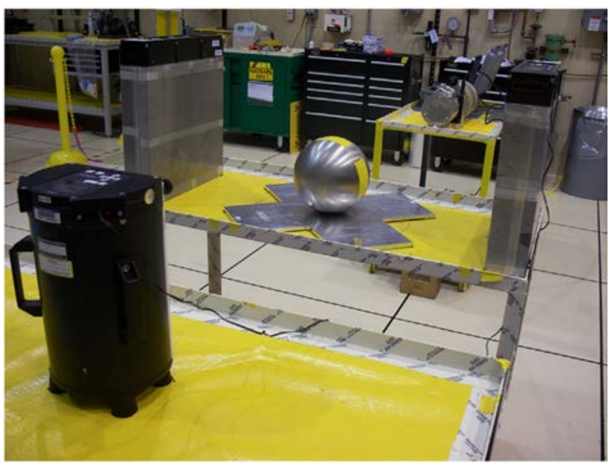

Fig. 3. Picture of the BeRP-Ni benchmark experiment being conducted at the National Criticality Experiments Research Center (NCERC).

Fig. 4. Picture of the BeRP-W benchmark experiment being conducted at NCERC.

the PTRAC output file. Fig. 5 shows plots of the multiplicity distributions, with tabular versions of the data given in Table 1. 2 MeV was chosen as a representative energy for induced fission due to the fact that the average energy of neutrons causing fission in the bare BeRP system is 1.98 MeV (Richard et al., 2016). To obtain an isolated 2 MeV induced fission multiplicity distribution for MCNP/FREYA and MCNP/CGMF, PTRAC files resulting from simulations of an isotropic 2 MeV neutron source hitting a thin film of pure ^{239}Pu were used.

Table 1 shows that the first moment of the spontaneous fission multiplicity distribution is significantly higher for CGMF compared to all of the other codes, while the first moment of the induced fission multiplicity distribution is significantly lower for FREYA. In addition, the standard deviation (the square root of the second moment) of the spontaneous fission multiplicity distributions are much higher for Lestone and Santi than for the fission event generators (FREYA and CGMF), while the standard deviations of the induced fission multiplicity distribution are more clustered together. Differences in $P(\nu)$ are likely a cause of discrepancies in Feynman histograms and doubles rates. Singles rates are expected to change only with the mean of the multiplicity distribution, $\bar{\nu}$, rather than with both the mean and the width (standard deviation), σ. This is expected because the singles and doubles rates depend on the first and second factorial moments of the binned list-mode data, respectively (see next section).

4.2. List-mode data and Feynman analysis

List-mode data, containing the time and detector tube corresponding to the particle interaction, are obtained from the PTRAC output files of MCNP, and the collision data file of PoliMi. The list-mode data is binned into Feynman histograms according to specified time widths using the data processing tool Momentum (Smith-Nelson, 2015). A Feynman histogram is a representation of the relative frequencies of various multiplets (i.e., 1 event, 2 events, etc.) occurring within the specified time width, as illustrated in Fig. 6.

The magnitude of the nth bin of the Feynman histogram at the specified time width τ is represented by the variable $C_n(\tau)$ in Eq. (5). Standard multiplicity equations, in the form of Eqs. (5)–(12) (Hutchinson et al., 2015), are applied to calculate the singles (R_1) and doubles (R_2) rates, as well as the leakage multiplication (M_L). The values C_1, C_2, and C_3 in Eq. (12) are unrelated to the $C_n(\tau)$ in Eq. (5). It should be noted that the derivation of these equations includes the assumption that the contribution of neutrons from (α, n) reactions is negligible, which is an acceptable assumption for plutonium metal systems such as the metal-reflected BeRP ball. The "singles" rate is defined as the rate of detection of single neutrons from a fission chain.

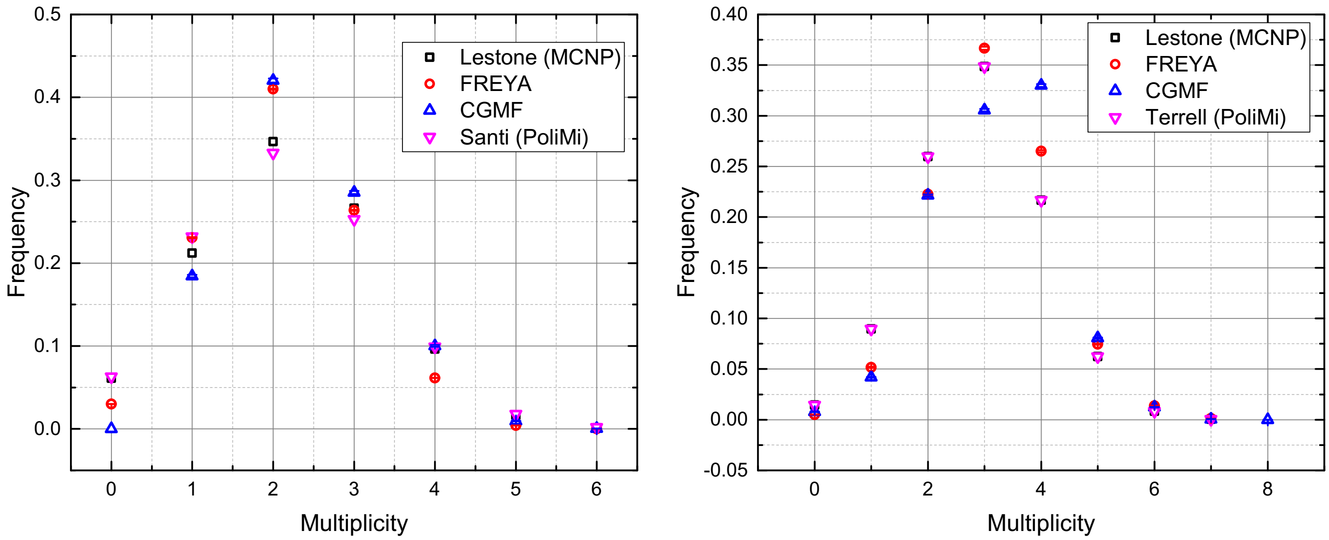

Fig. 5. ^{240}Pu spontaneous fission (left) and ^{239}Pu induced fission at 2 MeV incident neutron energy (right) multiplicity distributions utilized by the various codes.

Table 1
^{240}Pu spontaneous fission (SF) and ^{239}Pu induced fission (IF) multiplicity distribution parameters utilized by the various codes.

Code	SF $\bar{\nu}$	SF σ	IF $\bar{\nu}$	IF σ
MCNP	2.151 (Lestone)	1.151 (Lestone)	3.178 (ENDF)	1.140 (Lestone)
MCNP/FREYA	2.109	0.942	3.128	1.057
MCNP/CGMF	2.225	0.949	3.202	1.191
PoliMi	2.093 (Santi)	1.199 (Santi)	3.178 (ENDF)	1.140 (Terrell)

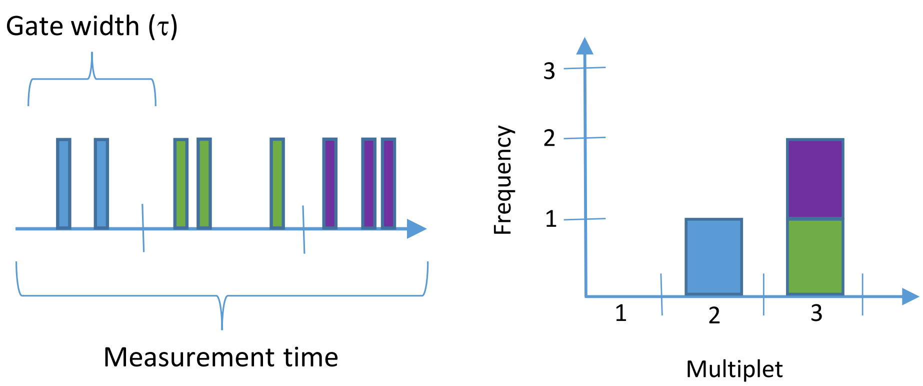

(a) (b)

Fig. 6. The binning method (a) used to generate Feynman histograms (b) in this work.

The "doubles" rate is defined as the rate of detection of two neutrons from the same fission chain. Leakage multiplication is the number of neutrons escaping a multiplying system per a single neutron injected into the system. In the following equations the symbols λ, ϵ , ν_{Ii} and ν_{si} represent the inverse neutron lifetime, detector absolute efficiency, ith factorial moment of the induced fission multiplicity distribution, and ith factorial moment of the spontaneous fission multiplicity distribution, respectively. Y_2 is directly proportional to the Feynman Y value, which is a measure of the deviation of the histogram from a Poisson distribution.The inverse of the neutron lifetime can be obtained by fitting the curve of Y_2 versus time width, because Y_2 is proportional to ω_2 (Cifarelli and Hage, 1986). The inverse of the neutron lifetime is then used as an input to ω_2. Table 2 lists the most commonly used units for many of the variables presented in this section.

Table 2
Most commonly used units for many of the variables used in this work for correlated neutron detection.

Variable	Units
τ	μs
$C_n(\tau)$	# of occurrences
$R_1(\tau)$	s^{-1}
$R_2(\tau)$	s^{-1}
λ	s^{-1}
ϵ	unitless
M_L	unitless

$$p_n(\tau) = \frac{C_n(\tau)}{\sum_{n=0}^{\infty} C_n(\tau)} \tag{5}$$

$$m_r(\tau) = \frac{\sum_{n=0}^{\infty} n(n-1)\dots(n-r+1)p_n(\tau)}{r!} \tag{6}$$

$$R_1(\tau) = \frac{m_1(\tau)}{\tau} \tag{7}$$

$$Y_2(\tau) = \frac{m_2(\tau) - \frac{1}{2}[m_1(\tau)]^2}{\tau} \tag{8}$$

$$\omega_2(\lambda, \tau) = 1 - \frac{1 - e^{-\lambda\tau}}{\lambda\tau} \tag{9}$$

$$R_2(\tau) = \frac{Y_2(\tau)}{\omega_2(\lambda, \tau)} \tag{10}$$

$$M_L = \frac{-C_2 + \sqrt{C_2^2 - 4C_1C_3}}{2C_1} \tag{11}$$

$$C_1 = \frac{\nu_{s1}\nu_{I2}}{\nu_{I1} - 1},\ C_2 = \nu_{s2} - \frac{\nu_{s1}\nu_{I2}}{\nu_{I1} - 1},\ C_3 = -\frac{R_2(\tau)\nu_{s1}}{R_1(\tau)\epsilon} \tag{12}$$

4.3. Uncertainty and correlation analysis

Uncertainties associated with the multiplicity distributions obtained from simulation output files are calculated using Poisson counting statistics (because radioactive decay is a Poissonian process, the predicted standard deviation can be calculated as the square root of the experimental mean (Knoll, 2010)). The uncertainty associated with each possible number of neutrons emitted during fission is equal to the square root of the number of times the given number of neutrons was emitted in the simulation. Feynman histogram uncertainties are also calculated using Poisson counting statistics. The uncertainty associated with each bin in the histogram is equal to the square root of the number of multiplets in the given bin. Reference (Hutchinson et al., 2015) contains equations for the uncertainties in R_1, R_2, and M_L. All uncertainties for other derived quantities (such as (C-E)/E) are calculated using standard uncertainty propagation, according to Eq. (13).

$$\sigma_z^2 = \left(\frac{\delta z}{\delta x}\right)^2 \sigma_x^2 + \left(\frac{\delta z}{\delta y}\right)^2 \sigma_y^2 + \dots \tag{13}$$

In order to investigate the existence of correlation between different observables and nuclear data items of interest, the Pearson correlation coefficient was used. Eq. (14) is used to calculate the sample Pearson correlation coefficient. If $r = -1, r = 0$, or $r = 1$, then x and y are considered to be completely anti-correlated, completely uncorrelated, or completely correlated, respectively. As applied to this work, each sample consists of a single observable and single nuclear data item for a single configuration of a single benchmark experiment, across all of the different radiation transport codes being compared.

$$r = \frac{\sum_{i=1}^{n}(x_i - \bar{x})(y_i - \bar{y})}{\sqrt{\sum_{i=1}^{n}(x_i - \bar{x})^2}\sqrt{\sum_{i=1}^{n}(y_i - \bar{y})^2}} \tag{14}$$

As applied to this work, in Eq. (14), n is the number of codes being compared, x_i is the value of a single observable of interest for the ith code, y_i is the value of a single nuclear data item of interest for the ith code, $\bar{x}$ is the mean of all values of x, and $\bar{y}$ is the mean of all values of y. Because this work includes 3 observables of interest (R_1, R_2, and M_L), 4 nuclear data items of interest (SF and IF $\bar{\nu}$ and σ), and 8 different configurations of the BeRP-W benchmark, 96 values of r exist.

5. Results

5.1. Multiplicity distributions

Fig. 7 shows induced fission multiplicity distributions for a few representative configurations of the BeRP-W benchmark for MCNP, MCNP/FREYA, MCNP/CGMF, and PoliMi. The induced fission multiplicity distributions include all incident neutron energies and are obtained from the PTRAC output files for MCNP based codes, and the collision output file for PoliMi. The multiplicity distribution mean ($\bar{\nu}$) and width (σ) values in Table 3 were obtained using the statistical definitions of mean and standard deviation. Appendix A plots the multiplicity distribution means and widths across all BeRP-W configurations.

As expected, the widths of the MCNP and PoliMi distributions do not change for different energies (reflector thicknesses). Overall, the means decrease slightly with decreasing energy, as do the widths for MCNP/FREYA and MCNP/CGMF. The multiplicity distributions do not vary much for the different reflector thicknesses because the neutron energy spectrum remains quite fast for all configurations. Between codes $P(\nu)$ is similar, with most discrepancies being located to the center of the distribution. Regarding the discrepancies between $P(\nu)$ for the fission event generators, the CGMF and FREYA fission event generators both compute the decay of a large ensemble of fission fragments formed in excited states, following the emission of prompt neutrons and gamma rays sequentially and on an event-by-event basis. There are many differences between those codes that can explain differences observed in $P(\nu)$, but of particular importance is the distribution of fission fragments in total kinetic energy (TKE). While the average TKE correlates strongly with $\bar{\nu}$, the higher moments of the TKE distribution correlate strongly with the higher factorial moments of $P(\nu)$. However, other model parameters and assumptions that significantly differ between FREYA and CGMF can also explain discrepancies in this distribution.

5.2. Observables

Feynman histograms, singles rates R_1, doubles rates R_2, and leakage multiplication M_L are compared between the various codes for all BeRP-Ni and BeRP-W benchmark configurations. All results are calculated using a time width of $\tau = 1000\,\mu s$. It should be noted that because MCNP/CGMF requires significantly more computer time to reach the same statistical confidence as the other codes, and there were limitations on the available computer time, MCNP/CGMF results have much larger corresponding uncertainties.

5.2.1. BeRP-Ni configurations

Fig. 8 shows Feynman histograms for a few representative BeRP-Ni configurations. Appendix B contains Feynman histograms for all other BeRP-Ni configurations. All histograms are plotted on the same axes to make trends as a function of reflector thickness easier to observe. Measured results are also shown for comparison. Tables 4 present figure of merit (FOM) values, calculated according to Eq. (15) (Arthur et al., 2017), to quantify the discrepancy between the measured and various simulated Feynman histograms. In the FOM equation, N_{bins} represents total number of bins in the measured Feynman histogram being compared. M_i and S_i are the magnitudes of the ith bins of the measured and simulated histograms, respectively. $\sigma_{M,i}$ and $\sigma_{S,i}$ are the standard deviations corresponding to the ith measured and simulated bins. $|\frac{dM_L}{dC_i}|_{norm}$ is the normalized magnitude of the sensitivity of leakage multiplication to the ith bin in the measured Feynman histogram being compared. Because the sensitivity of leakage multiplication to each

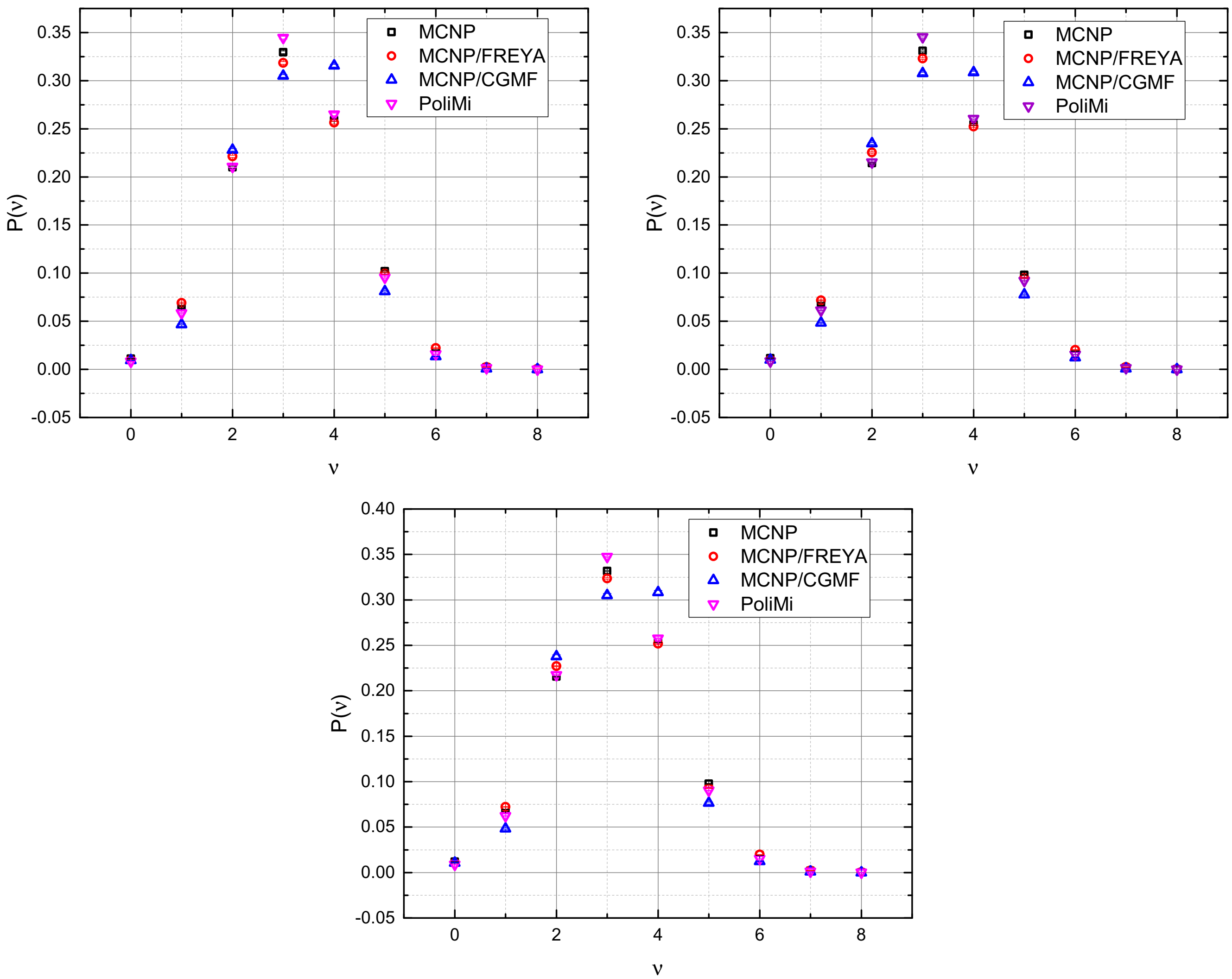

Fig. 7. ^{239}Pu induced fission multiplicity distributions for 0 (left), 1.5 (middle), and 3.0 (right) in. W thickness.

Table 3
^{239}Pu induced fission multiplicity distribution parameters for 0, 1.5, and 3.0 in. W thickness.

Code	$\bar{\nu}$	σ	$\bar{\nu}$	σ	$\bar{\nu}$	σ
W thickness (in.)	0	0	1.5	1.5	3.0	3.0
MCNP	3.16	1.43	3.13	1.43	3.12	1.43
MCNP/FREYA	3.15	1.47	3.12	1.45	3.10	1.44
MCNP/CGMF	3.17	1.25	3.14	1.24	3.14	1.25
PoliMi	3.16	1.31	3.13	1.31	3.12	1.31

bin in the histogram is included in the FOM equation, discrepancies between higher multiplet bins (which M_L is more sensitive to) affect the FOM more than discrepancies at multiplet bins that M_L is not very sensitive to. The ideal FOM value is unity.

$$FOM = \sum_{i=1}^{N_{bins}} \frac{(M_i - S_i)^2}{\sigma^2_{M,i} + \sigma^2_{S,i}} \left| \frac{dM_L}{dC_i} \right|_{norm} \tag{15}$$

From the tabulated FOM values, which Fig. 9 shows in plot form, it is clear that according to this metric MCNP/CGMF performs the best for almost all nickel thicknesses (for the 1 in. reflected configuration MCNP/CGMF shows slightly worse performance than PoliMi). PoliMi shows the next best performance, followed by MCNP. Finally, MCNP/FREYA shows the worst performance according to this FOM, especially at smaller (0–1.5 in.) reflector thicknesses. The MCNP/FREYA FOM values show a clear downward trend between 0.5 and 2.0 in. nickel thickness. However, it should be noted that it is not technically correct to compare the FOM values for MCNP/CGMF Feynman histograms to the FOM values corresponding to the other codes. As can be determined from Eq. (15), the FOM values are affected by the magnitude of the uncertainties. Therefore, accurate comparisons between FOM values can only truly be made between histograms that have similar uncertainties. The uncertainties corresponding to MCNP/CGMF histograms, especially at large reflector thicknesses, are up to an order of magnitude larger than those corresponding to the other codes. This is why Fig. 8 clearly shows that MCNP/CGMF data do not compare to the measured data as well as the other codes, yet the FOM value in Table 4 indicates very good matching of experimental data, as compared to the other codes.

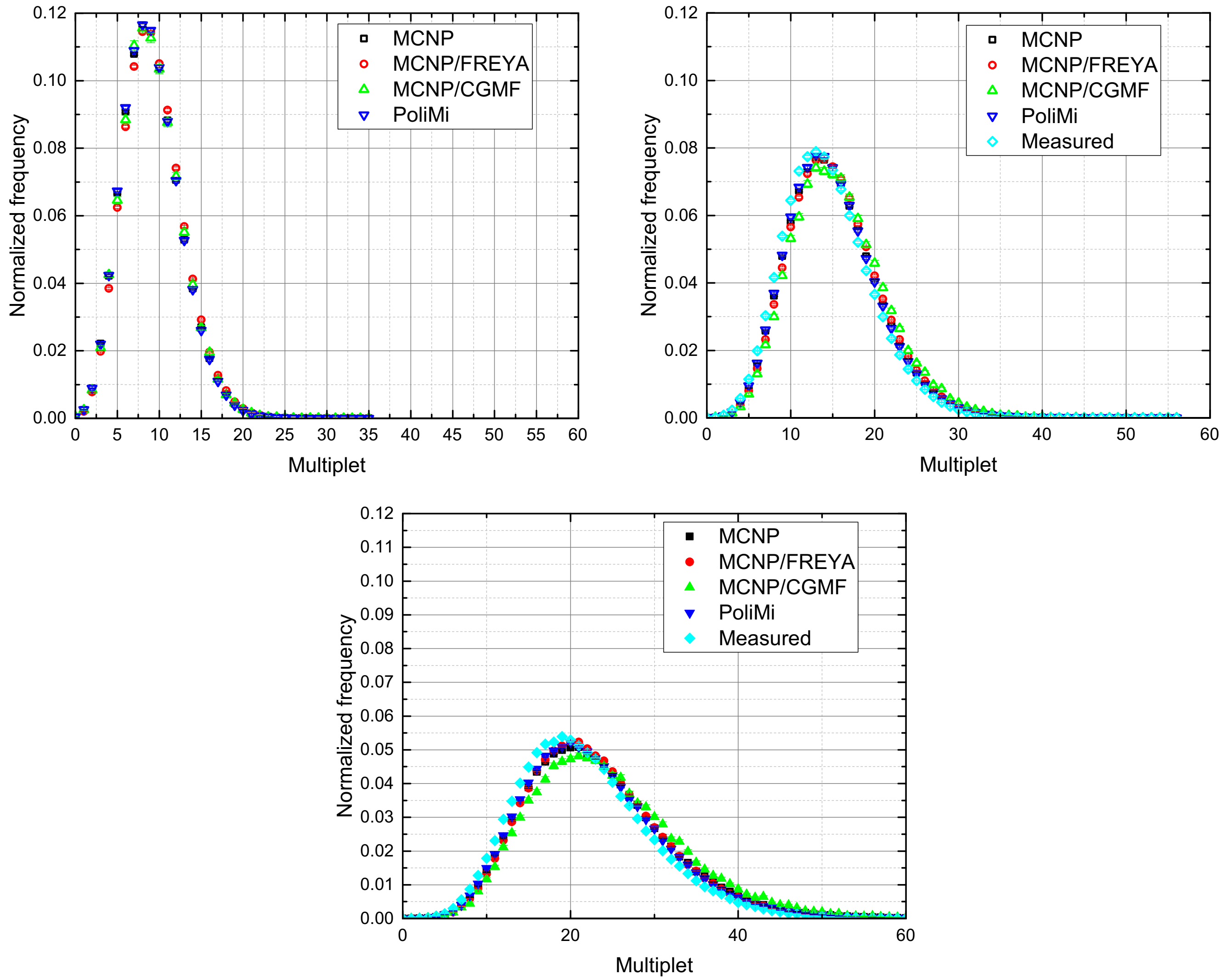

Fig. 8. Feynman histograms for 0 (left), 1.5 (middle), and 3.0 (right) in. Ni thickness.

Table 4
FOM values for the various simulated Feynman histograms, as compared to the measured histogram, for 0, 1.5, and 3.0 in. Ni thickness.

Code	0 in. Ni thickness	1.5 in. Ni thickness	3.0 in. Ni thickness
MCNP	24	39	38
MCNP/FREYA	82	55	32
MCNP/CGMF	5.9	24	24
PoliMi	19	25	24

Figs. 10 and 11 are plots of singles and doubles rates.

Overall, PoliMi seems to show the best match to experimental singles and doubles results, while MCNP/CGMF shows the most deviation from experimental results. MCNP performance seems to worsen as a function of nickel thickness, while MCNP/FREYA shows the opposite trend.

Fig. 12 plots leakage multiplication for the various BeRP-Ni configurations.

Unlike with singles and doubles rates, MCNP shows the best agreement with leakage multiplication. PoliMi shows a consistent under-bias, while MCNP/CGMF shows a consistent over-bias.

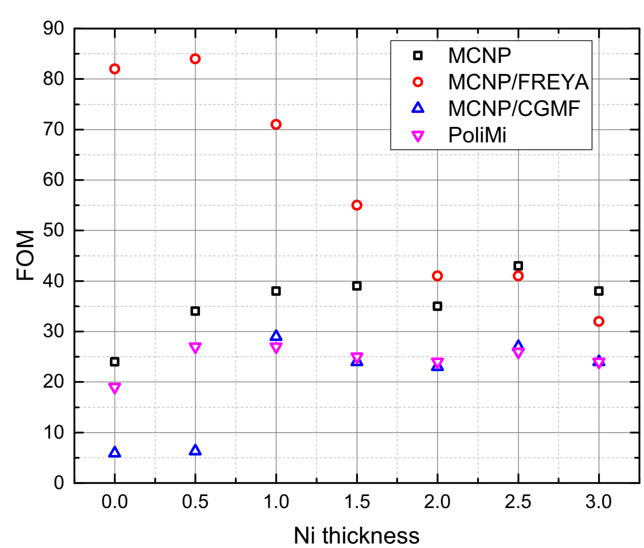

Fig. 9. Feynman histogram FOM values for all codes and all Ni thicknesses.

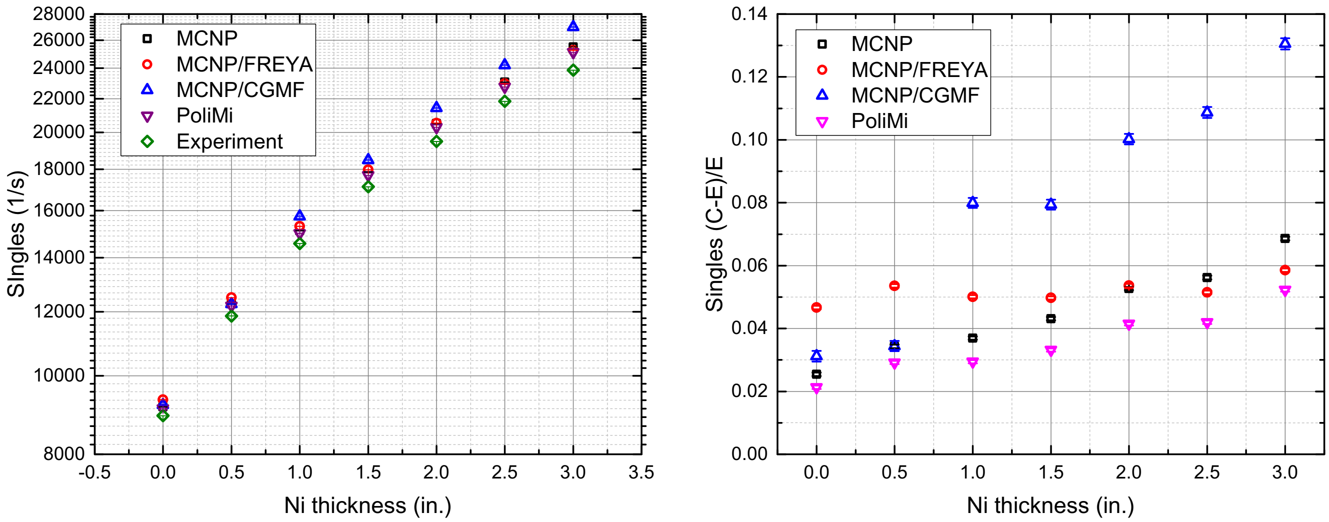

Fig. 10. Singles rates for all BeRP-Ni configurations.

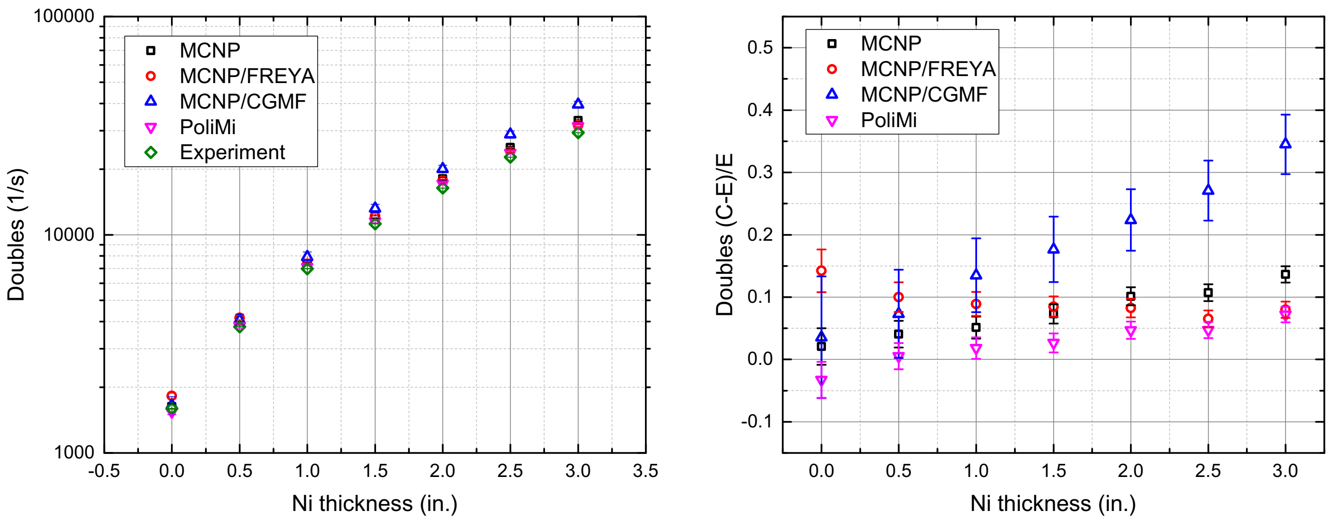

Fig. 11. Doubles rates for all BeRP-Ni configurations.

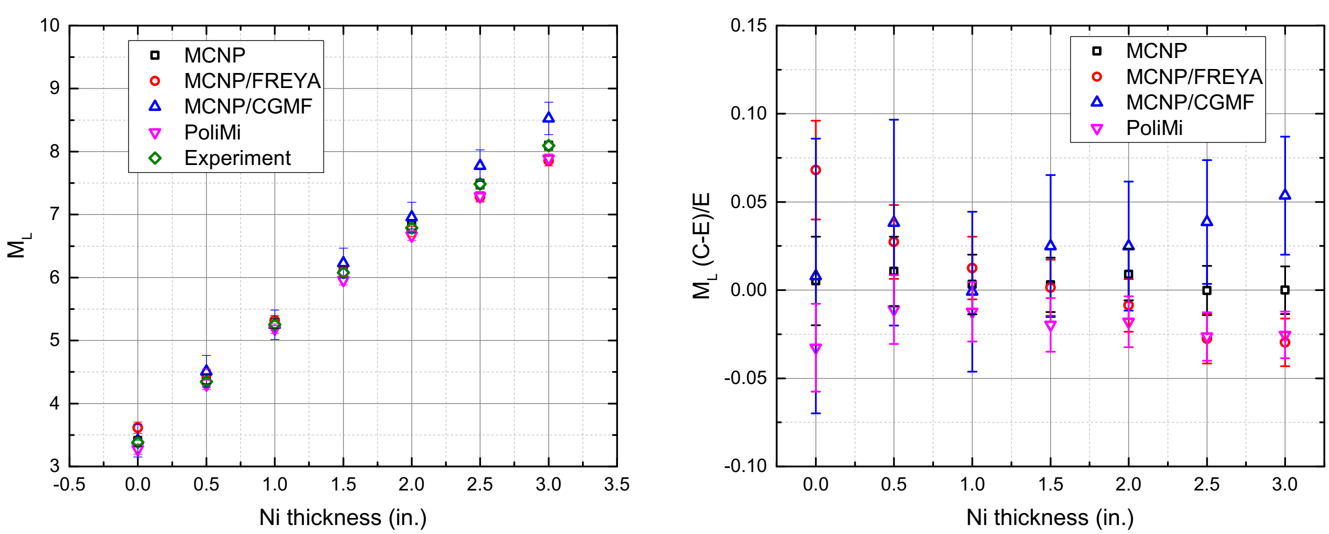

Fig. 12. Leakage multiplication for all BeRP-Ni configurations.

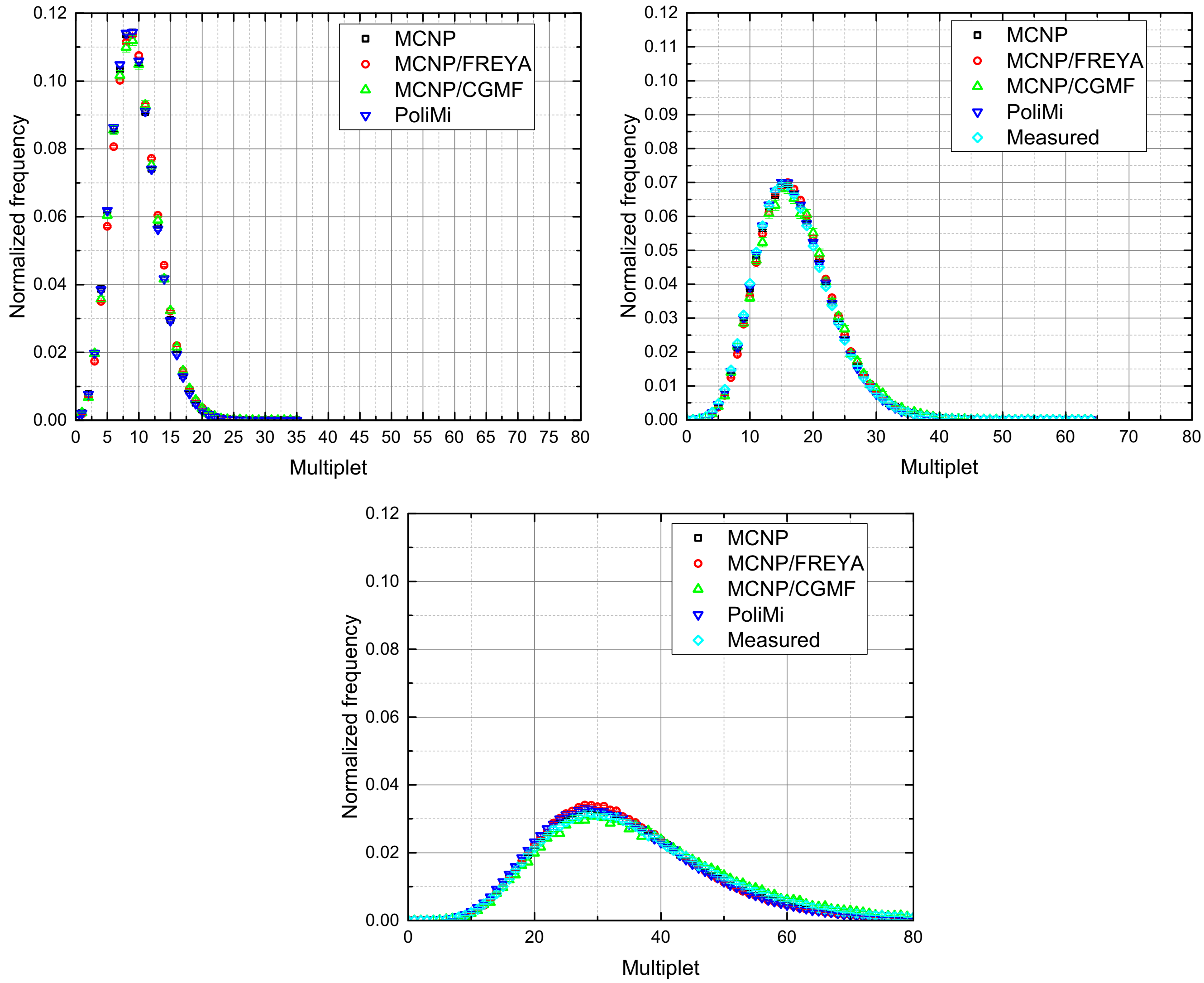

Fig. 13. Feynman histograms for 0 (left), 1.5 (middle), and 3.0 (right) in. W thickness.

MCNP/FREYA performance seems to improve with increasing nickel thickness, and then begin to worsen again after 1.5 in. of nickel reflection.

5.2.2. BeRP-W configurations

Fig. 13 shows Feynman histograms for a few representative BeRP-W configurations. Appendix B contains Feynman histograms for all other BeRP-W configurations. All histograms are plotted on the same axes to make trends as a function of reflector thickness easier to observe. Measured results are also shown for comparison. Table 5 presents FOM values to quantify the discrepancy between the measured and various simulated Feynman histograms.

Table 5
FOM values for the various simulated Feynman histograms, as compared to the measured histogram, for 0, 1.5, and 3.0 in. W thickness.

Code	0 in. W thickness	1.5 in. W thickness	3.0 in. W thickness
MCNP	88	1.8	1.1
MCNP/FREYA	$1.9 * 10^2$	4.9	5.8
MCNP/CGMF	19	3.0	2.5
PoliMi	78	1.8	4.8

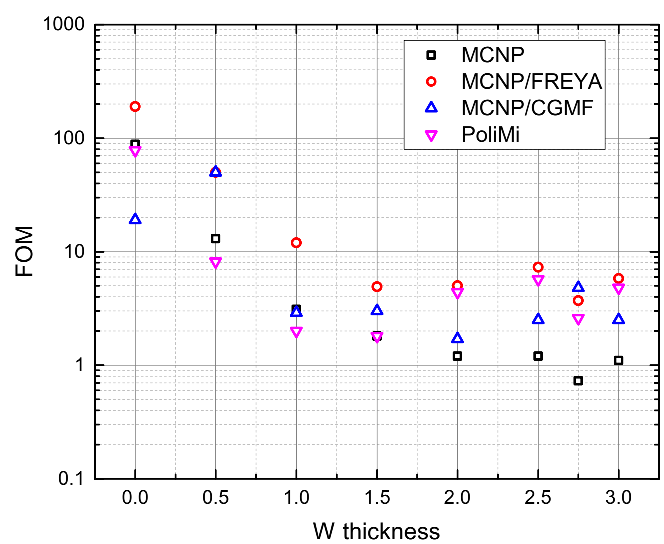

Fig. 14. Feynman histogram FOM values for all codes and all W thicknesses.

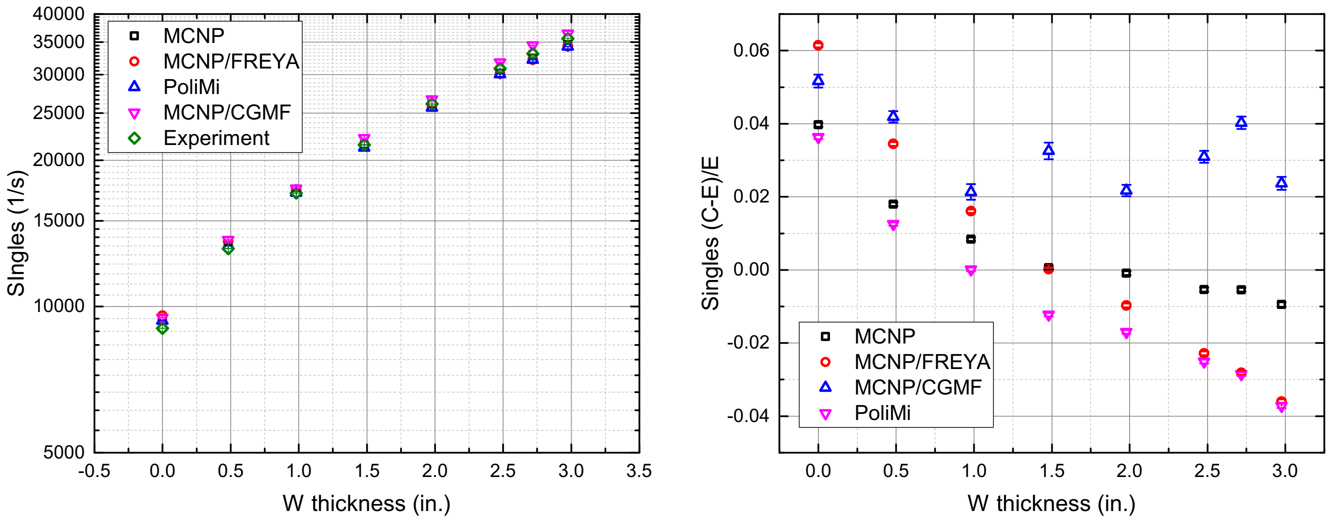

Fig. 15. Singles rates for all BeRP-W configurations.

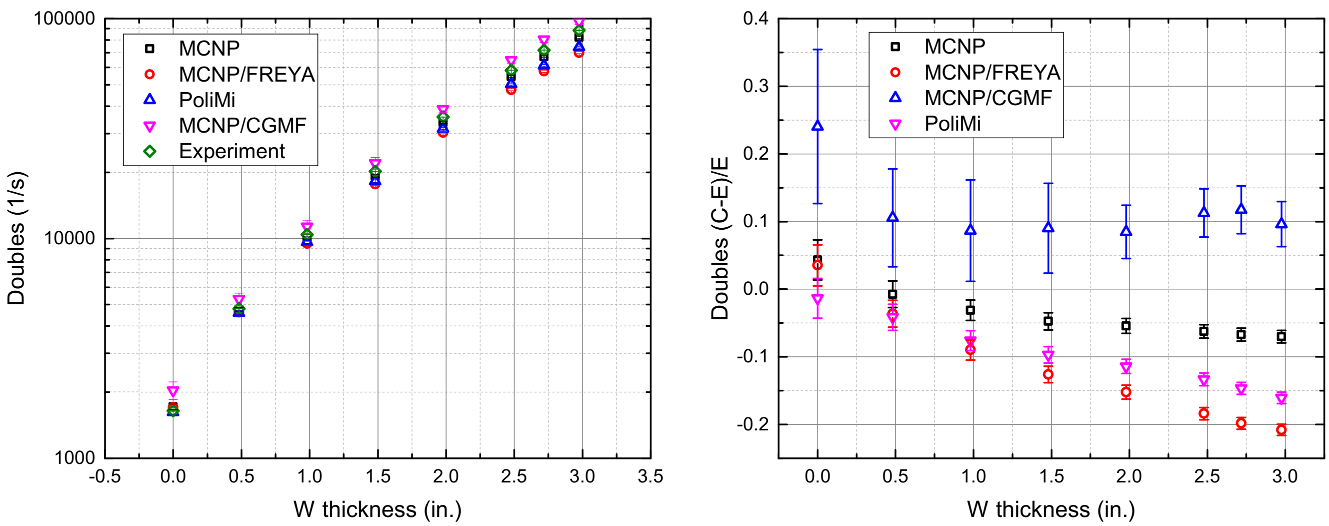

Fig. 16. Doubles rates for all BeRP-W configurations.

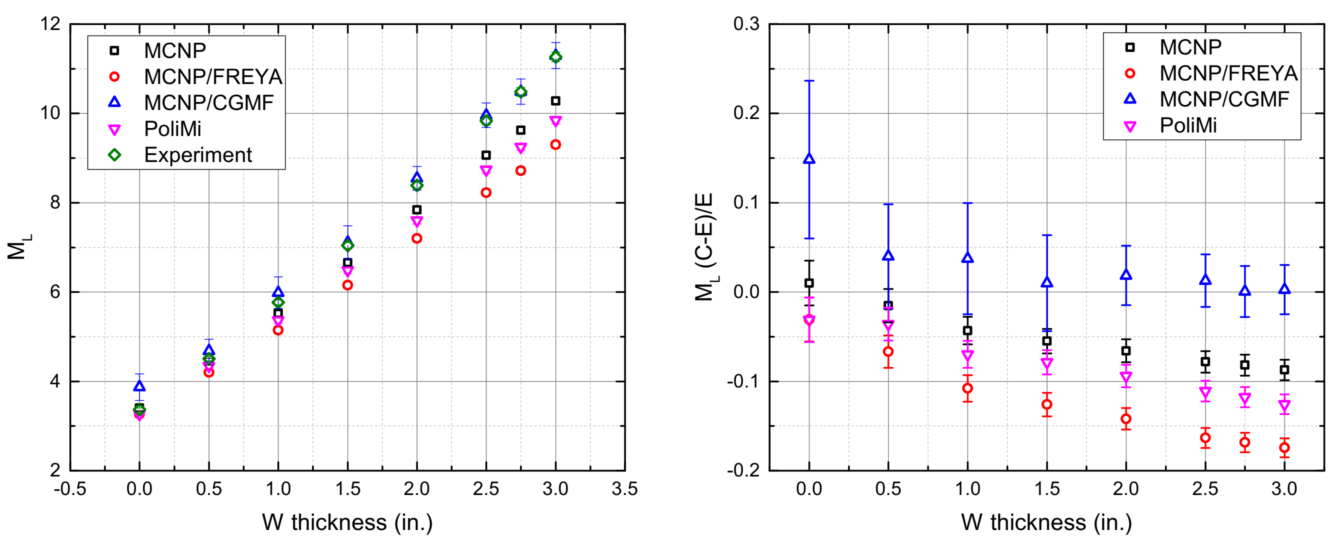

Fig. 17. Leakage multiplication for all BeRP-W configurations.

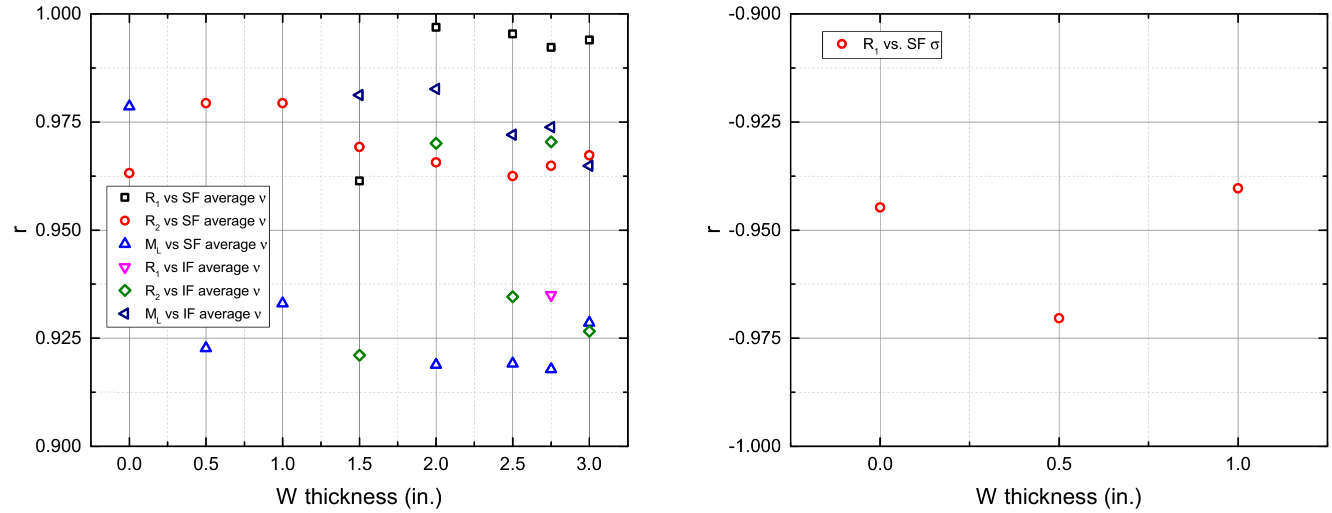

Fig. 18. Pearson correlation coefficient "r" plotted for the most highly correlated combinations of observables and nuclear data items of interest, across all configurations of the BeRP-W benchmark.

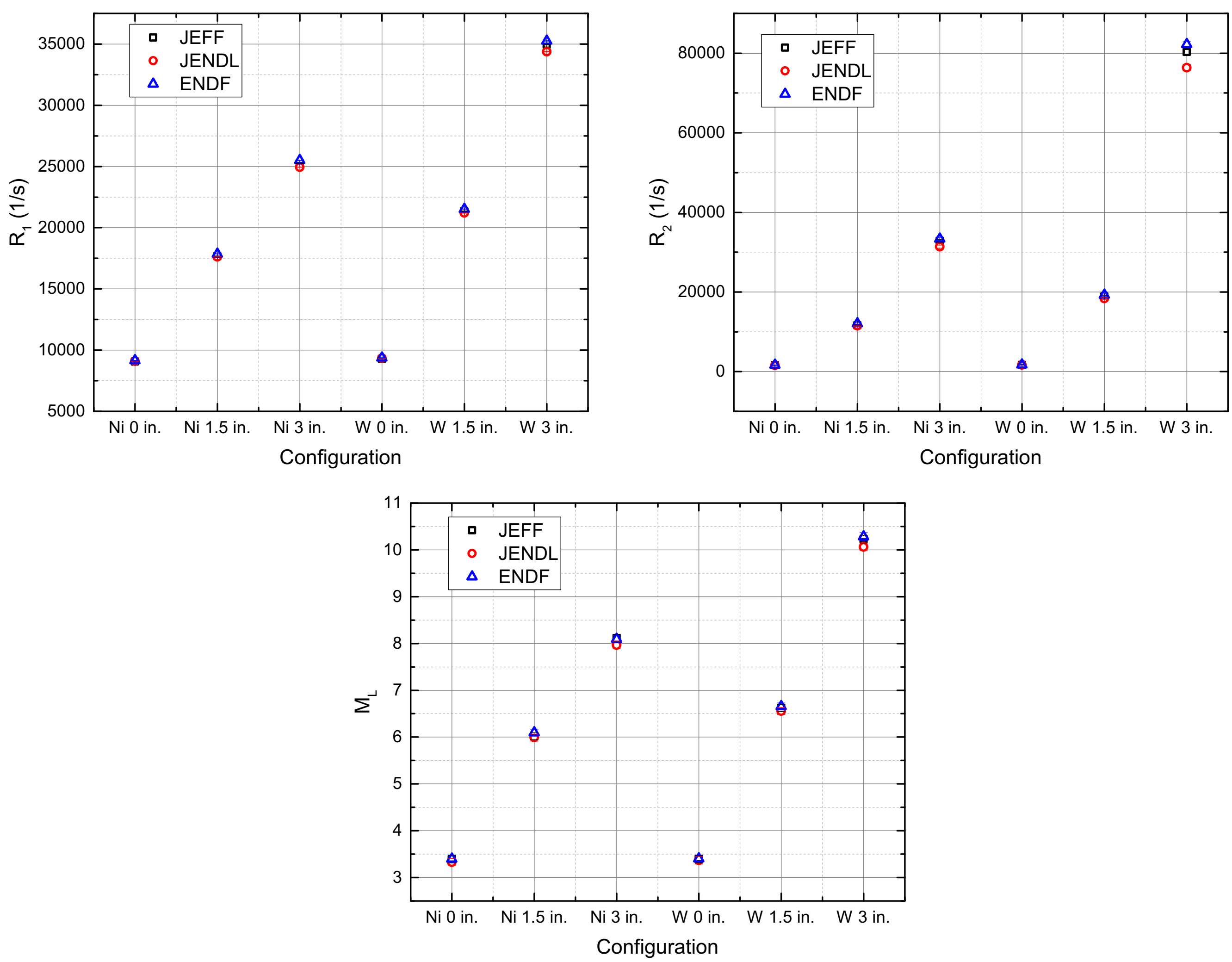

Fig. 19. BeRP-Ni and BeRP-W maximum (3 in.), middling (1.5 in.), and minimum (0 in.) reflected configurations, run with ^{239}Pu and ^{240}Pu nuclear data taken from JEFF-3.2 and JENDL-4.0, as compared to ENDF/B-VII.1.

Except for the poorer code performance for the small reflector thickness configurations, the tabulated FOM values, which Fig. 14 shows in plot form, are quite good (<10) and very close together. For 1.5-3 in. W reflector thickness, MCNP shows the best performance, followed by PoliMi for 1.5-2 in. W thickness and MCNP/CGMF for 2.5-3 in. W thickness. MCNP/FREYA shows the worst performance, according to this FOM, for all configurations.

Figs. 15 and 16 are plots of singles and doubles rates.

MCNP seems to show the best agreement with measured singles and doubles rates for cases with thick tungsten reflection. MCNP/CGMF is the most discrepant from measured singles rates, but similar in deviation from experiment to both PoliMi and MCNP/FREYA for doubles rates. MCNP/CGMF has a consistent over-bias in both singles and doubles rates, while PoliMi and MCNP/FREYA show consistent under-biases in doubles rates.

Fig. 17 plots leakage multiplication for the various BeRP-W configurations.

MCNP/CGMF shows the best agreement with experimental leakage multiplication data. MCNP shows the next best agreement, followed by PoliMi, and then MCNP/FREYA. MCNP, PoliMi, and MCNP/FREYA all show significant under-bias for predicting interred leakage multiplication.

5.2.3. Correlations with nuclear data

Correlations are observed to exist between differences in the multiplicity distribution nuclear data (induced and spontaneous fission $\bar{\nu}$ and σ) used by or extracted from the various codes, and differences in observables of interest (R_1, R_2, and M_L). As previously mentioned, 96 Pearson correlation coefficients exist over all configurations of the BeRP-W benchmark. These are plotted in Appendix C. The coefficients showing the largest correlations (defined as a correlation or anti-correlation value above 90%) are plotted in Fig. 18.

The strongest correlations are between R_1, R_2, and M_L, and both SF and IF $\bar{\nu}$, especially for the highly reflected configurations. The strongest anti-correlations are between R_1 and SF σ, for the less reflected configurations. The observed correlations between multiplicity distribution nuclear data and observables of interest may aid in future subcritical benchmark experiment design, by allowing experimenters to focus on observables that seem most sensitive to the nuclear data quantity of interest.

5.2.4. Other nuclear data libraries

The minimum, middling, and maximum reflected cases of the BeRP-Ni and BeRP-W benchmarks were run with MCNP, with the ENDF/B-VII.1 nuclear data for ^{239}Pu and ^{240}Pu replaced by JEFF-3.2 nuclear data, and JENDL-4.0 nuclear data. Fig. 19 shows the results. Fig. 20 plots comparisons to experimental results.

The results from the three nuclear data libraries (ENDF, JEFF, and JENDL) do show some variation, which should be investigated further. It should be noted that the significant worsening in leakage multiplication (C-E)/E value for configuration 7 of the BeRP-W benchmark is not unexpected. As the trend in Fig. 17 shows,

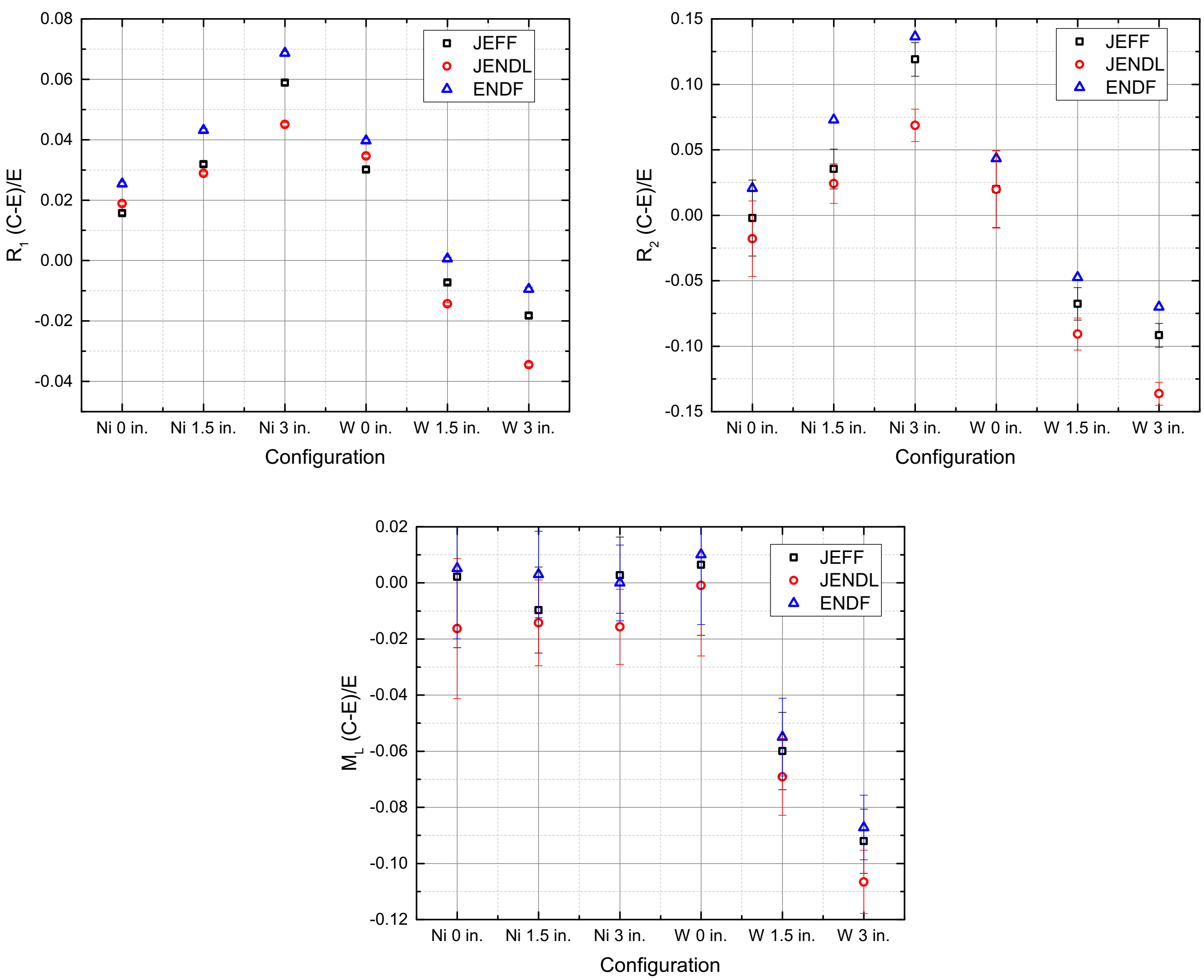

Fig. 20. BeRP-Ni and BeRP-W maximum (3 in.), middling (1.5 in.), and minimum (0 in.) reflected configurations, run with ^{239}Pu and ^{240}Pu nuclear data taken from JEFF-3.2 and JENDL-4.0, as compared to ENDF/B-VII.1.

simulated leakage multiplication values often compare less well as reflection, and therefore leakage multiplication itself, increases.

6. Conclusions

This work established a method to compare codes that take into account the correlated physics of fission. As more subcritical benchmark configurations become available, this method will continue to be utilized to help in code comparison. The results of this work clearly show that there is currently no best performer among the various radiation transport codes investigated here. In fact, based on the current status of these codes, there does not seem to be much reason to use the more computationally intensive fission event generator codes (MCNP/FREYA and MCNP/CGMF) over the others, for the specific application of subcritical neutron multiplication inference benchmarks. Due to the fact that the MC codes investigated in this work show different discrepancies for different measured configurations and different correlated neutron observables, it is difficult to determine which codes show best overall performance in this area. In addition, the CGMF and FREYA fission event generators are fairly recent capabilities that are still part of ongoing work for validation and improvements, and this work is part of a collaboration with the individuals currently implementing CGMF and FREYA in MCNP. Because of this continuing development process, the fission event generators are still changing with time and it is difficult to truly dive into the physical effects at this time.

If better performance is defined as less deviation from measured results, MCNP/CGMF and MCNP perform best for BeRP-Ni and BeRP-W Feynman histogram results, respectively. PoliMi performs best for BeRP-Ni singles and doubles rates. However, MCNP performs best for BeRP-Ni leakage multiplication. MCNP performs best for BeRP-W singles and doubles rates, while MCNP/CGMF performs better for BeRP-W leakage multiplication. One disadvantage to the plutonium measurements is that all of the observables are linked to both induced and spontaneous fission. In the future it would be interesting to look at a passive high-enriched uranium system(s) in which only induced fission plays a significant role (with the downside of worsened statistics), and possibly other uranium system measurements as well (Arthur et al., 2018; Hutchinson et al., 2013; Hutchinson et al., 2012; Hutchinson et al., 2014; Chapelle et al., 2014). More investigation is necessary to determine which codes truly perform better in which areas, and how such information can be used to improve simulation capabilities overall. However, it is clear that the MC radiation transport codes used in this work do not show adequate agreement to measured data. Especially for the fields of safeguards and criticality safety, even better agreement is desired (Trahan et al., 2016; Hutchinson et al., 2016). As more subcritical benchmark configurations become available, this method will continue to be utilized to help in code comparison.

Although it is difficult to determine which radiation transport code shows the best overall performance in simulating subcritical neutron multiplication inference benchmark measurements, it is clear that correlations exist between the underlying nuclear data utilized by (or generated by) the various codes, and the correlated neutron observables of interest. According to the Pearson correlation coefficient, strong (r>0.90) correlations exist between R_1, R_2, and M_L, and both SF and IF $\bar{\nu}$, especially for the highly reflected configurations of the BeRP-W benchmark. Strong (r<-0.90) anti-correlations exist between R_1 and SFσ for the less reflected configurations.. This could prove useful in nuclear data validation and evaluation applications, in which a particular moment of the neutron mulitplicity distribution is of more interest than the other moments. In addition, interesting trends of performance versus metal reflector thickness have been observed, which trends differ between codes. It would be very beneficial to investigate what aspects of each code cause these trends in performance quality. Finally, the variations in observables of interest caused by replacing ENDF/B-VII.1 ^{239}Pu and ^{240}Pu nuclear data with JEFF-3.2 and JENDL-4.0 nuclear data should be investigated further. The types of comparisons investigated in this work will become even more important as additional subcritical benchmark configurations are published as it may then be easier to distinguish which codes and nuclear data evaluations perform the best for the measured observables.

Acknowledgments

This material is based upon work supported in part by the Department of Energy National Nuclear Security Administration under Award Number(s) DE-NA0002576. This work was also supported in part by the DOE Nuclear Criticality Safety Program, funded and managed by the National Nuclear Security Administration for the Department of Energy.

Appendix A

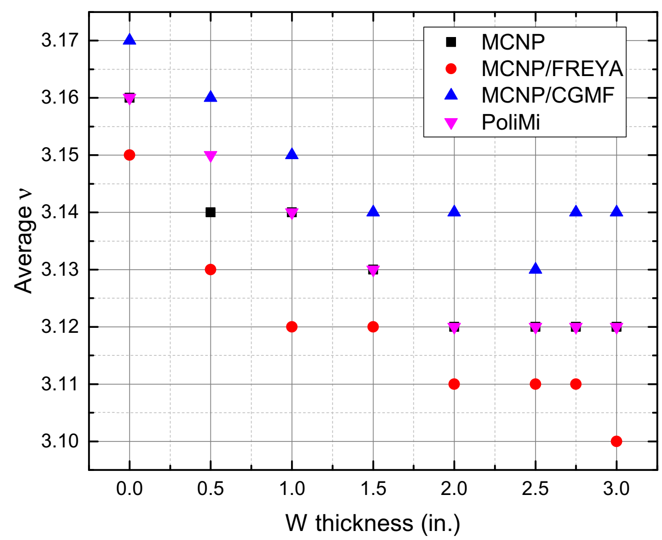

Fig. 21. ^{239}Pu induced fission $\bar{\nu}$ as a function of W thickness.

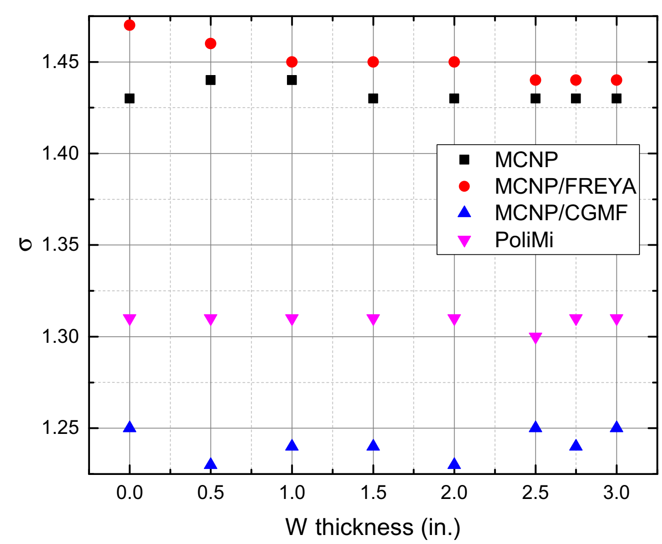

Fig. 22. ^{239}Pu induced fission σ as a function of W thickness.

Appendix B

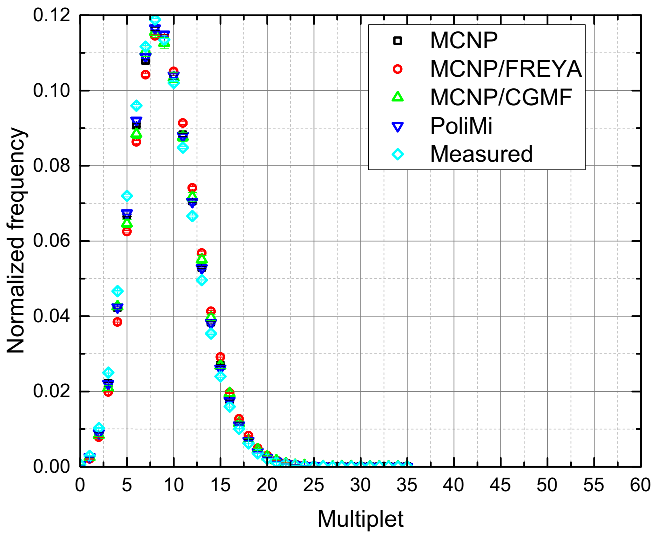

Fig. 23. Feynman histograms for 0.5 in. Ni thickness.

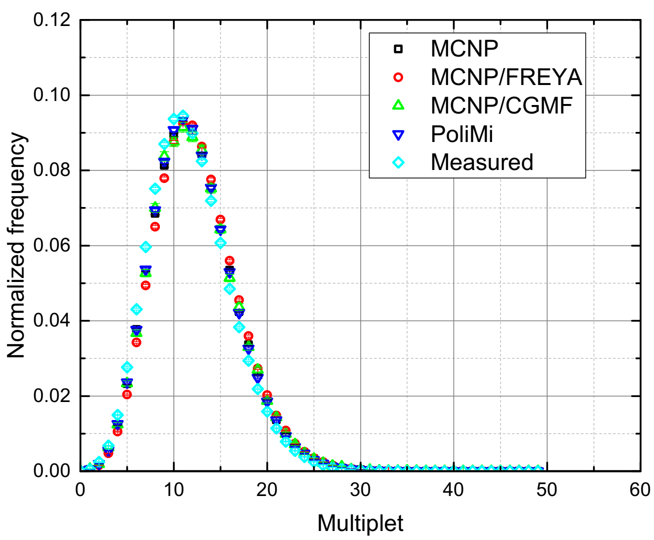

Fig. 24. Feynman histograms for 1 in. Ni thickness.

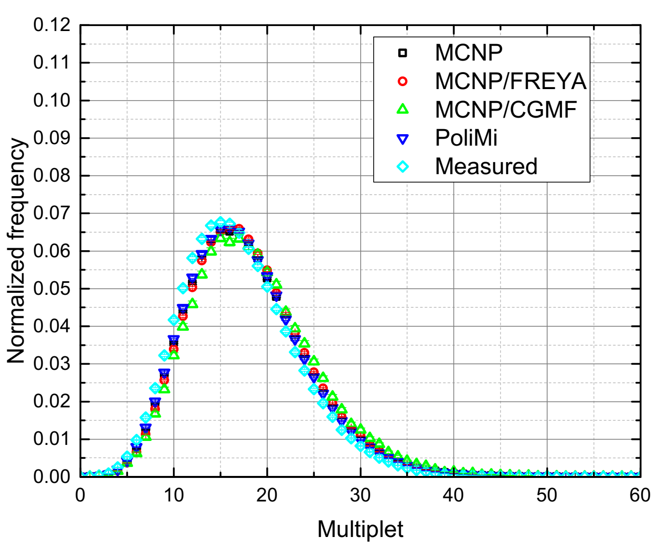

Fig. 25. Feynman histograms for 2 in. Ni thickness.

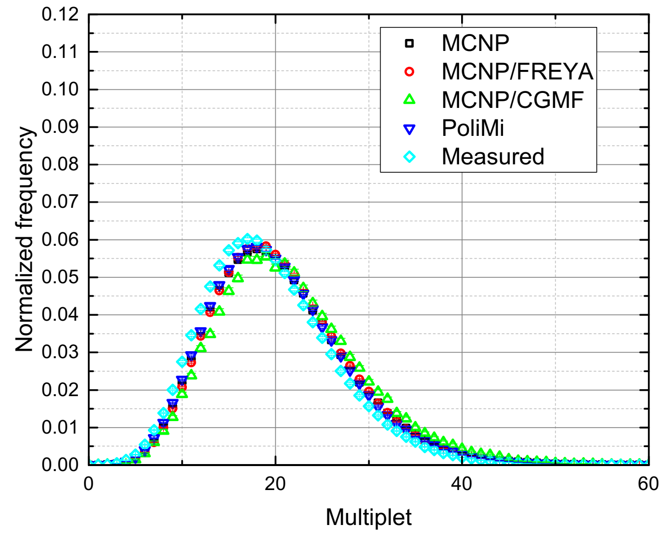

Fig. 26. Feynman histograms for 2.5 in. Ni thickness.

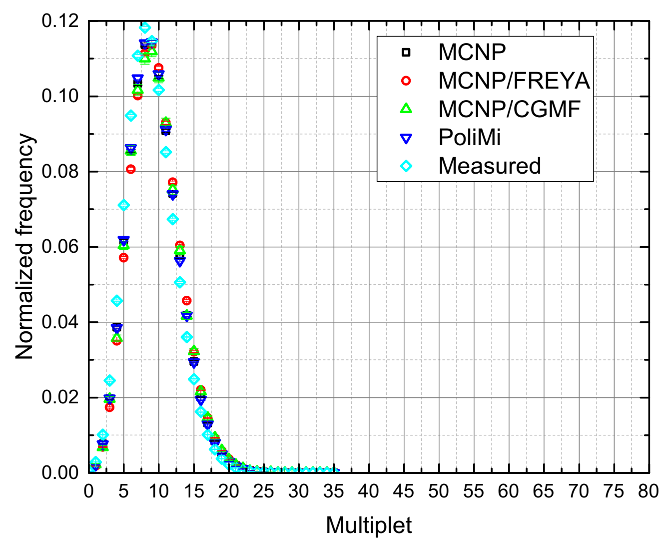

Fig. 27. Feynman histograms for 0.5 in. W thickness.

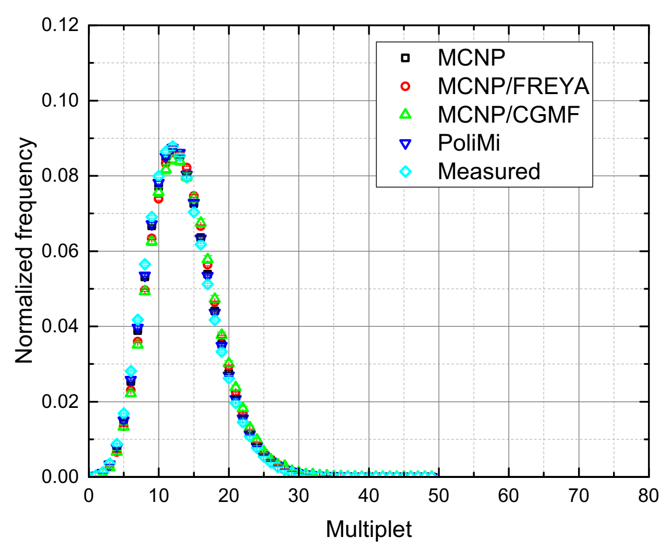

Fig. 28. Feynman histograms for 1 in. W thickness.

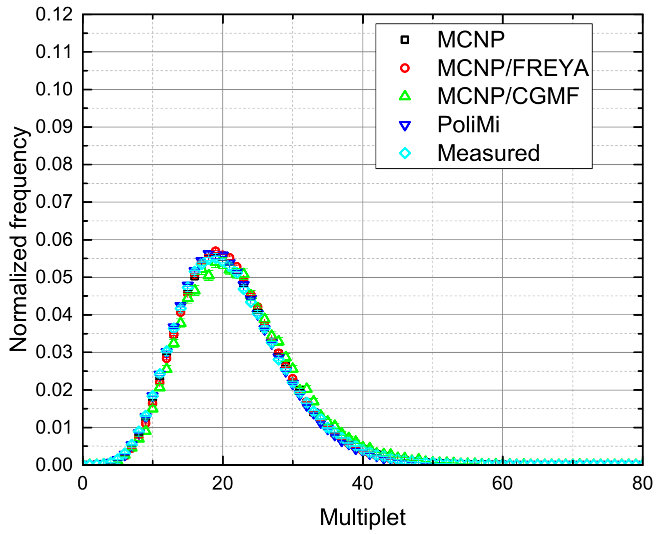

Fig. 29. Feynman histograms for 2 in. W thickness.

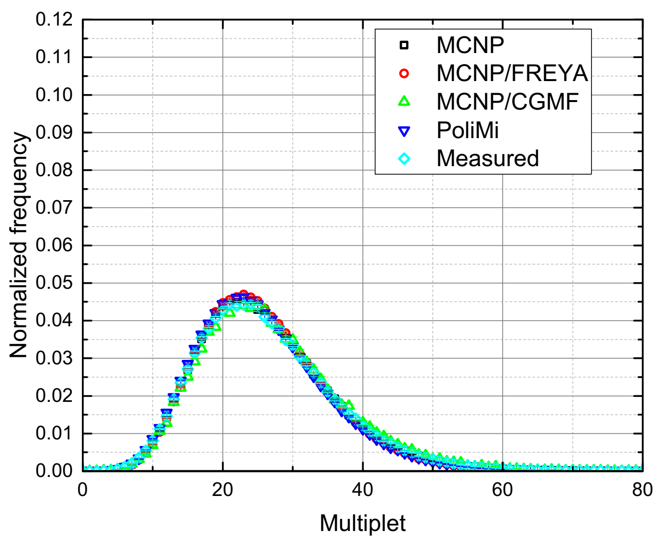

Fig. 30. Feynman histograms for 2.5 in. W thickness.

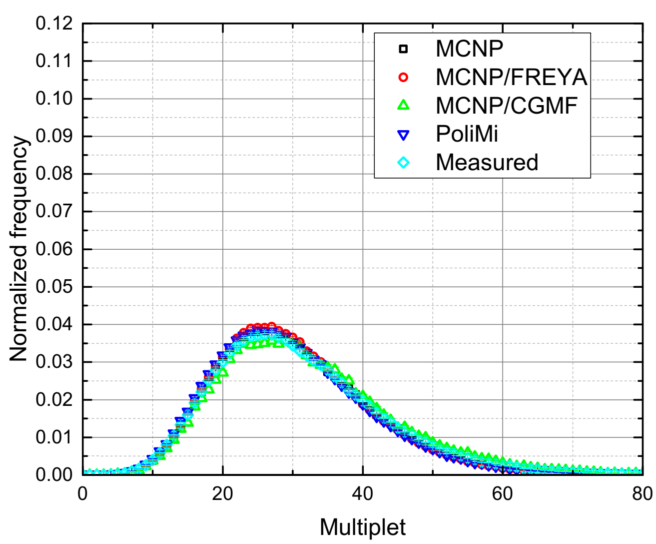

Fig. 31. Feynman histograms for 2.75 in. W thickness.

Table 6
FOM values for the various simulated Feynman histograms, as compared to the measured histogram, for 0.5, 1.0, 2.0, and 2.5 in. Ni thickness.

Code	0.5 in. Ni thickness	1.0 in. Ni thickness	2.0 in. Ni thickness	2.5 in. Ni thickness
MCNP	34	38	35	43
MCNP/FREYA	84	71	41	41
MCNP/CGMF	6.3	29	23	27
PoliMi	27	27	24	26

Table 7
FOM values for the various simulated Feynman histograms, as compared to the measured histogram, for 0.5, 1.0, 2.0, 2.5, and 2.75 in. W thickness.

Code	0.5 in. W thickness	1.0 in. W hickness	2.0 in. W thickness	2.5 in. W thickness	2.75 in. W thickness
MCNP	13	3.1	1.2	1.2	0.73
MCNP/FREYA	50	12	5.0	7.3	3.7
MCNP/CGMF	50	2.9	1.7	2.5	4.8
PoliMi	8.2	2.0	4.4	5.7	2.6

Appendix C

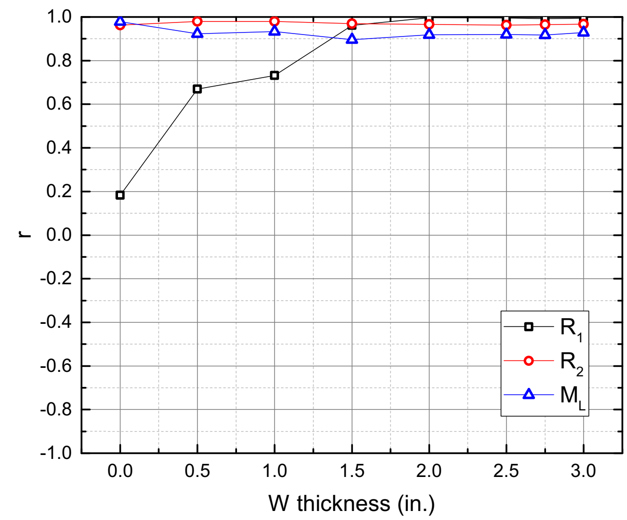

Fig. 32. Pearson correlation coefficient "r" plotted for all observables of interest vs. SF $\bar{\nu}$, across all configurations of the BeRP-W benchmark.

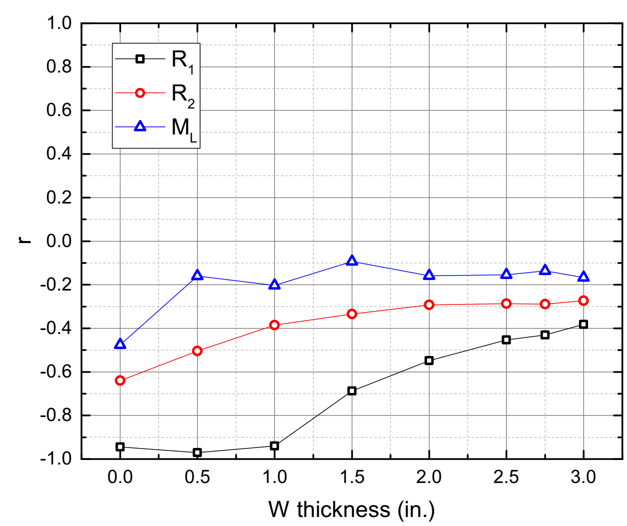

Fig. 33. Pearson correlation coefficient "r" plotted for all observables of interest vs. SF σ, across all configurations of the BeRP-W benchmark.

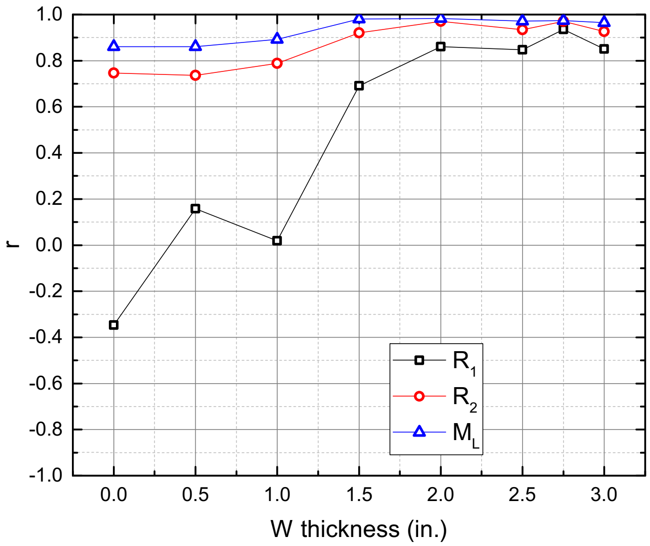

Fig. 34. Pearson correlation coefficient "r" plotted for all observables of interest vs. IF $\bar{\nu}$, across all configurations of the BeRP-W benchmark.

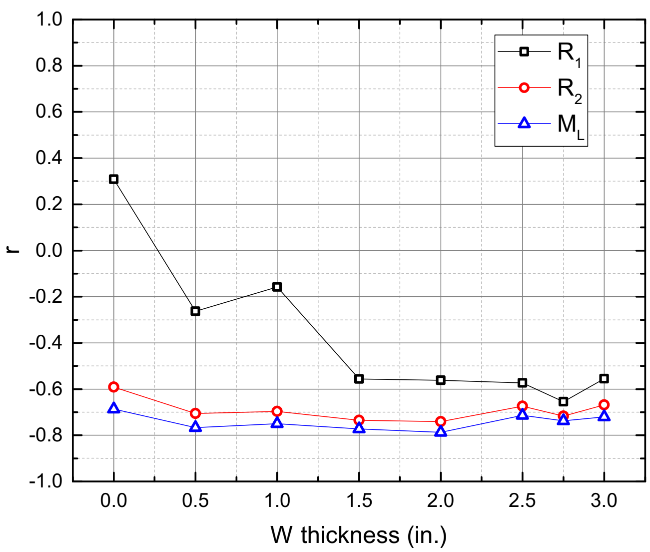

Fig. 35. Pearson correlation coefficient "r" plotted for all observables of interest vs. IF σ, across all configurations of the BeRP-W benchmark.

References

Arthur, J.A., Bahran, R.M., Hutchinson, J.D., Rising, M.E., Pozzi, S.A., 2016. Comparison of the performance of various correlated fission multiplicity monte carlo codes. In: Transactions of the American Nuclear Society Winter Meeting and Technology Expo.

Arthur, J., Bahran, R., Hutchinson, J., Grove, T., Pozzi, S., 2017. Improved figure of merit for feynman histograms. In: Transactions of the American Nuclear Society Winter Meeting and Technology Expo.

Arthur, J., Bahran, R., Hutchinson, J., Sood, A., Thompson, N., Pozzi, S., 2018. Development of a research reactor protocol for neutron multiplication measurements. Prog. Nucl. Energy 106, 120–139.

Bahran, R., Hutchinson, J., 2016. Subcritical copper-reflected α-phase plutonium (SCRαP) integral experiment design. Trans. Am. Nucl. Soc. 114, 527–529.

Bahran, R., Hutchinson, J., Richard, B., Sood, A., 2014. List-mode simulations of the Thor core benchmark sensitivity experiments. Transactions of the American Nuclear Society Annual Meeting, vol. 111, pp. 805–808.

Bahran, R., Croft, S., Hutchinson, J., Smith, M., Sood, A., 2014. A survey of nuclear data deficiences affecting nuclear non-proliferation. In: Proceedings of the 2014 INMM Annual Meeting, Atlanta GA.

Barnard, E., Ferguson, A., McMurray, W., Heerden, I.V., 1965. Time-of-flight measurements of neutron spectra from the fission of U^{235}, U^{238}, and Pu^{239}. Nucl. Phys. 71, 228–249.

Boldeman, J.W., Hines, M.G., 1985. Prompt neutron emission probabilities following spontaneous and thermal neutron fission. Nucl. Sci. Eng. 91, 114–116.

Bolding, S.R., Solomon, C.J., 2013. Simulations of multiplicity distributions with perturbations to nuclear data. Trans. Am. Nucl. Soc. 109, 251–254.

Briggs, J.B., 2003. The international criticality safety benchmark evaluation project (ICSBEP). In: International Conference on Nuclear Energy for New Europe.

Briggs, J. et al., 2014. Integral benchmark data for nuclear data testing through the ICSBEP & IRPhEP. Nucl. Data Sheets 118, 396–400.

Chadwick, M. et al., 2006. ENDF/B-VII.0: next generation evaluated nuclear data library for nuclear science and technology. Nucl. Data Sheets 107, 2931–3060.

Chadwick, M. et al., 2011. ENDF/B-VII.1 nuclear data for science and technology: cross sections, covariances, fission product yields and decay data. Nucl. Data Sheets 112, 2887–2996.

Chapelle, A., Casoli, P., Authier, N., Myers, W., Hutchinson, J., Sood, A., Rooney, B., 2014. Joint neutron noise measurements on metallic reactor caliban. Nucl. Data Sheets 118, 558–560.

Cifarelli, D., Hage, W., 1986. Models for a three-parameter analysis of neutron signal correlation measurements for fissile material assay. Nucl. Instrum. Methods A251, 550–563.

Flerov, N.N., Talyzin, V.M., 1960. Average numbers ν and η of neutrons in the fission of ^{233}U and ^{239}Pu by 14 MeV neutrons. Transl. Atomnaya Energiya 10, 68–69.

Goorely, J. et al., 2012. Initial MCNP6 release overview. Nucl. Technol. 180, 298–315.

Hagmann, C. et al., 2013. FREYA-A new monte carlo code for improved modeling of fission chains. IEEE Trans. Nucl. Sci. 60, 545–549.

Hauser, W., Feshbach, H., 1952. The inelastic scattering of neutrons. Phys. Rev. 87.

Holden, N.E., Zucker, M.S., 1988. Prompt neutron emission multiplicity distribution and average values (nubar) at 200 m/s for the fissile nuclides. Nucl. Sci. Eng. 98 (2), 174–181.

Howerton, R., 1977. Nucl. Sci. Eng. 62, 438–454 (Revisited).

Hutchinson, J., Loaiza, D., 2007. Plutonium sphere reflected by beryllium. In: International Handbook of Evaluated Criticality Safety Benchmark Experiments, NEA/NSC/DOC/(95)03/I, PU-MET-FAST-038.

Hutchinson, J., Sood, A., Myers, W., Smith-Nelson, M., Dinwiddie, D., 2012. Comparison of heu measurements using measured and simulated data. Trans. Am. Nucl. Soc.

Hutchinson, J., Rooney, B., Myers, W., Sood, A., Smith-Nelson, M., 2013. CALIBAN measurements near delayed critical using subcritical measurement methods. In: 2013 American Nuclear Society Winter Meeting, Washington DC.

Hutchinson, J., Sood, A., Myers, W., Smith-Nelson, M., Dinwiddie, D., 2013. Comparison of HEU measurements using measured and simulated data. Trans. Am. Nucl. Soc. 106, 487–489.

Hutchinson, J., Rooney, B., Myers, W., Sood, A., Smith-Nelson, M., 2013. Caliban measurements near delayed critical using subcritical measurement methods. In: Transactions of the American Nuclear Society Winter Meeting and Technology Expo.

Hutchinson, J., Smith-Nelson, M.A., Sood, A., Goda, J.M., Bounds, J.A., 2014. Joint LANL/CEA measurements on Godiva IV. In: 2014 American Nuclear Society Annual Meeting, Reno NV.

Hutchinson, J., Nelson, M.A., Sood, A., Hayes, D.K., Sanchez, R.G., 2015. Neutron noise measurements on HEU foils moderated by lucite. In: 2015 American Nuclear Society Annual Meeting, San Antonio TX.

Hutchinson, J., et al., 2015. Estimation of uncertainties for subcritical benchmark measurements. In: International Conference on Nuclear Criticality.

Hutchinson, J. et al., 2016. Subcritical multiplication experiments & simulations: Overview and recent advances, Advances in Nuclear Nonproliferation Technology and Policy Conference.

Hutchinson, J., Bahran, R., Cutler, T., et al., 2017. Subcritical copper-reflected α-phase plutonium (scrαp) measurements and simulations. In: International Conference on Mathematics and Computational Methods Applied to Nuclear Science and Engineering, LA-UR-17-20621.

Iyer, R.H., Naik, H., Pandey, A.K., Kalsi, P.C., Singh, R.J., Ramaswami, A., Nair, A.G.C., 2000. Measurement of absolute fission yields in the fast neutron-induced fission of actinides: ^{238}U, ^{237}Np, ^{238}Pu, ^{240}Pu, ^{243}Am, and ^{244}Cm by track-etch-cum-gamma spectrometry. Nucl. Sci. Eng. 135, 227–245.

Knoll, G.F., 2010. Radiation Detection and Measurement. Wiley.

Lestone, J., 2005. Energy and isotope dependence of neutron multiplicity distributions. Nucl. Sci. Eng.

Madland, D.G., Nix, J.R., 1982. New calculation of prompt fission neutron spectra and average prompt neutron multiplicities. Nucl. Sci. Eng. 81, 213–271.

Mattingly, J., 2009. Polyethylene-reflected plutonium metal sphere: Subcritical neutron and gamma measurements, Sandia National Laboratory Report SAND2009-5804.

MCNP6™ User's Manual, Version 1.0, May 2013.

Miller, E.C., 2012. Characterization of Fissionable Material using a Time-correlated Pulse-height Technique for Liquid Scintillators. University of Michigan (PhD Thesis).

Miller, E.C., Mattingly, J.K., Dennis, B.D., Clarke, S.D., Pozzi, S.A., 2010. Simulations of neutron multiplicity measurements with MCNP-PoliMi, Technical Report SAND2010-6830, Sandia National Laboratory, 2010.

Moss, C., Sorenson, E., Nelson, M., 2016. Multiplicity Counter-15 (MC-15) User Manual, Los Alamos National Laboratory, LA-UR-16-27099.

Naika, H., Mulikb, V., Prajapatic, P., Shivasankard, B., Suryanarayanae, S., Jagadeesanf, K., Thakaref, S., Sharmae, S., Goswamia, A., 2013. Mass distribution in the quasi-mono-energetic neutron-induced fission of ^{238}U. Nucl. Phys. A 913, 185–205.

NRDC-Network, 2017. CSISRS/EXFOR library of experimental cross sections,www.nndc.bnl.gov/exfor.

Padovani, E., Pozzi, S.A., Clarke, S.D., Miller, E.C., 2012. MCNPX-PoliMi User's Manual, C00791 MNYCP, Radiation Safety Information Computational Center. Oak Ridge National Laboratory.

Pozzi, S. et al., 2012. MCNPX-PoliMi for nuclear nonproliferation applications. Nucl. Instrum. Methods Phys. Res., Sect. A 694, 119–125.

Pozzi, S.A., Padovani, E., Marseguerra, M., 2003. MCNP-PoliMi: a Monte Carlo code for correlation measurements. Nucl. Instrum. Methods Phys. Res. A 513, 550–558.

Richard, B., Hutchinson, J., 2016. Tungsten-reflected plutonium-metal-sphere subcritical measurements. In: International Handbook of Evaluated Criticality Safety Benchmark Experiments, NEA/NSC/DOC/(95)03/I, FUND-NCERC-PU-HE3-MULT-002.

Richard, B., et al., 2016. Nickel-reflected plutonium-metal-sphere subcritical measurements. In: International Handbook of Evaluated Criticality Safety Benchmark Experiments, NEA/NSC/DOC/(95)03/I, FUND-NCERC-PU-HE3-MULT-001.

Rising, M., et al., 2014. Correlated neutron and gamma-ray emissions in MCNP6, 2014 ANS Winter Meeting and Nuclear Technology Expo.

Rising, M., 2013. Evaluation and uncertainty quantification of prompt fission neutron spectra of uranium and plutonium isotopes. Nucl. Sci. Eng. 175 (1), 81–93.

Santamarina, A., Bernard, D., Blaise, P., et al., 2009. The JEFF-3.1.1 nuclear data library, JEFF Report 22.

Santi, P., Miller, M., 2008. Reevaluation of prompt neutron emission multiplicity distributions for spontaneous fission. Nucl. Sci. Eng. 160, 190–199.

Shibata, K., Iwamoto, O., Nakagawa, T., Iwamoto, N., Ichihara, A., Kunieda, S., Chiba, S., Furutaka, K., Otuka, N., Ohsawa, T., Murata, T., Matsunobu, H., Zukeran, A., Kamada, S., Katakura, J., 2011. JENDL-4.0: A new library for nuclear science and engineering. J. Nucl. Sci. Technol. 48 (1), 1–30.

Smith-Nelson, M., 2015. Momentum: version 0.36.3, LANL Software.

Sood, A., Solomon, C.J., Hutchinson, J.D., Bahran, R., 2014. A review of recent R&D efforts in sub-critical multiplication measurements and simulations. In: Transactions of the American Nuclear Society Annual Meeting, 2014.

Talou, P. et al., 2013. Prompt fission neutrons and gamma rays in a Monte Carlo Hauser-Feshbach formalism. Phys. Procedia 47, 39–46.

Terrell, J., 1957. Distributions of fission neutron numbers. Phys. Rev. 108, 783–789.

Trahan, A., 2016. Utilization of the Differential Die-away Self-interrogation Technique for Characterization of Spent Nuclear Fuel. University of Michigan (Ph.D. thesis).

Verbeke, J., Randrup, J., Vogt, R., 2015. Fission reaction event yield algorithm, FREYA – for event-by-event simulation of fission. Comput. Phys. Commun. 191, 178–202.

Verbeke, J.M., Randrup, J., Vogt, R., 2016. Fission reaction yield algorithm FREYA user manual 2.0, Lawrence Livermore National Laboratory report LLNL-SM-705798.

Wagemans, C., 1991. The Nuclear Fission Process. CRC Press, Boca Raton.

Progress in Nuclear Energy 106 (2018) 120–139

Contents lists available at ScienceDirect

Progress in Nuclear Energy

journal homepage: www.elsevier.com/locate/pnucene

Development of a research reactor protocol for neutron multiplication measurements

Jennifer Arthur[a,b,*], Rian Bahran[a], Jesson Hutchinson[a], Avneet Sood[a], Nicholas Thompson[a], Sara A. Pozzi[b]

[a] Los Alamos National Laboratory, Los Alamos, NM 87545, United States
[b] University of Michigan Department of Nuclear Engineering and Radiological Sciences, Ann Arbor, MI 48109, United States

ARTICLE INFO

Keywords:
Research reactor
Neutron multiplicity
Monte carlo simulations
Protocol

ABSTRACT

A new series of subcritical measurements has been conducted at the zero-power Walthousen Reactor Critical Facility (RCF) at Rensselaer Polytechnic Institute (RPI) using a ^{3}He neutron multiplicity detector. The Critical and Subcritical 0-Power Experiment at Rensselaer (CaSPER) campaign establishes a protocol for advanced subcritical neutron multiplication measurements involving research reactors for validation of neutron multiplication inference techniques, Monte Carlo codes, and associated nuclear data. There has been increased attention and expanded efforts related to subcritical measurements and analyses, and this work provides yet another data set at known reactivity states that can be used in the validation of state-of-the-art Monte Carlo computer simulation tools. The diverse (mass, spatial, spectral) subcritical measurement configurations have been analyzed to produce parameters of interest such as singles rates, doubles rates, and leakage multiplication. MCNP®6.2 was used to simulate the experiment and the resulting simulated data has been compared to the measured results. Comparison of the simulated and measured observables (singles rates, doubles rates, and leakage multiplication) show good agreement. This work builds upon the previous years of collaborative subcritical experiments and outlines a protocol for future subcritical neutron multiplication inference and subcriticality monitoring measurements on pool-type reactor systems.

1. Introduction

Subcritical measurements have been continually performed since the 1940s. The results of these experiments have provided data used for simulations of special nuclear material (SNM) systems in the fields of nuclear nonproliferation, safeguards, and criticality safety. Improvements in nuclear detection instrumentation and SNM availability in the 1950s and 1960s lead to increased research activity in both the theory and practice of multiplication and reactivity measurements. Multiplication is an extremely important parameter in SNM systems, as it can give information about the type, enrichment, and risk level of the SNM being investigated for nuclear security reasons. In addition, for criticality safety purposes, it is extremely important to be able to accurately predict the multiplication of systems for various processes and experiments. Multiplication inference measurements take advantage of the fact that neutrons emitted during fission are correlated in time and can be used to gain knowledge about the system being measured.

Multiplying system parameters of interest include leakage multiplication M_L, total multiplication M_T, the multiplication factor k_{eff}, and the prompt multiplication factor k_p. M_L represents the number of neutrons escaping a system for every neutron injected into the system, while M_T represents the number of prompt neutrons created on average by a single neutron in the multiplying system. k_{eff} is a measure of the ratio of the total number of neutrons in the current generation to the total number of neutrons in the previous generation. k_p is similar to k_{eff}, except that it only takes into account prompt neutrons. These parameters are sensitive to the distribution of the number of neutrons emitted per fission. Simulation capabilities were historically developed alongside the measurements for comparison purposes. Comparisons between neutron multiplication measurements and simulations are used to validate multiplication inference techniques and radiation particle transport codes, and to identify and correct deficiencies in underlying nuclear data quantities such as $\bar{\nu}$ (average number of neutrons emitted per fission) (Arthur et al., 2016; Bahran et al., 2014a; Sood et al., 2014; Bolding and Solomon, 2013; Miller et al., 2010; Mattingly, 2009; Bahran et al., 2014b). Most notably, recent (1990s and 2000s) methods of obtaining list mode data (time stamps of neutron

* Corresponding author. Los Alamos National Laboratory, Los Alamos, NM 87545, United States.
E-mail address: jennifera@lanl.gov (J. Arthur).

https://doi.org/10.1016/j.pnucene.2018.02.024
Received 21 September 2017; Received in revised form 22 February 2018; Accepted 24 February 2018

events registered in a detector) from both measurements and simulations have also been developed and allow for a more detailed comparison between the two (Hutchinson et al., 2016).

More recently, there has been significant progress on the design and execution of benchmark quality subcritical neutron multiplication measurements for radiation transport code and nuclear data validation. The majority of these experiments have involved a 4.5 kg alpha-phase plutonium sphere (BeRP ball) surrounded by copper (Bahran and Hutchinson, 2016), tungsten (Richard and Hutchinson, 2016), and nickel (Richard and Hutchinson, 2014). Evaluations of the nickel and tungsten measurements have both been accepted into the International Criticality Safety Benchmark Evaluation Project (ICSBEP) Handbook (Briggs et al., 2014). The ICSBEP handbook contains hundreds of benchmark quality critical and subcritical measurement evaluations. The purpose of the handbook is to provide benchmark quality data that can be used for validation and improvement of nuclear databases and radiation transport codes. The nickel benchmark was the first ICSBEP-accepted evaluation of measurements analyzed with the Hage-Cifarelli formalism based on the Feynman Variance-to-Mean method (Cifarelli and Hage, 1986), and was the culmination of many years of collaborative subcritical experiment research (Arthur et al., 2016; Bahran et al., 2014a; Sood et al., 2014; Bolding and Solomon, 2013; Miller et al., 2010; Mattingly, 2009; Hutchinson et al., 2016; Richard and Hutchinson, 2014, 2016; Hutchinson et al., 2013a, 2013b, 2014, 2015a). Although the state-of-the-art has been advancing throughout the years, benchmark measurements have only been done with simple SNM geometries. There is no protocol on how to best perform, and what can be learned from, measurements on increasingly complex reactor systems, such as zero-power pin-type pool research reactors. Furthermore, these types of measurements can also inform protocol for future subcriticality monitoring measurements on accelerator driven reactor systems (Dulla et al., 2014; Chabod et al., 2014; Uyttenhove et al., 2014).

2. Establishing a research reactor protocol

The Critical and Subcritical 0-Power Experiment at Rensselaer (CaSPER) measurement campaign was designed to establish a protocol for neutron multiplicity measurements on research reactors as the next step in advanced subcritical neutron multiplication inference measurements. Such measurements can help identify deficiencies and quantify uncertainties in nuclear data, as well as validate predictive radiation transport simulation capabilities related to subcritical neutron multiplication inference techniques. CaSPER includes integral experimental configurations at different achieved reactivity states which have been measured at the Walthousen Reactor Critical Facility (RCF) (Thompson et al., 2015) at Rensselaer Polytechnic Institute (RPI). The RCF achieves different reactivity states by varying the control rod (CR) and water height in the reactor core. It is a benefit that the system is able to reach a wide range of multiplication states, by using both fine and coarse reactivity control in the form of CR and water height, respectively. It is also useful to know the possible reactivity states ahead of time, through the use of reactivity worth curves. The diversity of the CaSPER configurations are unique in contrast to previous subcritical benchmark measurements in that they are the first neutron multiplication inference measurements on a zero-power pool-type reactor which offers spatial complexity, different materials (fuel, moderator, CR material, etc.) and system-specific neutron cross-section sensitivities (various energy ranges and neutron reaction contributions).

2.1. Measurements at 0-power reactor

Nominally, a 0-power reactor is the ideal type of pool-type reactor for conducting neutron multiplicity measurements. A substantial benefit of a 0-power reactor is the ability to directly adjust fuel rods as desired. The detector system can be placed in close proximity to the core without the disadvantage of possible radiation damage to the detector system electronics or materials. Additionally, the detector system is much less likely to be overwhelmed in the relatively lower neutron flux of a 0-power reactor. Due to the absence of noticeable burnup, the fuel inside a 0-power reactor is typically very well characterized as compared to fuel from reactors with significant burnup. The fuel rods also do not become distorted (i.e. cracking, swelling, or melting) from burnup while residing in a 0-power reactor (distortion occurs when the heat from fission reactions causes the fuel to melt and fuse into distorted geometries). In addition to changing the fuel composition and geometry, the high burnup of some research reactors can preclude entering the core for direct manipulation of experiment equipment. Due to the buildup of fission products, the gamma ray flux inside the reactor core can become quite significant. Although ^{3}He tubes are relatively insensitive to gamma rays, a large flux may significantly increase the noise signal even in ^{3}He detectors (Trahan, 2016). Specific to a 0-power pin-type reactor, the symmetry of typical fuel rod arrangement (rather than the fuel plates used within some reactors) is beneficial to neutron multiplicity measurements. A 0-power reactor best matches the criterion in neutron multiplicity measurements of understanding the dimensions and components of the system to be measured as well as possible.

2.2. Correlated neutron detection

Correlated neutron detection involves detecting fission neutrons that are correlated in time, energy, angle, and number. The time of emission, kinetic energy, directional angle of emission, and number of emitted neutrons are all dependent upon each other in a true fission reaction (Wagemans, 1991). Multiplying system parameters of interest in correlated neutron benchmark measurements include the singles rate R_1, the doubles rate R_2, and the leakage multiplication M_L. The "singles" rate is defined as the rate of detection of single neutrons from a fission chain. The "doubles" rate is defined as the rate of detection of two neutrons from the same fission chain. M_L represents the average number of neutrons that would escape the system following the introduction of a single neutron to the system. The following sub-sections outline how the parameters of interest are obtained from raw measured and simulated data.

2.2.1. Measured data processing

Neutron multiplicity measurements record list-mode data, which consists only of the time of neutron detection and the tube in which the detection occurred. In this work, the ^{3}He detector system records only these two pieces of information. The list-mode data can be used for many different types of multiplicity analysis methods; for this work the data was analyzed with the Hage-Cifarelli formalism based on the Feynman Variance-to-Mean method. The list-mode data were binned into Feynman histograms according to specified time widths using the data processing tool Momentum (Smith-Nelson, 2015). A Feynman histogram is a representation of the relative frequencies of various multiplets (i.e., 1 event, 2 events, etc.) occurring within the specified time width, as shown in Fig. 1.

The magnitude of the n^{th} bin of the Feynman histogram at the specified time width τ is represented by the variable $C_n(\tau)$ in Equation (1). Standard multiplicity equations, in the form of Equations (1)–(9) (Hutchinson et al., 2015b), are applied to calculate the singles (R_1) and doubles (R_2) rates, as well as the leakage multiplication (M_L). Equation (6) is a specific form of Equation (5) when the subscript is 2, which is needed to calculate the doubles rate. Equations for the uncertainties in R_1, R_2, and M_L can be found in reference (Hutchinson et al., 2015b). In the following equations, the symbols λ, ε, ν_{Ii} and ν_{si} represent the prompt neutron decay constant, detector absolute efficiency, i^{th} moment of the induced fission multiplicity distribution, and i^{th} moment of the spontaneous fission multiplicity distribution, respectively. $m_r(\tau)$ is the r^{th} factorial moment of the Feynman histogram. Y_2 is directly

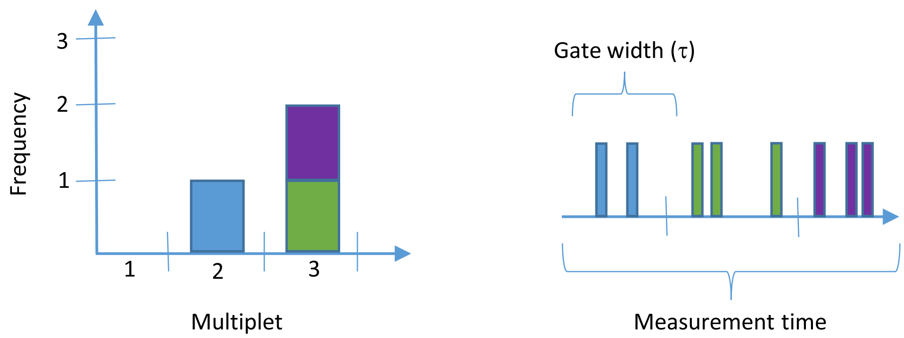

(a)

Fig. 1. The binning method used to generate Feynman histograms in this work.

proportional to the Feynman Y value, which is a measure of the deviation of the histogram from a Poisson distribution. The prompt neutron decay constant can be obtained by fitting the curve of Y_2 versus time width to the form of Equation (6). The most commonly used units in this work for many of the variables presented in this section are listed in Table 1.

$$p_n(\tau) = \frac{C_n(\tau)}{\sum_{n=0}^{\infty} C_n(\tau)} \tag{1}$$

$$m_r(\tau) = \frac{\sum_{n=0}^{\infty} n(n-1)...(n-r+1)p_n(\tau)}{r!} \tag{2}$$

$$R_1(\tau) = \frac{m_1(\tau)}{\tau} \tag{3}$$

$$Y_2(\tau) = \frac{m_2(\tau) - \frac{1}{2}[m_1(\tau)]^2}{\tau} \tag{4}$$

$$\omega_\mu(\lambda, \tau) = \sum_{K=0}^{\mu-1} \binom{\mu-1}{K} (-1)^K \frac{1-e^{-\lambda\tau K}}{\lambda\tau K} \tag{5}$$

$$\omega_2(\lambda, \tau) = 1 - \frac{1-e^{-\lambda\tau}}{\lambda\tau} \tag{6}$$

$$R_2(\tau) = \frac{Y_2(\tau)}{\omega_2(\lambda, \tau)} \tag{7}$$

$$M_L = \frac{-C_2 + \sqrt{C_2^2 - 4C_1C_3}}{2C_1} \tag{8}$$

$$C_1 = \frac{\nu_{s1}\nu_{I2}}{\nu_{I1}-1},\ C_2 = \nu_{s2} - \frac{\nu_{s1}\nu_{I2}}{\nu_{I1}-1},\ C_3 = -\frac{R_2(\tau)\nu_{s1}}{R_1(\tau)\varepsilon} \tag{9}$$

Equations (8) and (9) are true only if the (α, n) neutron emission rate from the fission source is assumed to be negligible. Theoretically, this would be the case in a system consisting of only a ^{252}Cf starter source and low-enriched uranium fuel. However, the large contribution to the measured signal from the RCF PuBe source (roughly 1E7 $\frac{n}{s}$ in strength) above the core renders this assumption inaccurate. Equations (10)–(13) are used instead of the previous equations when the (α, n) neutron contribution is not negligible. These equations also assume that the (α, n) source and the fission source are coincident point sources; i.e., a small sample of uranium or plutonium oxide. Therefore, they are also not completely valid for this work. Appendix B details the method that was used to calculate M_L.

$$R_1 = \varepsilon[b_{11}F_s + b_{12}S_\alpha] \tag{10}$$

$$R_2 = \varepsilon^2[b_{21}F_s + b_{22}S_\alpha] \tag{11}$$

Table 1
Most commonly used units for many of the variables used in this work for correlated neutron detection.

Variable	Units
τ	s
$C_n(\tau)$	# of occurrences
$R_1(\tau)$	s^{-1}
$R_2(\tau)$	s^{-1}
λ	s^{-1}
ε	unitless
M_L	unitless

$$b_{11} = M_L\nu_{s1}\ b_{12} = M_L \tag{12}$$

$$b_{21} = M_L^2\left[\nu_{s2} + \frac{M_L-1}{\nu_{I1}-1}\nu_{s1}\nu_{I2}\right] b_{22} = M_L^2\frac{M_L-1}{\nu_{I1}-1}\nu_{I2} \tag{13}$$

Rossi data is a histogram of time differences between events in the list-mode data, as shown in Fig. 2. The decay constant (Rossi-alpha value) is obtained from a fit of the Rossi data versus time to Equation (14). The prompt neutron decay constant λ in Equation (14) is traditionally represented as α, but in this work λ is being used to represent the prompt neutron decay constant. The first term of Equation (14) is the constant background of uncorrelated counts, while the second term includes all correlated counts. A, B, and Δ are the coefficient of the uncorrelated count contribution, the coefficient of the correlated count contribution, and an infinitesimal time window, respectively. Type I binning is used in this work, although other methods of Rossi binning exist (McKenzie, 2014; Hansen et al., 1968; Degweker and Rudra, 2016).

2.2.2. Simulated data processing

Simulated results are produced by processing simulated list-mode files in the same way as measured list-mode files are processed. Simulated list-mode files are created by pulling the necessary information from the PTRAC output file of MCNP®6.2[1] (Goorley et al., 2012). The PTRAC file contains information about all particle interactions that occurred during the MCNP simulation. In order to produce list-mode data the MCNP input file must be run in analog mode, such that the weights of all particles are always unity. Using a script from the MCNPtools package (Solomon, 2014), the time and detector of interaction corresponding to each event is pulled from the PTRAC file and input into a list-mode data file containing only those two pieces of

[1] MCNP® and Monte Carlo N-Particle® are registered trademarks owned by Los Alamos National Security, LLC, manager and operator of Los Alamos National Laboratory.

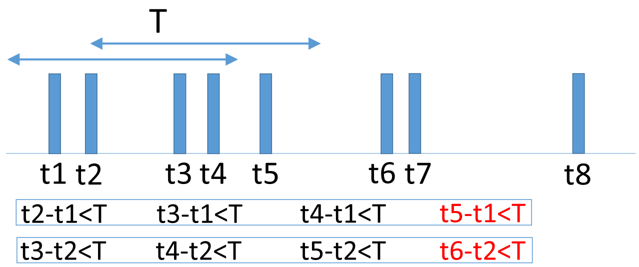

Fig. 2. The time differences between events used to generate Rossi data.

$$P(t)\Delta = A\Delta + Be^{-\lambda t}\Delta \tag{14}$$

information. Finally, the list-mode data are converted into the correct format to be processed by Momentum, alongside measured data, using a PERL script (Temple, 2009).

3. Experiment

3.1. Experiment design

The CaSPER measurements at the RPI-RCF were designed to include distinct configurations at various reactivity states ranging from subcritical to above delayed critical. Nine different configurations were achieved by varying the control rod and water height in the reactor core. The RCF core has low-enriched uranium (LEU) fuel in the form of SPERT-type F-1 fuel pins at an enrichment level of 4.81% U-235 by weight (Thompson et al., 2015). Fuel pins are encased in stainless steel cladding and boron-impregnated iron rods serve as CR's. When the tank is filled the water serves as a moderator. The large water tank containing the core is large enough to accommodate a sizable detector system(s), including the standard Los Alamos National Laboratory (LANL) ^{3}He portable neutron multiplicity detector systems which were retrofitted for water submersion.

The detector system used in CaSPER is the LANL Neutron Multiplicity ^{3}He Array Detector (NoMAD), which is a slightly modified version of the state-of-the-art MC-15 neutron multiplicity counter (Moss et al., 2016), and the state-of-the-art detection system for obtaining list-mode data from highly multiplying systems. The NoMAD consists of 15 ^{3}He tubes encased in polyethylene moderator. The thickness of moderator between each tube is optimized for detection efficiency. The overall size and number of tubes contained in the detector system was chosen as a trade-off between increasing efficiency and decreasing portability. Every ^{3}He tube has a pressure of 150 psia (10.13 bars) and active dimensions of 0.97 × 15 in. (2.46 × 38.1 cm). The counter's fill gas is a mixture of ^{3}He with 2% CO2 as a quench gas (in atomic proportion). A removable cadmium shield can be placed on the front of the NoMAD to preferentially capture thermal neutrons and is often used to reduce contributions from neutrons that scatter from the environment surrounding fast multiplying systems. Because the neutrons inside a water-moderated reactor are predominantly thermal, the removable cadmium shield was not utilized for the CaSPER measurements. Representations of the NoMAD geometry, produced using the CAD software Solidworks® and the MCNP plotter, are shown in Fig. 3. In order to protect the NoMAD during submersion under water and to hold it in place, $\frac{1}{16}$in. thick aluminum housing and ratchet straps were used.

A photograph from the measurement campaign is shown in Fig. 4. This photo shows 2 NoMAD systems, although only a single system was used for these measurements. In addition, the aluminum housing and ratchet straps are not shown. The distance between the ^{252}Cf source, located at the center of the core in place of the center fuel pin, and the NoMAD is 48.5 cm. The vertical center of the NoMAD is level with the vertical center of the core. The ^{252}Cf source information is given in Table 2. Both the initial assay activity and the calculated activity at the

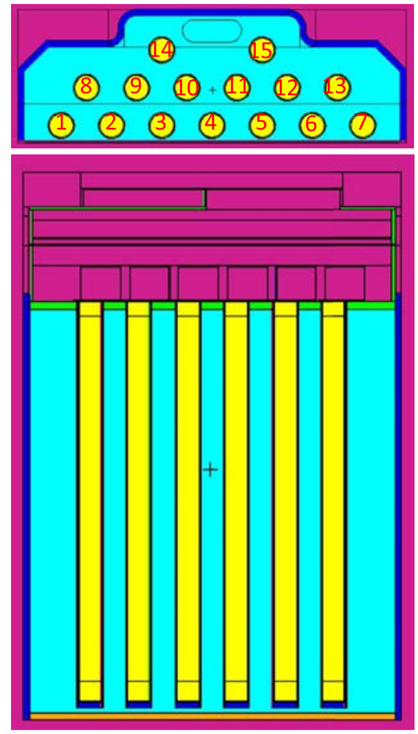

(a) MCNP plotter representation of the NoMAD geometry as seen from the top (upper image) and front (lower image)

(b) CAD representation of the NoMAD geometry

Fig. 3. MCNP plotter and CAD representations of the NoMAD geometry.

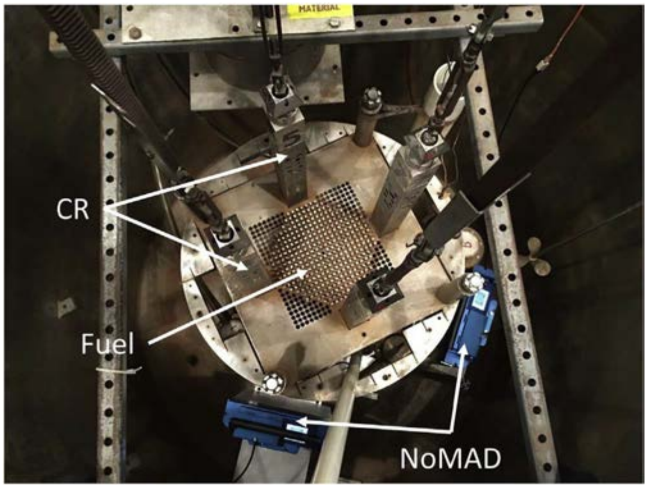

Fig. 4. Photograph of the CaSPER measurement campaign at the RPI-RCF with the water drained from the core tank.

Table 2
^{252}Cf source information.

Date	6/1/2006	7/25/2016
Activity (Bq)	1.54E7 (± 5.6%)	1.07E6
Strength (n/s)	1.79E6	1.25E5

Table 3
NoMAD count rate as a function of reactor core tank radius. The date for radii of 30–50 cm are from simulations, while the data for radii of 60–100 cm are from the extrapolated fit of the simulated data.

Tank radius (cm)	Singles rate (s^{-1})
30	3.27E+05
40	4.33E+04
50	8.13E+03
60	1.21E+03
70	1.90E+02
80	2.99E+01
90	4.70E+00
100	7.39E-01

time of the CaSPER campaign are shown.

During the design phase of the experiment, the MCNP model did not include the RCF PuBe source in its above-core shielding, as it was expected that its contribution would be negligible. Simulations were run with different ^{252}Cf source-detector distances, source strengths, and water and CR heights, with the goal of optimizing both the detector system count rates and the goodness of the doubles fits (quantified by the χ^2 value). The optimum count rate was considered to be between 1E3 and 1E5 s^{-1}, which represents a balance between the need for good statistical uncertainties and detector limitations. Based on these criteria it was determined that the optimized CaSPER configuration consisted of the NoMAD detector system at a distance of 35 cm from the center of the RCF core, with the ^{252}Cf source replacing the center fuel pin, and varying water and CR heights. However, the layout of the RCF core added some physical restrictions, and the NoMAD distance was changed to 48.5 cm. A parametric study was conducted to determine if the RPI-RCF water tank size would allow for placement of the NoMAD outside of the tank. The position of the NoMAD in the CaSPER MCNP model, at a water height of 67 in. and control rods fully withdrawn, was changed from inside the reactor core tank, to just outside the tank. The tank radius in the MCNP model was then set to be 30, 40, and 50 cm, while keeping the NoMAD position to be just outside the tank. Count rates were obtained at these distances and an exponential fit was used to extrapolate the data out to a tank radius of 100 cm. Extrapolation of a fit was used to generate the data at 60–100 cm because of the extensive computation time that would have been required to obtain simulated data at those tank radii. Equation (15) shows the exponential fit, and all results are listed in Table 3. An exponential fit was used both because exponential attenuation of neutrons in the water is expected to outweight the reduction in flux due to the $\frac{1}{distance^2}$ reduction in solid angle, and because an exponential fit followed the data trend well.

$$y = 8*10^7 e^{-0.185x} \tag{15}$$

Because the results of the parametric study indicate that the RCF water tank is too large for a high enough neutron signal to be obtained from outside of the tank, this detector system placement was not investigated further. The final experiment design included Monte Carlo simulations of the full system: neutron multiplicity detector, ^{252}Cf source which was included to increase the number of fissions and associated count rate for statistical adequacy, the PuBe starter source that is always located in a shielding container above the core, and the reactor configuration (fuel/rods/water). Ratchet straps were not included in the model because it was assumed they would have negligible impact

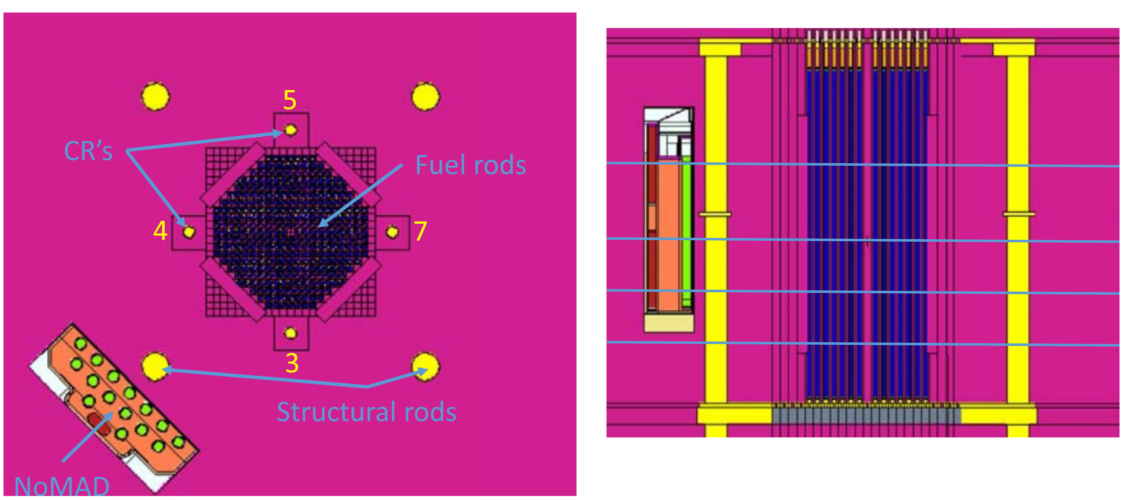

Fig. 5. MCNP plotter representation of the CaSPER geometry as seen from above and the side. The ^{252}Cf source is located in the center of the fuel region and the CR numbers are shown. The light blue lines show the water level in relation to the NoMAD at 24 in., 30 in., 36 in., and 44 in. water height. (For interpretation of the references to colour in this figure legend, the reader is referred to the Web version of this article.)

Table 4
Completed measurement configurations.

Configuration #	Water height	CR3 height	CR4 height	CR5 height	CR7 height	Intended reactivity
1	24 in.	36 in.	36 in.	36 in.	36 in.	–
2	30 in.	36 in.	36 in.	36 in.	36 in.	–
3	36 in.	36 in.	36 in.	36 in.	36 in.	–
4	44 in.	36 in.	36 in.	36 in.	36 in.	–
5	67 in.	0 in.	0 in.	0 in.	0 in.	–
6	67 in.	16 in.	16 in.	16 in.	16 in.	-$1.00
7	67 in.	20 in.	20 in.	20 in.	20 in.	-$0.50
8	67 in.	25 in.	25 in.	25 in.	25 in.	Delayed critical
9	67 in.	36 in.	36 in.	21 in.	21 in.	Delayed critical

on the observables of interest. The standard simulation model is shown in Fig. 5. The PuBe source spectrum used in the model was taken from Anderson and Neff (1972).

3.2. Experiment execution

The RCF core configuration at the time of the CaSPER experiment was an octagonal lattice of 332 fuel pins, separated by a pitch of 1.63 cm. The center 333rd fuel pin was removed and the ^{252}Cf source was put in its place. The CR height can vary from 0 in., full insertion, to 36 in., full removal. During reactor operations in which the CR height is above 0 in., the water height is allowed vary between 19.5 in. and 67 in. The equipment used in the measurements includes the NoMAD detector, along with the aluminum housing and aluminum stands used to keep the detector water tight and in position within the tank, as well as lead bricks strapped to the bottom of the NoMAD housing to prevent

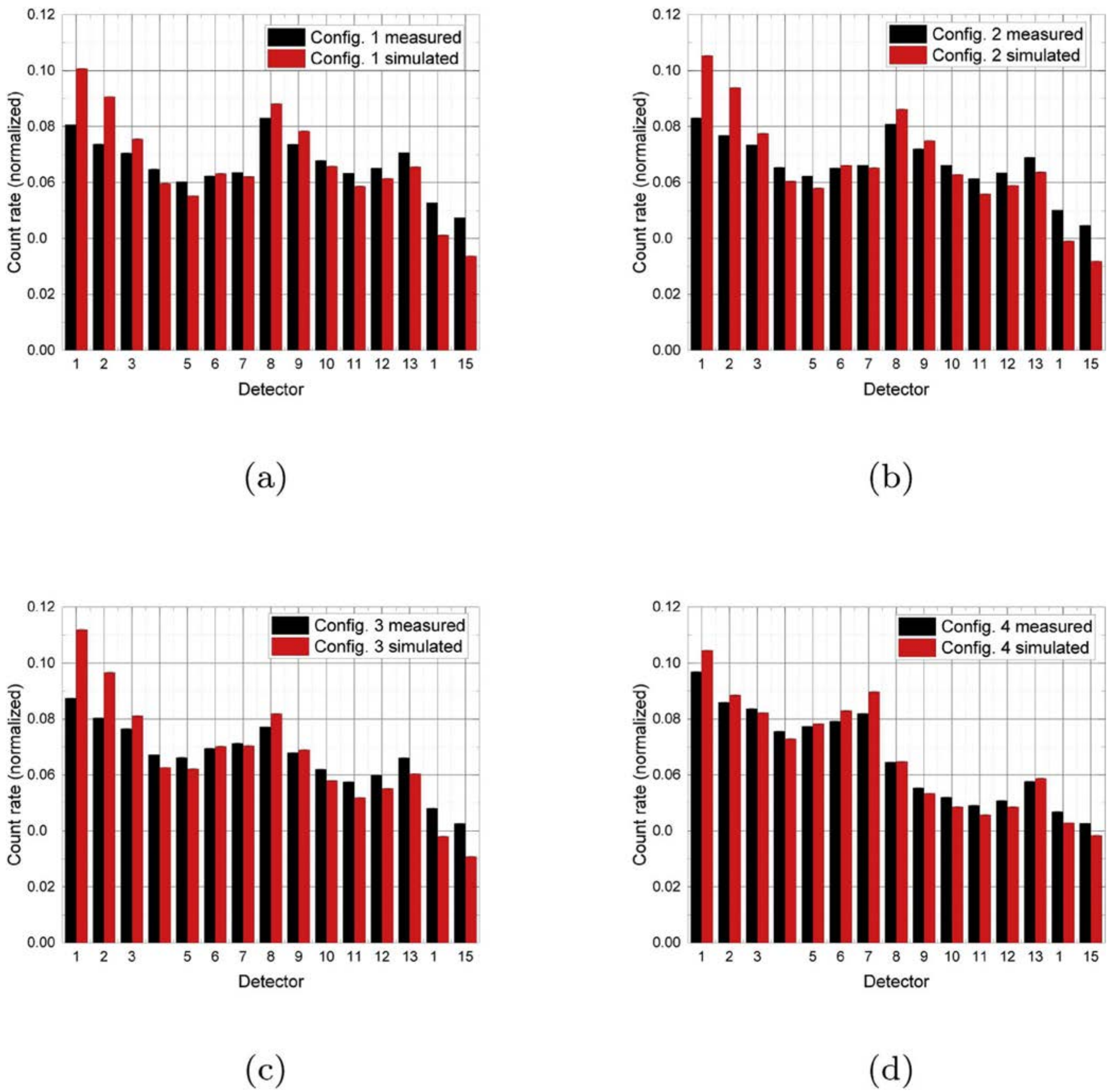

Fig. 6. Normalized count rates per ^{3}He tube for configurations 1–4.

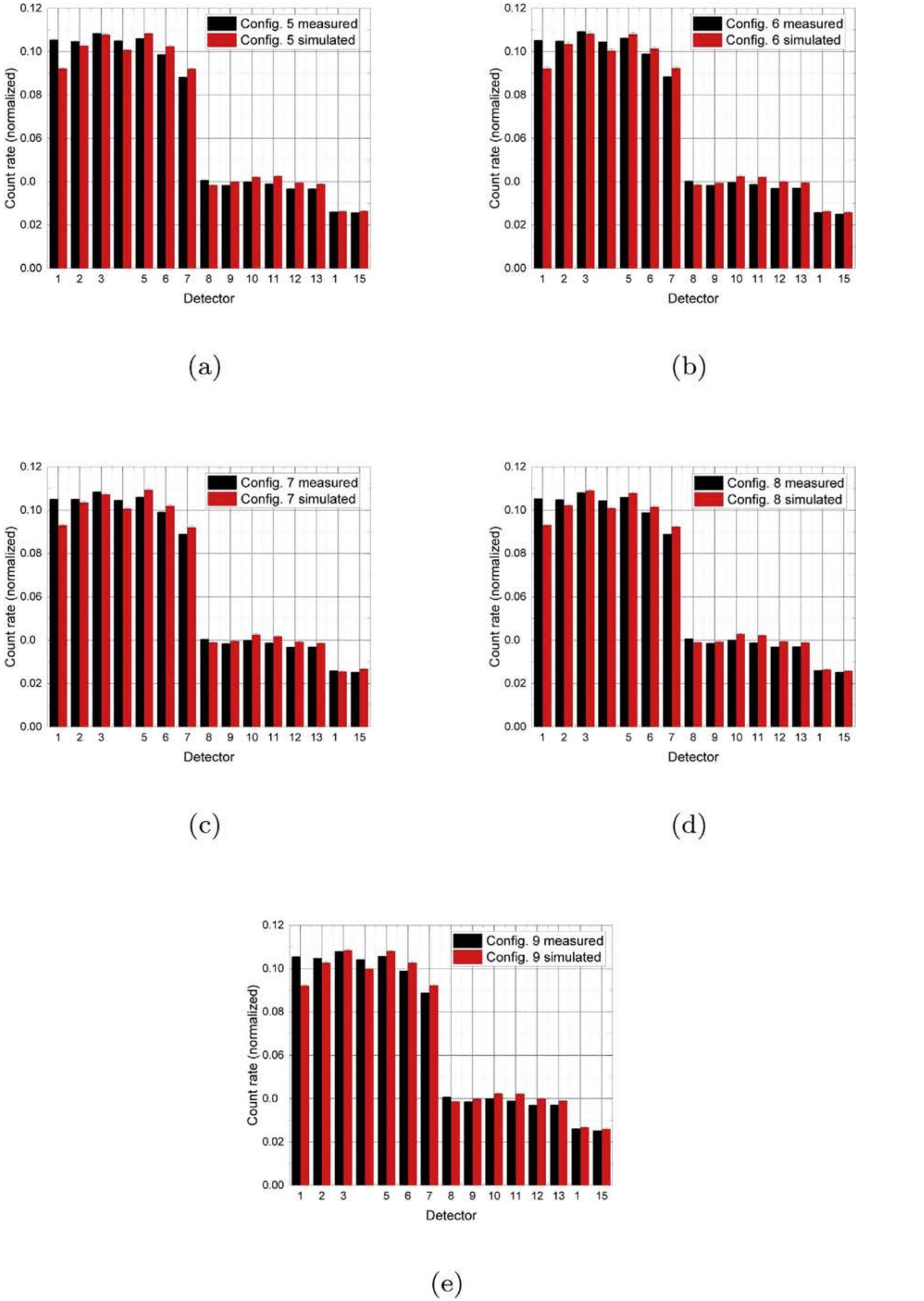

Fig. 7. Normalized count rates per ^{3}He tube for configurations 5–9.

Table 5
FOM values for simulated and measured count rates per detector tube comparisons.

Configuration	FOM
1	69876
2	79135
3	66822
4	5717
5	3109
6	645
7	533
8	944
9	1094

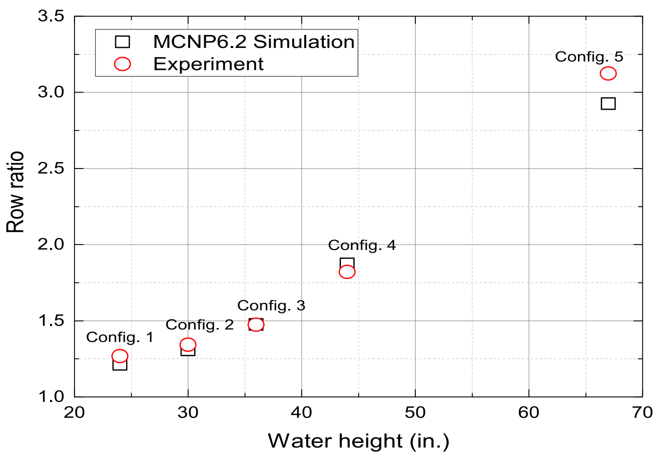

Fig. 8. Row ratio vs. water height.

flotation. A summary of the completed measurement configurations, excluding efficiency measurements, is presented in Table 4. The completed efficiency measurements, the purpose of which are to calculate absolute detector efficiency by taking the ratio of the detected count rate to the ^{252}Cf source strength in a non-multiplying system, are identical to the configurations listed in Table 4 but with all of the fuel pins removed from the core.

Using the method presented in Equations (1)–(9), efficiency is required to calculate leakage multiplication. Ideally efficiency would have been calculated from the no-fuel "efficiency measurements" in which no fission is occurring and therefore the true absolute efficiency is measured. However, due to the large contribution of the above-core RCF PuBe starter source to the measured signal, this method is no longer valid. Several different possible methods were investigated and rejected, including taking a measurement of the CaSPER ^{252}Cf source at a 48.5 cm source-detector distance (the same distance as in the actual CaSPER measurements) to determine efficiency, and defining the ratio of the singles rate with fuel to the rate without fuel as M_L. The method that was chosen is explained in Appendix B.

4. Results

The measured data are a novel set of subcritical neutron multiplicity data that involves new and more complex spatial, material, and energy regimes. Normalized count rates per detector tube are plotted in Figs. 6 and 7 for each completed measurement configuration. These data show the normalized count rate observed in each of the 15 ^{3}He tubes that make up the NoMAD detection system. Simulated results are also plotted for comparison, and figure of merit (FOM) values quantifying the deviations are listed in Table 5. The values are calculated according to Equation (16) (Bolding, 2013). In Equation (16), N represents the total number of bins in the histogram. S_i and E_i are the values of the ith normalized bins in the simulated and experimental data, respectively.

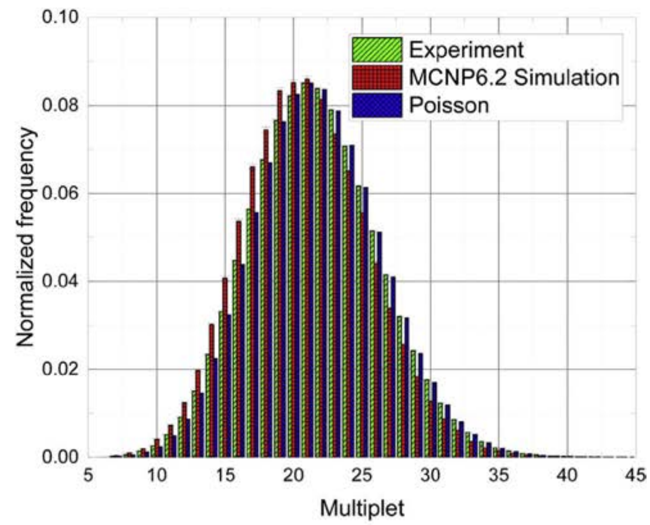

(a) 24 in., Configuration 1.

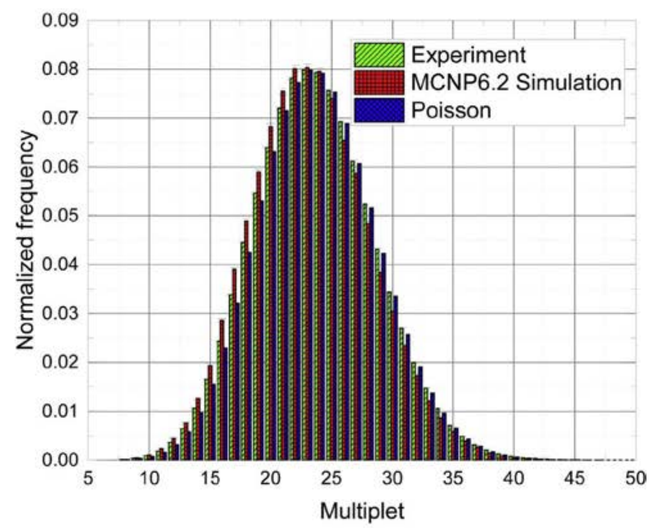

(b) 30 in., Configuration 2.

Fig. 9. Feynman histograms for various water heights.

The variances of the ith bins in the simulated and experimental data are represented by $\sigma^2(S_i)$ and $\sigma^2(E_i)$, respectively. The ideal FOM value is 1, representing a deviation between simulated and experimental histogram results that is equal to the combined uncertainties.

$$FOM = \frac{1}{N-1}\sum_{i=1}^{N}\frac{(S_i - E_i)^2}{\sigma^2(S_i) + \sigma^2(E_i)} \tag{16}$$

From visual inspection, it is clear that there is generally good agreement between simulated and experimental normalized count rates per ^{3}He tube. According to the FOM values, best agreement (defined as a FOM value closer to unity) is shown for the highest water height configurations, namely configurations 6–9 (67 in.). This effect is most likely due to the fact that these configurations are less affected by the PuBe source, because of the water shielding neutrons from the PuBe source as well as the increase in neutrons coming from the core at the higher multiplication. The asymmetry in the count rate distributions for

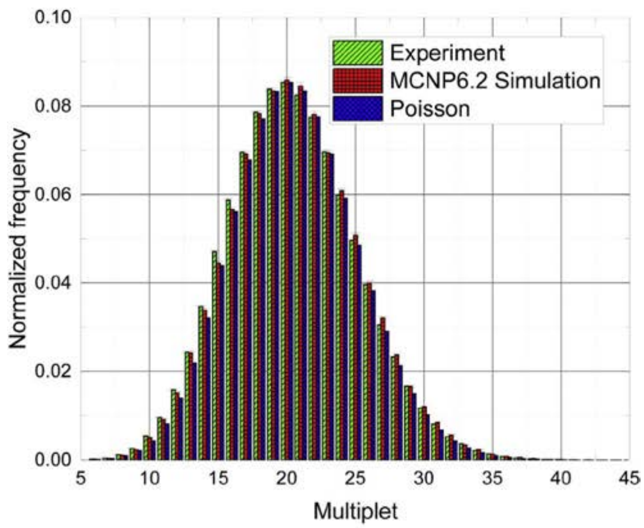

(a) 36 in., Configuration 3.

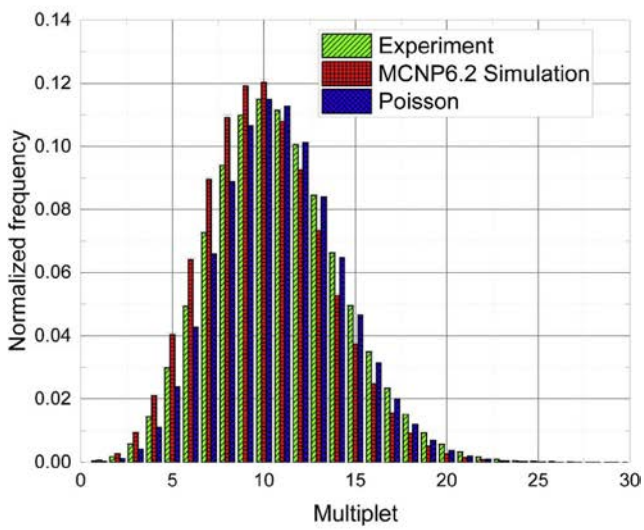

(b) 44 in., Configuration 4.

Fig. 10. Feynman histograms for various water heights.

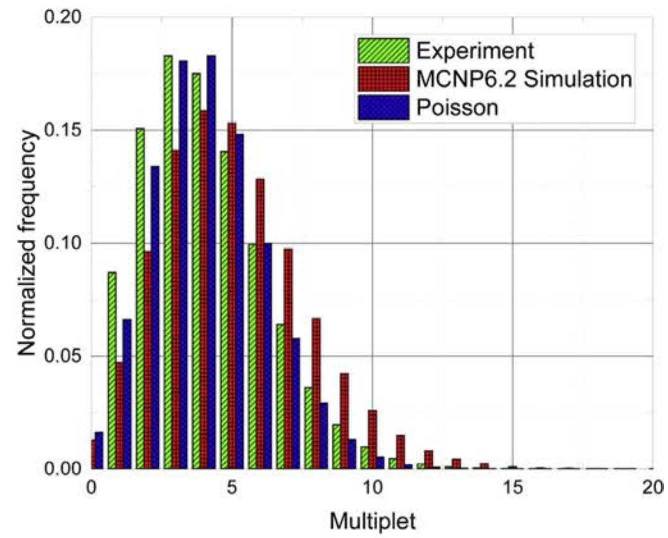

(a) 0 in., Configuration 5.

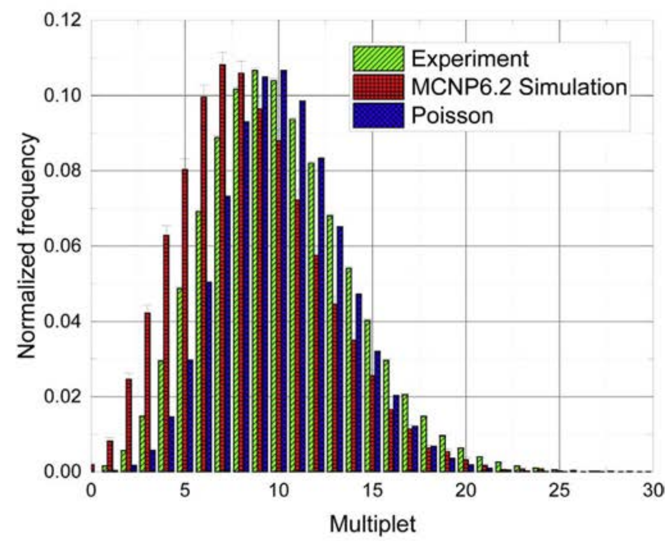

(b) 16 in., Configuration 6.

Fig. 11. Feynman histograms for various CR heights.

configurations 1–4 is caused by contributions from the non-centrally located PuBe starter source for the RCF. If the PuBe source were not present the outer tube pairs (1 and 7, as well as 8 and 13) would be expected to have similar count rates to each other. However, because the PuBe source is located towards the side of the MC15 containing tubes 1 and 8, these tubes display much higher count rates than tubes 7 and 13.

The RCF PuBe starter source, which is located above the core within a layer of paraffin wax shielding, was not well characterized at the time of the CaSPER measurement. Neither the source strength nor the diameter of the hole containing the source inside the wax shielding was well known. A series of simulations was therefore performed in order to ascertain the PuBe strength and shielding specifications that gave the best match to the CaSPER measurements. The details are summarized in Appendix A.

Measured and simulated row ratios, the ratio of the number of counts in the front row (tubes 1–7 in Fig. 3) of the NoMAD to the number of counts in the middle row (tubes 8–13) of the NoMAD, are plotted in Fig. 8 as a function of water height. As the neutron spectrum becomes softer, the row ratio increases. This is expected because lower energy neutrons require less moderation in the polyethylene before reaching the energy range at which they can be detected by the ^{3}He tubes. Therefore, at lower energies the neutrons are more likely to interact with the front rather than the middle row of ^{3}He tubes.

Measured and simulated Feynman histograms for various water and CR heights are shown in Figs. 9–12. Poisson distributions constructed using the mean of each measured histogram are plotted as well. A measurement of a non-multiplying system would be expected to produce a Poisson-shaped Feynman histogram; the deviation from Poisson is correlated with the multiplication of a system. A list of FOM values for the Feynman histograms is shown in Table 6.

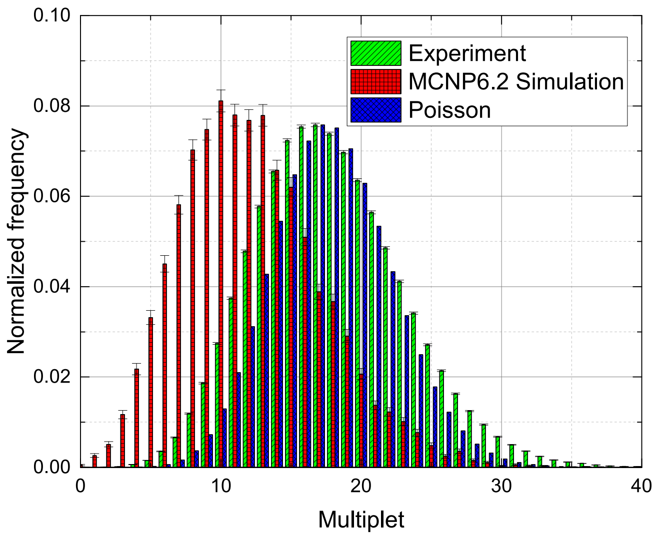

Fig. 12. Feynman histograms for 20 in. CR height.

Table 6
FOM values for simulated and measured Feynman histogram comparisons.

Configuration	FOM
1	3975
2	1372
3	119
4	6834
5	20358
6	1845
7	21364

The Feynman histograms show an interesting trend with increasing water height. Initially, the histogram begins to shift to higher multiplets. At a certain turning point at which increasing shielding outweighs increasing multiplicity, the histograms begin to shift back to lower multiplets. It is expected that measured and simulated histograms deviate more at the highest water heights, due to the increased multiplication. This is because as multiplication increases the variance (width) of the histogram is also increasing. At high multiplication neutrons are more likely to be detected in small bursts over short periods of time. Because multiplication is proportional to the deviation from Poisson statistics, the Feynman histograms at higher multiplication also show more deviation from Poisson. The FOM values show that 44 in. water height does indeed show more deviation between simulated and measured histograms than any of the lower water height configurations. The data at 36 in. water height show the best agreement according to the FOM values as expected due to the fact that the RCF PuBe source configuration optimization (Appendix A) was conducted using simulations of the 36 in. water height configuration. This configuration was chosen because it is a mid-level water height and therefore the most representative of all of the measured configurations. To simplify the PuBe source model optimization process, only this representative configuration was used.

Fig. 13 shows plots of Y_2 vs. gate width (see Equation (4)). These plots were used to determine at which gate width to obtain singles, doubles, leakage multiplication, and Feynman histogram results. Ideally a gate width at which all Y_2 plots have reached an asymptote is chosen, because this yields the “true” count rates. A gate width of $\tau = 3368\,\mu s$ was chosen. Although not all configurations have reached an asymptote at this gate width, data processing limitations did not allow for a larger gate width to be chosen. Because comparisons between simulated and measured results are of primary interest, and both simulated and measured results were taken at the same gate width, this is not a concern. It is interesting to note that Y_2 reaches a larger asymptote at a longer gate width as water height increases. Although this behavior could be caused by other factors, in the case of the CaSPER measurement the larger asymptote is most likely due to the increase in multiplication, while the longer gate width is due to the increase in moderation.

Measured and simulated, using MCNP6.2, singles and doubles rates are plotted in Fig. 14 as functions of water height, in Fig. 15 as functions of control rod height, and in Fig. 16 for the delayed critical configurations.

The trends shown in Fig. 14 are the result of the trade-off between increasing multiplication and shielding with increasing water height. As the water height is increased from lower levels, both the singles (R_1) and doubles (R_2) rates increase due to increasing multiplication. However, as the water begins to shield the detector from the core (at 30 in. the water has just begun covering the bottom of the NoMAD), the singles rate decreases. This is because the increased shielding is now overcoming the increasing multiplication and fewer neutrons are reaching the detector. The doubles rate does not seem to decrease within the range of water heights measured, however. This is most likely due to the fact that the doubles rate depends more heavily on multiplication, as compared to the singles rate. A true doubles event can only come from fission, and the fission rate is directly related to multiplication, while singles events can occur in any system regardless of the multiplication. Additionally, the correlated neutrons are emitted at fast energies and require moderation to reach the energy range in which the NoMAD is sensitive to neutrons.

Increasing CR height (removing CR's from the core) increases multiplication without increasing shielding. As expected, therefore, Fig. 15 shows trends of purely increasing singles and doubles rates with increasing CR height. Because multiplication is very high for configurations 5–9, small discrepancies in the model will lead to large differences in simulated and measured singles and doubles rates. The measured results for the delayed critical configurations in Fig. 16 are an order of magnitude larger than the simulated results. The magnitude discrepancy is most likely due to the exponential increase in neutron population that occurred when the reactor was briefly brought to a delayed supercritical state during the approach to critical procedure. The neutron population remained at this elevated level during the subsequent measurements at delayed critical, and because the supercritical excursion was not modeled in MCNP, this behavior was not included in the simulation. It is interesting to note that both simulated and experimental results are very similar between the two delayed critical configurations, even though the CR setup was different for each.

Neutron lifetime, the inverse of the prompt decay constant, was obtained from fits of the measured Rossi data. Rossi data plots are shown in Figs. 20 and 21. Alternatively, lifetime could have been obtained from fits of the Y_2 plots. However, the residuals trends displayed much worse behavior than the corresponding Rossi residuals. See Fig. 19 for a representative example. It is much more preferable to have residual values center around zero with no increasing or decreasing trends, as in the Rossi residual plot. Neutron lifetime, $\frac{1}{\lambda}$, and leakage multiplication, M_L, are plotted versus water and CR heights in Figs. 17 and 18. The method used to calculate ε, and therefore M_L, is discussed in Appendix B. Only measured Rossi data and lifetime fits were obtained, and these measured lifetimes were used to calculate simulated doubles and leakage multiplication results.

Both neutron lifetime and leakage multiplication increase with increasing water and CR height, as expected. The increase in neutron lifetime is due to the increased time the neutrons surrounded by water spend in the slowing down range. It is interesting to note that neutron lifetime and leakage multiplication follow similar trends as a function of water height. This behavior has been previously observed for thermal uranium systems (Hutchinson et al., 2015a).

In order to separate the multiplying system and detector lifetimes,

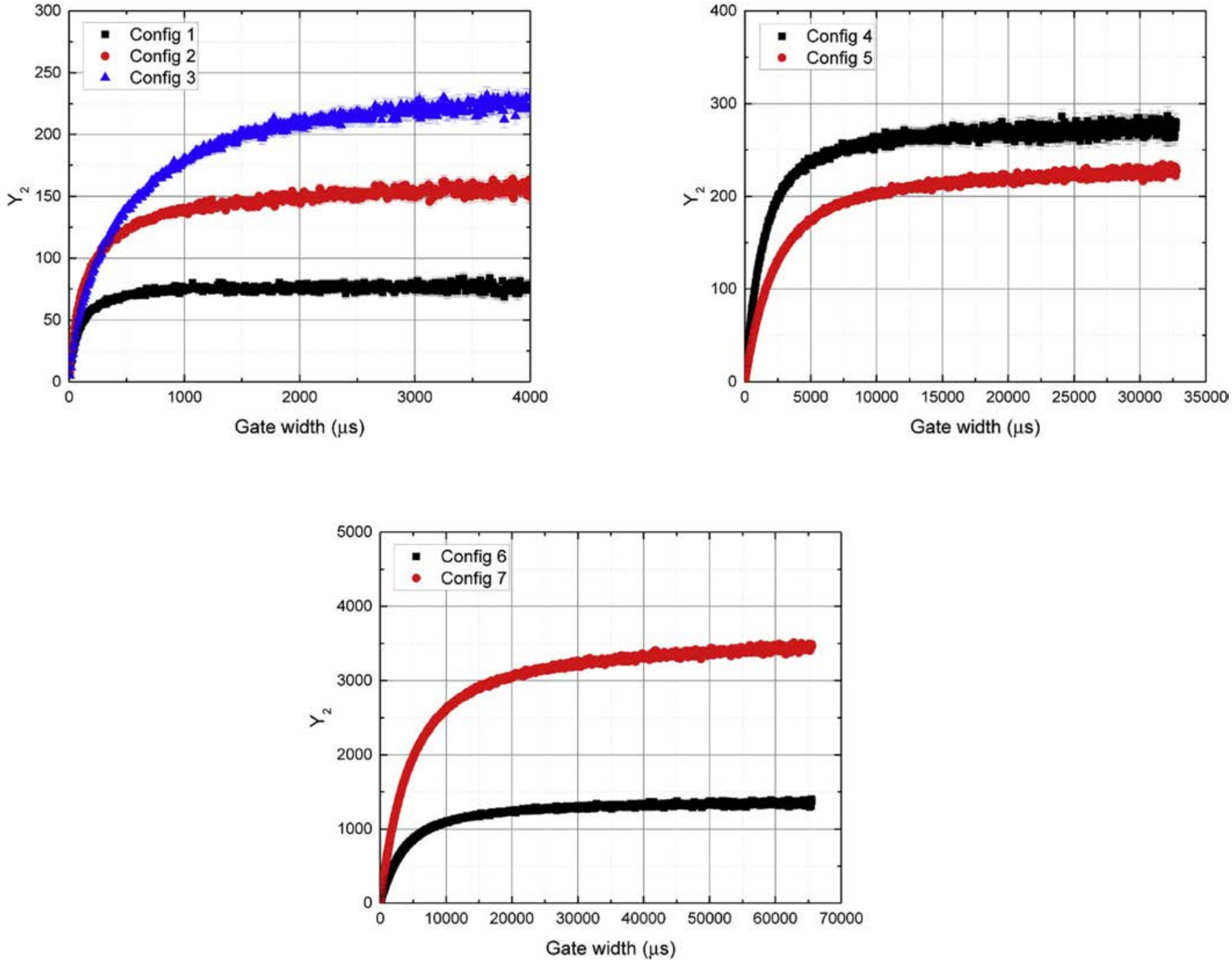

Fig. 13. Y_2 vs. gate width for various configurations.

double rather than single exponential fits were used to fit the Rossi data for configurations 1–4. For the other configurations, the detector lifetime is small enough compared to the system lifetime that only a single exponential fit is required.

Because of the difficulties determining efficiency and leakage multiplication in the CaSPER measurement, an efficiency-independent ratio (Equation (17)) (Smith-Nelson and Hutchinson, 2014) is also plotted in Fig. 22. It is encouraging that this efficiency-independent parameter compares well between simulated and measured results.

$$S_{m2} = \frac{R_2}{R_1^2} \tag{17}$$

4.1. Physical uncertainties

In order to determine the sensitivity of simulated results to physical parameter uncertainties (systematic uncertainties), perturbation analysis was carried out for various physical parameters of interest. For each parameter of interest, the parameter was varied by an amount equal to 5 times its uncertainty. This was performed using the model of configuration 3 from Table 4. The resulting changes in singles and doubles rates, per standard deviation change in the physical parameter, are listed in Table 7.

It is apparent that singles and doubles rates are most sensitive to changes in PuBe strength and NoMAD distance, followed by ^{252}Cf strength and water height, and are very insensitive to changes in CR height. It is expected for the results to be much more sensitive to changes in coarse (water) than fine (CR's) reactivity control. However, it should be noted that the uncertainty analysis was carried out in a fairly insensitive region of the CR reactivity worth curve. If configuration 6 or 7 were used instead of configuration 3, the sensitivities to CR height would be expected to be larger. The fact that changes in PuBe strength have the largest effect on the observables once again highlights the fact that the RCF PuBe source was unwisely neglected during the design phase of the CaSPER campaign.

It should also be noted that not all possible physical uncertainties were investigated. There are uncertainties associated with fuel composition and density, water temperature, CR boron content, etc. However, these parameters are expected to have smaller sensitivities than the investigated parameters. Because this work is meant to be a

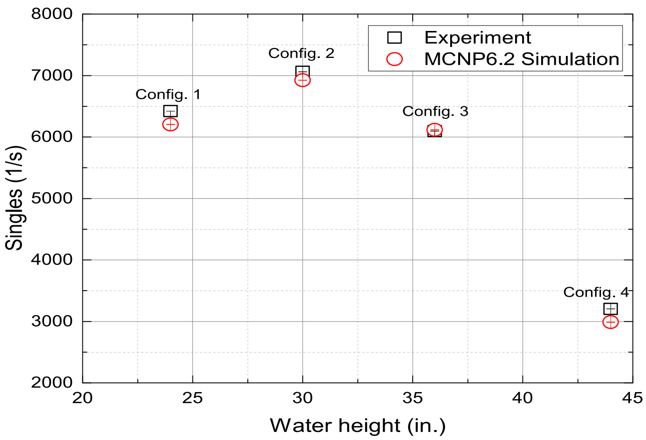

(a)

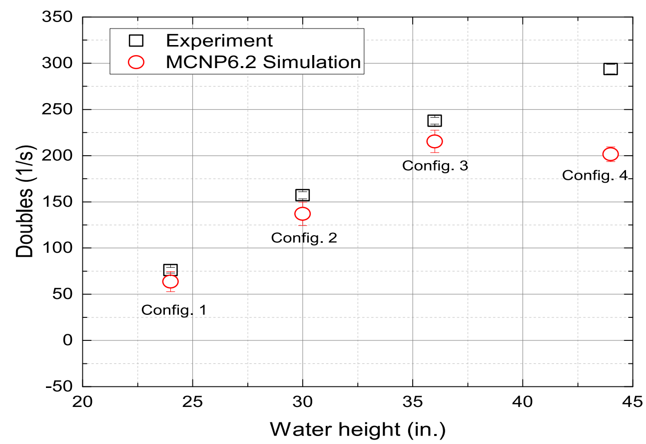

(b)

Fig. 14. R_1 and R_2 as functions of water height. The R_1 trend illustrates the trade-off between shielding and multiplication in a water moderated system.

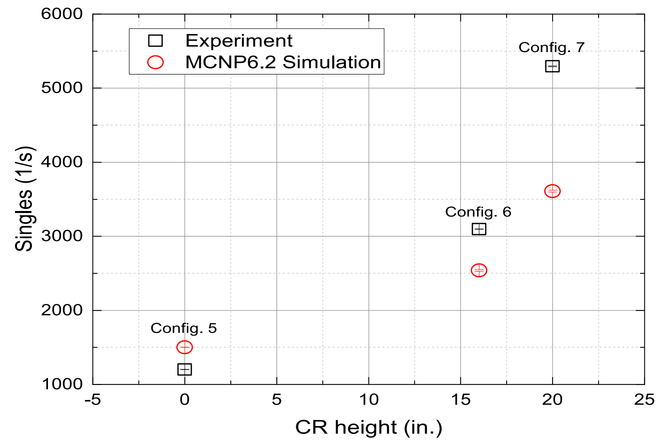

(a)

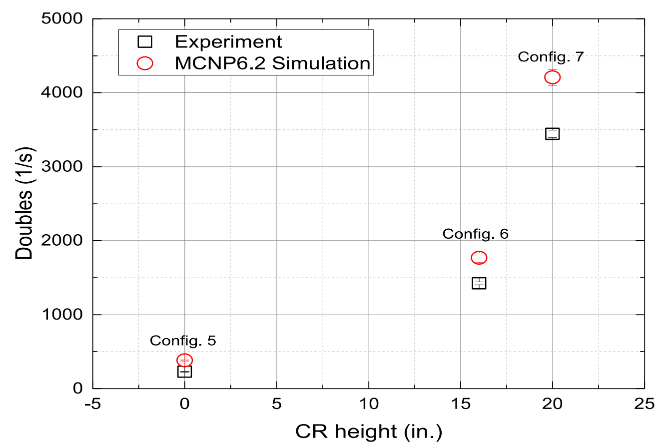

(b)

Fig. 15. R_1 and R_2 as functions of CR height, for a water height of 67 in.

starting point for future measurements rather than a benchmark itself, an exhaustive uncertainty analysis was not carried out. Due to the presence of an above-core starter source that is not well characterized, a benchmark of the CaSPER measurements would be impossible.

4.2. Research reactor protocol

The Critical and Subcritical 0-Power Experiment at Rensselaer (CaSPER) campaign was designed and executed to establish a protocol for advanced subcritical research reactor measurements. For past subcritical benchmarks (Hutchinson et al., 2016; Richard and Hutchinson, 2014, 2016), protocol has consisted of measuring a multiplying system (historically symmetric) with ^{3}He multiplicity detectors around 50 cm away on either side of the system. Measurements were taken both with a bare multiplying system and with symmetric metallic reflectors. Data analysis was conducted using the Hage-Cifarelli formalism based on the Feynman Variance-to-Mean method. Even with various reflector materials, the neutron spectra remained predominantly epithermal. This protocol does not particularly apply to a pool-type research reactor measurement campaign. A multiplying pool-type research reactor system is not symmetric, a large amount of water reflection is used in place of metal reflectors, the neutron spectra span a range between fast and thermal at different water heights, etc. Many lessons were learned throughout the execution of the CaSPER measurements, that helped contribute to a modified protocol, and will be expounded upon here for the benefit of future experimenters.

For the RCF, the water temperature is just over 80 °F, and the fuel reaches the same temperature as the water in steady state. 80 °F is very close to room temperature. Because water density and nuclear data may vary at different temperatures, nuclear data libraries evaluations exist at temperatures other than room temperature. However, the closest evaluations are either below 0 °F or in the hundreds of ºF. Therefore, the evaluation at room temperature was used in this work. For future benchmark-quality pool-type research reactor measurements, however, the temperature of the moderating water in the reactor core may need to be taken account.

Additionally, one must be aware of the trade-off between shielding and multiplication in a water moderated system. This trade-off is shown in the trends of singles and doubles rates as functions of water height. In

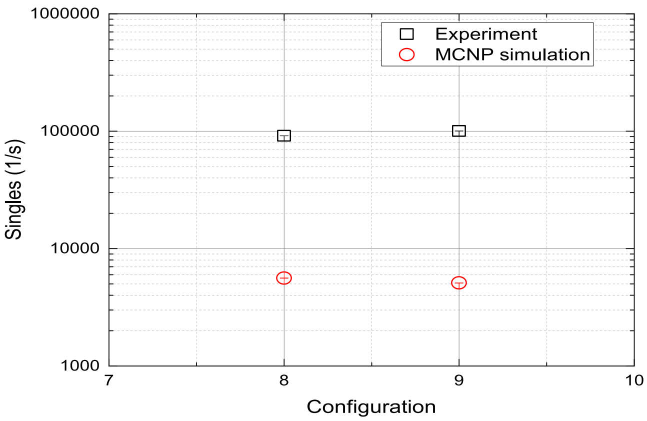

(a)

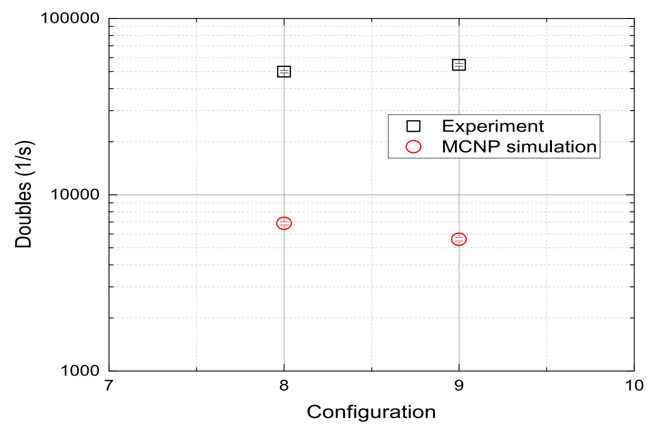

(b)

Fig. 16. R_1 and R_2 for the delayed critical configurations.

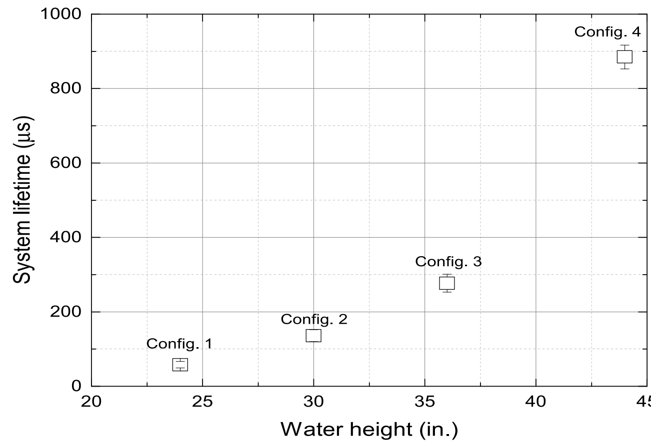

(a)

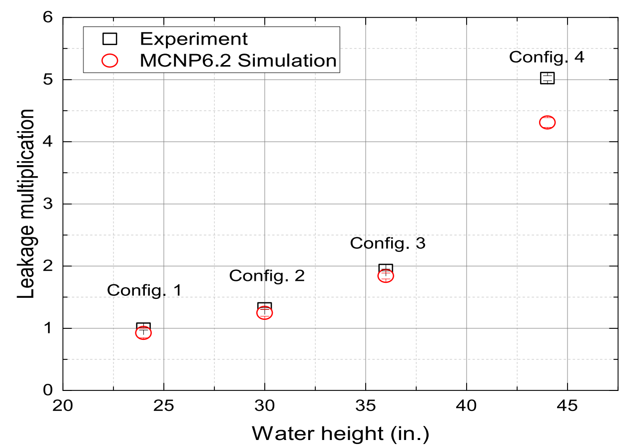

(b)

Fig. 17. Neutron lifetime and multiplication as functions of water height.

Fig. 14, R_1 first increases as a function of water height, reaches a turning point, and then begins decreasing with further increases in water height. While this turning point is not reached in the CaSPER measurement for R_2, perhaps future experimenters will be able to further observe and predict this behavior.

Practically, an extremely robust watertight system must be made available to protect the neutron multiplicity detector from water damage inside a water moderated reactor core if the detector is placed directly in the core. Additional material (i.e., Pb blocks, straps) may be required to lock the detection system into place and keep it from floating or otherwise deviating from the desired measurement position. In the CaSPER measurement, ratchet straps were used to tie the NoMAD detector housing and a layer of Pb bricks to an aluminum stand that held the detection system in place inside core. However, the detector system does not always have to be placed directly inside the core in pool-type research reactor measurements. If the core is small enough that the water does not attenuate the neutron flux significantly, the detector system can be placed outside the core. The detector system can also be placed on a stand above the core. For CaSPER, the reactor core was too large to allow for an acceptably large signal outside the core (parametric study results indicate that this would have been possible if the reactor tank radius had been less than 60 cm). In addition, both the direct upward neutron streaming from the ^{252}Cf source in the center of the fuel rods and the presence of the above-core PuBe source caused the above-core detector system placement option to be rejected. Sources contained in and around the reactor that are normally neglected by reactor operators (i.e., a PuBe startup source) cannot be neglected in the case of neutron multiplicity measurements. Indeed, potential contributions from neglected external radiation sources have been an Achilles heel for many experimentalists; for example, in the case of bubble fusion, one of the main sources of contention was whether or not the sources of neutrons had been properly characterized (Mullins, 2005).

In addition to comparing configurations at the same reactivity with differing control rod heights (configurations 8 and 9), it would be interesting to obtain the same reactivity from different water and control rod height combinations to determine if changing both the fine (control rod) and coarse (water) reactivity controls would compare better or

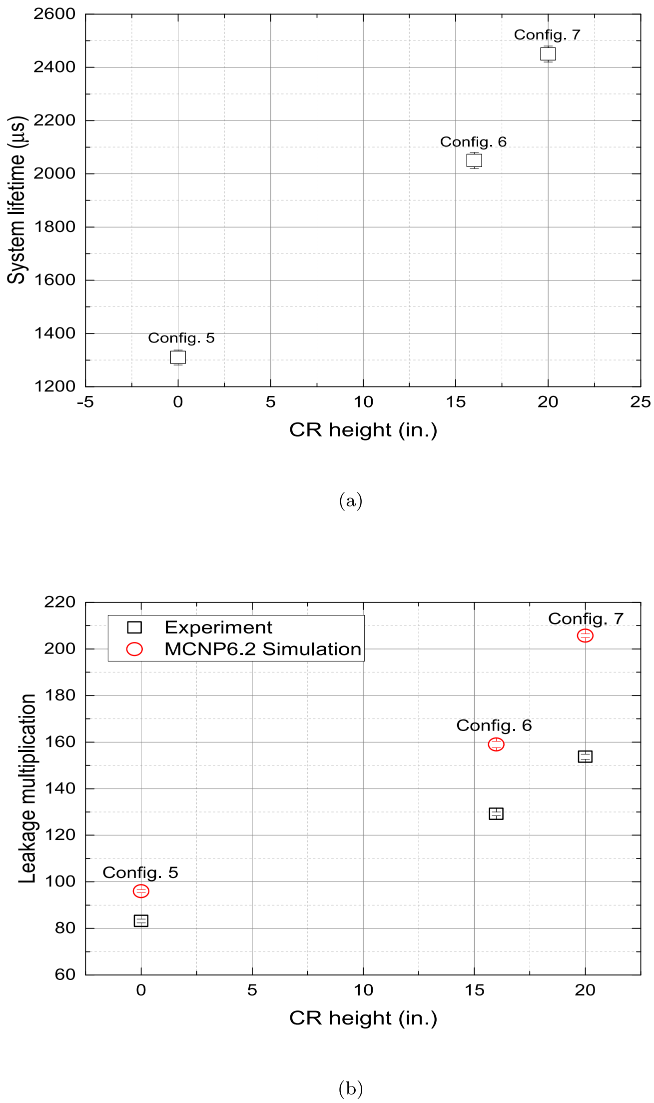

Fig. 18. Neutron lifetime and multiplication as functions of CR height.

worse than changing only the fine reactivity control. It is interesting to note that, according to Fig. 17, leakage multiplication and system neutron lifetime follow similar trends as a function of water height. This has been observed in previous thermal subcritical measurements involving enriched uranium. It is also important to note that the extremely large discrepancies between simulated and measured results at delayed critical, as seen in Fig. 16, were likely caused by a previous excursion into a delayed supercritical state. As previously discussed, an exponential increase in neutron population occurred when the reactor was briefly brought to a delayed supercritical state during the approach to critical procedure. The neutron population remained at this elevated level during the subsequent measurements at delayed critical, and because the supercritical excursion was not modeled in MCNP, this behavior was not exhibited in the simulation. In future critical measurements, this discrepancy can be avoided by bringing the reactor down to a subcritical state, after the approach to critical process, to allow the neutron population to die down. The reactor can then be brought back up to a critical state without the increase in neutron population caused by the supercritical excursion.

Table 7 shows that the observables in this experiment are most sensitive to changes in NoMAD distance and RCF PuBe source strength. Conversely, singles and doubles rates are not very sensitive to changes in control rod height. Therefore, for subcritical research reactor measurements of this type it is most desirable to be able to very accurately measure both the core-detector distance and the characteristics of any strong in-core starter source. However, larger uncertainties on fine reactivity control are allowable when operating in a generally insensitive region of the fine reactivity control worth curves.

Part of the protocol determined during the CaSPER measurements is related to data analysis. Applying a FOM (Equation (16)) to comparisons between simulated and measured Feynman histograms (Table 6) is a useful method for quantifying the deviation between simulated and measured histogram results, such as that are seen in Figs. 9 and 11, rather than simply using qualitative inspection. The FOM also proves useful when applied to comparisons between simulated and measured counts-per-tube plots (Table 5), especially for determining an optimal match between simulated and measured results (see Appendix A). Several issues arose in determining both the prompt neutron decay constant and the absolute detector efficiency required to calculate leakage multiplication. Although the Hage-Cifarelli formalism based on the Feynman Variance-to-Mean method can take into account contributions from (α, n) sources, there is no provision for (α, n) sources that aren't coincident with the fission source (see Appendix B for how this difficulty was addressed). Both the Y_2 and the Rossi fitting method were used to determine the prompt neutron decay constants for configurations 1–4. In order to separate the multiplying system and detector lifetimes, double rather than single exponential fits were used in both cases. In typical fast SNM subcritical measurements, the detector

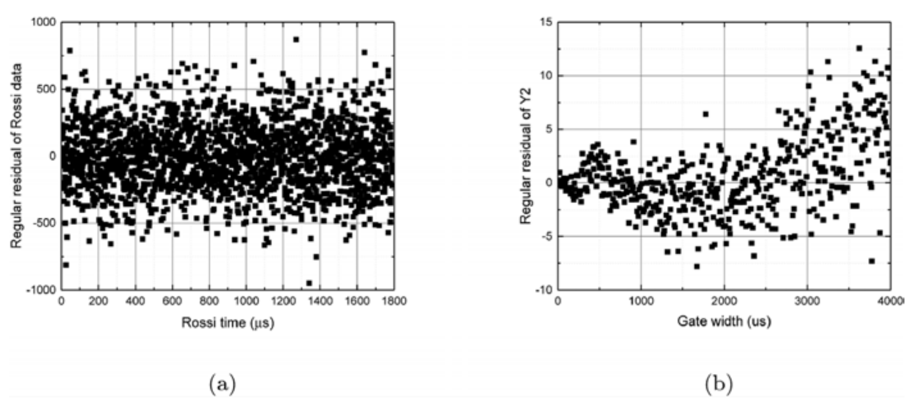

Fig. 19. Regular residual plots for Rossi and Y_2 fits at 36 in. water height, using double decay constant fits. The Rossi residual shows a much more desirable trend.

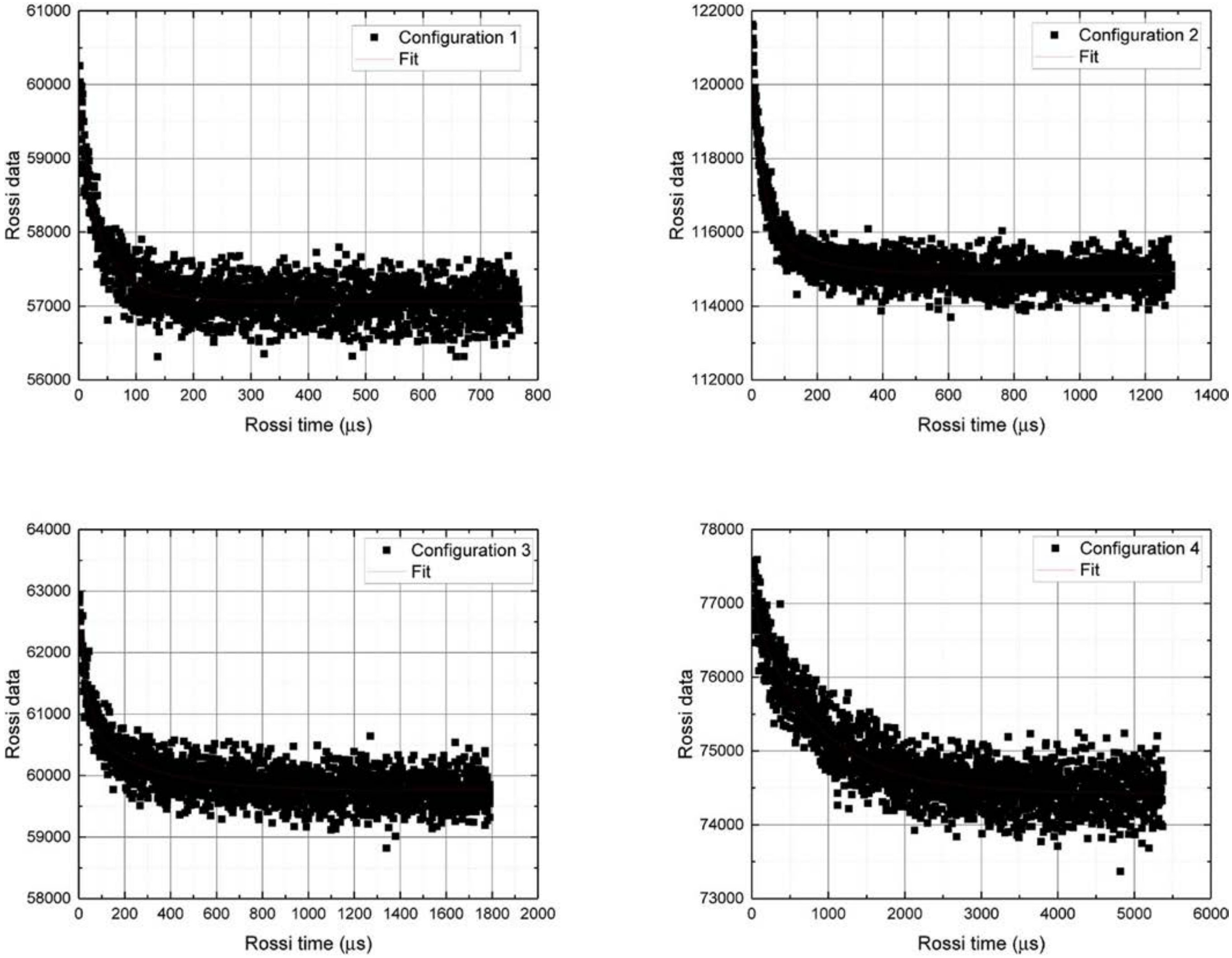

Fig. 20. Rossi data vs. Rossi time for measured configurations 1–4. Double exponential fits were used.

lifetime is longer than the multiplying system lifetime. For CaSPER, the experimenters consider the system to include everything inside the reactor tank. In this case, the system lifetime is much longer than the detector lifetime and results can be calculated, using the system lifetime, at large enough gate widths that the detector lifetime has died out. By comparing residual plots of Y_2 and Rossi fits (Fig. 19), it was determined that Rossi alpha fitting is a better method to obtain neutron lifetime in highly reflected and moderated systems, such as research reactors. Measured doubles rates were calculated at $\tau = 32\ \mu s$, before the detector lifetime had died out, and at $\tau = 3368\ \mu s$, after the detector lifetime had died out, as shown in Fig. 23. It seems that in this case the detector lifetime has a small effect on the results. This is most likely due to the fact that for such a thermal system, the system neutron lifetime is very long compared to the detector lifetime, and therefore the detector lifetime can be neglected even at short times (small gate widths).

5. Conclusions

The CaSPER campaign is the first advanced subcritical measurement to be performed at a 0-power pool-type research reactor. This work builds upon the previous years of collaborative subcritical experiments and has helped establish a protocol for future subcritical neutron multiplication inference measurements on pool-type reactor systems. In the CaSPER campaign, the NoMAD detection system was placed inside the RPI-RCF core and used to measure correlated neutron observables of interest at various water and control rod heights. Measured and simulated observables such as Feynman histograms, singles rates, doubles rates, and leakage multiplication comparisons show overall good agreement. As expected, larger discrepancies exist at configurations with higher multiplication, especially at and near delayed critical. The experimental observables of interest are the most sensitive to uncertainties in neutron multiplicity detector distance to the fuel and the reactor starter source strength. Interesting trends of observables versus water and control rod heights were observed and present opportunities for further investigation. The singles rate initially increases with increasing water height, reaches a turning point, and begins to decrease with further increases in water height. The doubles rate steadily increases with water height for the range of water heights measured in

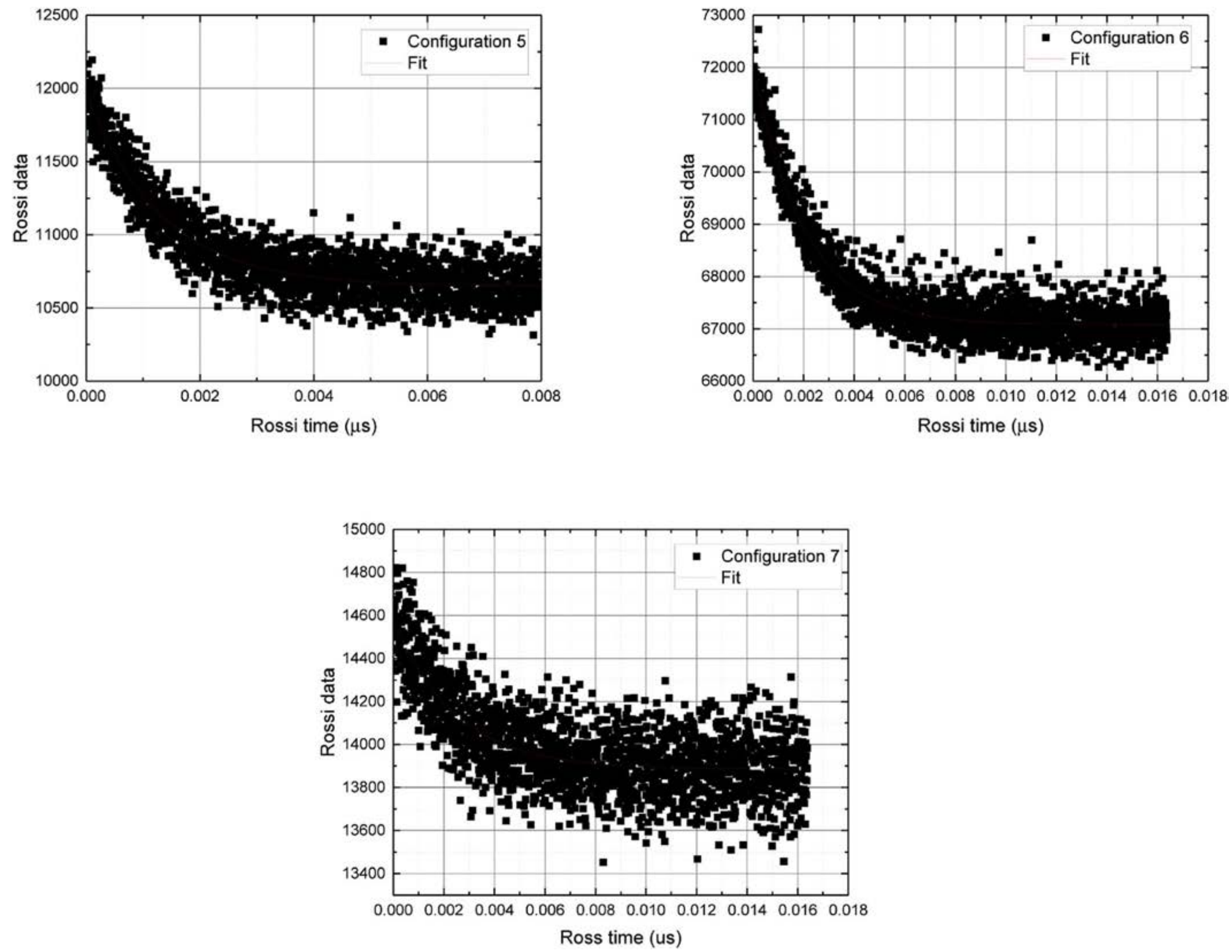

Fig. 21. Rossi data vs. Rossi time for measured configurations 5–7. Single exponential fits were used.

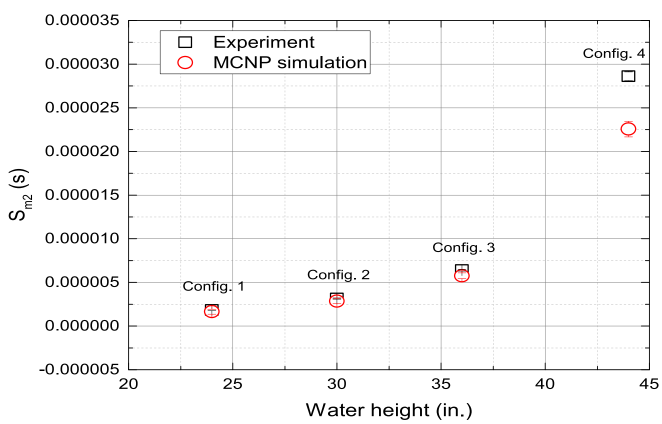

Fig. 22. Efficiency-independent ratio plotted for simulated and measured data.

this work, but it is expected that a turning point also exists at a higher water height for the doubles rate. The CaSPER measurement will be the first in a series of advanced subcritical neutron multiplication measurements, and associated simulations, that will further validate multiplication inference techniques and Monte Carlo codes, as well as identify and correct deficiencies in underlying nuclear data quantities, such as $\bar{\nu}$. Although the CaSPER measurement itself cannot be a benchmark, this work is paving the way towards an ICSBEP benchmark-quality experiment at the RPI-RCF, or other research reactor facilities. The IPEN/MB-01 research reactor in Brazil (dos Santos et al., 2014), the Sandia National Laboratory (SNL) research reactor (Harms, 2013), the

Table 7
Change in observables, per standard deviation perturbation of the parameter of interest, obtained using configuration 3.

Physical parameter	Standard deviation	Singles sensitivity	Doubles sensitivity
Water height	1 in.	$91s^{-1}$	$7s^{-1}$
CR height	1 in.	$2s^{-1}$	$1s^{-1}$
NoMAD distance	2 cm	$252s^{-1}$	$25s^{-1}$
^{252}Cf strength	1860 s.f./s	$112s^{-1}$	$9s^{-1}$
PuBe strength	1.4E6 n/s	$404s^{-1}$	$26s^{-1}$

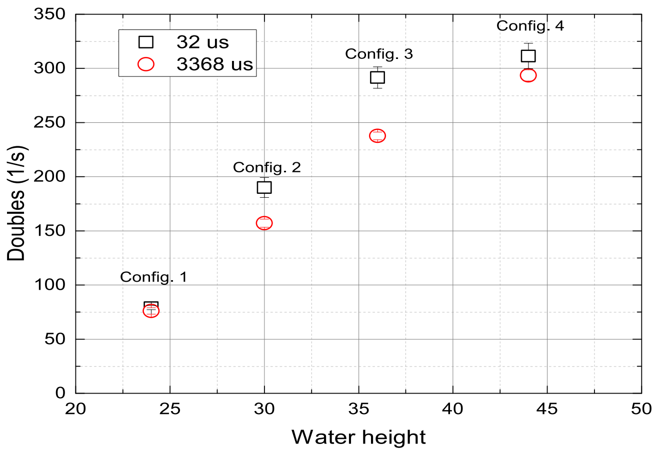

Fig. 23. Measured R_2 results before (τ = 32μs) and after (τ = 3368 μs) the detector lifetime dies out.

Minerve reactor at CEA Cadarache (Geslot et al., 2017), and the VR-1 Training Reactor in the Czech Republic (Crha, 2016) are other possible future advanced subcritical low-power pool-type research reactor benchmark measurement locations.

Acknowledgments

This material is based upon work supported in part by the Department of Energy National Nuclear Security Administration under the Consortium for Nonproliferation Enabling Capabilities (CNEC) Fellowship, Award Number DE-NA0002576. This work was also supported in part by the DOE Nuclear Criticality Safety Program, funded and managed by the National Nuclear Security Administration for the Department of Energy.

The authors would like to thank Mark Smith-Nelson of LANL for his invaluable help in operating the NoMAD detection system and conducting the CaSPER measurement.

Appendix A. RCF PuBe source

The PuBe shielding is a cylinder with outer dimensions of 12″ × 12”. It is known to be made of paraffin wax with a hole in the center in which the source resides. It is assumed that the hole is cylindrical and extends from the top to the bottom of the shielding. According to RCF records, the source strength is on the order of 1E7 n/s and the hole diameter is on the order of 1 in. Using this shielding configuration and source strength in the CaSPER configuration 3 simulations did not yield a good match between simulated and measured results, as shown in Fig. 24. It was judged that either the source strength, shielding, or both could not be correct.

The source strength and hole diameter were then varied until a good match between simulated and experimental results for configuration 3 was found, as shown in Fig. 25. The optimized hole diameter and source strength are 3.8 in. and 1.4E7, respectively.

The PuBe source constitutes the largest contribution to the singles rate. Fig. 26 and Table 8 show only roughly 33–40% of singles are due to the ^{252}Cf source. Because this is simulated data it was possible to separate out the count rate due to ^{252}Cf alone, by simply not modeling the PuBe source.

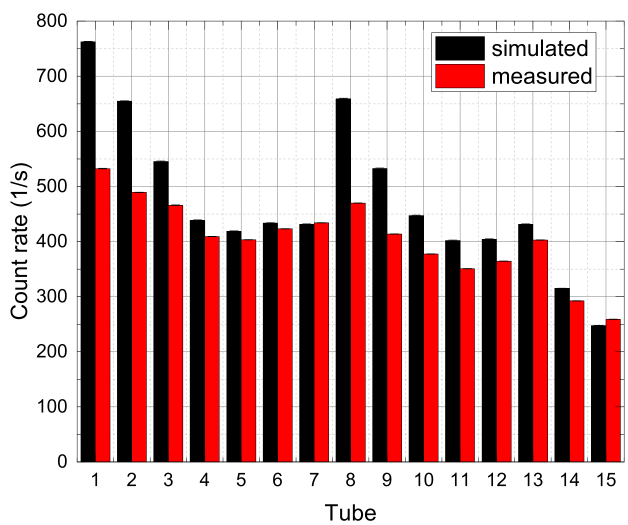

Fig. 24. Initial comparison between simulated and measured counts-per-tube histograms for configuration 3. The FOM value characterizing this comparison is 201686.

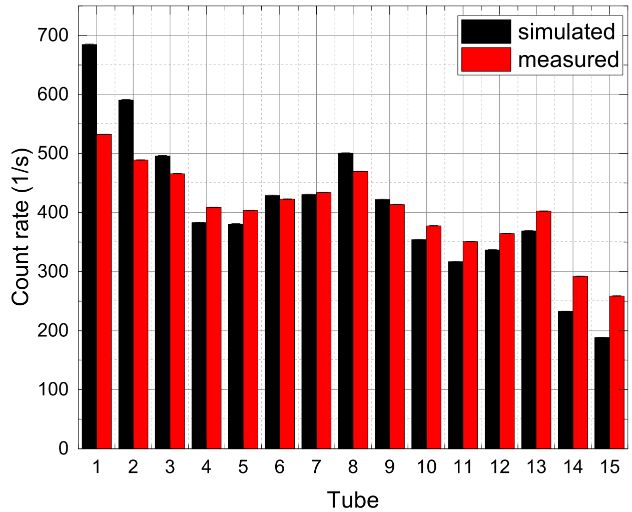

Fig. 25. Final comparison between simulated and measured counts-per-tube histograms for configuration 3. The FOM value characterizing this comparison is 49597.

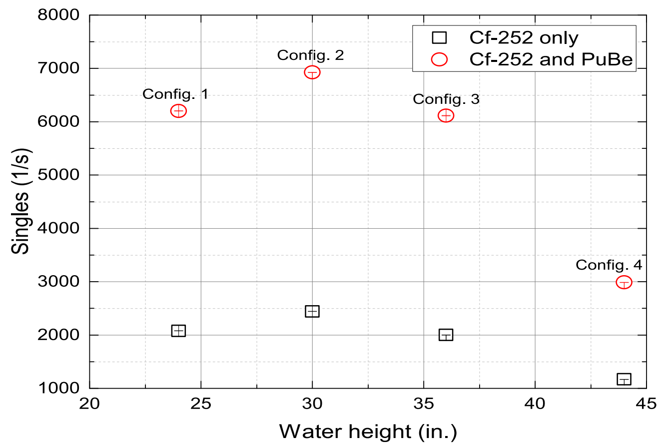

Fig. 26. Simulated contribution of the RCF PuBe starter source to the singles rate at different water heights, as compared to the singles rate due to ^{252}Cf alone.

Table 8
Comparison of percentage contributions of the RCF PuBe source and the ^{252}Cf source.

Water height (in.)	^{252}Cf % contribution	PuBe % contribution
24	34	66
30	35	65
36	33	67
44	39	61

Table 9
Adjusted efficiencies for each water height.

Water height (in.)	Efficiency	Adjusted efficiency
24	0.0506	0.00759
30	0.0530	0.00800
36	0.0430	0.00645
44	0.0149	0.00223
67	0.0001	0.00002

Appendix B. Leakage multiplication calculations

Due to the large contribution of the above-core RCF PuBe starter source to the measured CaSPER signal, Equation (8) is no longer valid. Two new methods for calculating leakage multiplication were primarily investigated. In method 1, it is assumed that $M_L = 1$ at the 24 in. water height configuration. Therefore, efficiency can be solved for at this configuration. This calculated efficiency is, as expected, very different from the value obtained using the typical method of taking the ratio of the singles rate in the corresponding no-fuel measurement to the known ^{252}Cf source strength. The ratio of the “adjusted efficiency” to the typically calculated efficiency is then used as a multiplier to calculate adjusted efficiencies at all

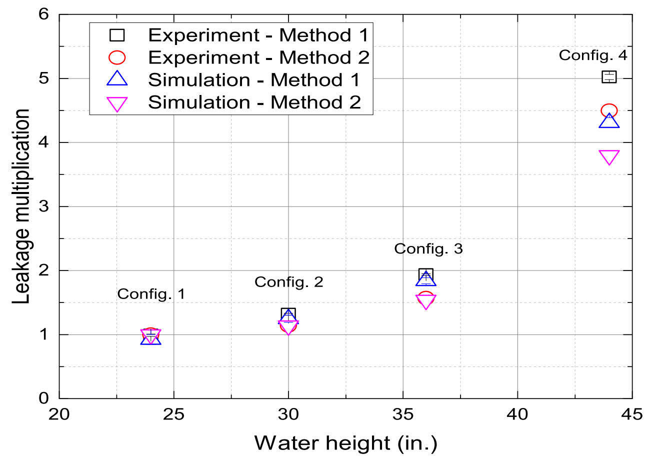

Fig. 27. Neutron leakage multiplication as a function of water height.

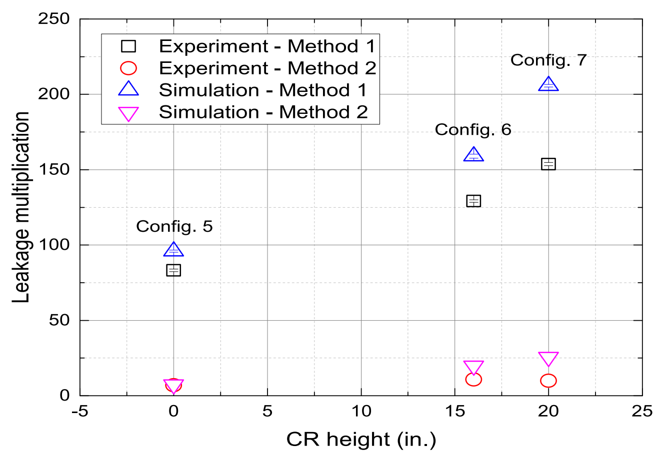

Fig. 28. Neutron leakage multiplication as a function of CR height.

other water heights. Table 9 lists the original and adjusted efficiencies for each water height. These adjusted efficiencies are used to calculate leakage multiplication.

It is clear that the original efficiencies are incorrect. From previous measurements with the NoMAD it is known that the absolute efficiency at a distance of 50 cm away from a ^{252}Cf source in air is on the order of 1%. Because the source-detector distance is 48.5 cm and at 24 in. water height the water level has not yet reached the bottom of the NoMAD, the efficiency value is expected to be much closer to 1% than 5%. Therefore, the adjusted efficiency values are much more realistic.

In method 2, equations for R_1 and R_2 (Hutchinson et al., 2015b) are manipulated to separate the contributions from the ^{252}Cf and PuBe sources. Efficiency is assumed to be a constant multiplied by the relative contributions of each source. It is also assumed that $M_L = 1$ at the 24 in. water height configuration. As shown in Equations (18) and (19), this becomes a system of 2 equations and 2 unknowns (efficiency constant ε and (α,n) source strength S_α). Because the solution of this system of equations yields the PuBe source strength, 1.12E5 $\frac{n}{s}$ (which is more of an effective source strength that treats the shielded above-core PuBe source as an unshielded point source coincident in space with the ^{252}Cf spontaneous fission source), this value can be input into the system of equations in 20 and 22. Therefore, ε and M_L can be solved for at all other configurations.

$$R_1 = \varepsilon[f_{Cf}\nu_{s1}F_s + f_{PuBe}S_\alpha] \tag{18}$$

$$R_2 = \varepsilon^2\left[f_{Cf}^2\nu_{s2}F_s + f_{PuBe}^2 S_\alpha\right] \tag{19}$$

$$R_1 = \varepsilon[f_{Cf}b_{11}F_s + f_{PuBe}b_{12}S_\alpha] \tag{20}$$

$$b_{11} = M_L\nu_{s1}\; b_{12} = M_L \tag{21}$$

$$R_2 = \varepsilon^2\left[f_{Cf}^2 b_{21}F_s + f_{PuBe}^2 b_{22}S_\alpha\right] \tag{22}$$

$$b_{21} = M_L^2\left[\nu_{s2} + \frac{M_L - 1}{\nu_{I1} - 1}\nu_{s1}\nu_{I2}\right] b_{22} = M_L^2\frac{M_L - 1}{\nu_{I1} - 1}\nu_{I2} \tag{23}$$

Both methods of calculating leakage multiplication yield reasonable results for configurations 1–4, as seen in Fig. 27. However, method 2 shows an unreasonable trend versus CR height for configurations 5–7, as shown in Fig. 28. Therefore, method 1 was used to calculate final leakage multiplication results for this work. This complication with efficiency and leakage multiplication calculation is one of the reasons why the CaSPER measurements cannot be a benchmark. Additional measurements taken during the execution of CaSPER may have provided better estimates of efficiency.

References

Anderson, M.E., Neff, R.A., 1972. Neutron energy spectra of different size ^{239}Pu-Be(α, n) sources. Nucl. Instrum. Meth. 99, 231–235.

Arthur, J.A., Bahran, R.M., Hutchinson, J.D., Rising, M.E., Pozzi, S.A., 2016. Comparison of the performance of various correlated fission multiplicity monte carlo codes. In: Transactions of the American Nuclear Society Winter Meeting and Technology Expo.

Bahran, R., Hutchinson, J., 2016. Subcritical copper-reflected α-phase plutonium (SCRαP) integral experiment design. Trans. Am. Nucl. Soc. 114, 527–529.

Bahran, R., Hutchinson, J., Richard, B., Sood, A., 2014a. List-mode simulations of the Thor core benchmark sensitivity experiments. Transactions of the American Nuclear Society Annual Meeting 111, 805–808.

Bahran, R., Croft, S., Hutchinson, J., Smith, M., Sood, A., 2014b. A survey of nuclear data deficiences affecting nuclear non-proliferation. In: INMM Annual Meeting, Atlanta GA, Proceedings of the.

Bolding, S., 2013. Design of a Neutron Spectrometer and Simulations of Neutron Multiplicity Experiments with Nuclear Data Perturbations. M.S. thesis. Kansas State University.

Bolding, S.R., Solomon, C.J., 2013. Simulations of multiplicity distributions with perturbations to nuclear data. Trans. Am. Nucl. Soc. 109, 251–254.

Briggs, J., Bess, J., Gulliford, J., 2014. Integral benchmark data for nuclear data testing through the ICSBEP & IRPhEP. Nucl. Data Sheets 118, 396–400.

Chabod, S., Billebaud, A., Lecolley, F., Lecouey, J., Lehaut, G., Marie, N., Ban, G., Doligez, X., Kochetkov, A., Baeten, P., Krasa, A., Uyttenhove, W., Vittiglio, G., Wageman, J., Mellier, F., Villamarin, D., 2014. Reactivity Measurements at Guinevere Facility Using the Integral K_p Method, PHYSOR. The Role of Reactor Physics Toward a Sustainable Future.

Cifarelli, D., Hage, W., 1986. Models for a three-parameter analysis of neutron signal correlation measurements for fissile material assay. Nucl. Instrum. Meth. 251, 550–563.

Crha, J., 2016. Neutron imaging on the VR-1 reactor. J. Phys. 746 Conference Series.

Degweker, S., Rudra, R., 2016. On the relation between Rossi alpha and Feynman alpha methods. Ann. Nucl. Energy 94, 433–439.

dos Santos, A., de Andrade e Silva, G.S., Diniz, R., Yamaguchi, M., Mura, L.F.L., Fuga, R., Gonnelli, E., Lee, S.M., Jerez, R., 2014. Subcritical Loading Configurations of the IPEN/MB-01 Reactor, International Handbook of Evaluated Criticality Safety Benchmark Experiments NEA/NSC/DOC/(95)03/IV. SUB–LEU–COMP–THERM–002.

Dulla, S., Nervo, M., Ravetto, P., 2014. A Method for Reactivity Monitoring in Subcritical Source-driven Systems, PHYSOR. The Role of Reactor Physics toward a Sustainable Future.

Geslot, B., Gruel, A., Walczak, P., Leconte, P., Blaise, P., 2017. A hybrid pile oscillator experiment in the Minerve reactor. Ann. Nucl. Energy 108, 268–276.

Goorley, T., James, M., Booth, T., Brown, F., Bull, J., et al., 2012. Initial MCNP6 release overview. Nucl. Technol. 180, 298–315.

Hansen, G., Helmick, H., Orndoff, J., 1968. Neutron Counting Statistics in Basic Fast Critical Assemblies, Transactions of a Japan-United States Seminar on Nuclear Reactor Noise Analysis.

Harms, G.A., 2013. Water-moderated Square-pitched U(6.90)O_2 Fuel Rod Lattices with 0.52 Fuel-to-water Volume Ratio (0.855 Cm Pitch), International Handbook of Evaluated Criticality Safety Benchmark Experiments NEA/NSC/DOC/(95)03/IV. LEU–COMP–THERM–078.

Hutchinson, J., Rooney, B., Myers, W., Sood, A., Smith-Nelson, M., 2013a. CALIBAN measurements near delayed critical using subcritical measurement methods. In: American Nuclear Society Winter Meeting, Washington DC.

Hutchinson, J., Sood, A., Myers, W., Smith-Nelson, M., Dinwiddie, D., 2013b. Comparison of HEU measurements using measured and simulated data. Trans. Am. Nucl. Soc. 106, 487–489.

Hutchinson, J., Smith-Nelson, M.A., Sood, A., Goda, J.M., Bounds, J.A., 2014. Joint LANL/CEA measurements on Godiva IV. In: American Nuclear Society Annual Meeting, Reno NV.

Hutchinson, J., Nelson, M.A., Sood, A., hayes, D.K., Sanchez, R.G., 2015a. Neutron noise measurements on HEU foils moderated by lucite. In: American Nuclear Society Annual Meeting, San Antonio TX.

Hutchinson, J.D., Smith-Nelson, M.A., Cutler, T.E., Richard, B.L., Grove, T.J., 2015b. Estimation of uncertainties for subcritical benchmark measurements. In: International Conference on Computing, Networking and Communications.

Hutchinson, J., Mustafa, B., Smith-Nelson, M.A., Myers, W., Cutler, T.E., Solomon, C.J., Sood, A., Dinwiddie, D.R., Grove, T.J., 2016. Subcritical multiplication experiments & simulations: overview and recent advances. In: Advances in Nuclear Nonproliferation Technology and Policy Conference.

Mattingly, J., 2009. Polyethylene-reflected Plutonium Metal Sphere: Subcritical Neutron and Gamma Measurements, Sandia National Laboratory Report SAND2009–5804.

McKenzie, G., 2014. Modern Rossi Alpha Measurements. M.S. Thesis. University of Illinois at Urbana-Champaign.

Miller, E.C., Mattingly, J.K., Dennis, B.D., Clarke, S.D., Pozzi, S.A., 2010. Simulations of Neutron Multiplicity Measurements with MCNP-PoliMi, Technical Report SAND2010–6830, Sandia National Laboratory.

Moss, C., Sorenson, E., Nelson, M., 2016. Multiplicity Counter-15 (MC-15) User Manual, Los Alamos National Laboratory, LA-UR-16–27099.

Mullins, J., 2005. Pop!. N. Sci. 38, 40–44.

Richard, B., Hutchinson, J., 2014. Nickel Reflected Plutonium Metal Sphere Subcritical Measurements, International Handbook of Evaluated Criticality Safety Benchmark Experiments NEA/NSC/DOC/(95)03/I. FUND–NCERC–PU–HE3–MULT–001.

Richard, B., Hutchinson, J., 2016. Tungsten-reflected Plutonium-metal-sphere Subcritical Measurements, International Handbook of Evaluated Criticality Safety Benchmark Experiments NEA/NSC/DOC/(95)03/I. FUND–NCERC–PU–HE3–MULT–002.

Smith-Nelson, M., 2015. Momentum: Version 0.36.3, LANL Software.

Smith-Nelson, M.A., Hutchinson, J.D., 2014. The Sm2 Ratio for Evaluating Neutron Multiplicity Models, Los Alamos National Laboratory Report, LA-UR-14–29047.

Solomon, C., 2014. The Mcnptools Package, Tech. rep., LA-UR-14–27075.

Sood, A., Solomon, C.J., Hutchinson, J.D., Bahran, R., November 2014. A review of recent R&D efforts in sub-critical multiplication measurements and simulations. Trans. Am. Nucl. Soc. 111, 799–802.

Temple, B., 2009. User's Manual for the convert.Pl PERL Script, LA-UR-09–05257.

Thompson, N., Bahran, R., Winters, G., Frantz, E., Gazda, R., McDermott, B., Wei, J., Caracappa, P., Trumbull, T., Thompson, J., Danon, Y., 2015. Nuclear engineering education at the RPI walthousen reactor critical facility. In: Proceedings of the Institute of Nuclear Materials Management 56th Annual Meeting.

Trahan, A., 2016. Utilization of the differential die-away self-interrogation technique for characterization of spent nuclear fuel. Ph.D. thesis. University of Michigan.

Uyttenhove, W., Baeten, P., Kochetkov, A., den Eynde, G.V., Vittiglio, G., Wagemans, J., Lathouwers, D., Kloosterman, J., van der Hagen, T., Billebaud, A., Chabod, S., Mellier, F., Lecouey, J., Lecolley, F., Lehaut, G., Marie, N., Doligez, X., Carta, M., Becares, V., Villamarin, D., 2014. Static Modal Analysis of the Current-to-flux Subcriticality Monitor for Accelerator-driven Systems, PHYSOR. The Role of Reactor Physics toward a Sustainable Future.

Wagemans, C., 1991. The Nuclear Fission Process. CRC Press, Boca Raton.

Annals of Nuclear Energy 125 (2019) 342–359

Contents lists available at ScienceDirect

Annals of Nuclear Energy

journal homepage: www.elsevier.com/locate/anucene

Validation of statistical uncertainties in subcritical benchmark measurements: Part II – Measured data

Jesson Hutchinson [a,*], Rian Bahran [a], Theresa Cutler [a], Mark Nelson [a], Travis Grove [a], Jennifer Arthur [a,b], George McKenzie [a], Wilfried Monange [c], Eric Dumonteil [c]

[a] Los Alamos National Laboratory, Los Alamos, NM 87545, United States
[b] University of Michigan, Department of Nuclear Engineering and Radiological Sciences, Ann Arbor, MI 48109, United States
[c] Institut de Radioprotection et de Sûreté Nucléaire (IRSN), PSN-EXP, SNC, Fontenay-aux-Roses 92262, France

ARTICLE INFO

Article history:
Received 4 June 2018
Received in revised form 8 October 2018
Accepted 10 October 2018
Available online 2 November 2018

Keywords:
Neutron multiplicity
Feynman Variance-to-mean
Subcritical measurements
Neutron noise

ABSTRACT

Part I of this work presented an uncertainty approach which incorporates the singles and doubles counting rates determined by the Hage-Cifarelli formalism of the Feynman Variance-to-Mean method. This moments-based approach utilizes time correlations between prompt neutrons detections to assess the system multiplication. In addition, it presented a validation which utilized simulated data generated using a 0-D point-kinetics Monte Carlo code. In Part II, this same method and validation approach is applied to measured data of a subcritical benchmark experiment. These measurements were performed with a 4.5 kg sphere of alpha-phase weapons grade plutonium reflected by copper and/or polyethylene. The results of 17 configurations are shown including detailed validation for four of the configurations.

Published by Elsevier Ltd.

1. Introduction

Subcritical neutron noise experiments provide data for applications in nuclear nonproliferation, safeguards, and criticality safety. Part I (Hutchinson et al., 2019) of this work presented the methodology that will be applied to measured data and included a validation using 0-D simulations. This part will focus on applying the same methodology to measured data of the Subcritical Copper-Reflected α-phase Pu (SCRαP) experiment, which included a 4.5 kg alpha-phase weapons grade plutonium sphere surrounded by copper and polyethylene (Bahran and Hutchinson, 2016; Hutchinson et al., 2017). This Pu sphere is called the Beryllium-Reflected Plutonium (BeRP) ball (Loaiza and Hutchinson, 2007). These data will be in a future version of the *International Criticality Safety Benchmark Evaluation Project* (ICSBEP) handbook (International Handbook of Evaluated Criticality Safety Benchmark Experiments Nuclear Energy Agency, 2016). The ICSBEP handbook contains hundreds of critical and subcritical benchmark evaluations, which can be used for validation and improvement of nuclear databases and radiation transport codes. The SCRαP experiment is similar to two previous subcritical benchmarks, both of which involved the same plutonium sphere, but with tungsten (Richard and Hutchinson, 2016a) and nickel (Richard and Hutchinson, 2016b) reflectors. These evaluations are categorized as fundamental physics benchmarks because they provide fundamental physics measurement data applicable to criticality safety applications; in this case, the benchmark parameters which are quantified include the singles counting rate (R_1), doubles counting rate (R_2), and leakage multiplication (M_L). This is different from critical benchmark evaluations which use k_{eff} as the benchmark parameter. The singles counting rate R_1 is the count rate observed in the detection system, the doubles counting rate R_2 is the rate at which two neutrons from a single fission chain are detected, and leakage multiplication M_L is the number of neutrons which escape the system boundary per starter neutron. These parameters were described in detail in Section 3 of Part I.

2. Experiment description

2.1. Experiment design

Subcritical benchmark experiments are designed to validate nuclear data and computational methods. This particular experiment is useful for Pu and Cu nuclide cross-section validation. To that end, there were three main objectives of the SCRαP experiment:

1. Maximize the integrated sensitivities of ^{63}Cu and ^{65}Cu total cross-sections.

* Corresponding author.
E-mail address: jesson@lanl.gov (J. Hutchinson).

https://doi.org/10.1016/j.anucene.2018.10.021
0306-4549/Published by Elsevier Ltd.

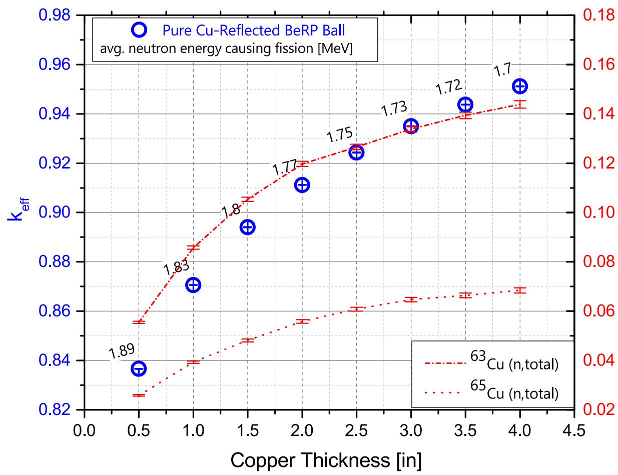

Fig. 1. k_{eff} and sensitivities as a function of copper thickness.

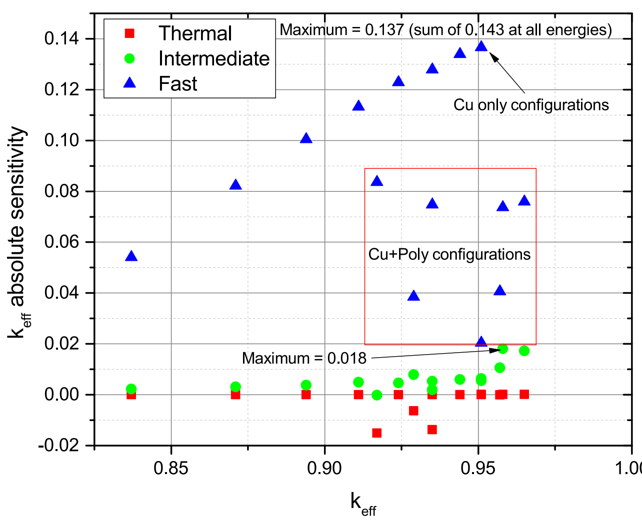

Fig. 2. k_{eff} sensitivity for ^{63}Cu total cross-section.

2. Include configurations that increase these sensitivities in the intermediate energy region (defined here as 0.625 eV–100 keV).
3. Include a variety of configurations that cover a wide range of multiplication values.

To aid in the design, both sensitivity and criticality simulations were performed with MCNP® version 6[1] (Goorley et al., 2012). Fig. 1 shows the simulated effective multiplication factor (k_{eff}) as a function of Cu thickness. It can be seen that k_{eff} increases from a value of 0.837 at 0.5 inch-thick Cu to 0.951 at 4.0 inches-thick. The bare BeRP ball is known to have a simulated k_{eff} of 0.776 from a previous subcritical benchmark (Richard and Hutchinson, 2016a). The sensitivities that are shown are the change in k_{eff} which is experienced when a 1% change occurs in either the ^{63}Cu or ^{65}Cu total cross-section. Previous work shows that k_{eff} sensitivities can be used to estimate sensitivities in singles counting rate (R_1), doubles counting rate (R_2), and leakage multiplication (M_L) (Hutchinson and Cutler, 2016). If the sensitivity is positive, then an increase in the

[1] MCNP® and Monte Carlo N-Particle® are registered trademarks owned by Los Alamos National Security, LLC, manager and operator of Los Alamos National Laboratory.

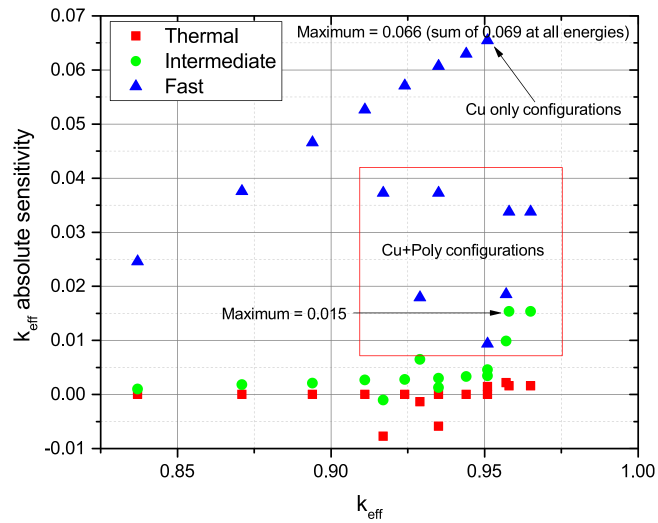

Fig. 3. k_{eff} sensitivity for ^{65}Cu total cross-section.

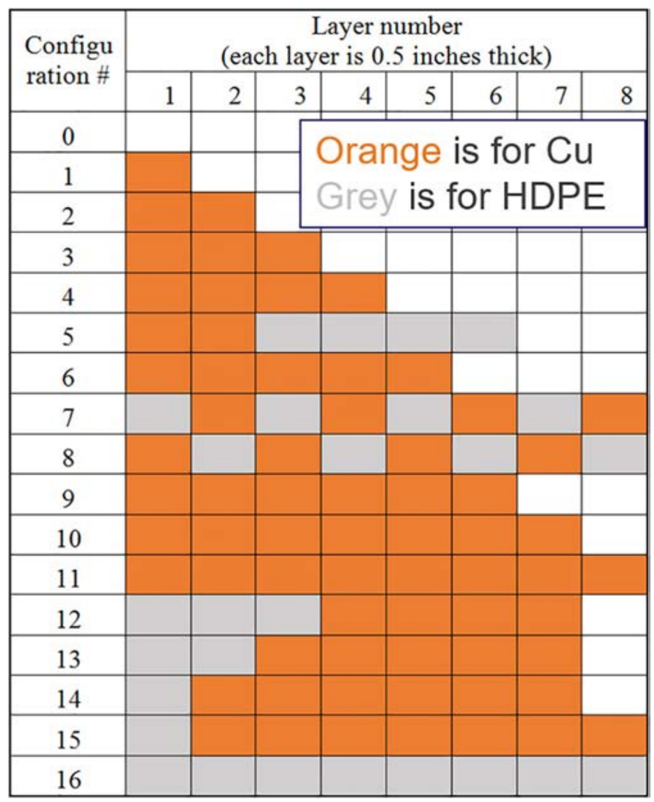

Fig. 4. Configurations for the SCRαP experiment.

cross-section results in an increase in k_{eff} (and they are therefore positively correlated). Having a variety of Cu thicknesses out to 4 inches satisfies design criteria numbers 1 and 3.

To help increase sensitivities in the intermediate energy region, simulations were performed in which high-density polyethylene (HDPE) shells were present (inside the Cu, outside the Cu, and interleaved between the Cu). The k_{eff} absolute sensitivity for ^{63}Cu and ^{65}Cu total cross-sections are shown in Figs. 2,3. The results presented here include a subset of the different HDPE and Cu combinations that were investigated. The resulting sensitivities have been compared to critical configurations in the ICSBEP handbook

(International Handbook of Evaluated Criticality Safety Benchmark Experiments Nuclear Energy Agency, 2016). It should be noted that there are a limited number of copper-reflected critical experiments in the handbook (8 experimental series with U fuel and 2 experimental series with Pu fuel). The maximum total ^{63}Cu sensitivity for the 16 subcritical configurations in SCRαP (0.143) is greater than the two Pu experimental series (0.126) but less than that for some of the U experimental series (0.200). In the intermediate energy regime, the maximum ^{63}Cu sensitivity for the 16 configurations (0.018) is greater than the two Pu experimental series by nearly an order of magnitude (0.002), but similarly less than that for some of the U experimental series (0.051). It is promising that the sensitivities in the intermediate energy can be increased even though all of these systems are still fast. The trends for ^{65}Cu are identical to ^{63}Cu as shown in Fig. 3.

The final design also included cost, criticality safety, measurement time, and practicality considerations and has been previously described (Bahran and Hutchinson, 2016). It was desired to have measurement uncertainties of less than 1% in leakage multiplication for as many configurations as possible.

2.2. Experiment configurations

Based on the final experiment design, 17 configurations were measured as shown in Fig. 4. Configuration 0 includes only the bare BeRP ball. This configuration is important to compare with the previous BeRP benchmarks (Richard and Hutchinson, 2016b; Richard and Hutchinson, 2016a). Eight configurations (1, 2, 3, 4, 6, 9, 10, and 11) included the BeRP ball reflected solely by various thicknesses of Cu hemishells. Seven configurations (5, 7, 8, 12, 13, 14, and 15) included the BeRP ball reflected by Cu and HDPE hemishells. Configuration 16 included the BeRP ball reflected by only HDPE. Configurations 0–15 are sorted in ascending order of k_{eff} based on the final design simulations. Configuration 16 was added

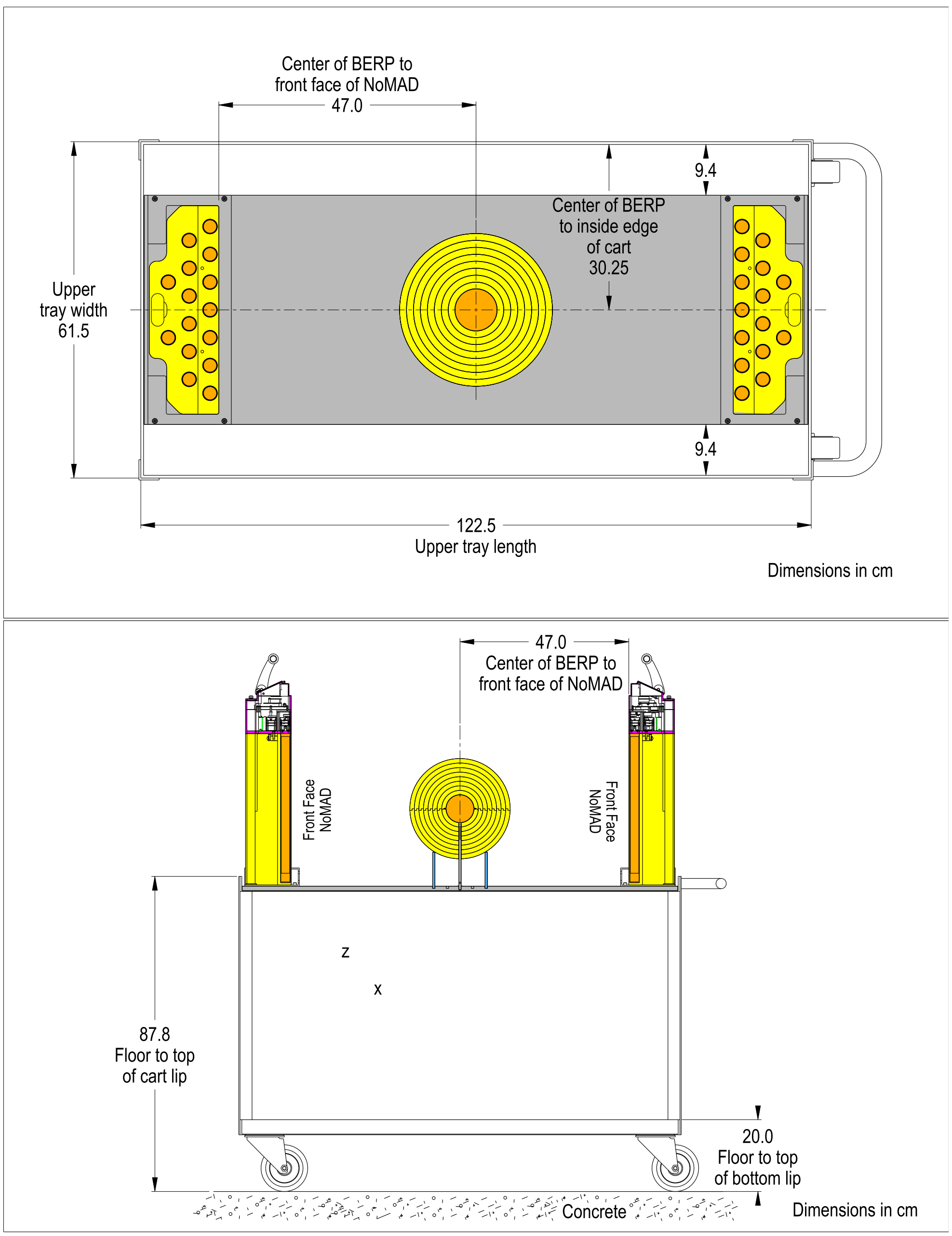

Fig. 5. Experiment overview.

during the experiment as it was desired to have a configuration with only HDPE (and is known to have a lower k_{eff} than many of the other configurations). An overview of the assembly is shown in Fig. 5. For each configuration, ^{252}Cf source replacement measurements were also performed; these measurements had an identical setup but with a ^{252}Cf source present at the equivalent location to the center of the BeRP ball in order to determine detector efficiency.

The following sections will include some results for all 17 configurations, but validation results will only be shown for configurations 0, 11, 15, and 16. These configurations were selected because they bound the problem set. Configuration 0 is a fast system and has the lowest multiplication. Configuration 11 contains the full 4.0 inch-thick Cu reflector and therefore is a fast system with a fairly high multiplication. Configuration 15 has the highest multiplication of all of the configurations. Configuration 16 includes the full 4.0 inch-thick HDPE reflector and therefore is the slowest system among all of the configurations. Figs. 6–9 show photographs of these 4 configurations. (see Fig. 10).

2.3. Plutonium sphere information

In October 1980, an α-phase plutonium sphere known as the BeRP ball was cast and clad in stainless steel (SS). This sphere was made for use in a critical experiment to address uncertainties in beryllium-plutonium systems (Loaiza and Hutchinson, 2007).

Fig. 6. Configuration 0: the bare BeRP ball.

The plutonium sphere was initially cast and turned to a mean diameter of 7.5876 cm with a density of the plutonium sphere calculated as 19.6039 g/cm^3, based on a weight of 4483.884 g and a calculated volume of 228.72 cm^3 (Richard and Hutchinson, 2016b).

The thin cladding shell of Stainless Steel-304 around the Pu sphere has a nominal thickness of 0.012 in. (0.03048 cm). The SS-304 cladding consists of two identical hemispheres and has an inner and outer diameter of 3.014 and 3.038 inches (7.65556 and 7.71652 cm), respectively. The cladding has a flange with an outer diameter of 3.4456 inches (8.751824 cm) and a nominal thickness of 0.036 inches (0.09144 cm).

Information from the isotopic analysis performed in 1980 is given in Table 1. Additional information on the BeRP ball is provided in several benchmark evaluations (Loaiza and Hutchinson, 2007; Richard and Hutchinson, 2016b; Richard and Hutchinson, 2016a).

2.4. Copper and polyethylene information

As mentioned in Section 2.2, two sets of matching nesting hemishells were used for these experiments: Copper C101 alloy and High Density Polyethylene (HDPE) designed to meet specifications listed in ASTMD4976 Rev. A. Both sets of hemishells used the same engineering drawings. Each reflector (i.e. layer) has a thickness of approximately 0.5 inches. In reality, the thickness of each hemishell was smaller to ensure that the BeRP ball could properly fit in the inner reflector hemishells and to ensure that all of the copper and polyethylene reflectors would fit together without getting

Fig. 7. Configuration 11: 4.0 inch-thick Cu around the BeRP ball.

stuck. The reflectors are nested together so that eight different total thicknesses can be obtained as shown in Table 2 and Fig. 4. Four of the configurations with polyethylene hemishells had a gap which ranged from 0.04–0.15 inches; this will be described in detail in the upcoming ICSBEP evaluation.

2.5. Detector information

The detectors used for this experiment are referred to as NoMAD detectors (Neutron Multiplicity ^{3}He Array Detectors). Each NoMAD detector unit includes 15 ^{3}He proportional counters. Every ^{3}He tube

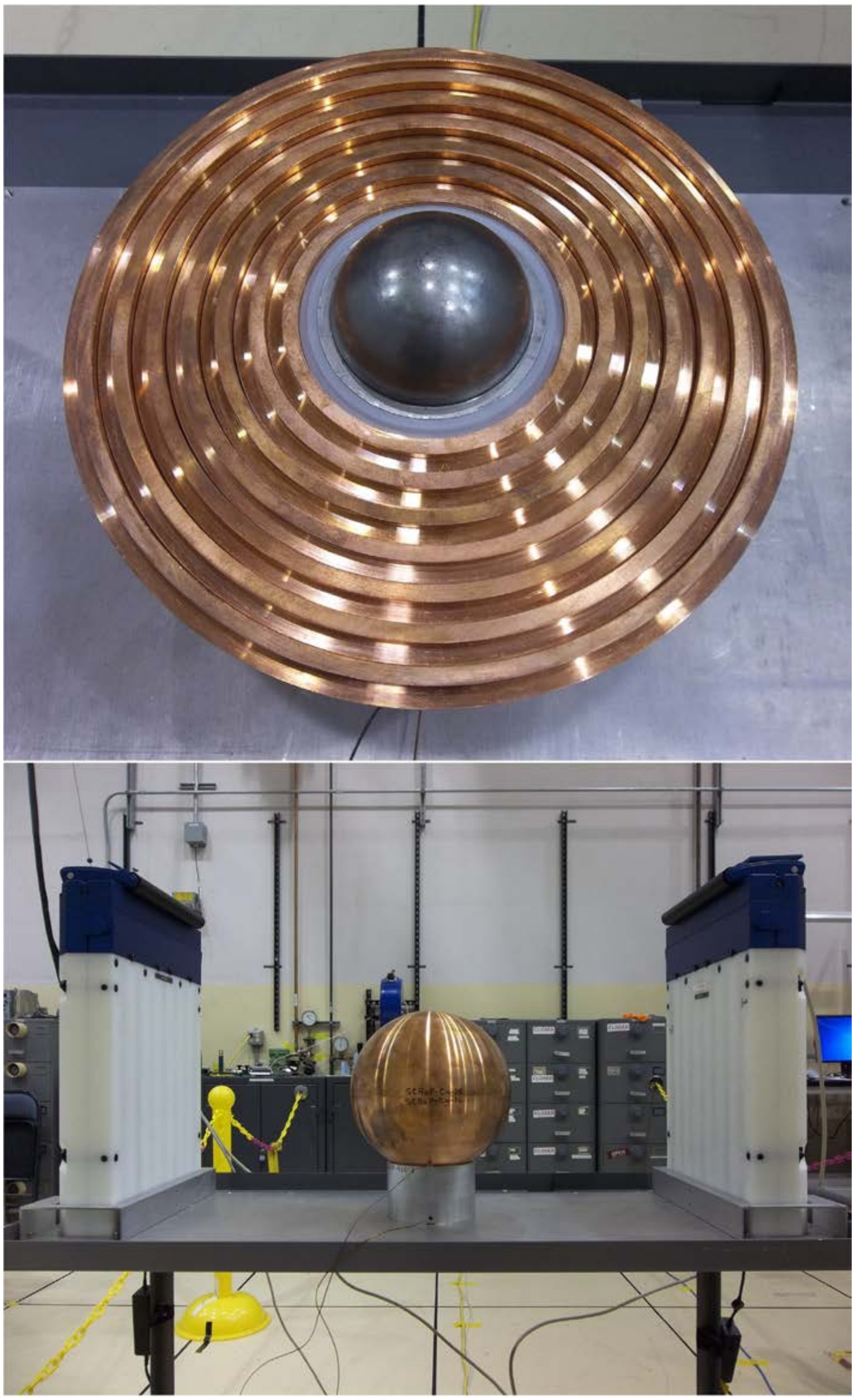

Fig. 8. Configuration 15: The BeRP ball surrounded by 0.5 inch-thick HDPE and 3.5 inch-thick Cu.

has a pressure of 150 psia (10.13 bars) and active diameter and length of 0.97 $\times$ 15 in. (2.46 $\times$ 38.1 cm). Table 3 lists the specifications of the tubes for the NoMAD. The tubes have an aluminum-1100 cladding that is 1.00 in. (2.54 cm) in outer diameter. These tubes are aligned inside two polyethylene blocks in three rows: a front row of seven tubes, a middle row of six tubes, and a back row of two tubes. The pitch between tubes in a row is 2.0 in. (5.08 cm), and the tubes of the front and middle rows are staggered; the two tubes in the back row line up with the third and fifth tubes in the front row. Fig. 11 depicts the configuration of the detector system.

This detector arrangement contains a data-acquisition system that produces list-mode data (a data list that includes the time and channel in which each event was recorded in the detector system). Table 4 shows an example of list-mode data. This particular example shows the first 10 events recorded in a measurement for configuration 0. It can be seen that the list includes the time (in ns) and the channel number (a 1 in the list of 32 channels indicates which channel(s) recorded an event at that time). The channel number starts at the right, so event 1 was a detection that occurred in channel 18; this channel is actually the second ^{3}He tube in the second NoMAD detector, since 16 channels are allotted to each unit (even though there are only 15 ^{3}He tubes). The data acquisition system has a tick size of 128 nsec, which is why all of the values in Table 4 are divisible by 128.

The detector system was located 47.0 cm from the center of the plutonium sphere to the surface of the front face of the NoMAD. For

Fig. 9. Configuration 16: 4.0 inch-thick HDPE around the BeRP ball.

these measurements, the efficiency (ϵ) is defined as the number of neutrons detected in any of the 30 ^{3}He tubes in one of the NoMAD detectors per neutrons emitted by the BeRP ball assembly (from spontaneous and induced fissions). Note that for this experiment, the two NoMAD detectors each collect data on identical clock cycles (the two systems are synchronized). There are several possible methods to determine the efficiency of the NoMAD detector; this work utilized ^{252}Cf source replacement measurements. A ^{252}Cf source was placed at the same location as the center of the BeRP ball and every reflected configuration was measured. The efficiency is taken by dividing the detector count rate by the reported source emission rate. When the measurements were performed, the fission source strength of the ^{252}Cf source was 759336.12 fissions/s ± 1.0 %.

2.6. Surrounding materials

The NoMAD detectors were placed in an adaptor plate which held them in place at a known position relative to the BeRP ball. The adaptor was attached to a base plate. This base plate had recesses in which alignment sleeves were placed to center the BeRP ball (and/or reflector materials). The base plate was placed on a mild carbon steel cart. An aluminum tube was present inside the lower reflectors to accommodate a thermocouple. Figs. 6–9 show all of these elements. Additional information on the adaptors, base plate, aluminum stands, aluminum tube, and concrete in the facility will be given in the upcoming benchmark evaluation.

3. Method

Details of the methodology applied to this experiment were described in Part I of this work. The text in this section will refer to Equation numbers from Part I. Fig. 12 shows a flow diagram of how the methodology is applied to the measured data, which will be further described in this section. As mentioned in Sections 2.2 and 2.5, ^{252}Cf source replacement measurements were performed for each configuration which included a holder to keep the source in the same location that the center of the BeRP ball would occupy. There are therefore two sets of data files for each configuration: one with the BeRP ball and one with the ^{252}Cf source. For both sets of data, multiple files may have been recorded for a given configuration. Step 1 of the process involves combining the multiple files for a configuration into a single file. The process listed as step 2 involves splitting the measured files into much smaller files. Between 200 and 800 smaller files were produced for each configuration, each of which had approximately 5×10^{5} detection events. The process of splitting files was only performed on the BeRP data and the primary purpose of doing so was to help estimate the uncertainty in the prompt neutron decay constant (λ). The time associated with this decay constant ($\frac{1}{\lambda}$) includes the slowing-

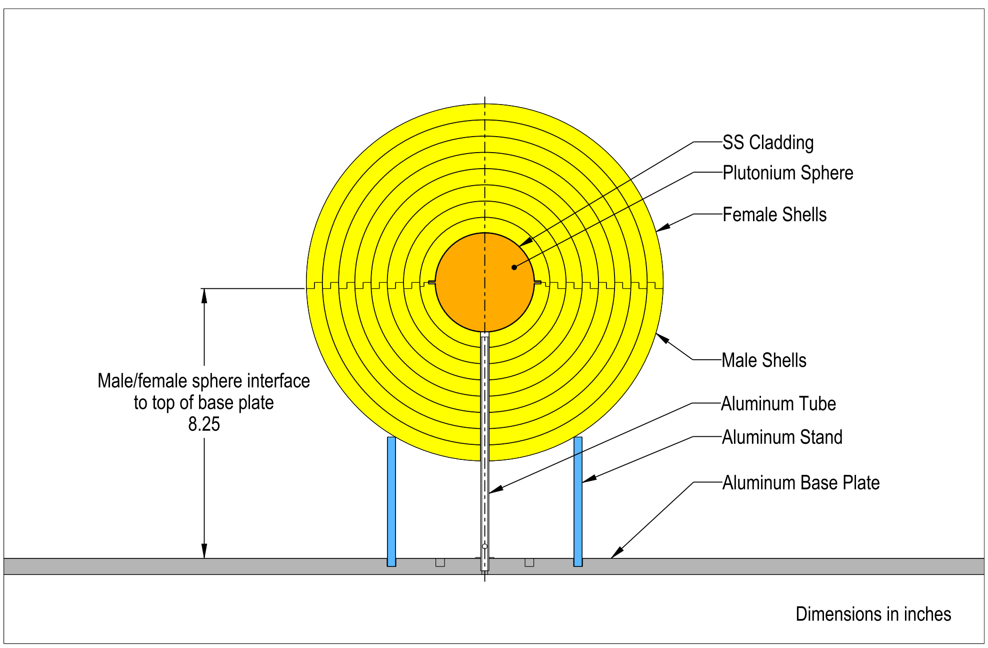

Fig. 10. SCRαP Assembly Close-Up.

Table 1
Composition of the BeRP Ball in 1980.

Nuclides	wt.% (Analysis 1)		wt.% (Analysis 2)		at.% (Analysis 1)	at.% (Analysis 2)	Assay Report Date
	Mean	σ	Mean	σ			
^{238}Pu	0.02	0.0007	0.02	0.0007	0.02	0.02	9-29-1980
^{239}Pu	93.73	0.0009	93.74	0.0009	93.75	93.77	9-29-1980
^{240}Pu	5.96	0.002	5.94	0.002	5.93	5.92	9-29-1980
^{241}Pu	0.268	0.0002	0.269	0.0002	0.266	0.267	9-29-1980
^{242}Pu	0.028	0.0002	0.028	0.0002	0.027	0.028	9-29-1980
^{241}Am				557 ppm			9-23-1980

Table 2
Copper and Polyethylene Reflector Nominal Dimensions.

Configuration number	Copper/Polyethylene total thickness	
	inches	cm
1	0.465	1.1811
2	0.955	2.4257
3	1.445	3.6703
4	1.935	4.9149
6	2.425	6.1595
5, 9	2.915	7.4041
10,12,13,14	3.405	8.6487
Configuration number	Inner radius of outermost hemishells	
	inches	cm
1	1.535	3.8989
2	2.010	5.1054
3	2.510	6.3754
4	3.010	7.6454
6	3.510	8.9154
5, 9	4.010	10.1854
10,12,13,14	4.510	11.4554
Configuration number	Outer radius of outermost hemishells	
	inches	cm
1	2.000	5.0800
2	2.500	6.3500
3	3.000	7.6200
4	3.500	8.8900
6	4.000	10.1600
5, 9	4.500	11.4300
10,12,13,14	5.000	12.7000

Table 3
NoMAD ^{3}He tube specifications.

Manufacturer	Reuter-Stokes
Model Number	RS-P4-0815-103
Body Material	Aluminum 1100
External Diameter	1.00 inch
Thickness	1/32 inch
Height (including cladding)	41.6 cm
^{3}He Pressure	150 psia
Active Length	15.0 inch

down time in the polyethylene in the NoMAD detectors. All parameters were calculated using the combined, individual, and split (for BeRP data only) files. The results between these were compared (and were used to determine potential outliers in the data or potential mistakes in the data analysis).

The flow diagram starts off with the ^{252}Cf source measurements. The detector efficiency is calculated from the ^{252}Cf source data using Eq. (49) and the uncertainty is calculated using Eq. (50). In addition to the measured data, determination of the efficiency requires $\bar{\nu_{S1}}$, which is a nuclear data parameter for ^{252}Cf; for this work a value of 3.757 was used (Santi and Miller, 2008). Similarly, information on the ^{252}Cf source is also required; this was provided by the source certificate (759336.12 fissions/s ± 1.0 % at the time of the measurement).

For the BeRP measurements, the first process is to perform the Rossi-α analysis (listed as step 4 in the figure). For this analysis two decays constants were used as shown in Eq. (38) (this is step 5 in the process diagram). The decay constants were determined using a Levenberg-Marquardt algorithm. As discussed in Part I, the uncertainty in the prompt neutron decay constant(s) (λ) is not easy to quantify and will be the focus of future research. For this work, the split files were used to determine the uncertainty in the decay constants. This was done by using Eq. (61). This method likely overestimates the true uncertainty in the decay constant, which is why it will be the focus of future research. The uncertainty calculated from the split files was then used during the analysis for all three file types (combined files, individual files, and split files).

Next the Feynman analysis, listed as step 6 in the process diagram, was performed. This included splitting each file into small time intervals (τ), creating Feynman histograms, and then applying Eqs. 1–29. It should be noted that Eq. (29) is used to determine the uncertainty in Y_2 (not Eq. (25)). Next the prompt neutron decay constant information is used along with the Y_2 results to calculate R_2 and associated uncertainty using Eqs. (30)–(36) (step 7 in the process diagram). Once these parameters are known, the leakage multiplication (M_L) can be calculated (step 8 in the process diagram). This is done using Eq. (53) for the value and Eq. (55) for the uncertainty. Last, the spontaneous fission rate (F_S) can be determined (step 9 in the process diagram) using Eq. (57) for the value and Eq. (58) for the uncertainty. Both M_L and F_S require nuclear data information for the spontaneous and induced fission isotopes. Section 3.1 has the values used in this analysis. It is assumed that all of the spontaneous fission neutrons are emitted from ^{240}Pu and all of the induced fission neutrons are emitted from ^{239}Pu.

4. Results

4.1. File information

For the SCRαP experiment, 17 configurations were measured. For each of these configurations, multiple list-mode data files were produced (each file contained time information for all 30 ^{3}He tubes). The amount of time spent measuring each configuration was based upon the final design simulations (Bahran and Hutchinson, 2016). Table 5 includes information on the measured files of the BeRP ball. The left section of the table is labeled "individual files" and includes information on the raw files that were recorded, including the number of files, the measurement time of each file, and the number of events in each file. The middle section of the table is labeled "combined files" and includes the total measurement time and number of events (only 1 combined file was created per configuration). The right section of the table is labeled "split files" and has the number of files and measurement time associated with the smaller files used to determine the uncertainty in λ and used for the validation in Section 4.3. Note that as shown in Fig. 12, the "individual files" are the files that are actually output from the detector and the "combined" and "split" files are generated during the data analysis process.

4.2. Measurement results

All of the results which are shown as a function of configuration number were binned using a time interval of 2048 μs. Figs. 13, 15, 16, 18, 20, and 22 include squares which represent the material of each layer; an orange square represents a Cu layer and a gray square represents an HDPE layer. The dark gray circle at the bottom represents the BeRP ball. Figs. 14, 17, 19, and 21 include a shorthand for which layers include Cu or HDPE; for example, configuration 5 shows Cu12P3456 which means that the first two layers are composed of Cu but layers 3–6 are composed of HDPE.

The detector efficiency was determined using ^{252}Cf source measurements. The detector efficiency (ϵ) is defined as the number of neutrons detected (in all divided 30 ^{3}He tubes of the two NoMAD systems) by the number of neutrons emitted (including all sources such as spontaneous fission,(α, n), and induced fission) in the same time period. Fig. 13 shows the efficiency determined from these

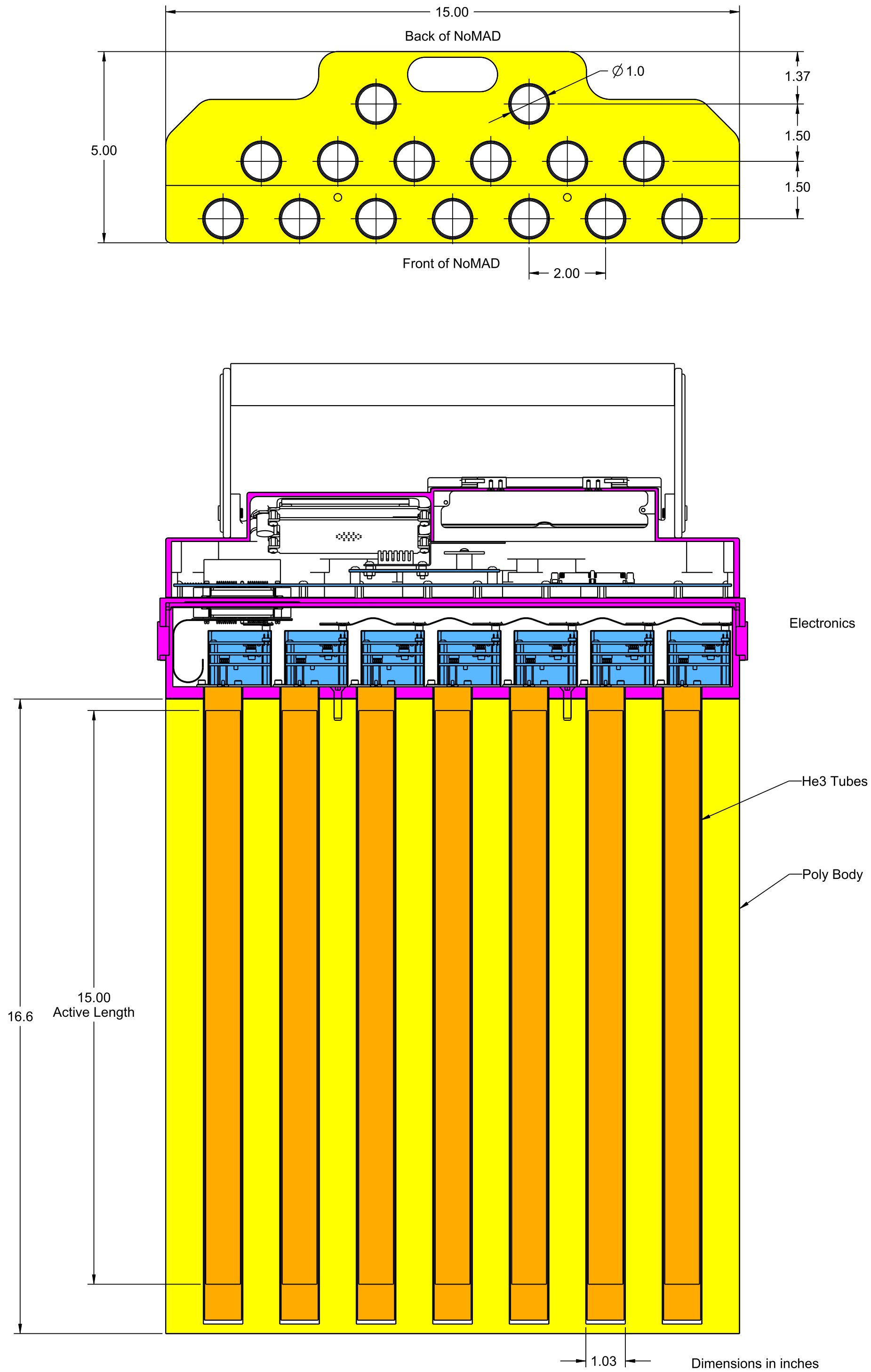

Fig. 11. NoMAD detector.

measurements. The efficiency at 50 cm for a single detector system measuring bare material is known to be approximately 1% from previous measurements (Richard and Hutchinson, 2016b; Richard and Hutchinson, 2016a), so the efficiency with two detector systems at 47 cm is expected to be slightly over 2% (which adds confidence to the configuration 0 result). The efficiency increases slightly for the configurations with only copper and the configurations with thin polyethylene; this is expected as the detector system is under-moderated. The detector efficiency decreases when thick polyethylene is present due to neutron absorption in the reflector material. Configuration 16, with four inch-thick polyethylene, is a much slower system than the rest of the configurations and therefore has very different results when compared to the other configurations for nearly all parameters.

The Rossi-α results are shown in Fig. 14. The A and B terms in Eq. (38) all increase as the system multiplication increases and this is reflected in these results. Note that these results are not normalized (so the reason that the configuration 11 results are higher than the configuration 15 results is due to the counting times of the configurations). All of these curves were fit to Eq. (38) to determine the

Table 4
List-mode data example containing the first 10 events of a measured file for configuration 0.

Event	Time (ns)	Channel
1	70400	0000 0000 0000 0010 0000 0000 0000 0000
2	103936	0000 0001 0000 0000 0000 0000 0000 0000
3	124032	0000 0000 0000 1000 0000 0000 0000 0000
4	233600	0000 0000 0000 0000 0000 0000 0000 1000
5	293888	0000 0000 0000 0000 0001 0000 0000 0000
6	336768	0000 0000 0001 0000 0000 0000 0000 0000
7	344832	0000 0010 0000 0000 0000 0000 0000 0000
8	446592	0000 0000 0000 0000 0000 0001 0000 0000
9	487424	0000 0000 0000 0000 0000 0100 0000 0000
10	618368	0000 0000 0000 0000 0000 0000 0001 0000

prompt neutron decay constants (λ_1 and λ_2). As previously stated, one can get different prompt neutron decay constants based on the data which are included in the fit or the type of fit used. For this reason, the split files were used to determine the uncertainty in this parameter. As previously stated, this is an area of future work. Fig. 15 shows the inverse of the prompt neutron decay constant ($\frac{1}{\lambda}$), which is called either the neutron lifetime or the slowing-down time (for the purposes of this work these two terms are considered equivalent). This parameter includes the time in which neutrons scatter within the polyethylene inside the detector system, prior to absorption. The slowing-down time associated with a very similar detector system has been previously reported as 42–43 μs (Richard and Hutchinson, 2016b; Richard and Hutchinson, 2016a). This value was expected for the bare and copper only configurations (and can be seen that these values were observed in Fig. 15). It can be seen from this figure that the slowing-down time and efficiency are anti-correlated. This is not surprising since the increase in slowing-down time is due to scattering in the HDPE hemishells, but as more scattering occurs more absorption will also occur (due to a larger proportion of lower energy neutrons).

The singles count rate (R_1) results are shown in Fig. 16. It can be seen that the count rate generally increases across configurations (as multiplication is increasing). The count rate is proportional to both leakage multiplication and detector efficiency. However, the count rate decreases for configurations in which the decrease in efficiency has a greater effect than that from the increase in multiplication.

Results for the Y_2 parameter, related to the excess variance using Eq. (23), are shown in Fig. 17. This parameter increases as multiplication increases, which is why the bare configuration is at the bottom and configuration 15 (the system with the highest multiplication) is at the top. It can clearly be seen that configuration 16 has a very different shape (and therefore large slowing-down time) due to the large amount of polyethylene.

Results for the doubles count rate (R_2) are shown in Fig. 18. As shown in Eq. (35), R_2 is simply Y_2 divided by ω_2. At large gate widths, ω_2 will approach 1, so the Y_2 results in Fig. 17 at 2048 μs are nearly identical to the R_2 results in Fig. 18. Similar to R_1, this parameter increases as multiplication increases, but it is also affected by the detector efficiency. For some configurations (such as 7, 8, and 12), R_1 and R_2 decreases, because the increase in these parameters due to multiplication is not as large as the decrease due to the efficiency (caused by the polyethylene absorption).

As stated in Section 3.3, the uncertainty in R_2 can be used to determine optimal time intervals for analysis as shown in Fig. 19. It can be seen from this figure that any time interval greater than about 750 μs is large enough to minimize these uncertainties for the bare configuration and those with only copper reflection. For the configurations that include polyethylene, however, a larger time interval is needed. This is not surprising, as these configurations have a much larger neutron slowing-down time (and corresponding larger uncertainty). From these results, a time interval of 2048 μs will be used for all configurations. One could use a unique time interval for each configurations, but in this work a sin-

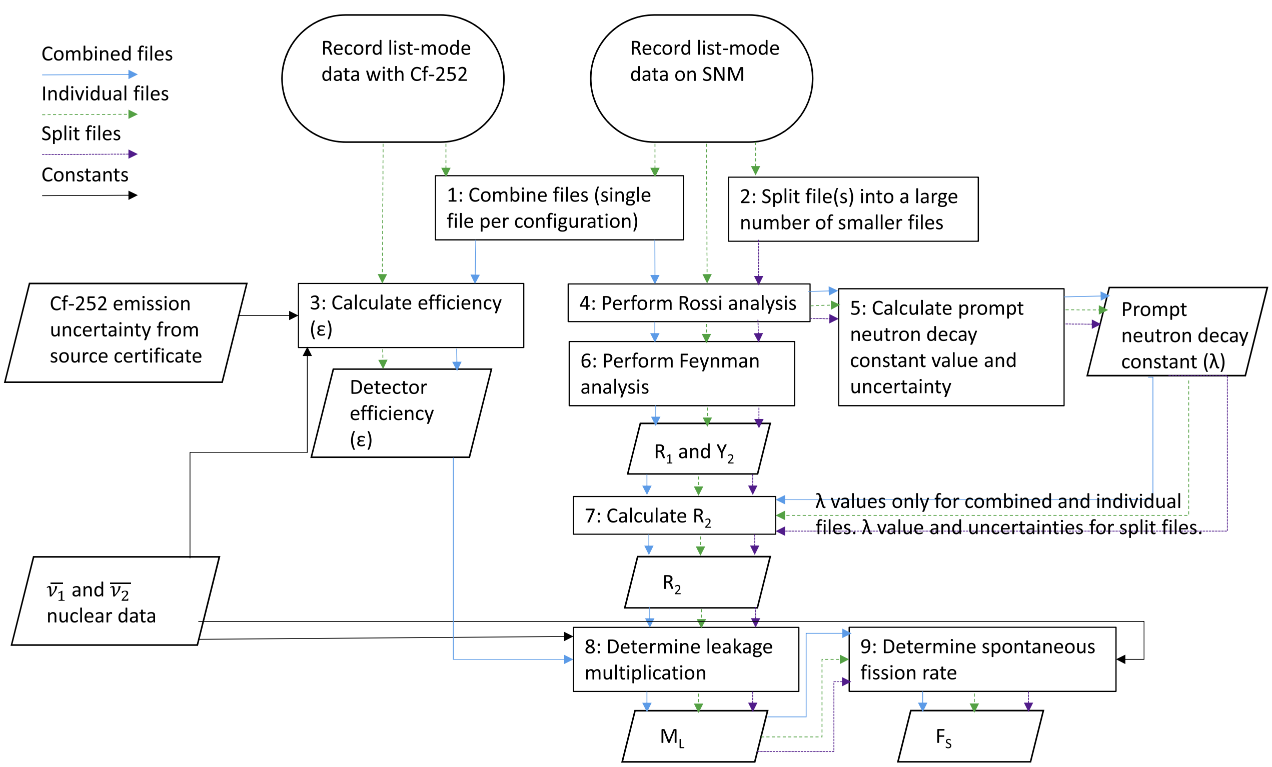

Fig. 12. Data analysis process.

Table 5
SCRαP Benchmark Data Information.

Configuration #	Individual files			Combined files		Split files	
	# Files	Measurement time (s)	# Events	Measurement time (s)	# Events	# Files	Measurement time (s)
0	6	1800	3.43E+07	10800	2.06E+08	408	26.5
1	3	1800	4.58E+07	5400	1.37E+08	270	20.0
2	5	900	2.87E+07	4500	1.44E+08	285	15.8
3	4	900	3.48E+07	3600	1.39E+08	276	13.0
4	3	900	5.48E+07	2700	1.64E+08	332	10.8
5	4	900	4.14E+07	3600	1.66E+08	328	11.0
6	2	1800	9.60E+07	3600	1.92E+08	380	9.5
7	3	900	5.80E+07	2700	1.74E+08	272	13.2
8	4	900	3.50E+07	3600	1.40E+08	280	12.9
9	4	900	5.47E+07	3600	2.19E+08	436	8.3
10	4	900	6.16E+07	3600	2.46E+08	480	7.5
11	5	900	6.86E+07	4500	3.43E+08	650	6.9
12	5	900	5.11E+07	4500	2.55E+08	505	8.9
13	5	900	6.33E+07	4500	3.16E+08	600	7.5
14	6	900	5.72E+07	5400	3.43E+08	780	6.9
15	2	900	7.85E+07	1800	1.57E+08	300	6.0
16	6	1800	6.53E+07	10800	3.92E+08	780	13.8

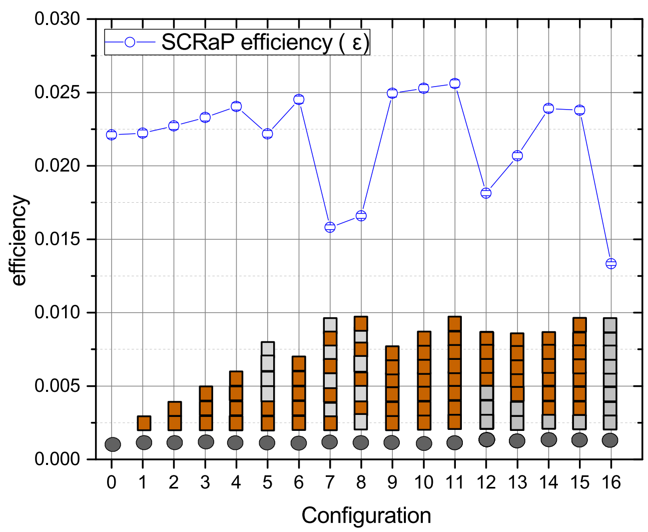

Fig. 13. Detector efficiency (ϵ) for all SCRαP configurations (determined using ^{252}Cf source measurements).

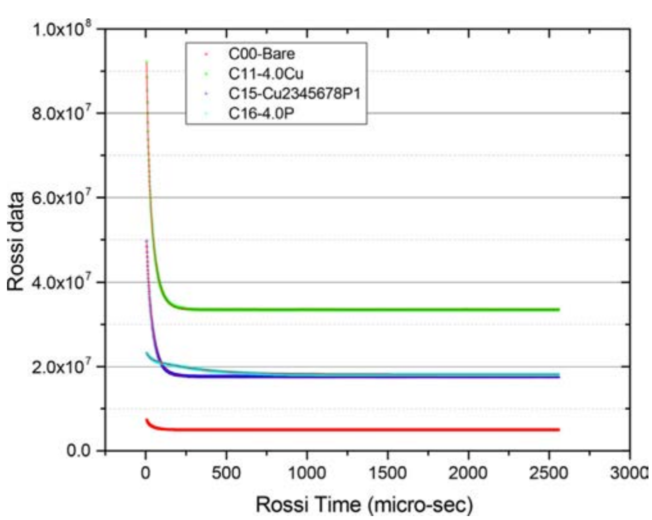

Fig. 14. Rossi-α results for all SCRαP configurations.

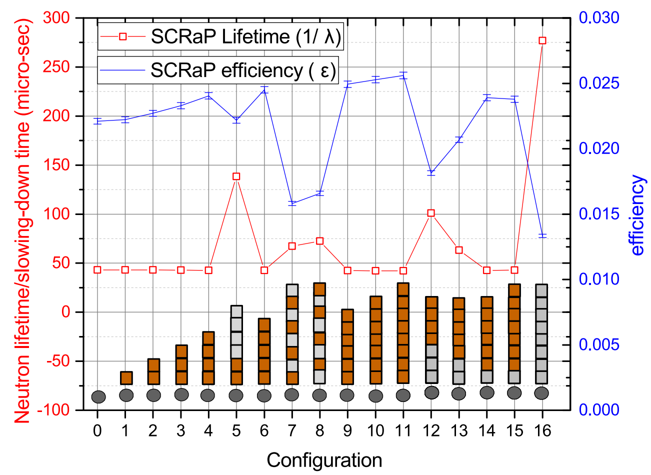

Fig. 15. Neutron slowing-down time ($\frac{1}{\lambda}$) and efficiency for all SCRαP configurations.

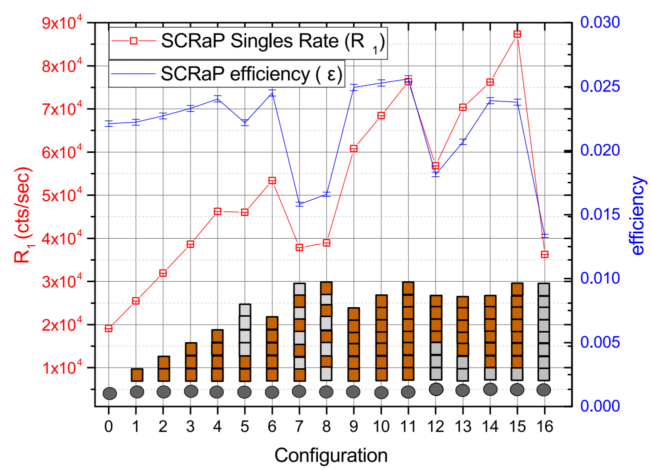

Fig. 16. Singles count rate (R_1) and efficiency (ϵ) for all SCRαP configurations.

gle time interval was used for all configurations since the results from different configurations are often compared.

The leakage multiplication (M_L) results are shown in Fig. 20. It can be seen that the leakage multiplication generally increases as

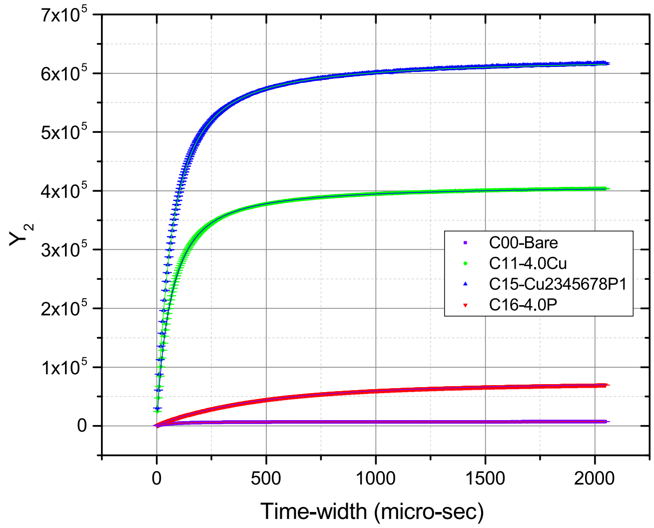

Fig. 17. Y_2 for all SCRαP configurations.

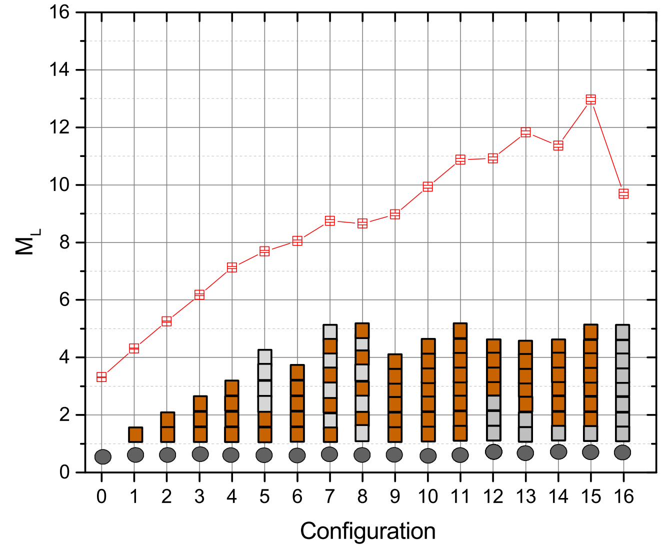

Fig. 20. Leakage multiplication (M_L) for all SCRαP configurations.

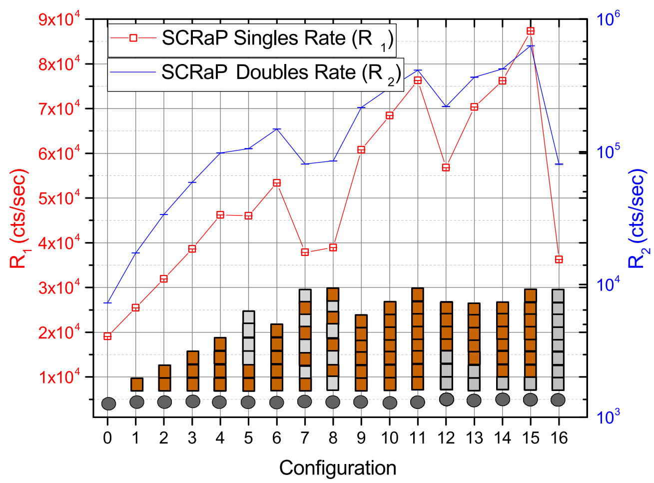

Fig. 18. R_1 (left y-axis) and R_2 (right y-axis) for all SCRαP configurations.

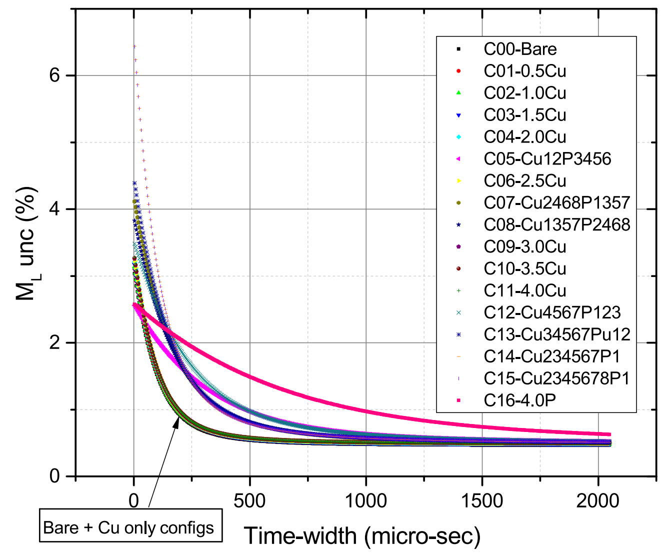

Fig. 21. M_L uncertainty (in %) for all SCRαP configurations.

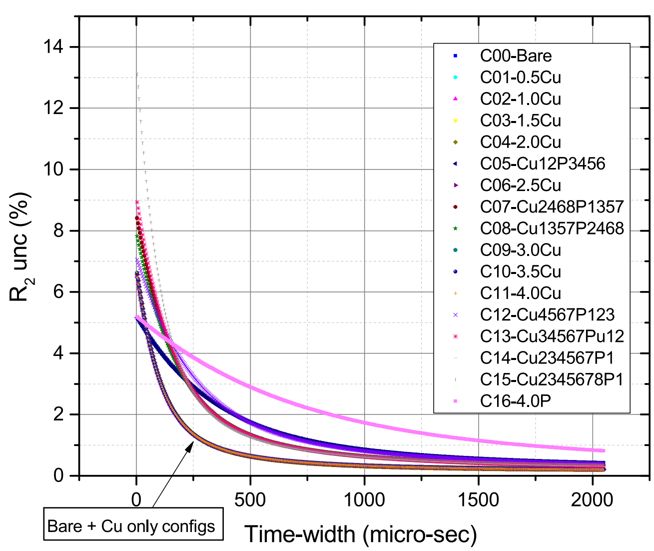

Fig. 19. R_2 uncertainty (in %) for all SCRαP configurations.

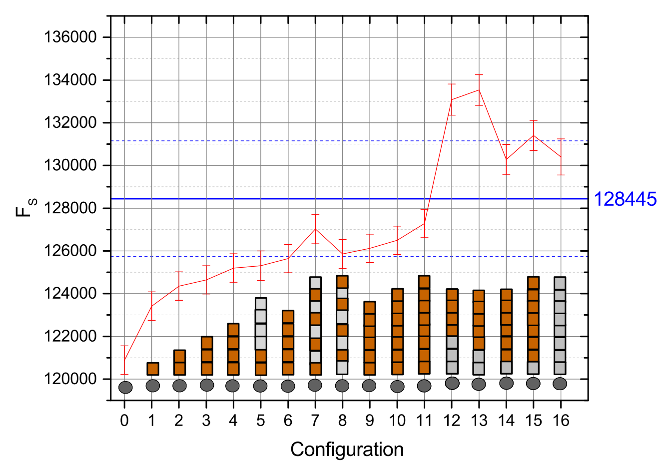

Fig. 22. Spontaneous Fission Rate (F_S) for all SCRαP configurations.

the configuration number increases, as expected (it was noted that configuration 16 was expected to have a lower inferred multiplication). There were three pairs of configurations that were expected to have nearly identical multiplication values: 8/9, 11/12, and 13/14. The observed multiplication for those pairs were very similar as expected, but the multiplication for configurations 7 and 8 were closer to each other than predicted during the design simulations. The uncertainty (in %) of leakage multiplication as a function of time interval is shown in Fig. 21. These curves have identical trends to those of R_2, as seen in Fig. 19, and therefore the conclusions related to time interval selection remains the same. It is expected that these curves would have these trends due to the fact that the R_2 uncertainties are much larger than the R_1 uncertainties and the detector efficiency is independent of the time interval (and these are the only three terms associated with this uncertainty as shown in Eq. (55)).

Results for the spontaneous fission rate (F_S) are shown in Fig. 22. The blue solid horizontal line in this figure corresponds to 128445 spontaneous fissions/s, which is the assumed rate in the BeRP ball from a decay correction of the measured isotopics in the Pu sphere. The two dashed lines correspond to a 1% change in the ^{240}Pu mass.

Table 6 compares the results of the bare configuration (C00 or configuration 0) to the previous bare configuration in the nickel (Richard and Hutchinson, 2016b) and tungsten (Richard and Hutchinson, 2016a) evaluations. The top row is the nickel evaluation, the second row is the tungsten evaluation, and the bottom row is this work. The rates in Table 6 are quite different. This is because while all of the evaluations used a fairly similar detector system and measurement setup, the two detector units were not linked together for the previous evaluations. Having both detector units output data into the same time list doubles the singles count

Table 6
Comparison of bare BeRP configurations (at 128 μs).

Evaluation	Case	R_1	σ	R_2	σ	M_L	σ
FNPHM001	1	8926.62	1.78	1598.41	5.34	3.384	0.030
FNPHM002	1	9021.45	1.77	1643.72	5.27	3.371	0.030
FNPHM003	0	19057.08	1.64	7449.12	196.62	3.346	0.043

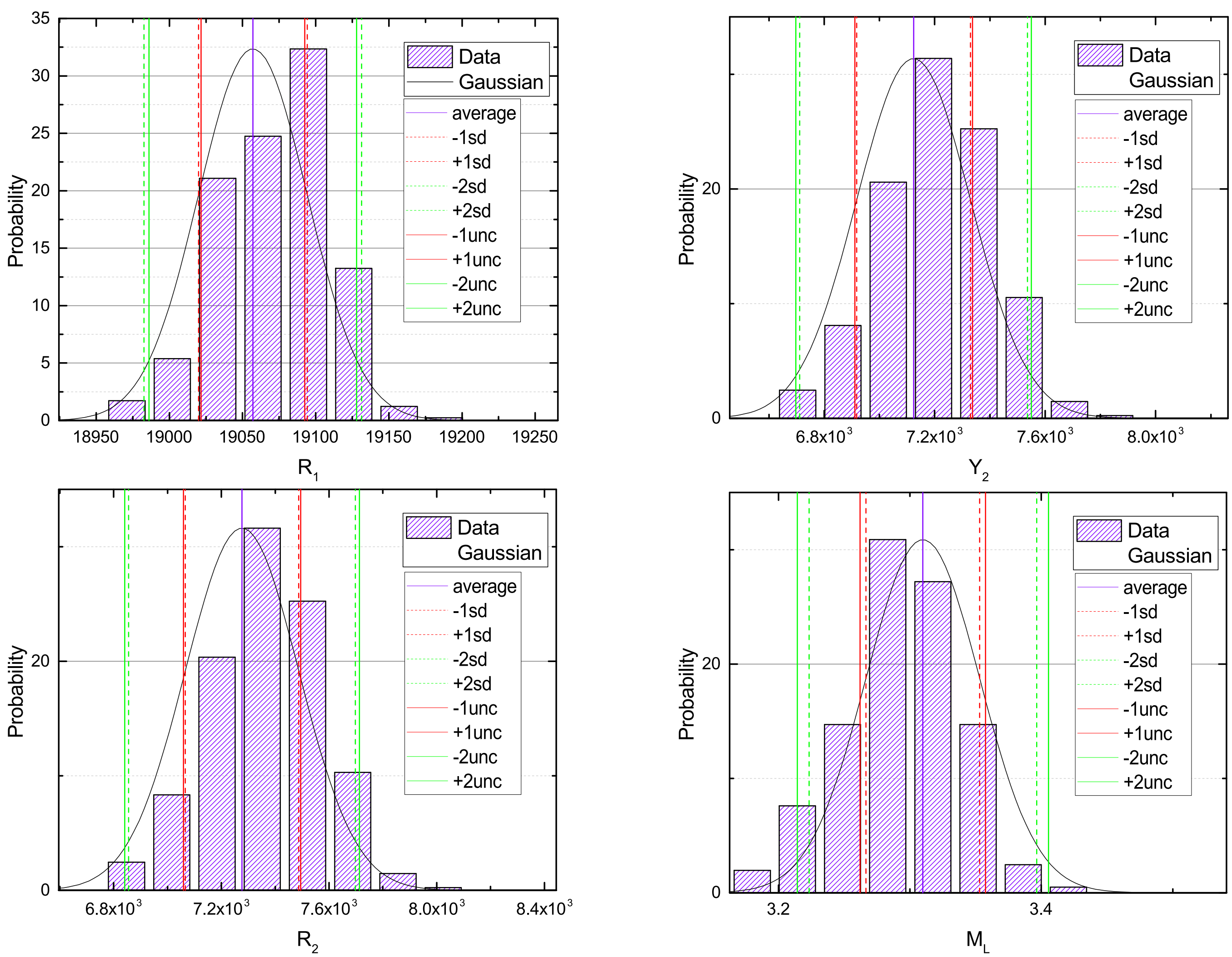

Fig. 23. Sample histograms for configuration 0.

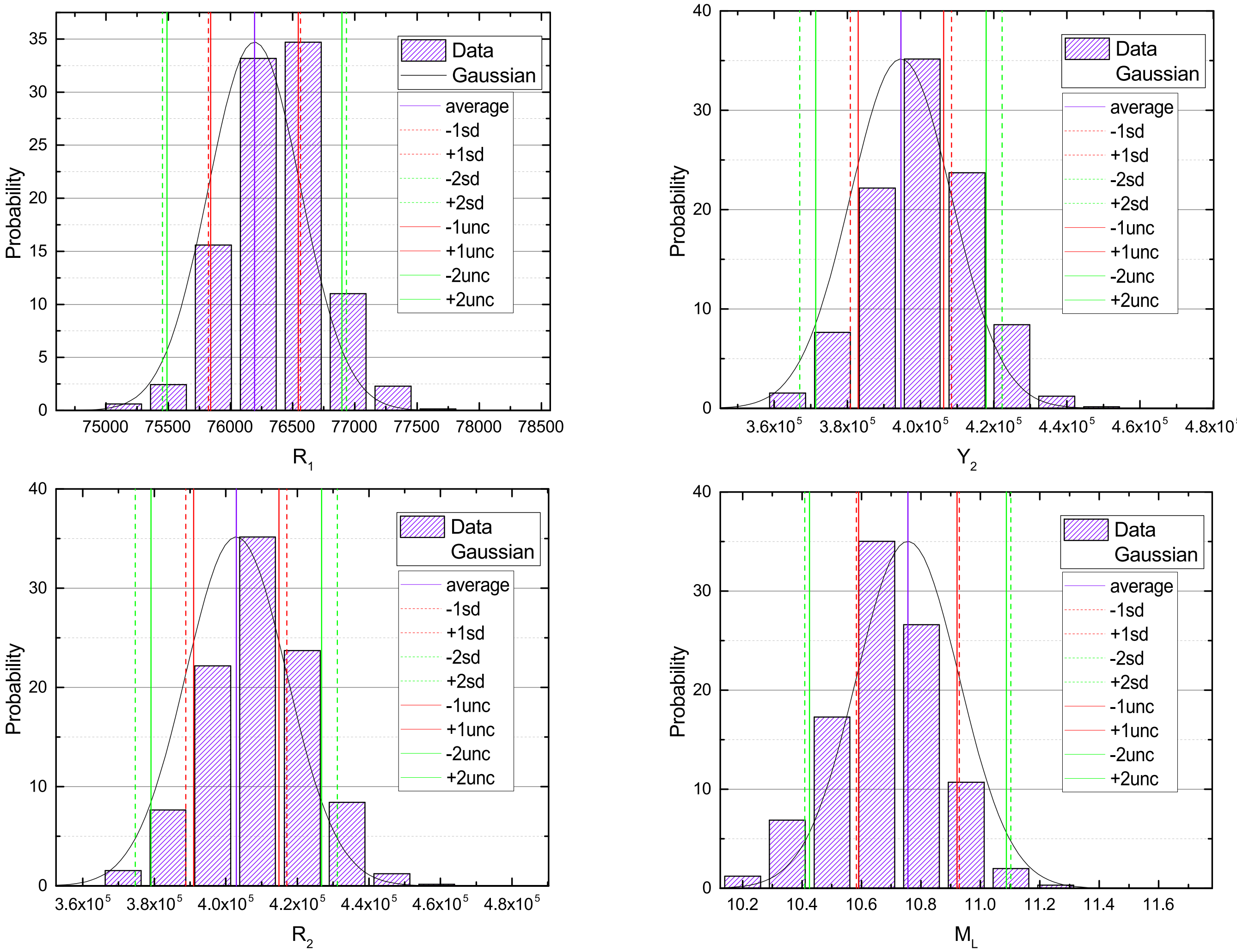

Fig. 24. Sample histograms for configuration 11.

rate but increases the doubles count rate by a factor of four (see Eq. (48) in which efficiency is squared for R_2), which results in lower uncertainties for the same analysis method. It can be seen in Table 6 that for SCRαP (FNPHM003), the R_1 rate is about double that of the previous evaluations and the rate of R_2 is about four times higher as expected. The uncertainty in R_2 is larger for the SCRαP experiment because of the conservative method used to determine the uncertainty in λ in this work. The systematic experimental uncertainties are likely larger than the statistical uncertainties in R_2 (so it should not be particularly concerning that the uncertainty in this parameter is quite a bit higher). It can be seen that the leakage multiplication results agree well between the three measurement campaigns. All of the results were shown at 128 μs, since that was the time interval chosen for the previous evaluations.

4.3. Validation

As shown in Table 5, all of the files were broken up into smaller files (between 5 and 30 s of measurement time). This process provides a validation of the uncertainty analysis used. The validation results focus on configurations 0, 11, 15, and 16. These configurations were selected because they bound the problem set (both in multiplication and in energy/slowing-down time). For the validation of each parameter, each split file was analyzed using the same process as the larger files. Frequency binning was performed on the smaller files. The standard deviation of the samples was compared with the average of the uncertainties calculated for each sample (using the method described in Part I). The data were also compared to a scaled Gaussian distribution as shown in Figs. 23–26. Finally, the percentage of samples that lie within bands around the mean were checked (the 68–95–99.7 rule) in Figs. 27–30.

In general, these results show that this method does a great job of correctly assessing the uncertainty for R_1, Y_2, R_2 and M_L. The uncertainties are quite close to the sample standard deviation, the data are roughly Gaussian, and there are no large outliers.

For configuration 0, it can be seen that the uncertainty values compare very well to the standard deviation of the samples for R_1, Y_2, and R_2. For M_L, however, the uncertainty methodology yielded results that were slightly larger than the standard deviation of the data (these results can be seen in Fig. 23 and on the left of Figs. 27–30). For configuration 11, the R_1 and M_L uncertainty results compare well with the standard deviation of the data. The Y_2 and R_2 uncertainties are both smaller than the sample standard deviation (Figs. 24,27,28,29,30). For configuration 15, all of the parameters have uncertainties that are smaller than the sample standard deviation (Figs. 25,27,28,29,30). This is the worst for R_1, which has an uncertainty that is much smaller than the sample standard deviation. This is due to the fact that this configuration only had two data files (most of the configurations had more than

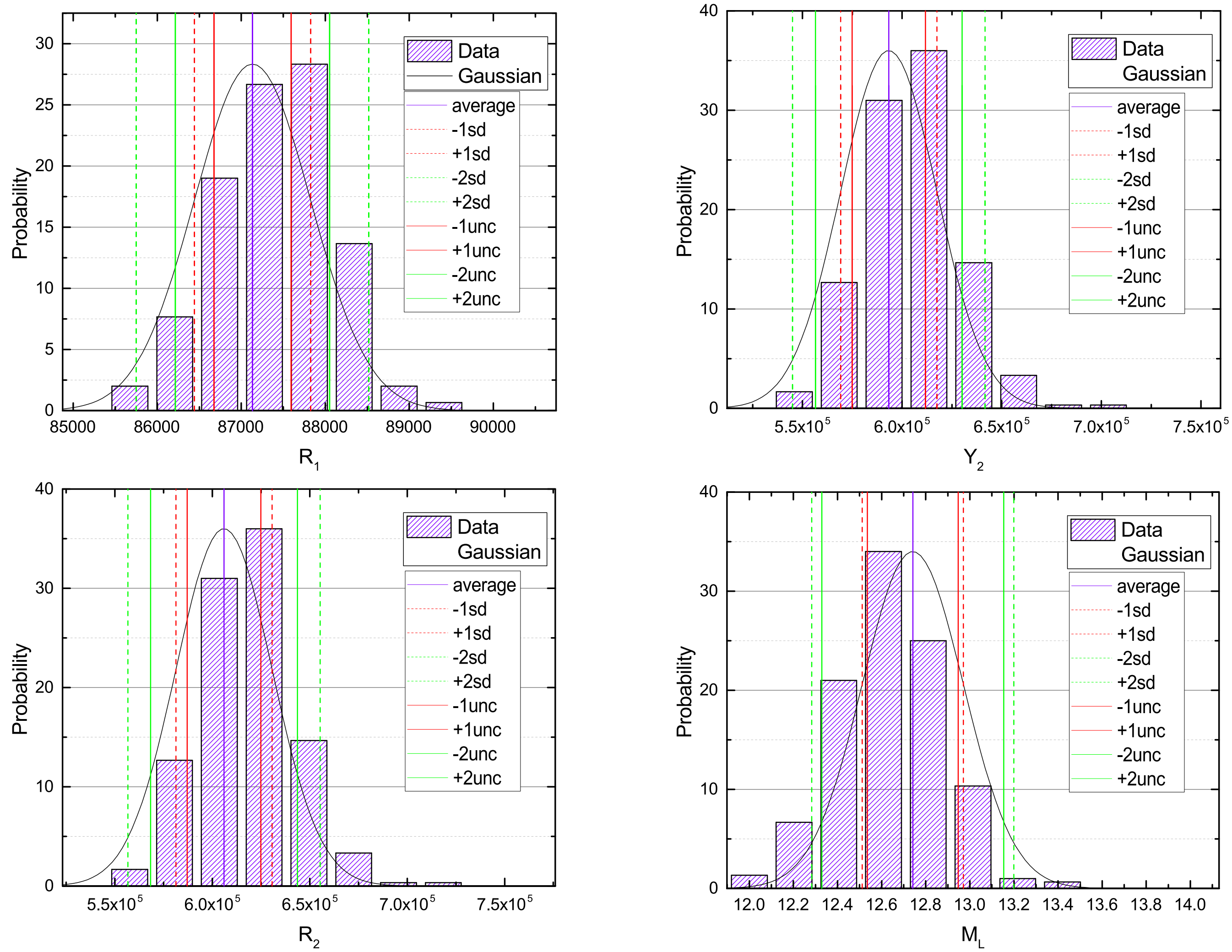

Fig. 25. Sample histograms for configuration 15.

two files) and the singles count rate is different for these two data files (there is no clear reason why one should choose or prefer one data file over the other). For configuration 16, all of the parameters agree fairly well, but the M_L uncertainty seems to be slightly larger than the sample standard deviation.

Figs. 27–30 show the percentage of samples that fall within 1, 2, or 3 standard deviations. Ideally, the results of the uncertainty analysis and standard deviation of the data would both reflect the behavior expected by a Gaussian distribution: 68% of the data would be within ±1, 95% within ±2, and 99.7% within ±3 standard deviations. It can be seen that the data do a good job in general of obeying this rule.

For R_1, it can clearly be seen that configurations 6, 15, and 16 are all different than the expected Gaussian behavior. It was stated above why it is believed that configuration 15 does not compare well. It is assumed that configuration 16 is different due to the thick polyethylene and it is unclear why the results for configuration 6 do not agree.

Results for Y_2 and R_2 are very similar and will be discussed together. It can be seen that the worst agreement is for configurations 5 and 11–15. This is likely due to the presence of polyethylene reflection.

For M_L, configurations 8 and 16 have the worst agreement, likely due to the polyethylene reflection. There is a general trend in which the leakage multiplication uncertainties are greater than the sample standard deviations. This result agrees with the results presented in Part I.

All of the results in Figs. 27–30 tend to show that for the slower systems the agreement is not as good (the uncertainties start to differ from the standard deviations). This is similar to the results in Part I, which discussed that for slower systems some of the assumptions of the method may be violated. Additional work should be performed with these types of systems to see if the method could be improved.

5. Conclusions

Seventeen configurations for the SCRαP (Subcritical Copper-Reflected α-phase Pu) experiment were measured and analyzed. These configurations were designed to maximize the ^{63}Cu and ^{65}Cu cross-section sensitivities (both over all energies and within the intermediate energy region) and to provide configurations which cover a wide range of multiplication values. An overview of the experiment was described including information on the Pu sphere, the spherical copper and polyethylene reflectors, the neutron detectors used for the measurements, and other surrounding materials. The analysis methodology was described and is presented in further detail in Part I of this work.

The results of the 17 configurations were presented. The range of leakage multiplication values among these configurations was

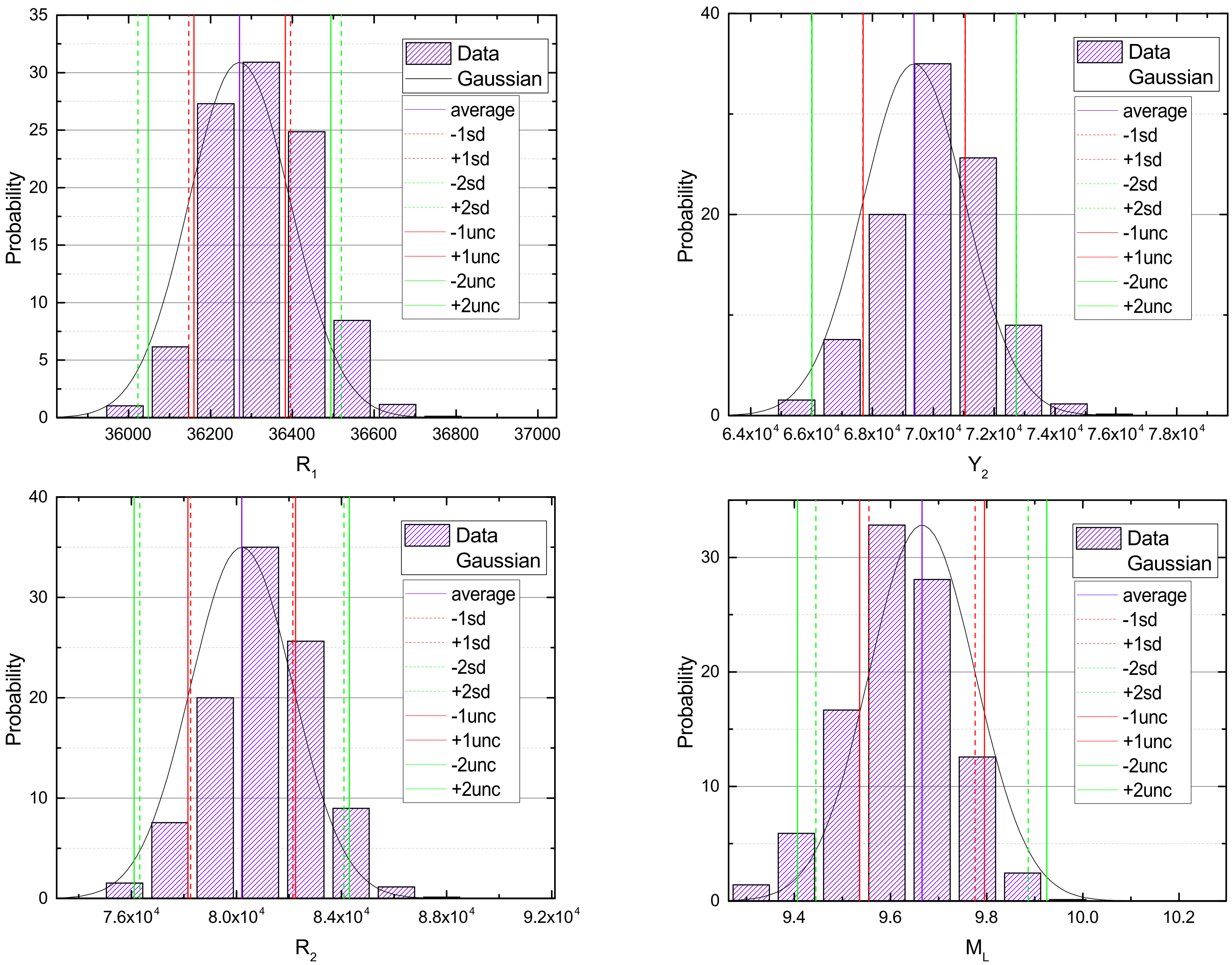

Fig. 26. Sample histograms for configuration 16.

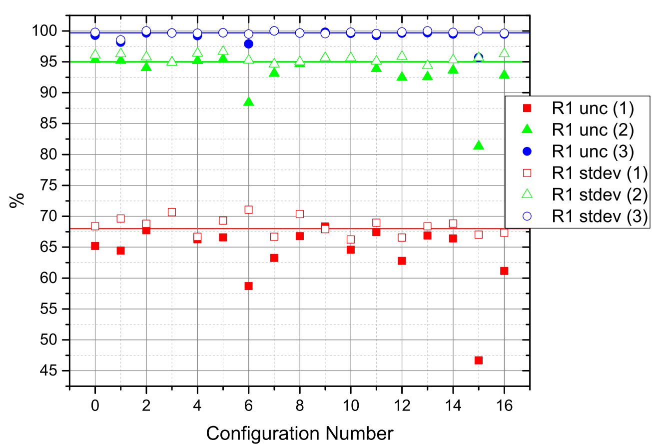

Fig. 27. Percentage of samples that fall within 1, 2, or 3 σ of the mean for R_1.

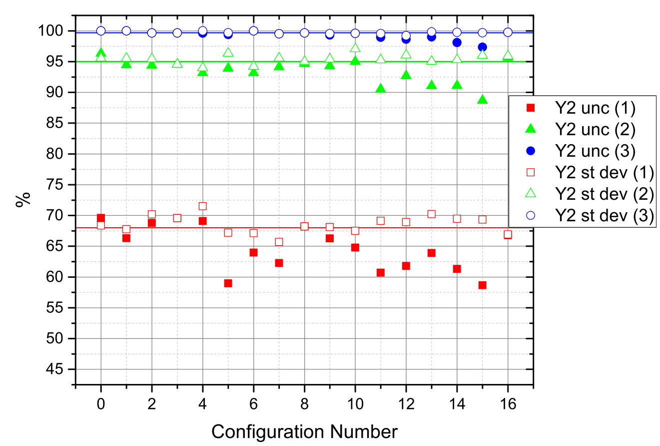

Fig. 28. Percentage of samples that fall within 1, 2, or 3 σ of the mean for Y_2.

3.5–13. All of these had measurement uncertainties in leakage multiplication of less than 1%. The use of polyethylene resulted in systems with a slowing-down time as high as about 275 μs. The bare configuration was compared to the other bare BeRP results in recent subcritical benchmarks.

A validation was performed in which the data files were broken up into smaller files (measurement times between 5 and 30 s each). These smaller files allow for a comparison of the uncertainty analysis method with the sample standard deviation. It was shown that the uncertainty method compared very well with the sample standard deviation. These data help to further validate the uncer-

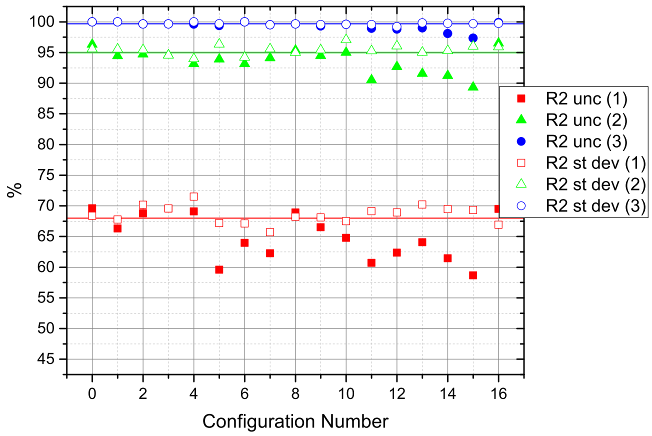

Fig. 29. Percentage of samples that fall within 1, 2, or 3 σ of the mean for R_2.

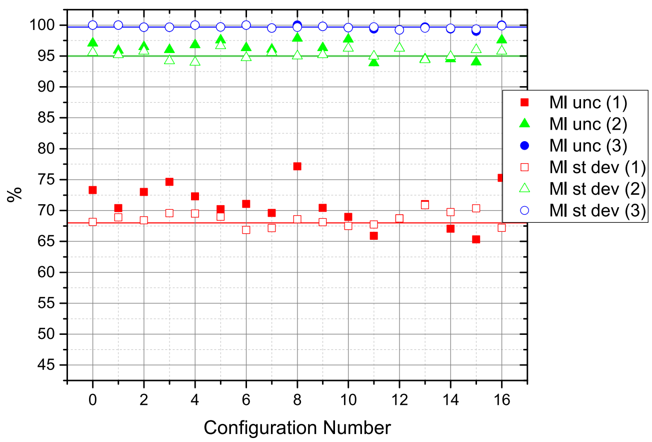

Fig. 30. Percentage of samples that fall within 1, 2, or 3 σ of the mean for M_L.

tainty methodology described in Part I. Specific differences were discussed.

Future work includes using the data from this work in a future ICSBEP evaluation. Results from simulations using multiple Monte Carlo codes and nuclear data libraries will be compared. These data will be useful for future computational methods and nuclear data validation efforts.

Acknowledgments

The authors would like to thank all involved in the success of these measurements (including all logistics to perform measurements in a nuclear facility) and thank those involved in developing/updating simulation capabilities used in this evaluation, especially C.J. Solomon. This work was supported by the Department of Energy Nuclear Criticality Safety Program, funded and managed by the National Nuclear Security Administration for the Department of Energy.

References

Bahran, R., Hutchinson, J., 2016. Subcritical copper-reflected α-phase plutonium (SCRαP) integral experiment design. Trans Am Nucl Soc 114, 527–529.

Goorley, T., James, M., Booth, T., Brown, F., Bull, J., et al., 2012. Initial MCNP6 release overview. Nucl. Technol. 180, 298–315.

Hutchinson, J., Cutler, T., 2016. Use of criticality eigenvalue simulations for subcritical benchmark evaluations. Trans. Am. Nucl. Soc. 115 (1), 939–942.

Hutchinson, J., Bahran, R., Cutler, T., Arthur, J., Nelson, M., 2017. Subcritical copper-reflected alpha-phase plutonium (scrap) measurements and simulations. M&C 2017 – International Conference on Mathematics & Computational Methods Applied to Nuclear Science & Engineering.

Hutchinson, J., Nelson, M., Grove, T., Arthur, J., McKenzie, G., Bahran, R., Cutler, T., 2019. Validation of statistical uncertainties in subcritical benchmark measurements: Part I-theory and simulations. Ann. Nucl. Energy. 125, 50–62.

International Handbook of Evaluated Criticality Safety Benchmark Experiments Nuclear Energy Agency, 2016. Paris: OECD Nuclear Energy Agency (NEA;7328).

Loaiza, D., Hutchinson, J., 2007. Plutonium sphere reflected by beryllium. In: International Handbook of Evaluated Criticality Safety Benchmark Experiments, [DVD]/Nuclear Energy Agency. – Paris: OECD Nuclear Energy Agency (NEA;7328).

Richard, B., Hutchinson, J., 2016. Tungsten-reflected plutonium-metal-sphere subcritical measurements. In: International Handbook of Evaluated Criticality Safety Benchmark Experiments, [DVD]/Nuclear Energy Agency. – Paris: OECD Nuclear Energy Agency (NEA;7328).

Richard, B., Hutchinson, J., 2016. Nickel reflected plutonium metal sphere subcritical measurements. In: International Handbook of Evaluated Criticality Safety Benchmark Experiments, [DVD]/Nuclear Energy Agency. – Paris: OECD Nuclear Energy Agency (NEA;7328).

Santi, P., Miller, M., 2008. Reevaluation of prompt neutron emission multiplicity distributions for spontaneous fission. Nucl. Sci. Eng. 160 (2), 190–199.

Subcritical Copper-Reflected α-phase Plutonium (SCRαP) Measurements and Simulations

J. Hutchinson, R. Bahran, T. Cutler, W. Monange, J. Arthur, M. Smith-Nelson, G. Caplin, E. Dumonteil

Los Alamos National Laboratory, P.O. Box 1663 P365, Los, Alamos, NM 87545
jesson@lanl.gov

Abstract - *A Subcritical Copper-Reflected α-phase Plutonium (SCRαP) integral benchmark experiment has been designed and measured. The experiment design is discussed and preliminary results are presented. In the future this experiment will be evaluated and documented as a subcritical benchmark evaluation.*

I. INTRODUCTION

A Subcritical Copper-Reflected α-phase Plutonium (SCRαP) integral benchmark experiment has been designed and measured. In this experiment, multiplication is approximated using correlated neutron data from a detector system consisting of ^{3}He tubes inside high density polyethylene (HDPE). Measurements were performed on various subcritical experimental configurations consisting of a weapons-grade plutonium sphere surrounded by different Cu thicknesses. In addition to the proposed base experimental configurations with Cu, additional configurations were performed with the plutonium ball nested in various thicknesses of interleaved HDPE spherical shells mixed in with the Cu shells. The HDPE is intended to provide fast neutron moderation and reflection, resulting in additional measurements with differing multiplication, spectra, and nuclear data sensitivity.

The experiments were performed at the National Criticality Experiments Research Center (NCERC). A 4.5-kg α-phase stainless-steel clad plutonium sphere, referred to as the BeRP (Beryllium-Reflected Plutonium) ball due to its historical use in a beryllium-reflected critical experiment [1], was the plutonium core for this experiment. More detail on the physical characteristics of the BeRP ball can be found in a Reference [2].

In 2012, similar subcritical measurements were performed with the BeRP ball surrounded by nickel and tungsten. Both measurement sets were documented as benchmark evaluations and accepted by the International Criticality Safety Benchmark Evaluation Project (ICSBEP) [2,3].

Similar to past measurements, the proposed work will help identify deficiencies and quantify uncertainties in nuclear data, and validate computational methods related to neutron multiplication inference for subcritical benchmark evaluations.

II. EXPERIMENT DESIGN

A Solidworks® rendering of the preliminary design of the SCRαP integral benchmark experiment is shown in Fig. 1. The BeRP ball is surrounded by Cu hemishells as shown in Fig. 2. The assembly is built on an aluminum stand such that the center of the BeRP ball is at the same height as the center of the He-3 tubes of the multiplicity counter detector system, called the MC15.

Fig. 1. Preliminary Solidworks® Computer-Aided Design (CAD) rendering of the SCRαP integral experiment. The BeRP ball inside nested Cu is in the center. Two MC15 detector systems are used to estimate the multiplication of each configuration.

The experiment design consisted of the BeRP ball nested in various thicknesses of Cu spherical shells and interleaved polyethylene spherical shells. In total, 16 different configurations were designed: 1 bare configuration, 8 copper-reflected configurations (up to a maximum of 4 inches-thick) and 7 configurations with polyethylene and copper reflection (also up to a maximum of 4 inches-thick). There are two purposes for the configurations with polyethylene: they allow for higher multiplication factor than with copper alone; and they allow for a different neutron spectra (and resulting sensitivity) for the same multiplication factor.

Fig. 2. Preliminary Solidworks® Computer-Aided Design (CAD) rendering of the SCRαP integral experiment. The BeRP ball can be seen in the center of the nested Cu (*bottom*) and Cu/polyethylene (*top*) shells.

The Cu alloy C101 was used for all of the hemishells. This alloy contains a minimum of 99.99 wt.% Cu. One of the Cu hemishells is shown in Fig. 3.

Fig. 3. A copper hemishell for use in the SCRαP experiment.

For this experiment, the MC15 multiplicity detector system was used. This detector consists of 15 He-3 tubes embedded in HDPE. The detector system records list-mode data (a time list of every recorded neutron event to a resolution of 128 nsec). Fig. 4 shows the MC15 detector system. For the SCRαP experiment, two MC15 systems were present and collected data in the same time list.

During the measurements, temperature data loggers were concurrently providing temperature data for the BeRP ball and its surroundings.

More information on the SCRαP experiment can be found in the final design documentation [4].

Fig. 4. Photograph and MCNP® model of the MC15 detector system.

1. Monte Carlo Simulation Results

The radiation transport tool used for the preliminary design simulations of the SCRαP integral benchmark experiment was the Los Alamos National Laboratory Monte Carlo N-Particle Code (MCNP®) version 6.1 [5]. MCNP® was used to determine the k_{eff} of different experimental configurations with increasing reflector thicknesses and material type. MCNP® was also used to generate nuclear data sensitivities to each energy-dependent, nuclide-reaction-specific cross-section data component for k_{eff}. For the preliminary design, simplified MCNP® models were adopted that only incorporated the BeRP Ball, stainless steel cladding, and pure copper/polyethylene spherical reflectors. The evaluated nuclear data library adopted for the simulations was ENDF7.1 [6].

The simulated KCODE results of each configuration and sensitivity for the Cu-63 and Cu-65 cross-sections are shown in Fig. 5. During the preliminary design, this plot showed that at around 4 inches, the average sensitivity to the Cu total cross section no longer increases with additional Cu thickness. In addition, other issues arise at around this thickness (difficulty in handling the hemishells, criticality safety concerns, etc); for these reasons, a maximum thickness of 4 inches was chosen for this experiment.

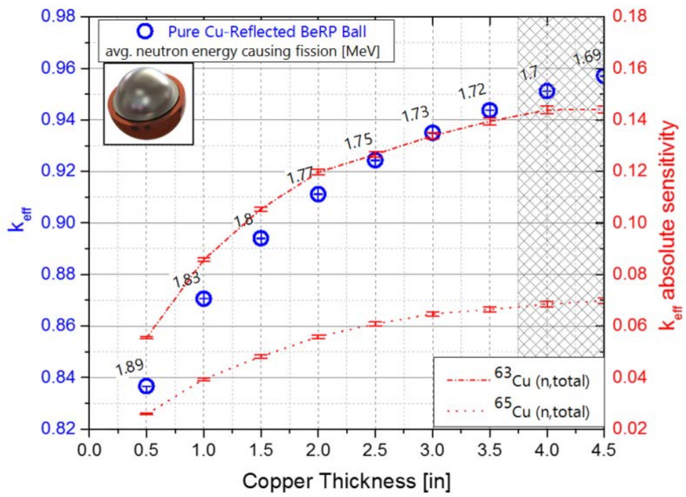

Fig. 5. MCNP® results for all Cu-reflected BeRP Ball base configurations highlighting the simulated k_{eff}, average neutron energy causing fission, and absolute copper total cross section sensitivity.

The k_{eff} absolute sensitivity for Cu-63 is shown in Fig. 6. A similar plot for Cu-65 will be shown at the meeting. These sensitivities have been compared to critical configurations in the ICSBEP handbook. It should be noted that there are a limited number of copper-reflected critical experiments in the handbook (8 experimental series with U fuel and 2 experimental series with Pu fuel). The maximum total Cu-63 sensitivity for the 16 subcritical configurations (0.143) is greater than the two Pu experimental series (0.126) but less than that for some of the U experimental series (0.200). In the intermediate energy regime, the maximum Cu-63 sensitivity for the 16 configurations (0.018) is greater than the two Pu experimental series by nearly an order of magnitude (0.002), but similarly less than that for some of the U experimental series (0.051). Similar results will be presented for Cu-65.

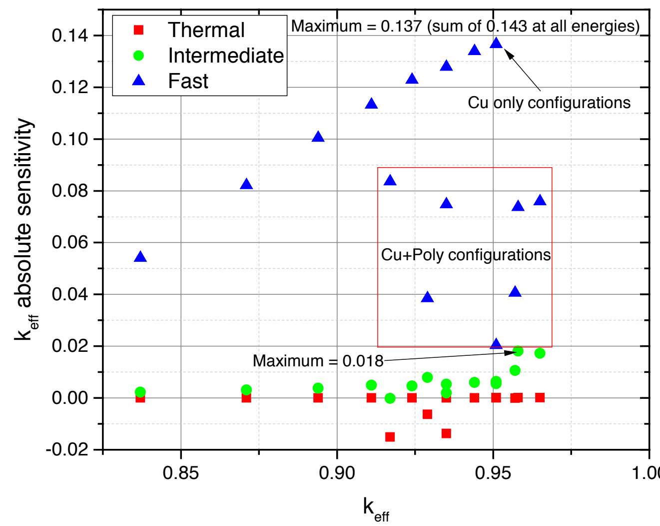

Fig. 6. k_{eff} sensitivity to Cu-63 as a function of k_{eff}.

The previous evaluated BeRP ball subcritical configurations (nickel and tungsten reflection) were used to predict some of the major experimental uncertainties that were be present for these measurements. A previous work shows that although simulations for subcritical experiments must be run in a different manner than critical experiments to allow for multiplicity analysis, criticality eigenvalue simulations can still be used to estimate experimental uncertainties for the primary subcritical benchmark parameters, allowing for tremendous savings in computational time (more than an order of magnitude on average) [7].

This method was used to estimate the experimental uncertainties for three benchmark parameters: detector singles count rate (R_1) i.e. the count rate in the detector system; the doubles count rate (R_2) i.e. the rate in the detector system in which two neutrons from the same fission chain are detected; and the leakage multiplication (M_L) i.e. the number of neutrons escaping a system per starter neutron. This was done for three different configurations; the results for one of these configurations (0.5 inch-thick HDPE surrounded by 3.5 inch-thick copper) is shown in Table I. It should be noted that the Cu mass was expected to be a minor uncertainty, which the table confirms.

Table I. Estimate of experimental uncertainties for Configuration 15 (0.5 inch-thick HDPE surrounded by 3.5 inch-thick copper).

Parameter	Experimental Uncertainty	Uncertainty
M_L	Pu radius ± 2 mils	0.18
	Pu isotopics ± 0.5%	0.19
	Cu thickness ± 0.3 cm	0.03
	Cu mass ± 0.5%	0.00006
R_1	Pu radius ± 2 mils	1024
	Pu isotopics ± 0.5%	1045
	Cu thickness ± 0.3 cm	141
	Cu mass ± 0.5%	0.34
R_2	Pu radius ± 2 mils	37450
	Pu isotopics ± 0.5%	41336
	Cu thickness ± 0.3 cm	5252
	Cu mass ± 0.5%	13.1

III. EXPERIMENT OVERVIEW

Seventeen different configurations were measured as shown in Table II. These included the 16 planned configurations and an additional configuration consisting of HDPE only. Additional information on these configurations is given in Table III; the simulations for the k_{eff} results in this table were performed during the experiment design with preliminary models. Fig. 7 shows configuration 7 during assembly. Fig. 8 shows the setup for the benchmark measurements. The two MC15 detector systems are connected together (for each measured file, a single file is created with 30 channels).

In order to determine the detector efficiency, Cf-252 source replace measurements were performed. These setup was identical to the benchmark configurations except a Cf-252 source was placed at the center of the assembly (instead of the Pu sphere) as shown in Fig. 9. An aluminum holder was made which places the source at the center of the inner-most hemishells for each configuration. The source strength of the Cf-252 source at the time of the measurements was 7.59e5 fissions/sec +/- 1.0%.

Table II. Hemishell layers which were present for each configuration. Orange represents Cu and light grey is used for HDPE. This pictorial color representation will be used in subsequent graph legends.

Configuration #	Layer number (each layer is 0.5 inches thick)							
	1	2	3	4	5	6	7	8
0								
1	Cu							
2	Cu	Cu						
3	Cu	Cu	Cu					
4	Cu	Cu	Cu	Cu				
5	Cu	Cu	HDPE	HDPE	HDPE	HDPE		
6	Cu	Cu	Cu	Cu	Cu			
7	HDPE	Cu	HDPE	Cu	HDPE	Cu	HDPE	Cu
8	Cu	HDPE	Cu	HDPE	Cu	HDPE	Cu	HDPE
9	Cu	Cu	Cu	Cu	Cu	Cu		
10	Cu	Cu	Cu	Cu	Cu	Cu	Cu	
11	Cu	Cu	Cu	Cu	Cu	Cu	Cu	Cu
12	HDPE	HDPE	HDPE	Cu	Cu	Cu	Cu	
13	HDPE	HDPE	Cu	Cu	Cu	Cu	Cu	
14	HDPE	Cu	Cu	Cu	Cu	Cu	Cu	
15	HDPE	Cu	Cu	Cu	Cu	Cu	Cu	Cu
16	HDPE	HDPE	HDPE	HDPE	HDPE	HDPE	HDPE	HDPE

Table III. Additional information on each configuration: total HDPE and Cu thickness and simulated k_{eff} values.

Configuration #	Thickness (inches)			Simulated k_{eff}	
	HDPE	Cu	HDPE+Cu	LANL	IRSN
0	0.0	0.0	0.0	0.774	0.777
1	0.0	0.5	0.5	0.837	0.829
2	0.0	1.0	1.0	0.871	0.862
3	0.0	1.5	1.5	0.894	0.884
4	0.0	2.0	2.0	0.911	0.900
5	2.0	1.0	3.0	0.917	0.907
6	0.0	2.5	2.5	0.924	0.914
7	2.0	2.0	4.0	0.929	0.921
8	2.0	2.0	4.0	0.935	0.919
9	0.0	3.0	3.0	0.935	0.923
10	0.0	3.5	3.5	0.944	0.933
11	0.0	4.0	4.0	0.951	0.939
12	1.5	2.0	3.5	0.951	0.939
13	1.0	2.5	3.5	0.957	0.943
14	0.5	3.0	3.5	0.958	0.942
15	0.5	3.5	4.0	0.965	0.948
16	4.0	0.0	4.0	-	-

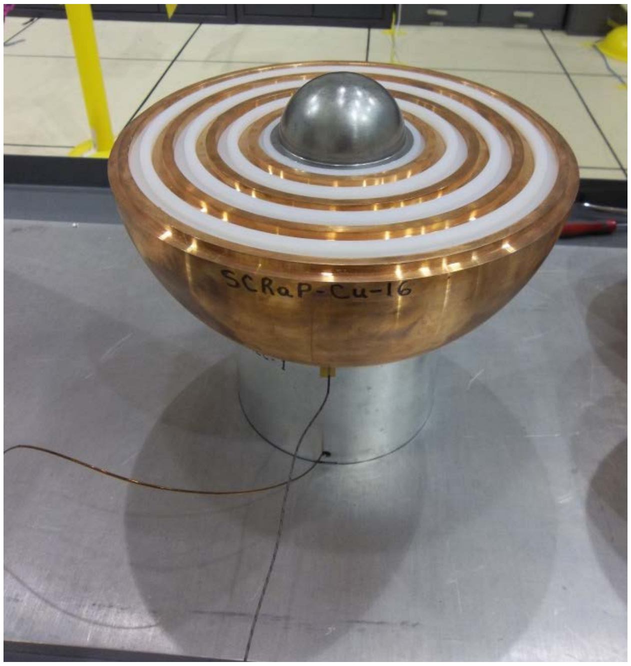

Fig. 7. Configuration 7 during assembly.

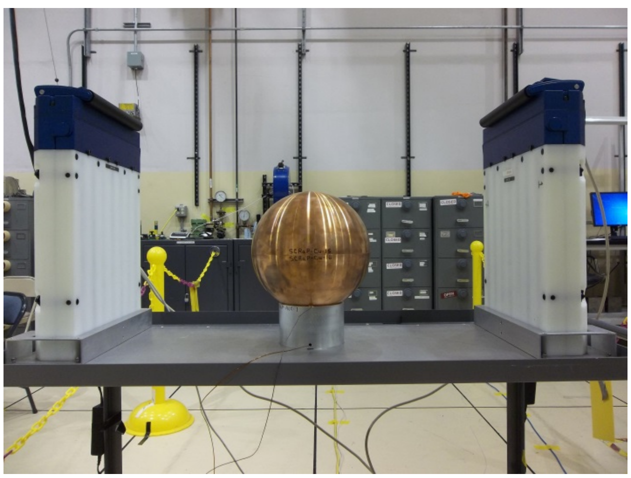
Fig. 8. Experimental setup for configuration 15.


Fig. 9: Configuration 8 during assembly for Cf-252 measurements.

IV. PRELIMINARY RESULTS

As previously mentioned, the MC15 detector system records list-mode data. This is a list of every recorded neutron event (with a timing resolution of 128 nsec). These type of data can be analyzed using a variety of neutron multiplicity methods. Most of these noise analysis methods involve looking at time gates (anywhere from the low micro-second to milli-second range) and observing some quantity (such as the number of neutrons in each time gate or the number of time differences in each time gate). Many of these analysis methods have been used since the 1960s and are described in other works [8-9]. All results presented in this paper are preliminary; the final results will be published in the ICSBEP handbook.

One basic way to look at list-mode data is to create Feynman histograms [10]. In order to construct a Feynman histogram, one simply goes through a measured file with a fixed gate-width time (τ) and determines the number of recorded events in each gate. The number of gates which recorded "n" events is referred to as C_n. The total counting time is equal to:

$$Time = \tau \sum C_n \tag{1}$$

It should be noted that there are multiple ways that one can bin data when constructing Feynman histograms; for this work the basic sequential method was used [11].

Fig. 10 shows Feynman histograms for a subset of the measured configurations (configurations 6-11). As the multiplication of a system increases, the observed histogram deviates more from a Poisson distribution (solid lines). It can easily be seen that for the pure copper systems, both the Poisson and Feynman histograms are moving to the right (they have more neutrons per gate).

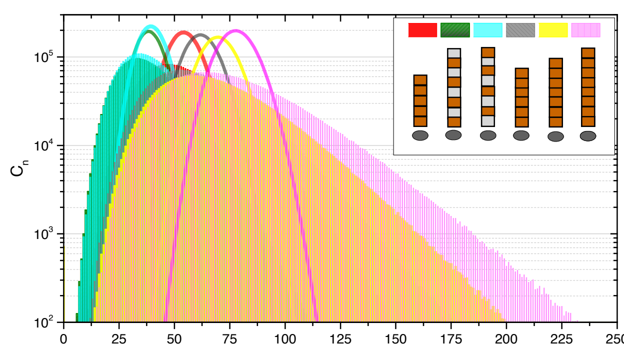

Fig. 10. Feynman histograms for configurations 6-11 with a gate-width of 1024 micro-sec.

After obtaining Feynman histograms, one can calculate the system multiplication using a system of equations. For this work, the Hage-Cifarelli formalism was used [12].

After preparing Feynman histograms, reduced factorial moments are calculated using the equation:

$$m_r(\tau) = \frac{\sum_{n=0}^{\infty} n(n-1)\cdots(n-r+1)\,p_n(\tau)}{r!} \tag{2}$$

where $p_n(\tau)$ is the normalized fraction of gates that recorded n events:

$$p_n(\tau) = \frac{C_n(\tau)}{\sum_{n=0}^{\infty} C_n(\tau)} \tag{3}$$

Note that the count rate (as called the singles count rate or R_1) can be calculated using the equation:

$$R_1(\tau) = \frac{m_1(\tau)}{\tau} \tag{4}$$

Fig. 11 shows the count rate of the benchmark measurements (with the BeRP ball) and the detector efficiency (measured using Cf-252 replacement measurements). The efficiency is simply defined as the ratio of the count rate (R_1) of the replacement measurements divided by the reported neutron emission rate:

$$\varepsilon = \frac{R_1(\tau)}{F_S \overline{\nu}_{S(1)}} \tag{5}$$

where F_S is the reported spontaneous fission emission rate of the Cf-252 source, $\overline{\nu}_{S(1)}$ is the average number of neutrons emitted per Cf-252 fission, and R_1 is the detector count rate for the Cf-252 measurement (not the Pu measurement). These two parameters are plotted together to show that the reason that the count rate goes down significantly for the configurations with HDPE is due to the decrease in efficiency (which is caused by neutron absorption primarily in the hydrogen).

It should also be pointed out that for the pure copper cases (such as configurations 0-4 or 9-11) the slope of the count rate is much sharper than the increase in detector efficiency. This is because the detector count rate is proportional to both efficiency and system multiplication.

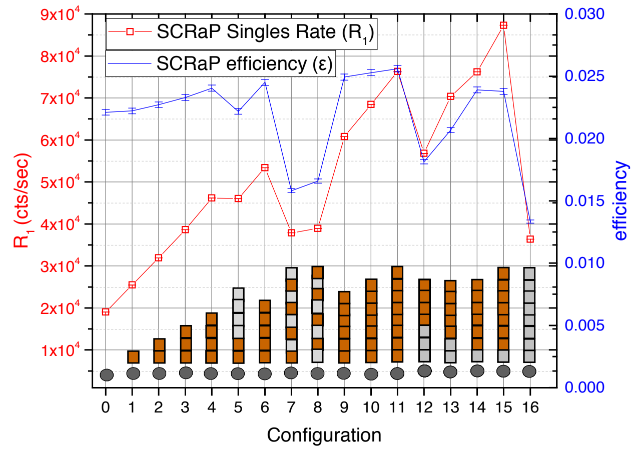

Fig. 11. Count rate (R_1) and detector efficiency (ε) for SCRαP configurations.

The excess variance (deviation of a Feynman histogram from a Poisson distribution) is proportional to Y_2, given by:

$$Y_2(\tau) = \frac{m_2(\tau) - \frac{1}{2}\left[m_1(\tau)\right]^2}{\tau} \tag{6}$$

This parameter is shown for all of the Cu-only configurations in Fig. 12. As expected, the amount of excess variance increases with Cu thickness (due to an increase in the system multiplication).

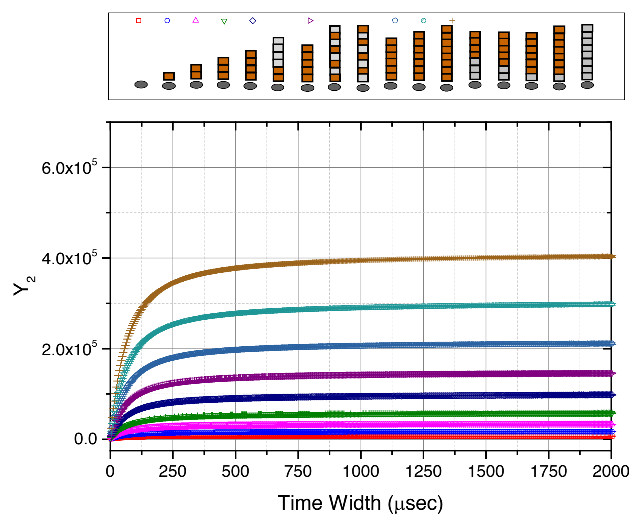

Fig. 12. Y_2 for Cu-reflected configurations.

A fit can be performed on the Y_2 curves to calculate the neutron lifetime/slowing-down time (1/λ) using the equation:

$$\omega_2(\lambda,\tau) = 1 - \frac{1-e^{-\lambda\tau}}{\lambda\tau} \tag{7}$$

Note that the MC15 detector system has a slowing-down time of around 35 micro-seconds (this is the time for neutrons to slow down in the HDPE present in the detector system prior to absorption in the He-3). Therefore the true lifetime is not being measured for fast systems. For this experiment, the lifetime/slowing-down time is shown in Fig. 13. It can be seen that for the configurations with Cu only, the result is approximately 35 micro-seconds as expected, but it is significantly larger for the configurations that include HDPE hemishells.

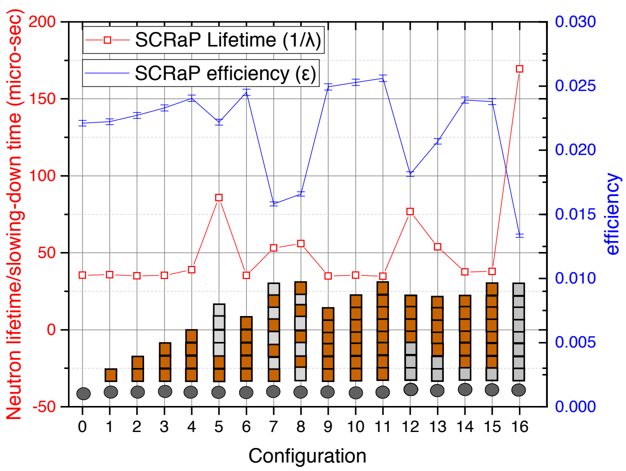

Fig. 13. Neutron lifetime/slowing-down time.

After determining the lifetime/slowing-down time, one can calculate the doubles counting rate (R_2) using Eq 8. This is the rate at which two neutrons from a single fission chain is detected. Fig. 14 shows the doubles counting rate for all of the configurations.

$$R_2(\tau) = \frac{Y_2(\tau)}{\omega_2(\lambda,\tau)} \tag{8}$$

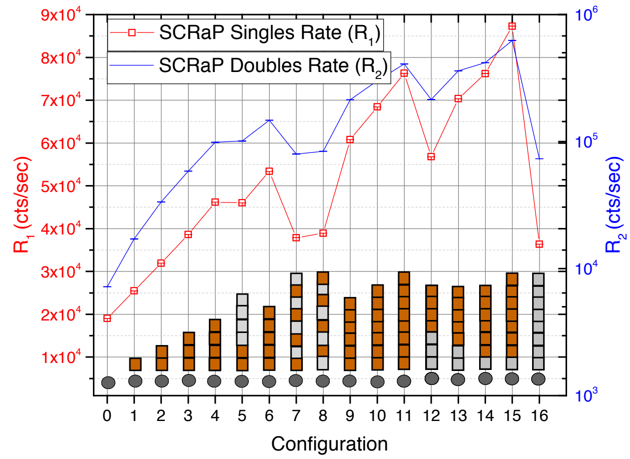

Fig. 14. Doubles counting rate (R_2).

If one assumes that there is no (α,n) neutron emission (a valid assumption for a fast metal system), then the system leakage multiplication, M_L, can be calculated using:

$$\begin{aligned} M_L &= \frac{-C_2 + C_4}{2C_1} \\ &\textit{with} \\ C_1 &= \frac{\bar{\nu}_{S(1)}\bar{\nu}_{I(2)}}{\bar{\nu}_{I(1)} - 1} \\ C_2 &= \bar{\nu}_{S(2)} - \frac{\bar{\nu}_{S(1)}\bar{\nu}_{I(2)}}{\bar{\nu}_{I(1)} - 1} \\ C_3 &= -\frac{R_2(\tau)\bar{\nu}_{S(1)}}{R_1(\tau)\varepsilon} \\ C_4 &= \sqrt{C_2^2 - 4C_1C_3} \end{aligned} \tag{9}$$

The terms $\bar{\nu}_{S(1)}$, $\bar{\nu}_{S(2)}$, $\bar{\nu}_{I(1)}$, and $\bar{\nu}_{I(2)}$ are the first and second factorial moments of the P_ν distribution where S refers to the isotope producing spontaneous fission neutrons and I refers to the isotope undergoing induced fission.

The leakage multiplication is shown for all of the configurations in Fig. 15. Appendix L of Reference 3 provides the equations that relate M_L to the multiplication factor (k_{eff}).

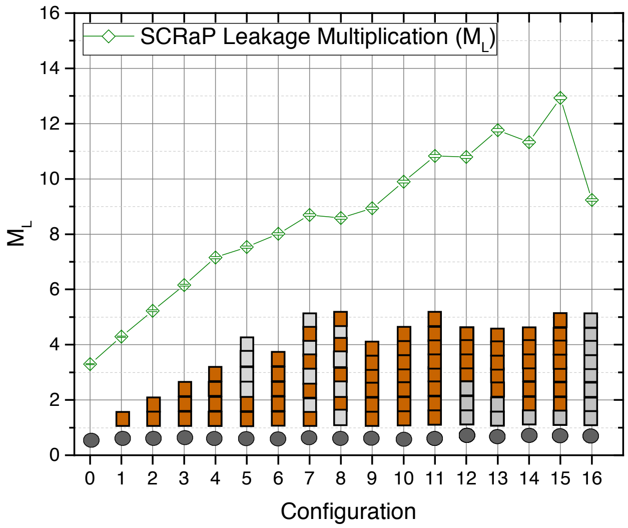

Fig. 15. Inferred leakage multiplication (M_L).

During the experiment design, the k_{eff} of each configuration was simulated using MCNP6 and MORET [13]. The leakage multiplication was calculated from the multiplication factor using basic equations with assumptions for the delayed neutron fraction. The MCNP models were simplified models (perfect spherical reflectors with no materials present outside the reflectors) but the MORET models had additional details (MC15 detectors, detailed reflector hemishells, etc.). It can be seen in Fig. 16 that the MORET results compare much better to the measured results than the MCNP simulations. In the future this will be investigated in detail. The (C/E)/E between the simulated IRSN results and the measured results are shown in Fig. 17.

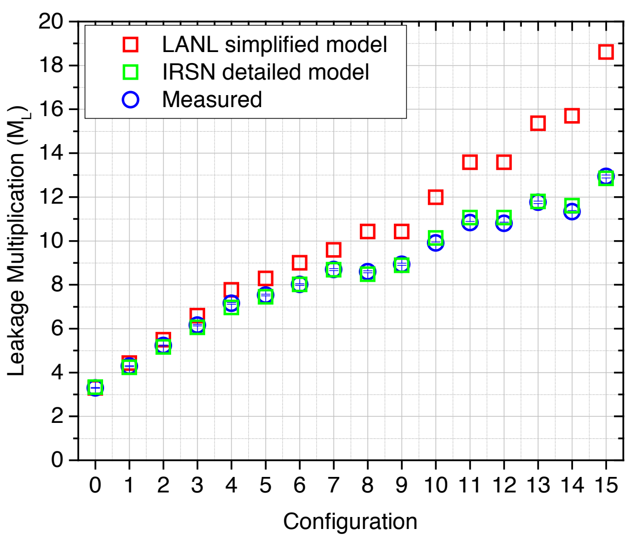

Fig. 16. Comparison of measured leakage multiplication to simulations in MCNP (performed by LANL) and MORET (performed by IRSN).

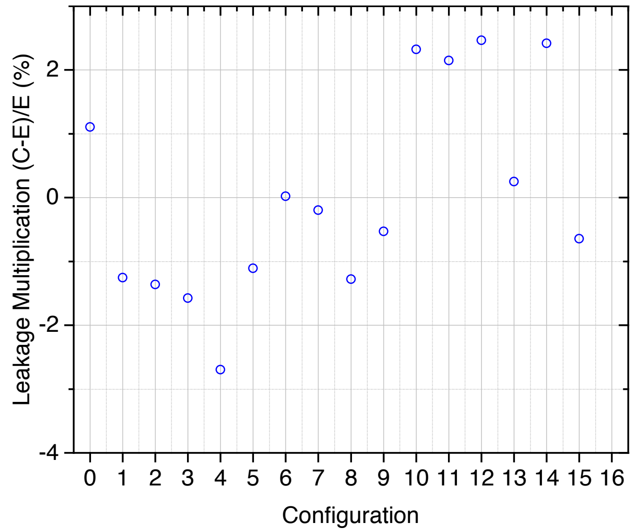

Fig. 17. (C-E)/E comparing IRSN simulated data to measured data.

V. FUTURE WORK

This experiment will be evaluated and documented in an upcoming version of the ICSBEP handbook. This work will help assess the potential impact of this integral measurement as it relates to international efforts to continuously improve current libraries (ENDF, JEFF, JENDL etc…) that still tend to over/under-estimate the measured results of integral experiments, sometimes significantly [14]. Deficiencies in underlying nuclear data quantities such as nubar have been shown to have an effect on inferred values from subcritical measurements as well [15-17]. This experiment and subsequent computational validation will help identify such deficiencies. It will also help validate new nuclear data evaluations, including one for Cu that was recently performed in the resolved region up to 100 MeV for Cu-65 and Cu-63 [18] which is expected to improve Cu-related benchmark simulation performance.

ACKNOWLEDGEMENTS

This work was supported by the Nuclear Criticality Safety Program, funded and managed by the National Nuclear Security Administration for the Department of Energy. This experiment is a joint collaboration with the French nuclear safety authority IRSN.

REFERENCES

[1] J. HUTCHINSON, D. LOAIZA, "Plutonium Sphere Reflected by Beryllium," International Handbook of Evaluated Criticality Safety Benchmark Experiments, NEA/NSC/DOC/(95)03/I, PU-MET-FAST-038.

[2] B. RICHARD, J. HUTCHINSON, “Nickel Reflected Plutonium Metal Sphere Subcritical Measurements,” International Handbook of Evaluated Criticality Safety Benchmark Experiments, NEA/NSC/DOC/(95)03/I, FUND-NCERC-PU-HE3-MULT-001 (2014).

[3] B. RICHARD, et. al., “Tungsten-Reflected Plutonium-Metal-Sphere Subcritical Measurements,” International Handbook of Evaluated Criticality Safety Benchmark Experiments, NEA/NSC/DOC/(95)03/I, FUND-NCERC-PU-HE3-MULT-002.

[4] T. CUTLER, et. al., “IER-422: Subcritical Copper-Reflected alpha-phase Plutonium (SCRαP) Integral Experiment,” Los Alamos Report LA-UR-16-26285, 2016.

[5] J.T. GOORLEY, et. al., “Initial MCNP®6 Release Overview,” Nuclear Technology, vol. 180, pp. 298-315 (2012).

[6] M. CHADWICK et al. “ENDF/B-VII.1 Nucl. Data for Sci. and Technology: cross sections, covariances, fission product yields and decay data,” Nuclear Data Sheets, vol. 112, no. 12, pp. 2887-2996 (2011).

[7] J. HUTCHINSON, T. CUTLER “Use of Criticality Eigenvalue Simulations for Subcritical Benchmark Evaluations” Transactions of the ANS Winter Meeting, Las Vegas, US (2016) – Accepted Paper (In Press).

[8] R. UHRIG, “Random Noise Techniques in Nuclear Reactor Systems,” John Wiley & Sons Inc, 1970.

[9] J. HUTCHINSON, et. al., “Subcritical Multiplication Experiments & Simulations: Overview and Recent Advances,” ANS Advances in Nonproliferation Technology and Policy Conference, Santa Fe NM, September 2016.

[10] A. ROBBA, E. DOWDY, H. ATWATER, “Neutron Multiplication Measurements Using Moments of the Neutron Counting Distribution,” Nuc. Instr. and Meth., 215, 473-479 (1983).

[11] T. CUTLER, M. SMITH-NELSON, J. HUTCHINSON, “Deciphering the Binning Method Uncertainty in Neutron Multiplicity Measurements,” ANS Winter Conference, Anaheim CA, November 2014.

[12] D. CIFARELLI, W. HAGE, “Models for a Three-Parameter Analysis of Neutron Signal Correlation Measurements for Fissile Material Assay,” Nuc. Instr. Meth. A251, 550-563, 1986.

[13] B. COCHET, et. al., “Capabilities overview of the MORET 5 Monte Carlo code,” Joint International Conference on Supercomputing in Nuclear Applications and Monte Carlo 2013 (SNA + MC 2013), La Cité des Sciences et de l'Industrie, Paris, France, October 27-31, 2013.

[14] S. C. VAN DER MARK, “Benchmarking ENDF/B-VII.1, JENDL-4.0 and JEFF-3.1.1 with MCNP®6,” Nuclear Data Sheets, vol. 113, pp. 2935-3005 (2012).

[15] E. MILLER, J. MATTINGLY et al. “Simulations of Neutron Multiplicity Measurements with MCNP®-PoliMi,” Tech. Rep. SAND2010-6830, Sandia National Laboratory (2010)

[16] J. HUTCHINSON, A. SOOD et al. “Comparison of HEU Measurements Using Measured and Simulated Data” Trans. Amer. Nucl. Soc., 106, 487-489 (2013)

[17] S. BOLDIN, C. SOLOMON “Simulations of Multiplicity Distributions with Perturbations to Nuclear Data” Trans. Amer. Nucl. Soc., 109, 251-254 (2013)

[18] P. PERESLAVTSEVA et al. “New Evaluation of n+63,65Cu Nuclear Cross Section Data up to 200 MeV Neutron Energy” Nuclear Data Sheets, vol. 118, pp. 1-636 (2014).

COMPARISON OF METHODS FOR DETERMINING MULTIPLICATION IN SUBCRITICAL CONFIGURATIONS OF A PLUTONIUM SYSTEM

Joetta Goda[1], Theresa Cutler[1], Travis Grove[1], Jesson Hutchinson[1], George McKenzie[1], Alex McSpaden[1], Mark Nelson[1], and Rene Sanchez[1]

[1]Los Alamos National Laboratory
PO Box 1663, MS B228
Los Alamos, NM 87545

jgoda@lanl.gov

ABSTRACT

In the course of building a new, copper-reflected, lead-moderated, plutonium critical system, the unique opportunity occurred to measure neutron multiplication at twelve subcritical configurations. In addition to the traditional 1/M (or inverse multiplication) method, a Neutron Multiplicity ^{3}He Array Detector (NoMAD) detector system was deployed to infer leakage multiplication through the Feynman Variance-to-Mean Reduction method. The results of both methods are shown and compared to MCNP® k-effective calculations.

KEYWORDS: neutron multiplication, critical assembly, lead, intermediate energy

1. INTRODUCTION

This paper will describe measurements of neutron multiplication made on various configurations of copper-reflected plutonium and lead system. The critical experiment was constructed for the purpose of measuring the reactivity worth of lead voids in the system and to provide a configuration that could be used as an integral experiment benchmark for lead cross sections. In the course of assembling the critical configuration, a dozen subcritical configurations were measured with Startup Counters (^{3}He neutron detectors used for the operation of critical assemblies at startup and low power) as well as the Neutron Multiplicity ^{3}He Array Detector (NoMAD) detector system in order to determine subcritical neutron multiplication. These measurements are compared against each other and with MCNP®[1] k-effective (k_{eff}) calculations.

[1] MCNP® and Monte Carlo N-Particle® are registered trademarks owned by Los Alamos National Security, LLC, manager and operator of Los Alamos National Laboratory. Any third party use of such registered marks should be properly attributed to Los Alamos National Security, LLC, including the use of the designation as appropriate. For the purposes of visual clarity, the registered trademark symbol is assumed for all references to MCNP within the remainder of this paper.

2. DESCRIPTION OF CRITICAL SYSTEM

The critical system was a copper-reflected, lead-moderated, plutonium system constructed on the Comet critical assembly [1-3] at the National Criticality Experiments Research Center (NCERC) [4]. The fuel consisted of stainless steel clad plutonium Zero Power Physics Reactor (ZPPR) plates [5]. The ZPPR plates were loaded vertically into aluminum boxes with lead plates sandwiched by thin Al plates (to minimize contact between bare lead and fuel). A "box unit" for this core consisted of two ZPPR plates, an Al/Pb/Al sandwich, two ZPPR plates, an Al/Pb/Al sandwich, and two ZPPR plates as seen in Fig.1. The lid for the box can be seen in the background.

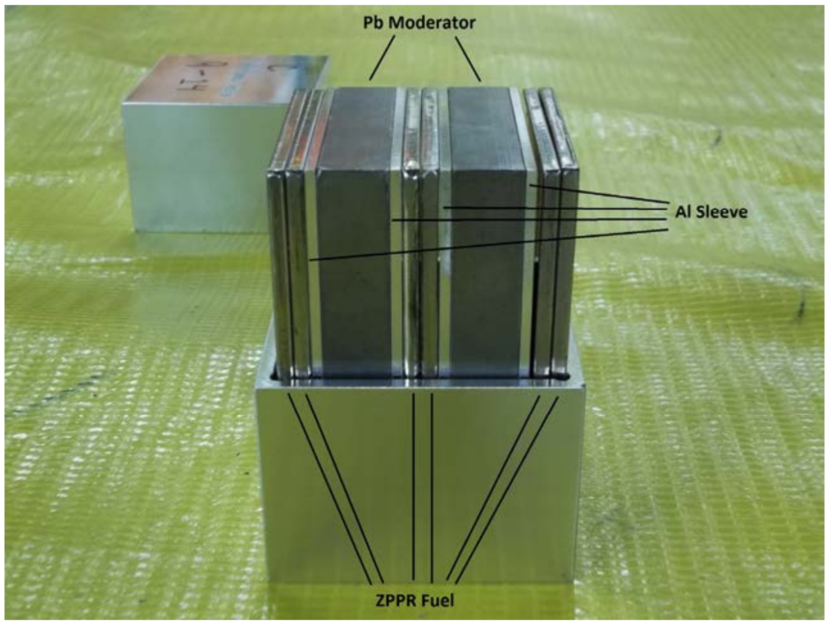

Figure 1. A box unit containing ZPPR plates and Pb with Al sleeves.

To achieve a critical system, multiple box units were assembled into stacked planar arrays surrounded by a thick copper reflector. Preliminary modeling predicted that three layers of a six-by-six array would be needed but that several array locations would contain no fuel. In place of fuel, these locations contained copper reflector blocks the same size as one of the Al boxes described in Fig. 1.

Three planar arrays were loaded on the Comet critical assembly. One layer was loaded on the stationary upper platform and two layers were loaded on the moveable, lower platform as shown in Fig. 2. The critical assembly was then operated by raising the lower level up into the outer reflector and into contact with the stationary upper layer.

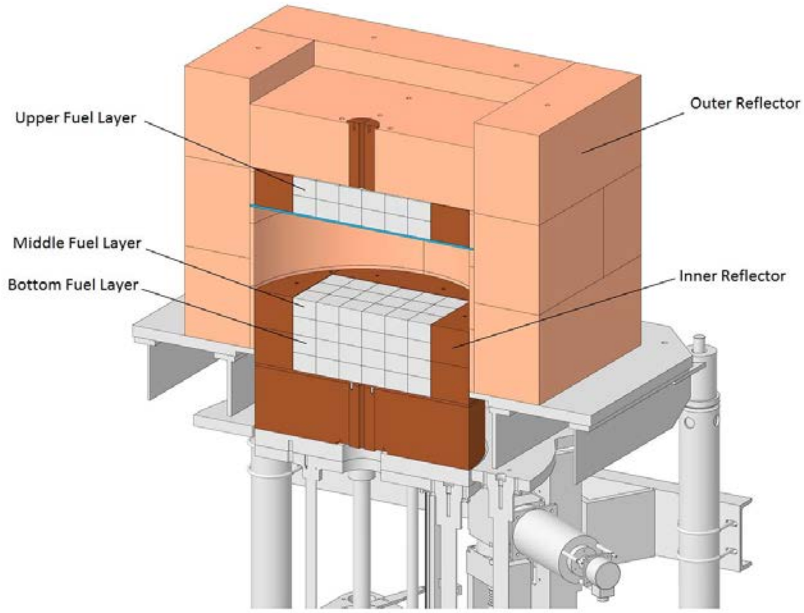

Figure 2. Cross Section of the Three-Layer Array.

3. APPROACH TO CRITICAL

As this was the first time the configuration was assembled, the final critical configuration was unknown. In such cases, the One-over-M approach to critical method is used to determine how the system is loaded. The One-over-M approach to critical method linearly interpolates the inverse of two relative multiplications to provide an estimate of the critical configuration. This approach works for any incremental approach i.e. separation of two masses, mass, number of units, or amount of reflector. To be correctly applied, the two initial subcritical configurations must be used as a starting point.

The two starting configurations used were a two-by-two array (four units) and a three-by-three array (nine units) in a single layer as shown in Fig. 3. Fig. 3 only shows the fuel configuration and does not show the copper reflector. The first configuration was loaded and raised into the reflector. A neutron count was taken with the four startup neutron detectors. The startup detectors are four ^{3}He tubes with 1" thick polyethylene sleeves. Counts were taken for 10 seconds and the sum of four detectors' counts was used. The initial count rate was assigned a relative multiplication of one. The configuration was lowered and the additional units were added to form the second configuration.

The second configuration was raised into the same position in the reflector and the next count rate taken. This count rate was compared to the initial rate and the configuration assigned a multiplication relative (M_{rel}) to the initial configuration. For the 1/M technique to be valid, it is essential that the ^{3}He startup neutron detectors are not moved between configurations as this will change the geometric efficiency of the detection system.

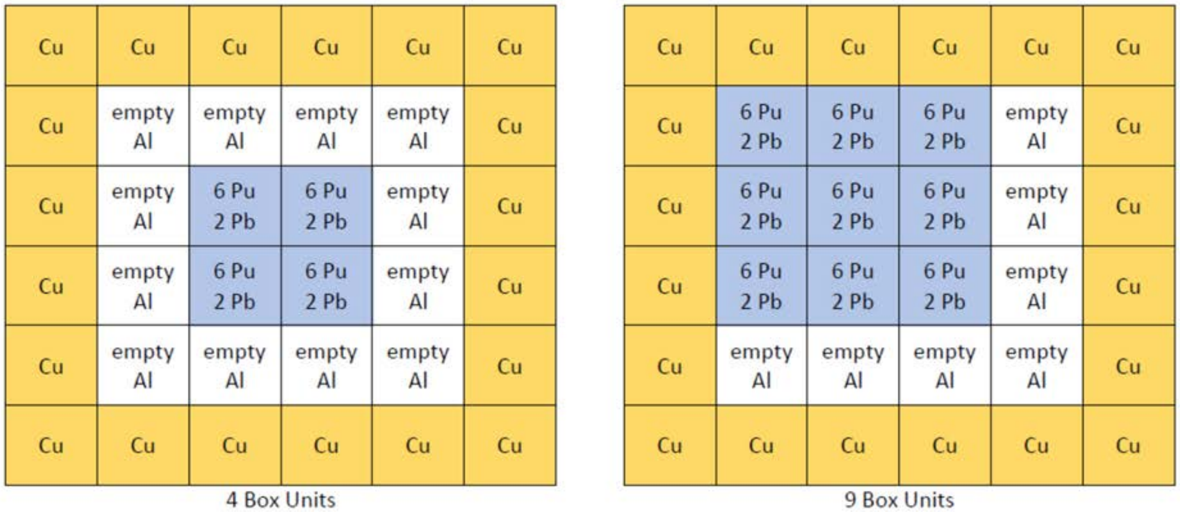

Figure 3. Initial two configurations of 4 and 9 units, respectively. Fuel positions only; Cu reflector not shown.

For low intrinsic neutron strength material, the observed reciprocal multiplication for a given incremental increase in reactivity, $1/M_i$, is determined as follows:

$$\frac{1}{M_i} = \frac{CR_0}{CR_i}, \tag{1}$$

For high intrinsic neutron strength materials, such as the Pu used in this assembly, the observed counts must be corrected to account for the added neutron source in each configuration. Reciprocal multiplication for a given incremental increase in reactivity ($1/M_i$) in this case is determined as follows:

$$\frac{1}{M_i} = \frac{CR_0}{CR_i}\frac{m_i}{m_0}, \tag{2}$$

where M_i is the Multiplication after addition i , CR_0 is the Initial count rate, CR_i is the Count rate after reactivity change i, m_i is the Total mass after addition i, and m_0 is the Initial material mass. Total counts are used in place of the count rate as the length of counting time was held constant during the One-over-M approach to critical process.

The change to intrinsic neutron population is proportional to the mass of ^{240}Pu added, so it is common practice to compare relative multiplications on a per unit mass ^{240}Pu basis. Since the ZPPR plates are essentially identical in mass of ^{240}Pu, the measured neutron count was divided by the number of plates instead of by the mass. It would have been possible to use the total plutonium mass, the ^{240}Pu mass, or the number of box units instead for the 1/M calculations.

After the initial two configurations were measured, their data was used to predict the number of units required for a critical configuration. Additions to the core were then made within the procedural limits based on those predictions. The complete sequence of configurations is shown in Table I which appears in Section 6 with results from other sections included.

Note that in a few cases there are two entries for the same number of units. Those occurred where a change was made to the arrangement of units without changing the total number of units. For example, at the point where 40 units were loaded, they were shifted so that the upper layer was filled. Because the fuel was moved from the middle layer of the core to the less reactive upper surface of the core, the multiplication decreased (and inverse multiplication increased). This adjustment was made because changes to the upper layer required removing the upper reflector with a forklift so completing the upper layer minimized the time required for successive changes.

Additions to the core proceeded based on predictions until a critical configuration was achieved at 79 units as shown in Fig. 4. The critical configuration (k_{eff} =1 by definition) can be used to show any bias in the MCNP calculations. Further adjustments were later made to attain a more symmetric critical configuration with no empty box in the middle layer but those configurations are outside the scope of this paper.

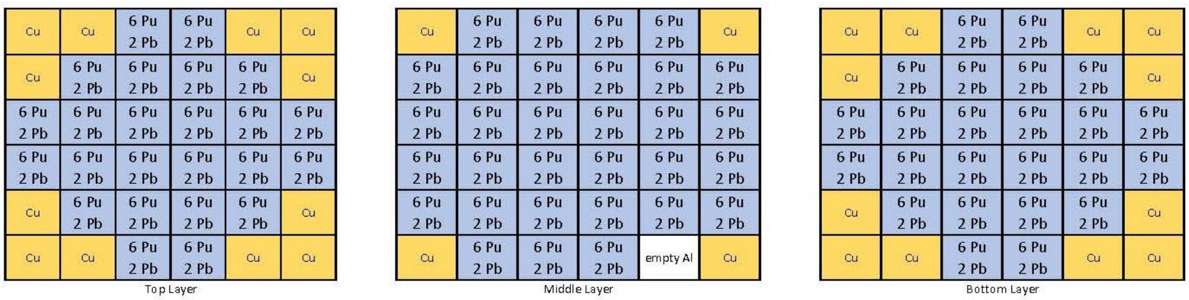

Figure 4. Critical Configuration of 79 box units.

4. FEYNMAN VARIANCE-TO-MEAN

To perform an alternate type of measurement to determine the multiplication of the various configurations, a Neutron Multiplicity ^{3}He Array Detector (NoMAD) detector system was used. The NoMAD consists of 15 ^{3}He tubes embedded in HDPE. The detector system records list-mode data (a list of times for every recorded neutron detection event to a resolution of 100 nsec). This data can be analyzed using a variety of neutron multiplicity methods. Most of these noise analysis methods involve dividing data into time gates and observing some quantity (such as the number of neutrons in each time gate or the number of time differences in each time gate). Many of these analysis methods have been used since the 1960s and are described in other works [6-7]. For this work, the Hage-Cifarelli formalism [8] of the Feynman Variance-to-Mean method [9] was used. This approach involves measuring singles (R_1) and doubles (R_2) counting rates in a detector system and relates these parameters to leakage multiplication (M_L), spontaneous fission rate (F_S), neutron emission from (α,n) reactions (S_α), and the detector efficiency (ε). This leaves a system of two equations with four unknowns. The LANL software Momentum was used to process the NoMAD data and determine leakage multiplication [10].

For this work, the first configuration (4 box units) was used to determine the detector efficiency; this was done by assuming that leakage multiplication was 1 and (α,n) emission was 0 (a valid assumption for the Pu metal plates). This efficiency was used for all subsequent configurations, which, while not a completely valid assumption, should still result in acceptable uncertainty in the results given the geometry and materials present for these configurations. For the other configurations, leakage multiplication and the spontaneous fission rate were determined using the measured singles and doubles count rates. Previous works describe the complete approach used for the analysis of the measured data [11-12].

Leakage multiplication (M_L) is defined as the total number of neutrons that escape the system divided by the number of starting neutrons in the same time period. Total multiplication, denoted as M_T, is defined as the total number of neutrons in the system divided by the number of starting neutrons over the same time period. One can solve for total multiplication using the Serber equation [13]:

$$M_T = \frac{M_L \bar{\nu} - 1 - \alpha}{\bar{\nu} - 1 - \alpha} \tag{3}$$

where $\bar{\nu}$ is the average number of neutrons created per fission, and α is the capture cross-section divided by the fission cross-section of the fissile material. For this work, α was assumed to be 0 and $\bar{\nu}$ was assumed to be 2.88 [14]. Both total and leakage multiplication are types of absolute multiplication (they are not relative to the other configurations and do not require any information about other configurations). For comparison purposes, the singles count rate (R_1) in the NoMAD detector was also used to determine a relative multiplication using the inverse of Eq. 2.

The NoMAD detector was placed on the upper platform of Comet with the center of the detector at 9.5 inches from the outer copper reflector as shown in Fig. 5 (with the exception of the 32 unit case the detector was mistakenly placed at a distance of 12 inches). The distance from the center of the assembly to the detector is approximately 68 cm and the distance from the edge of nearest ZPPR plates to the detector is approximately 52 cm. Counts were taken for five minutes on each fully closed configuration.

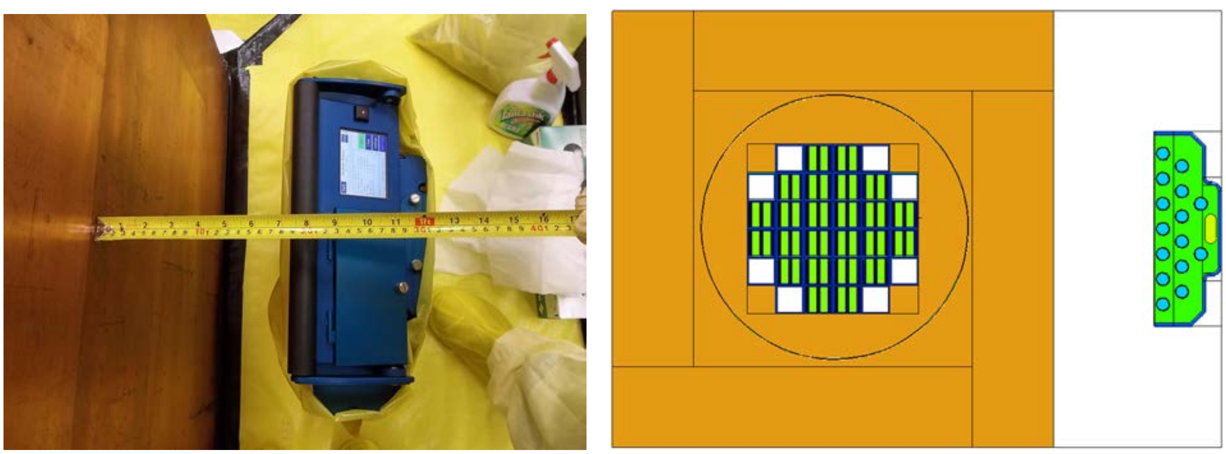

Figure 5. Photo and MNCP Plot of Placement of NoMAD Detector Next to Outer Reflector.

5. MCNP CALCULATION OF K-EFFECTIVE

In order to calculate k_{eff} for each of the fuel loading configurations, MCNP input files were created that include the KCODE criticality source card. These simulations were performed using MCNP6 version 1.0 [15], utilizing ENDF/B-VII.1 cross sections, and a separate file was run to match each experimental case. Six thousand cycles of ten thousand neutrons each were performed to compute k_{eff}. Vertical cross sections of the model showing the orientation of the copper reflectors, fuel units, and other components can be found in Fig. 7. Fig. 8, which shows a horizontal cross section of a filled lower layer of fuel units and the reflectors around it.

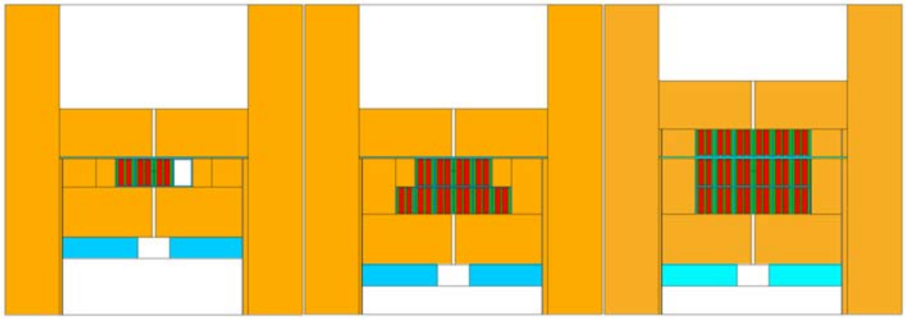

Figure 7: Vertical cross sections of MCNP models for one layer, two layers, and three layers. From left to right these images are from the 9 unit, 40 unit, and 80 unit cases respectively.

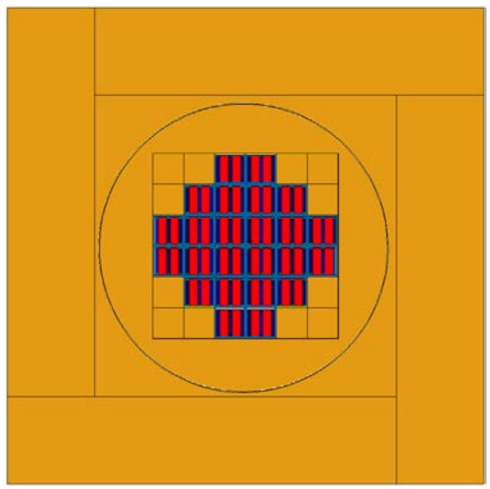

Figure 8: A horizontal cross section of the lower layer of the 78 unit configuration showing the fuel units and the surrounding reflectors.

When these simulations were performed, MCNP reported the final value of k_{eff} along with a standard deviation. These values are included in Table I. A general trend is that the simulated k_{eff} and therefore total multiplication values are much higher than those found in the experiment. For the 79 unit case which was critical as constructed, MCNP calculated a k_{eff} of 1.01241. It was not surprising that the MCNP calculation over-predicted the reactivity of the system and is probably due in part to the distribution of small spaces throughout the experiment as constructed that are not modeled. Efforts to get exact agreement may be performed as part of future critical experiment benchmark development. For the purpose of this paper, the difference between the calculated and experimental k_{eff} of 1, for the critical configuration was subtracted from all k_{eff} values. The k_{eff} was then converted to M_T using Eq. 4. Because all experimental values measure leakage multiplication, the calculated M_T is then converted to M_L using Eq. 3.

$$M_T = \frac{1}{1-k_{eff}} \tag{4}$$

6. COMPARISON OF METHODS TO CALCULATION

The startup counter data used for the One-over-M approach to critical is shown in Table I. As mentioned earlier, there are multiple arrangements of the same amount of fuel for the 9, 32 and 40 box unit cases. Of course, different multiplications are possible for the same amount of material depending on the geometry. In addition, the results from the Momentum calculation of M_L are included. The technique described in Section 4 effectively normalizes the results to a relative leakage multiplication of one at the starting configuration of four units. The last column includes the results of the MCNP calculation of k_{eff}.

Table I. Approach to Critical: Startup Counter Data, Inverse Relative Multiplication and Calculated k_{eff}.

# Box Units	# Plates	Sum of Counts	Sum/# Plates	Relative M_L	$1/M_{rel}$	Predicted Critical	NoMAD M_L	MCNP k_{eff}
4	24	2669	111.2	1.00	1.00	N/A	1.000	0.32205
9	54	7589	140.5	1.26	0.79	28.0	1.072	0.44938
9	54	7683	142.3	1.28	0.78	26.9	1.000	0.44938
12	72	10413	144.6	1.30	0.77	193.8	1.117	0.49789
16	96	14922	155.4	1.40	0.72	69.5	1.207	0.55833
24	144	25976	180.4	1.62	0.62	73.8	1.372	0.62371
32	192	43161	224.8	2.02	0.49	64.5	1.883	0.69789
32	192	42645	222.1	2.00	0.50	66.6	1.873	0.69789
40	240	74611	310.9	2.80	0.36	60.0	2.481	0.80091
40	240	68131	283.9	2.55	0.39	68.8	2.226	0.7696
49	294	100998	343.5	3.09	0.32	91.8	2.651	0.80899
64	384	232496	605.5	5.44	0.18	83.7	4.589	0.90614
72	432	605057	1400.6	12.59	0.08	78.1	10.276	0.9671
76	456	1533770	3363.5	30.25	0.03	78.9	20.524	0.99358
78	468	5471790	11691.9	105.13	0.01	78.8	19.935	1.00687

Fig. 9 shows a plot of the measured multiplication results. The NoMAD and Startup relative multiplication values agree fairly well for all of the measured configurations as might be expected from the usage of the same basic technique. The NoMAD singles rate sums the output from 15 3He tubes and the startup counter data sums four similar 3He detectors

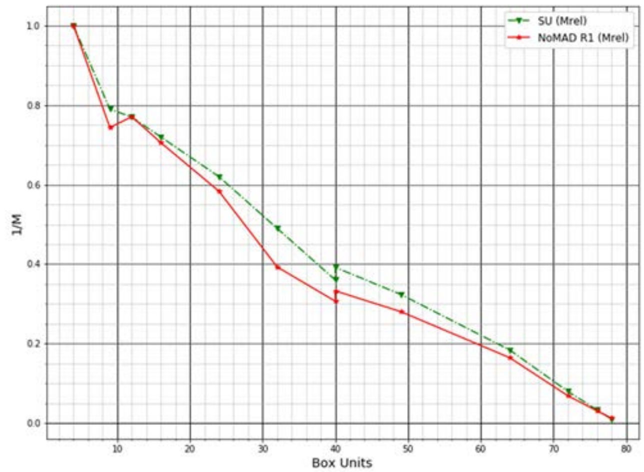

Figure 9: Plot of Inverse Multiplication

For comparison with the inferred leakage multiplication calculated by Momentum, the relative leakage multiplication calculated from the startup detectors and from the singles count rate of the NoMAD is shown in Fig. 10. The MCNP calculated data is also shown. It was calculated as described in Section 5 and then normalized to also start at a relative multiplication of one.

It should be noted that the count rate for the configuration with 78 box units was extremely high. The last data point is not reliable for the NoMAD, given that the high count rates are greatly influencing the measured results due to statistical uncertainties and detector dead time issues.

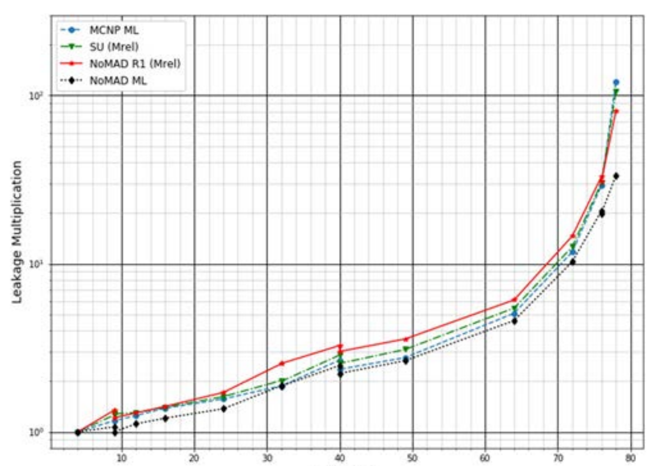

Figure 10: Plot of Leakage Multiplication

To better compare the methods for measuring leakage multiplication, Fig. 11 shows each experimental value plotted as a ratio to the calculated value. In addition to the caveat about detector saturation, it should be noted that in systems near critical (M>20), very small changes can lead to large changes in multiplication. Fig. 11 shows a divergence starting at 76 units for all methods.

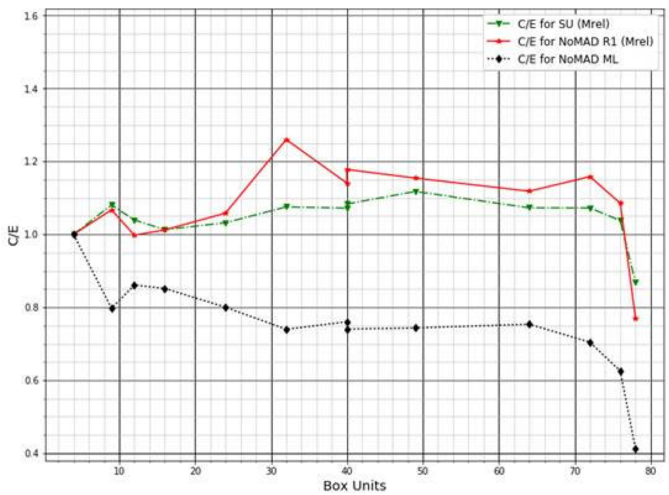

Figure 10: Plot of Calculation over Experiment Values for Leakage Multiplication

7. CONCLUSIONS

The One-over-M approach to critical method produces relative multiplications that are consistent with those calculated by MCNP until the system nears critical (M>100). The use of multiple data points continuously improves the accuracy of the predicted critical value.

The Feynman Variance-to-Mean technique also produces consistent results with the added advantage that the inferred leakage multiplication from the analysis is an absolute value. It is not relative to the other configurations and does not require any information about other configurations. The offset compared to calculation is due to effectively normalizing the values based on the four unit case by using that case to determine efficiency as described in Section 4. Particularly at such a low multiplication value, the efficiency of the detector needs to be determined independently. This is generally done by comparison with another detector that was not available for these experiments.

In future work this experiment may be evaluated and documented in the International Criticality Experiments Benchmark Evaluation Project (ICSBEP) handbook. This would be the first plutonium intermediate-energy experiment with lead included in the handbook.

ACKNOWLEDGMENTS

The critical experiment was designed jointly by researchers from Los Alamos National Laboratory (LANL) and the Japanese Atomic Energy Agency (JAEA). The authors thank Masahiro Fukushima and Akito Oizumi of the JAEA Fast Critical Assembly (FCA).

This work was supported by the DOE Office of Material Management and Minimization and by the DOE Nuclear Criticality Safety Program, funded and managed by the National Nuclear Security Administration for the Department of Energy.

This submission has been approved for release and is assigned the number 'LA-UR-17-29939.'

REFERENCES

1. R. MOSTELLER et al., "The Initial Set of Zeus Experiments: Intermediate-Spectrum Critical Assemblies with a Graphite-HEU Core Surrounded by a Copper Reflector," International Handbook of Evaluated Criticality Safety Benchmark Experiments, HEU-MET-INTER-006, NEA/NSC/DOC/(95)03/II.
2. D. HAYES, "Zeus: Fast-Spectrum Critical Assemblies With An Iron - HEU Core Surrounded By A Copper Reflector," International Handbook of Evaluated Criticality Safety Benchmark Experiments, HEU-MET-FAST-072, NEA/NSC/DOC/(95)03/II.
3. R. MOSTELLER, "The Unmoderated Zeus Experiment: A Cylindrical HEU Core Surrounded By A Copper Reflector," International Handbook of Evaluated Criticality Safety Benchmark Experiments, HEU-MET-FAST-073, NEA/NSC/DOC/(95)03/II.
4. TC1. D. HAYES et al. Nuclear Criticality Experimental Research Center (NCERC) Overview, Prepared for 2017 LANL Engineering Capability Review, Los Alamos Report LA-UR-17-21834, (2017)
5. R. LELL et al., "ZPPR-21 PHASE A: A CYLINDRICAL ASSEMBLY OF PU METAL REFLECTED BY GRAPHITE," International Handbook of Evaluated Criticality Safety Benchmark Experiments, PU-MET-FAST-033, NEA/NSC/DOC/(95)03/I.
6. R. UHRIG, *Random Noise Techniques in Nuclear Reactor Systems*, John Wiley & Sons Inc (1970).
7. J. HUTCHINSON, et al., "Subcritical Multiplication Experiments & Simulations: Overview and Recent Advances," ANS Advances in Nonproliferation Technology and Policy Conference, Santa Fe NM (2016).
8. D. CIFARELLI, W. HAGE, "Models for a Three-Parameter Analysis of Neutron Signal Correlation Measurements for Fissile Material Assay," Nuc. Instr. Meth. A251, 550-563 (1986).
9. R. P. FEYNMAN, F. de HOFFMAN, and R. SERBER, "Dispersion of the Neutron Emission in U-235 Fission," J. Nucl. Energy, 64–69 (1956).
10. M. NELSON, "Momentum: version 0.36.3," LANL Software, March 29, 2015.
11. B. RICHARD, J. HUTCHINSON, "Nickel Reflected Plutonium Metal Sphere Subcritical Measurements," International Handbook of Evaluated Criticality Safety Benchmark Experiments.
12. B. RICHARD et al., "Tungsten-Reflected Plutonium-Metal-Sphere Subcritical Measurements," International Handbook of Evaluated Criticality Safety Benchmark Experiments, NEA/NSC/DOC/(95)03/I, FUND-NCERC-PU-HE3-MULT-002 (2016).
13. R. SERBER, "The Definition of Neutron Multiplication," Los Alamos Report LA-335, 1945.
14. G. KEEPIN, *Physics of Nuclear Kinetics*, Addison-Wesley Publishing Company, 57 (1965).
15. T. GOORLEY et al., "Initial MCNP6 Release Overview," Nucl. Technol., 180, 298-315 (2012); http://dx.doi.org/10.13182/NT11-135.

Comparison of Predicted and Measured Subcritical Benchmark Uncertainties as a Function of Counting Time

J. Hutchinson, J. Arthur, R. Bahran, T. Cutler, T. Grove, A. McSpaden, M. Nelson

Los Alamos National Laboratory, P.O. Box 1663, Los Alamos, NM
jesson@lanl.gov

INTRODUCTION

During the final design phase of benchmark experiments, it is useful to estimate expected uncertainties. For subcritical benchmarks, the statistical uncertainties are generally a significant part of the overall experimental uncertainties [1]. Previously, a method was introduced to estimate statistical uncertainties of benchmark parameters as a function of counting time using simulated data [2]. This method was used during the design of a recent benchmark to guide measurement times. This work compares these predicted uncertainties versus the uncertainties which were measured.

BACKGROUND

Subcritical multiplication experiments and simulations are important for a variety of applications including nonproliferation, safeguards, and criticality safety monitoring. In recent years, LANL has designed and performed several subcritical benchmark experiments [3, 4, 5] which have been documented in the International Criticality Safety Benchmark Evaluation Project (ICSBEP) [6]. These measurements involve recording list-mode data, which is a list of times of every recorded neutron event in the detection system.

After list-mode data is acquired, the measured data can be analyzed using different analysis methods. Multiple prompt neutrons can be created immediately after a fission event (on a scale of 10^{-13} or 10^{-14} seconds) and are therefore correlated in time. Many subcritical analysis methods are based upon on this property of fission [7, 8]. One analysis approach is the Feynman Variance-to-Mean method [9] in which the number of recorded events in each time interval of a specified size is calculated [10]. This results in Feynman histograms, from which one can perform various analysis methods such as the Hage-Cifarelli formalism [11]. This method was used in these recent subcritical benchmarks.

For these evaluations, three parameters were used: the singles rate (R_1), doubles rate (R_2), and leakage multiplication (M_L). The singles rate is the rate at which one neutron from a fission chain is detected and the doubles counting rate is the rate at which two neutrons from a fission chain are detected. Leakage multiplication (sometimes called escape multiplication) is the average number of neutrons that exit the system per starter neutron (from spontaneous fission or (α,n) events). Recent work was performed to assess the statistical uncertainties associated with subcritical measurements [12, 13]. The uncertainties in R_1, R_2, and M_L due to uncertainties in all experimental parameters (mass, dimensions, and compositions of all components present in the experiment) are also determined via simulations in the benchmark evaluations.

After a method was established and validated to calculate the statistical uncertainties in the singles rate (R_1), doubles rate (R_2), and leakage multiplication (M_L), additional work was performed to estimate how the statistical uncertainties are reduced as a function of measurement time [2]. This was assessed using a 0-D point-kinetics Monte Carlo code [14]. Comparisons were made to measured data, but very limited comparisons were made (about 3 or 4 data points). This work utilizes recent tools which allow for these uncertainties to be easily determined for any time which is less than the total measurement time.

A recent subcritical benchmark used the method which was previously established to estimate statistical uncertainties as a function of counting time during the design phase. The design study used the same Monte Carlo code to estimate uncertainties at the following measurement times: 10, 60, 300, 600, 1800, 3600, 18000, and 36000 seconds. The inputs for the 0-D Monte Carlo code include the BeRP ball spontaneous fission rate (taken from previous BeRP ball benchmarks), the leakage multiplication (determined from MCNP® [15] criticality eigenvalue simulations), and the detector efficiency (based on historical measurements). This was used to help determine how long various configurations should be measured [16]. This work compares the uncertainty as a function of counting time that was measured for this experiment.

EXPERIMENT

The measured data presented in this work was from the Subcritical Copper-Reflected α-phase Plutonium (SCRαP) experiment [5]. This experiment included a 4.5 kg weapons grade α-phase Pu sphere known as the BeRP ball reflected by various thicknesses of copper and/or high-density polyethylene (HDPE). Figure 1 gives an overview of the configurations and Figure 2 shows one of the configurations during assembly and measurements.

RESULTS

In order to determine the uncertainty as a function of time from the measurements, the list-mode data files (which were 900-1800 sec each), were split into much smaller files. These files each had approximately $5\text{x}10^5$events which resulted in measurement times between 6-27 sec. The values and uncertainties for the parameters of interest (R_1, R_2, and M_L) were then determined for each of these smaller files. The cumulative uncertainty as a function of total measurement time was then determined.

Figure 3 shows the percentage uncertainty in R_1 as a function of counting time for the bare configuration (called C00). It can be seen that the predicted simulated uncertainties compare very well to the measured uncertainties when the counting time is greater than about 60 seconds. It is believed that the reason why there is a very large disagreement at small

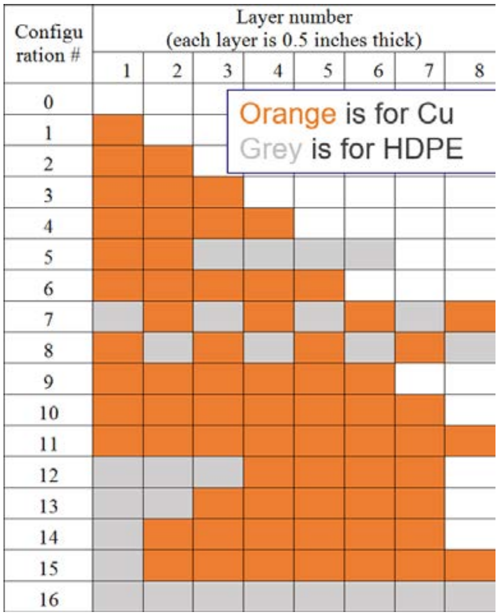

Figure 1. SCRαP Configurations.

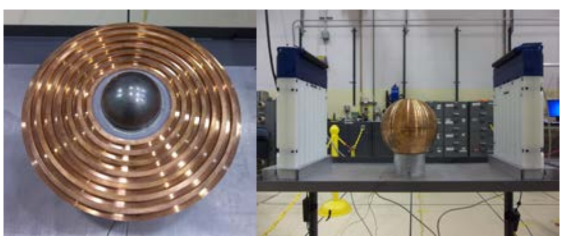

Figure 2. Configuration 15: during assembly in the left picture and fully assembled in the right picture.

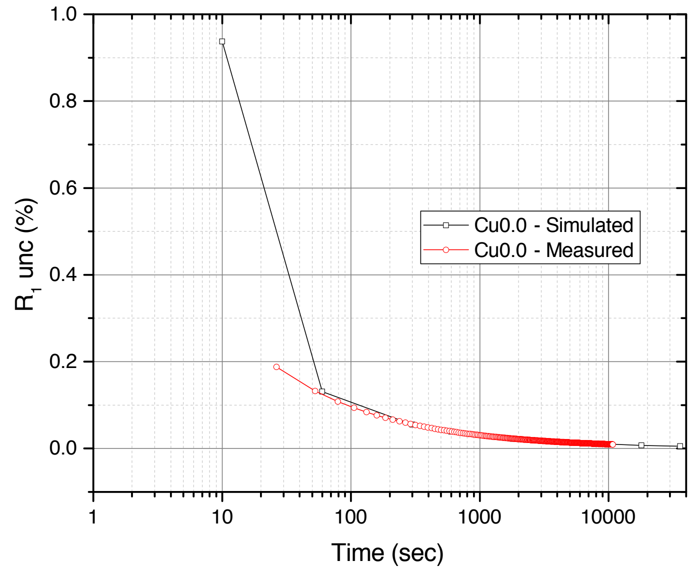

Figure 3. R_1 uncertainty (%) as a function of counting time for the bare configuration (C00).

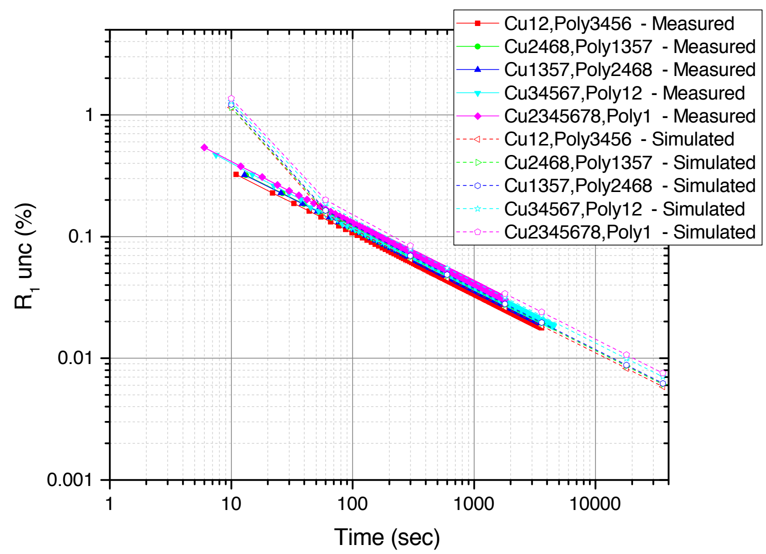

Figure 4. R_1 uncertainty (%) as a function of counting time for the configurations with only Cu reflection.

measurement time is due to the fact that for the simulated data, the first fissions start occurring just after t=0, so the count rate will be very low until the system reaches a steady state. This is not the case for the measurements (just after starting a measurement, data are recorded from neutrons born before t=0). For this reason, it is best to perform simulations for greater than the intended measurement time and then remove the initial 10 sec or so of data. This is done for the 3-D simulations that are performed for the benchmark evaluation, but was not done for these design simulations. Figures 4 and 5 show the uncertainty (in %) in R_1 and R_2 as a function of counting time for the configurations that included only Cu reflection (configurations 0, 1, 2, 3, 4, 6, 9, 10, and 11). It can be seen that they all agree very well for times greater than 60 seconds. It can also be seen that the measured uncertainties are generally slightly smaller than the simulated uncertainties.

Figure 6 shows the uncertainty (in %) in M_L as a function of counting time for the configurations that included only Cu reflection (configurations 0, 1, 2, 3, 4, 6, 9, 10, and 11). Similarly, Figure 7 includes only the configurations that have both Cu and HDPE reflection (configurations 5, 7, 8, 12, 13, 14, 15, and 16). Similar to the figures above, these results all agree very well for times greater than 60 seconds. As discussed in previous work [12], the uncertainty in leakage multiplication is a function of three parameters: R_1, R_2, and the detector efficiency (ϵ). As shown in Figures 3-5, the uncertainties in R_1 and R_2 will continue to decrease as the counting time increases (and would eventually go to zero at a counting time of infinity). The uncertainty on the detector efficiency, however, may or may not decrease as a function of counting time, depending on the method used to determine the detector efficiency. For these subcritical measurements, the detector efficiency is often determined by performing replacement measurements in which a ^{252}Cf source is placed at the same location in which the nuclear material (in this case the BeRP ball) would be placed. The efficiency is then determined using Eq. 1, where $\bar{\nu_{S1}}$ is the average number of neutrons emitted per ^{252}Cf spontaneous

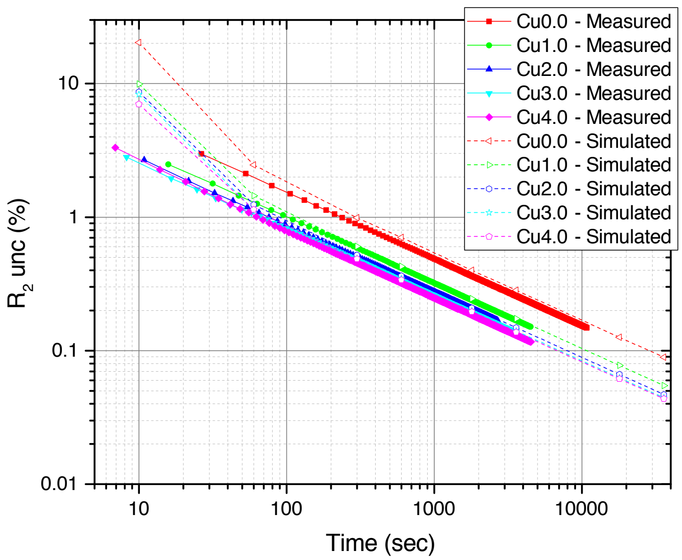

Figure 5. R_2 uncertainty (%) as a function of counting time for the configurations with only Cu reflection.

fission and F_S is the spontaneous fission rate. The value and uncertainty in the spontaneous fission rate used are those given in the certificate provided with the ^{252}Cf source. R_1 in this equation is the measured count rate in the ^{252}Cf replacement measurements.

$$\epsilon = \frac{R_1}{\bar{\nu_{S1}} F_S} \qquad (1)$$

If this method is used to determine the detector efficiency, then both the uncertainty in the detector efficiency and the uncertainty in leakage multiplication will be limited by the uncertainty in the ^{252}Cf source spontaneous fission rate. The percent uncertainty in the detector efficiency is equal to the percent uncertainty in the spontaneous fission rate. The uncertainty in leakage multiplication is proportional to the uncertainty in the detector efficiency (with the proportionality constant $\partial M_L/\partial\epsilon$). For this reason, the uncertainty in leakage multiplication does not decrease to zero at an infinite counting time as shown in Figures 6-7. These figures also include the minimum uncertainties in M_L achievable for infinite counting time. These values range from 0.46-0.49% (this is not a constant since $\partial M_L/\partial\epsilon$ changes for different configurations).

In the design document [16], it was stated that the goal was to have leakage multiplication uncertainties that are less than 2% greater than the theoretical minimum and if possible, the experimenters should try to get within 1%. Table I shows the times predicted by the design document which would be needed to achieve uncertainties in leakage multiplication that were 2% and 1% higher than the theoretical minimum M_L uncertainty for each configuration. The next column shows the actual measurement time that was achieved during the experimental campaign. Times listed in green are those that are greater than the predicted time for 1% above theoretical uncertainty. The time listed in red is less than that predicted for 2%. The last column shows the actual percentage greater than the theoretical uncertainty in M_L that was achieved using the measured data. It can be seen that the goal of less than 2%

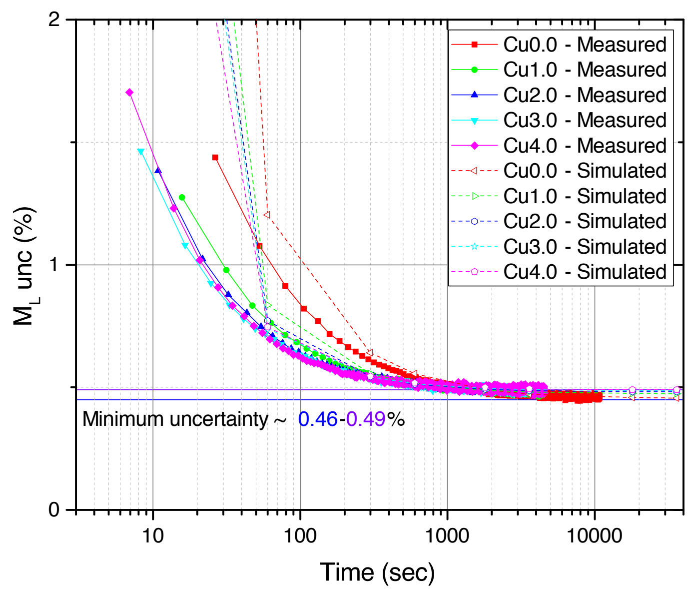

Figure 6. M_L uncertainty (%) as a function of counting time for the configurations with only Cu reflection.

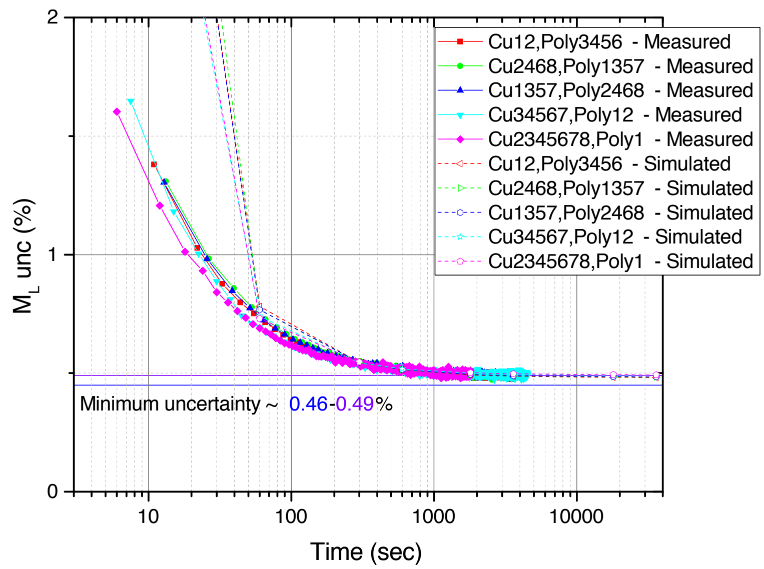

Figure 7. M_L uncertainty (%) as a function of counting time for the configurations with Cu and HDPE reflection.

was achieved for all configurations. Values listed in green are those that were less than 1%.

CONCLUSIONS

During the design phase of a subcritical benchmark experiment the statistical uncertainties as a function of counting time were determined via simulations. These results were used to help guide how long each configuration would be measured. After the measurements were performed, the uncertainties in the same parameters (singles rate (R_1), doubles rate (R_2), and leakage multiplication (M_L)) were determined as a function of

Table I. Measurement times by configuration.

Configuration	Time to 2% (sec)	Time to 1% (sec)	Actual Time (sec)	M_L Unc % greater
Cu0.0	4740	9360	10800	1.1
Cu0.5	2550	5070	5400	1.3
Cu1.0	1890	3750	4500	1.1
Cu1.5	1560	3210	3600	1.2
Cu2.0	1440	3030	2700	1.4
Cu2.5	1410	3090	3600	1.0
Cu3.0	1440	3330	3600	0.9
Cu3.5	1500	3780	3600	0.9
Cu4.0	1620	4440	4500	0.7
Cu12,Poly3456	1500	3120	3600	1.1
Cu2468,Poly1357	1440	3090	2700	1.5
Cu1357,Poly2468	1440	3180	3600	1.1
Cu4567,Poly123	1620	4440	4500	0.8
Cu34567,Poly12	1920	6120	4500	0.7
Cu234567,Poly1	1920	6120	5400	0.6
Cu2345678,Poly1	2610	10020	1800	1.7
Total (seconds)	30600	75150	68400	
Total (hours)	8.5	20.9	19	

counting time. These measured results were then compared to the design simulations. It can be seen that for counting times greater than 60 seconds, the measured and simulated results compared very well. This provides further validation to the method that was used. The design simulations were used to estimate the counting time required to reach certain desired uncertainties. A comparison was made to the actual measured times and resulting measred uncertainties. The results showed that the design estimates were successful in providing approximate counting times to reach desired uncertainties. This method will continue to be applied to future subcritical benchmark experiments.

ACKNOWLEDGMENTS

This work was supported by the DOE Nuclear Criticality Safety Program, funded and managed by the National Nuclear Security Administration for the Department of Energy.

REFERENCES

1. J. HUTCHINSON, T. CUTLER, T. GROVE, and M. NELSON, "A Study of Measured, Experimental, and Nuclear Data Uncertainties for Subcritical Benchmark Experiments," *M&C 2017 - International Conference on Mathematics & Computational Methods Applied to Nuclear Science & Engineering* (2017).
2. J. HUTCHINSON, T. GROVE, and M. NELSON, "Uncertainty as a Function of Time for Subcritical Experiment Parameters Using the Hage-Cifarelli Formalism," *Transactions of the American Nuclear Society Annual Meeting* (2016).
3. B. RICHARD and J. HUTCHINSON, "Nickel Reflected Plutonium Metal Sphere Subcritical Measurements," *International Handbook of Evaluated Criticality Safety Benchmark Experiments*, **NEA/NSC/DOC/(95)03/I**, FUND–NCERC–PU–HE3–MULT–001 (2014).
4. B. RICHARD and J. HUTCHINSON, "Tungsten-Reflected Plutonium-Metal-Sphere Subcritical Measurements," *International Handbook of Evaluated Criticality Safety Benchmark Experiments*, **NEA/NSC/DOC/(95)03/I**, FUND–NCERC–PU–HE3–MULT–002 (2016).
5. J. HUTCHINSON, R. BAHRAN, T. CUTLER, J. ARTHUR, and M. NELSON, "Subcritical Copper-Reflected alpha-phase Plutonium (SCRaP) Measurements and Simulations," *M&C 2017 - International Conference on Mathematics & Computational Methods Applied to Nuclear Science & Engineering* (2017).
6. "International Handbook of Evaluated Criticality Safety Benchmark Experiments," Tech. Rep. NEA;7328, Nuclear Energy Agency. - Paris : OECD Nuclear Energy Agency (2016).
7. R. UHRIG, *Random Noise Techniques in Nuclear Reactor Systems*, The Ronald Press Company (1970).
8. N. PACILIO, "Reactor-Noise Analysis in the Time Domain," Tech. Rep. TID-24512, Argonne National Laboratoryï¿œ (1969).
9. R. FEYNMAN, F. D. HOFFMANN, and R. SERBER, "Dispersion of the neutron emission in U-235 fission," *Journal of Nuclear Energy (1954)*, **3**, *1*, 64 – IN10 (1956).
10. T. CUTLER, M. NELSON, and J. HUTCHINSON, "Deciphering the Binning Method Uncertainty in Neutron Multiplicity Measurements," *Transactions of the American Nuclear Society Winter Meeting* (2014).
11. D. CIFARELLI and W. HAGE, "Models for a three-parameter analysis of neutron signal correlation measurements for fissile material assay," *Nuclear Instruments and Methods in Physics Research Section A: Accelerators, Spectrometers, Detectors and Associated Equipment*, **251**, *3*, 550 – 563 (1986).
12. J. D. HUTCHINSON, M. A. SMITH-NELSON, T. E. CUTLER, B. L. RICHARD, and T. J. GROVE, "Estimation of Uncertainties for Subcritical Benchmark Measurements," *International Conference on Nuclear Criticality 2015* (2015).
13. J. HUTCHINSON, B. RICHARD, M. NELSON, T. GROVE, and T. CUTLER, "Uncertainty analysis of subcritical benchmark experiments using the Hage-Cifarelli formalism," *Internal report*, **LA-UR-16-20375** (2016).
14. M. NELSON, "Neutron Generator: version 2.04," *LANL Software* (2016).
15. T. GOORLEY, M. JAMES, T. BOOTH, F. BROWN, J. BULL, and ET AL., "Initial MCNP6 Release Overview," *Nuclear Technology*, **180**, 298–315 (2012).
16. R. BAHRAN and J. HUTCHINSON, "Subcritical Copper-Reflected α-Phase Plutonium (SCRαP) Integral Experiment Design," *Transactions of the American Nuclear Society*, **114**, 527–529 (2016).

2-Exponential PDF and Analytic Uncertainty Approximations for Rossi-alpha Histograms

M. Y. Hua[1,2], J. D. Hutchinson[1], G. E. McKenzie[1], and M. A. Nelson[1]

1. NEN-2: Advanced Nuclear Technology, Los Alamos National Laboratory, Los Alamos, NM 87545
2. Department of Nuclear Engineering and Radiological Sciences, University of Michigan, Ann Arbor, MI 48109
mikwa@umich.edu

INTRODUCTION

A neutron-multiplying system's subcritical reactivity is often of interest in nuclear nonproliferation, criticality safety, and accelerator-driven systems. The subcritical reactivity can be inferred from the system's prompt neutron decay constant, α, which can be determined via the Rossi-α method. The method is predicated on fitting Rossi-α histograms [1]. In this summary, a probability density function (PDF) is developed from first-principles; the PDF supports a double exponential fit in the case of reflected and/or moderated systems. Development of the PDF enables an analytic approximation of the uncertainty in the parameters of the fit (and therefore α). In current experiments, the standard deviation of a population of measurements is used to approximate uncertainty. Using measured data from a 4.5 kg sphere of plutonium called the BeRP ball (Beryllium-Reflected Plutonium), the analytic method is compared against the sample standard deviation obtained from many iterations of the same measurement.

BACKGROUND

In a neutron chain-reacting (fission) system, neutron detections are not uniformly distributed in time due to the time-correlation between neutrons originating from the same fission-chain. The nonrandom phenomena can be observed by producing a histogram of the times between a neutron detection and following detections; this is the Rossi-α histogram [2] which can be seen in Fig.1.

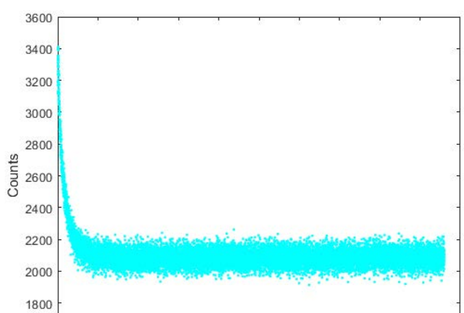

Fig. 1. A sample Rossi-α curve for a subcritical system.

Traditionally, the neutron population in the subcritical fissioning material has been described by

$$N = N_0 e^{\frac{k_p-1}{\ell}t} = N_0 e^{\alpha t} \tag{1}$$

which results in a PDF of the form

$$p^*(t) = A + Be^{\alpha t} \tag{2}$$

where k_p is the prompt-neutron multiplication factor, ℓ is the mean neutron lifetime, and N_0 is the number of neutrons in the system at $t = 0$. A represents uncorrelated/accidental counts, and $Be^{\alpha t}$ represents the correlated counts/prompt neutron decay [**?**, 3]. Note that the PDF describes the relative probability of detecting a neutron at time t after an initial detection at $t = 0$.

Prior work has also investigated the use of a two-exponential PDF

$$p^*(t) = A + B_1 e^{\alpha_1 t} + B_2 e^{\alpha_2 t} \tag{3}$$

in fitting Rossi-α histogram, showing that Eqn. (3) is a better fit than Eqn. (2) under certain conditions [4, 5]. Eqn. (3) performs better because it accounts for reflection/moderation; moderation (e.g. polyethylene) improves efficiency for standard He-3 detection systems. Prior work has assumed that one of α_1 and α_2 represented α while the other accounted for reflection; the forthcoming derivation of the two-exponential PDF shows that this is not the case. Both exponentials carry information on both α and reflection/moderation.

Prior Work on Reflector Considerations

In Ref. [6], the time-dependent neutron population of prompt neutrons in a reflected assembly is approximated by

$$\frac{dN_c}{dt} = \frac{k_c-1}{\ell_c}N_c + f_{rc}\frac{N_r}{\ell_r} \tag{4}$$

$$\frac{dN_r}{dt} = f_{cr}\frac{N_c}{\ell_c} - \frac{N_r}{\ell_r}, \tag{5}$$

where:

N_c is the number of neutrons in the fissile core region,
N_r is the number of neutrons in the reflector,
k_c is (k_p above) the multiplication factor in the fissile core region,
ℓ_c is (ℓ above) the mean neutron lifetime in the fissile core region,
ℓ_r is the neutron lifetime in the reflector region,
f_{cr} is the fraction of neutrons leaking from core to reflector, and
f_{rc} is the fraction of neutrons leaking from reflector to core.

Assuming $N_c(0) = N_0$ and $N_r(0) = 0$, Ref. [6] also solves the system of equations formed by Eqns. (4) and (5) yielding

$$N_c(t) = N_0\left[(1-R)e^{r_1 t} + Re^{r_2 t}\right], \tag{6}$$

where

$$r_j = \frac{(-1)^j\sqrt{4\ell_c\ell_r(f_{rc}f_{cr}+k_c-1)+(\ell_c-\ell_r(k_c-1))^2}-\ell_c+\ell_r(k_c-1)}{2\ell_c\ell_r}, \tag{7}$$

and

$$R = \frac{r_1-\alpha}{r_1-r_2}. \tag{8}$$

It can be shown that the r_j are negative and R lives in the interval $[0, 1]$.

PROBABILITY DENSITY FUNCTION DERIVATION

Following the PDF derivation in [3], Eqn. (6) implies that the probable number of fissions produced in dt about $t > 0$ is given by

$$dF = N_c \frac{dt}{\tau_f} = N_0 \frac{dt}{\tau_f} \left[(1-R)e^{r_1 t} + Re^{r_2 t}\right] \tag{9}$$

where τ_f is the mean life for fission. The number of resulting neutrons is given by

$$dN = \overline{\nu} N_0 \frac{dt}{\tau_f} \left[(1-R)e^{r_1 t} + Re^{r_2 t}\right] \tag{10}$$

where $\overline{\nu}$ is the mean number of neutrons produced per fission. To obtain the PDF $p^*(t)$ giving the relative probability of detecting a neutron at time t after a count at $t = 0$, expressions for the probability of a

I. fission at some time t_0 in dt_0,

II. count at t_1 as a result of a fission at t_0, and

III. correlated count at t_2 assuming a count at t_1

are needed. I is given in terms of the average fission rate in the system $\dot{F}_0$ as

$$\text{I.} \implies \dot{F}_0 dt_0. \tag{11}$$

Allowing ε to be efficiency in units of counts-per-fission, II and III can be expressed as

$$\text{II.} \implies \varepsilon\nu \frac{dt_1}{\tau_f} \left[(1-R)e^{r_1(t_1-t_0)} + Re^{r_2(t_1-t_0)}\right], \quad \text{and} \tag{12}$$

$$\text{III.} \implies \varepsilon(\nu-1) \frac{dt_2}{\tau_f} \left[(1-R)e^{r_1(t_2-t_0)} + Re^{r_2(t_2-t_0)}\right] \tag{13}$$

where ν is the number of neutrons emitted in the fission at t_0. The probability of a count at t_1 and a second count at t_2 from a common ancestor (not at t_1) is obtained by integrating the product of I, II, and III over $-\infty < t_0 < t_1$ and averaging over the distribution of neutrons emitted per fission. Note that this probability is $\varepsilon\dot{F}_0 dt_1$ multiplied by the probability of a second count following a count at t_1. Performing the integration for sub-prompt-critical systems gives

$$\begin{aligned} \varepsilon\dot{F}_0 dt_1 p(t_2) dt_2 = \dot{F}_0 \varepsilon^2 \overline{\nu(\nu-1)} \frac{dt_1 dt_2}{\tau_f^2} \dots \\ \times \left[(1-R)^2 \frac{e^{r_1(t_2-t_1)}}{-2r_1} + (R)^2 \frac{e^{r_2(t_2-t_1)}}{-2r_2} \dots \right. \\ \left. + \frac{(1-R)(R)\left(e^{r_2(t_2-t_1)} + e^{r_1(t_2-t_1)}\right)}{-(r_1+r_2)}\right]. \end{aligned} \tag{14}$$

Reckoning time from $t_1 = 0$ and including the chance/accidental probability yields

$$p^*(t) = C^* - \frac{\varepsilon\overline{\nu(\nu-1)}}{2\tau_f^2} \left[e^{r_1 t}\rho_1 + e^{r_2 t}\rho_2\right] \tag{15}$$

$$= C^* + A_1 e^{r_1 t} + A_2 e^{r_2 t} \tag{16}$$

where

$$\rho_1 = \frac{(1-R)^2}{r_1} + \frac{2(1-R)(R)}{r_1+r_2}, \quad \text{and} \tag{17}$$

$$\rho_2 = \frac{R^2}{r_2} + \frac{2(1-R)(R)}{r_1+r_2}. \tag{18}$$

Note that ρ_1 and ρ_2 are constants with respect to t. Eqn.(15) does not yet satisfy normalization requirements. Since the domain of t is $0 < t < \infty$, normalizing $p^*(t)$ can become obsolete for large t due to the constant term. To avoid such complications, and since the constant term can be determined with high confidence from baseline-subtraction-type analysis, it is often convenient to define

$$p(t) = p^*(t) - C^* = -\frac{\varepsilon\overline{\nu(\nu-1)}}{2\tau_f^2} \left[e^{r_1 t}\rho_1 + e^{r_2 t}\rho_2\right] \tag{19}$$

$$= -A\left[e^{r_1 t}\rho_1 + e^{r_2 t}\rho_2\right]. \tag{20}$$

noting that this is a newly defined constant A. α is given by

$$\alpha = r_1(1-R) + r_2 R. \tag{21}$$

ANALYTIC UNCERTAINTY APPROXIMATION

One way to approximate the uncertainty in the Rossi-alpha method is to first determine error bars (or standard deviations) for the number of counts in each bin. This is a nontrivial problem since the number of counts is not a Poisson random variable. Next, the upper and lower error bars can be individually fit with Eqn. (20). The α values obtained from the upper and lower error bars are then treated as the lower and upper bounds on α.

The next step is relatively straightforward and more intricate methods of utilizing the error bars are left to be performed/examined as future work. Thus, the main problem is in determining the error bars. The uncertainty originates from the time t at which a neutron is detected; if t is larger or smaller (horizontal error bars), the count may belong in another bin (hence vertical error bars). For each bin, the horizontal error bars can be modeled by assuming the counts are normally distributed about the mean time of the bin with some standard deviation. The vertical error bars can be modeled by observing the portions of the normal distribution that belong in other bins. This basic idea is illustrated in Fig. 2. Developing this idea with mathematical rigor will yield the vertical error bars.

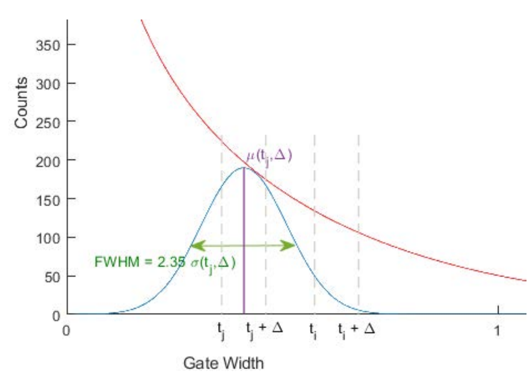

Fig. 2. Gaussian spread of gate widths across bins.

Given a set of measured data, the PDF in the form of Eqn. (20) is fit (where the fit parameters are A, r_1, r_2, and R). For simplicity, assume that the N histogram bins (made finite for realistic computation) are uniformly spaced with width Δ and edges $t_0, t_1, \dots, t_j, \dots, t_N$. Now that $p(t)$ is available, the mean time of detection in each bin $\mu(t_j, \Delta)$ as well as the associated standard deviations $\sigma(t_j, \Delta)$ can be calculated by

$$\mu(t_j, \Delta) = \int_{t_j}^{t_j+\Delta} t p(t) dt, \quad \text{and} \tag{22}$$

$$\sigma(t_j, \Delta) = \int_{t_j}^{t_j+\Delta} t^2 p(t) dt - \mu^2 \tag{23}$$

respectively. Before integrating in Eqns. (22) and (23), $p(t)$ must be normalized for the particular bin. Define $\eta(t_j, \Delta)$ as the normalization constant for the bin $[t_j, t_j + \Delta]$. $\eta(t_j, \Delta)$ is determined by solving

$$1 = \int_{t_j}^{t_j+\Delta} -\eta(t_j, \Delta) A \left(e^{r_1 t} \rho_1 + e^{r_2 t} \rho_2\right) dt \tag{24}$$

which yields

$$\eta(t_j, \Delta) = \frac{1}{A}\left[(1 - e^{r_1\Delta}) e^{r_1 t_j} \frac{\rho_1}{r_1} + (1 - e^{r_2\Delta}) e^{r_2 t_j} \frac{\rho_2}{r_2}\right]^{-1}, \tag{25}$$

and thus

$$p(t, t_j, \Delta) = \eta(t_j, \Delta) p(t). \tag{26}$$

Calculating $\mu(t_j, \Delta)$ and $\sigma(t_j, \Delta)$ respectively yield

$$\begin{aligned} \mu(t_j, \Delta) = &-A\eta(t_j, \Delta) \dots \\ &\times \left[\frac{\rho_1}{{r_1}^2} e^{r_1 t_j} \left(e^{r_1\Delta}\Delta + (e^{r_1\Delta} - 1)(r_1 t_j - 1)\right) \dots \right. \\ &\left. + \frac{\rho_2}{{r_2}^2} e^{r_2 t_j} \left(e^{r_2\Delta}\Delta + (e^{r_2\Delta} - 1)(r_2 t_j - 1)\right)\right], \end{aligned} \tag{27}$$

and

$$\sigma(t_j, \Delta) = \left[-A\eta(t_j, \Delta)\left(\frac{\rho_1}{{r_1}^3}\phi_1 + \frac{\rho_2}{{r_2}^3}\phi_2\right) - \mu(t_j, \Delta)^2\right]^{1/2} \tag{28}$$

where

$$\begin{aligned} \phi_1 = &\; e^{r_1(t_j+\Delta)}[2 + r_1(t_j + \Delta)(r_1(t_j + \Delta) - 2)] \dots \\ &- e^{r_1 t_j}[2 + r_1 t_j(r_1 t_j - 2)] \end{aligned} \tag{29}$$

$$\begin{aligned} \phi_2 = &\; e^{r_2(t_j+\Delta)}[2 + r_2(t_j + \Delta)(r_2(t_j + \Delta) - 2)] \dots \\ &- e^{r_2 t_j}[2 + r_2 t_j(r_2 t_j - 2)]. \end{aligned} \tag{30}$$

Now that the normal distributions for each bin have been obtained, the standard error of the total count in each bin β_j ($j = 0, 1, \dots, N-1$) can be calculated as

$$\beta_j = \sum_{i=0}^{N-1} p_i(j)(1 - p_i(j)) \tag{31}$$

where $p_i(j)$ is the portion of the normal distribution defined by $\mu(t_i, \Delta)$ and $\sigma_(t_i, \Delta)$ within the bounds $[t_j, t_j + \Delta]$. $p_i(j)$ is mathematically expressed as:

$$p_i(j) = \int_{t_j}^{t_j+\Delta} \frac{1}{\sqrt{2\pi}\sigma(t_i, \Delta)} \exp\left(\frac{-(\mu(t_i, \Delta) - t)^2}{2\sigma(t_i, \Delta)^2}\right) dt \tag{32}$$

$$= \frac{1}{2}\left[\operatorname{erf}\left(\frac{t_j + \Delta - \mu(t_i, \Delta)}{\sqrt{2}\sigma(t_j, \Delta)}\right) + \operatorname{erf}\left(\frac{\mu(t_i, \Delta) - t_j}{\sqrt{2}\sigma(t_j, \Delta)}\right)\right]. \tag{33}$$

The error bar in the j^{th} bin is equal to β_j times the number of counts in the bin. Note that these error bars do not account for systematic uncertainty, but only random fluctuation. It is possible to combine the two if the systematic uncertainty is known. Measured data will be used to observe the behavior of the analytic error bars.

MEASUREMENT SPECIFICATIONS

The measured data are obtained with two NPOD detectors. A NoMADs detector includes 15 He-3 gas proportional counters embedded in high-density polyethylene. Further details on the measurement setup and NoMADs detectors can be found in [7].

The measurement comprises six consecutive 1800 second measurements of the same setup. The six measurements were further divided into 68 files. Splitting the files allows for the calculation of sample standard deviation to compare to the analytic error bars.

COMPARISON BETWEEN ANALYTIC AND LARGE-SAMPLE METHODS

A comparison of the analytic error bars and the error bars generated from the sample standard deviation can be seen in Fig. 3.

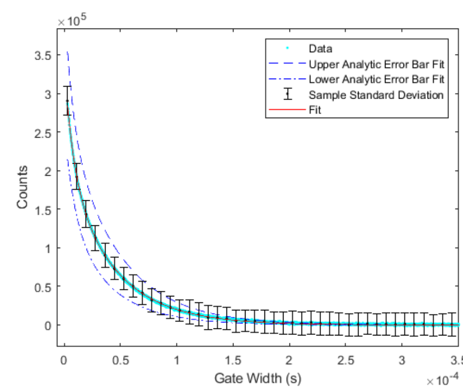

Fig. 3. A comparison of analytic uncertainty and uncertainty calculated from sample data.

Both methods generate error bars with the same trend, though the analytic method yields greater uncertainty in the correlated region whereas the sample method yields greater uncertainty in the uncorrelated region. The analytic approach produces a percent uncertainty and thus the uncorrelated region, centered around zero counts, exhibits very low uncertainty (which matches expectation). This makes fitting the upper and lower error bars with $p(t)$ realistic; doing so with the sample method is volatile since the exponentials need to decay to zero.

Another way to compare the methods is to calculate $(1/\alpha)$ for each of the files and then calculate the sample standard deviation. This can be compared to the $(1/\alpha)$'s obtained from fitting the upper and lower error bars in the analytic method. Prior to doing so, it is important to note that this is not a direct comparison whereas Fig. 3 is. The results of this alternative comparison can be seen in Fig. 4 for each of the six 1800 second measurements.

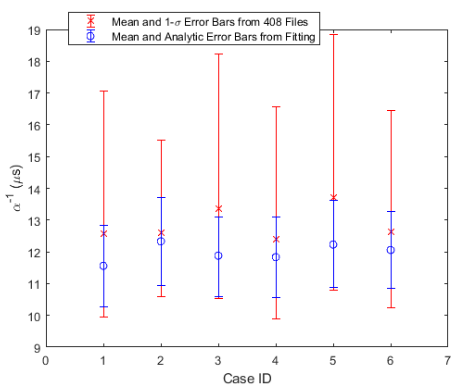

Fig. 4. Comparison of α^{-1} value and uncertainty for six 1800 second measurements.

Note that the error bars in the analytic method do not have to be symmetric about the mean since the lower and upper values are obtained from nonlinear fits. Furthermore, taking the inverse of α introduces asymmetry.

CONCLUSION AND FUTURE WORK

In Fig. 3, it is clear that the analytic method yields greater uncertainty in the correlated region, which is the region of interest. Furthermore, relative to the number of counts, the error bar values are similar. This suggests that the analytic method can accurately describe the uncertainty in the fission-chain dynamics of the system.

Fitting the upper and lower error bars in Fig. 3 results in consistent underestimates of the uncertainty. It is possible to scale the analytic method by scaling the $\sigma(t_j, \Delta)$ to introduce greater Gaussian spread. This is not advised since the error bars match well and already overestimate the uncertainty in Fig. 3. Instead, future work will entail investigating methods of utilizing the error bars to generate more extreme α and $(1/\alpha)$ values. For example, a larger α (than the α obtained from fitting the error bars) can be obtained by an exponential bounded by the error bars, but exhibiting a steeper trend (linearly decreasing the point at which is crosses the error bar).

ACKNOWLEDGMENT

This work was supported by the DOE Nuclear Criticality Safety Program, funded and managed by the National Nuclear Security Administration for the Department of Energy.

REFERENCES

1. R. FEYNMAN, F. DEHOFFMANN, and R. SERBER, “Dispersion of the neutron emission in U-235 fission,” **3**, 64–69 (08 1956).
2. F. DEHOFFMANN, “Statistical Fluctuations in the Water Boiler and the Dispersion of Neutrons Emitted Per Fission,” *LANL Report LA101* (1944).
3. J. ORNDOFF, “Prompt Neutron Periods of Metal Critical Assemblies,” *Nuclear Science and Engineering*, **2**, *4*, 450–460 (7 1957).
4. J. HUTCHINSON, G. MCKENZIE, J. ARTHUR, M. NELSON, and W. MONAGE, “Prompt Neutron Decay Constant Fitting Using the Rossi-alpha and Feynman Variance-to-Mean Methods,” *Transactions of the American Nuclear Society*, **117**, 986–989 (2017).
5. R. KURAMOTO, A. DOS SANTOS, R. JEREZ, R. DINIZ, U. BITELLI, T. MADI FILHO, and C. LUIS VENEZIANI, “Rossi-α Experiment in the IPEN/MB-01 Research Reactor: Validation of Two-Region Model and Absolute Measurement of β_{eff} and Λ,” **2006** (01 2006).
6. M. MONTERIAL, P. MARLEAU, and S. POZZI, “Characterizing subcritical assemblies with time of flight fixed by energy estimation distributions,” *Nuclear Instruments and Methods in Physics Research Section A: Accelerators, Spectrometers, Detectors and Associated Equipment*, **888**, 240 – 249 (2018).
7. J. HUTCHINSON, R. BAHRAN, T. CUTLER, J. ARTHUR, and M. NELSON, “Subcritical Copper-Reflected alpha-phase Plutonium (SCRaP) Measurements and Simulations,” *M&C 2017 - International Conference on Mathematics & Computational Methods Applied to Nuclear Science & Engineering* (2017).

Eliminating Detector Response in Neutron Multiplicity Measurements for Model Evaluation

Alex McSpaden, Mark Nelson, Jesson Hutchinson

Advanced Nuclear Technology Group, NEN-2, Los Alamos National Laboratory, Los Alamos, NM 87545

INTRODUCTION

It is common when performing neutron multiplicity measurements of special nuclear material to create a simulation representing that experiment. Comparing the results of the measured and simulated data can, among other things, serve to inform those carrying them out as to whether they are correctly modeling the underlying phenomena or the materials they are using in their experiment. However both the measurement and the simulation will have varying sources of uncertainty and error that can make this comparison less direct. One such source of uncertainty is in the position of the neutron-sensitive detector to be used. In simulations it is not difficult to place objects such as sources and detectors at exact positions, but in the real world there is going to be some measure of inaccuracy. This inaccuracy, even if small, can lead to appreciable differences in measured quantities such as count rates through a change in the absolute efficiency of the detector. If the goal of the comparison between the model and the measurement is to determine the ability of the model to represent the source material and its surroundings, but not necessarily the detector, then this added uncertainty makes such a determination more difficult.

Through the use of Hage-Cifarelli formalism [1], parameters based on ratios of count rate moments can be used to eliminate the detector efficiency. This ratio is therefore theoretically independent of where the neutron detector is placed relative to the source, and comparisons of this ratio between simulation and experimental data then only represent how well the nuclear material is simulated, and not the configuration of any detectors. Previously such ratios have been used to assist in characterization of neutron detection systems, for example in choosing a high voltage bias in a well coincidence counter [2], but here this ratio is used to completely eliminate the detector response, focusing analysis on the nuclear material itself. While it has been demonstrated previously [3] in lower fidelity simulations that this ratio shows independence with respect to detector position, here data from experiments and more detailed simulation models are analyzed and compared to see if this holds true.

THEORY

The ratio that is being investigated, previously termed the Sm_2 value, is based on the singles count rate R_1 and the doubles rate R_2 observed in a detector, as follows [3]

$$Sm_2 = \frac{R_2}{R_1^2} \tag{1}$$

Using the Hage-Cifarelli formalism, and assuming the rate of (a, n) reactions in the source is negligible, the singles count rate R_1 is a function of both detector response and material properties given by

$$R_1 = \varepsilon M_L \overline{\nu_{S1}} F_s \tag{2}$$

While R_2 can be expressed by

$$R_2 = \varepsilon^2 M_L^2 \left(\overline{\nu_{S2}} + \frac{M_L - 1}{\overline{\nu_{I1}} - 1} \overline{\nu_{S1}} \overline{\nu_{I2}} \right) F_s \tag{3}$$

In these equations, ε represents the absolute detector efficiency, M_L is the leakage multiplication of the system, $\overline{\nu_{Sn}}$ represents the nth reduced moment of the spontaneous fission multiplicity distribution, F_s is the spontaneous fission rate, and $\overline{\nu_{In}}$ represents the nth reduced moment of the induced fission multiplicity distribution [1]. When Eqs. (2) and (3) are substituted into Eq. (1), the following expression is produced

$$Sm_2 = \frac{\overline{\nu_{S2}} + \frac{M_L - 1}{\overline{\nu_{I1}} - 1} \overline{\nu_{S1}} \overline{\nu_{I2}}}{\overline{\nu_{S1}}^2 F_s} \tag{4}$$

which does not feature an efficiency term. This effectively eliminates the contribution of the detector response, meaning that the resulting quantity is only a function of the properties of the nuclear material being measured. According to standard error propagation, the uncertainty is this quantity can be represented by

$$\sigma_{Sm_2} = Sm_2 \sqrt{4 \left(\frac{\sigma_{R_1}}{R_1} \right)^2 + \left(\frac{\sigma_{R_2}}{R_2} \right)^2} \tag{5}$$

which is dependent on the error in the individual count rates that comprise the ratio.

Since this parameter is expected to be independent of the detector response, any given experimental setup for a source and reflecting material should have the same value for this count rate ratio. Because of this, any comparisons of this value between simulations and experiments should allow for a more direct analysis of the accuracy with which the material is modeled.

Additionally, other ratios can be put together to eliminate detector efficiency (e.g. R_3/R_2R_1 and R_3/R_1^3), but the focus of this work was only on Sm_2. Ratios that involve the triples rate R_3 may run into statistical issues, as there is likely to be far fewer triples counts than singles and doubles, and the additional statistical uncertainty may be detrimental to determining whether or not the source in question is depicted accurately.

METHODS

Measured Data

To generate the experimental data, measurements of a 4.5 kg sphere of α-phase plutonium, commonly referred to as the BeRP (Beryllium Reflected Plutonium) ball, were performed. The BeRP ball is composed of mostly ^{239}Pu, which is the primary isotope in which induced fission occurs, but also ~6% ^{240}Pu which serves as the source of neutrons from spontaneous fission, and smaller amounts of other isotopes and impurities. This is a commonly used source for subcritical experiments, and more information on it can be found in a series of reports and benchmark experiments [4, 5, 6, 7]. The measurements of interest for this investigation were done with the Los Alamos National Laboratory MC-15 neutron detection system, which is composed of an array of ^{3}He tubes embedded in a high-density polyethylene moderating matrix.

A series of 5-minute measurements were performed with the detector at a variety of distances between 30 and 77.5 cm in order to see if the measured values for Sm_2 followed the expected trend of remaining constant with varying detector solid angle. The direct result of each measurement is a file listing a series of time-tagged neutron interactions in the detector. Producing the count rates needed for the Sm_2 parameter involved the use of a program called Momentum [8], which implements a random time binning strategy. In this strategy, time bins are randomly placed in the event timeline, and the factorial moments are computed based on how many neutrons are found in a time bin, and that bin's corresponding width in time [1, 9]. This in turn gives values for the count rates and their uncertainties. After all of the output data is processed for each of the detector placement configurations, the desired values for the ratios can then be computed.

Simulated Data

For comparison to the measured data, simulations were run with [1]MCNP® version 6.1.1 [10] and ENDF/B-VII.1 cross sections. The model used is intended to be rather detailed, and includes the aluminum stand the source sits on, the cart that both the detector and source assembly rest on, and the walls and floor of the room. Enough particle histories were run in

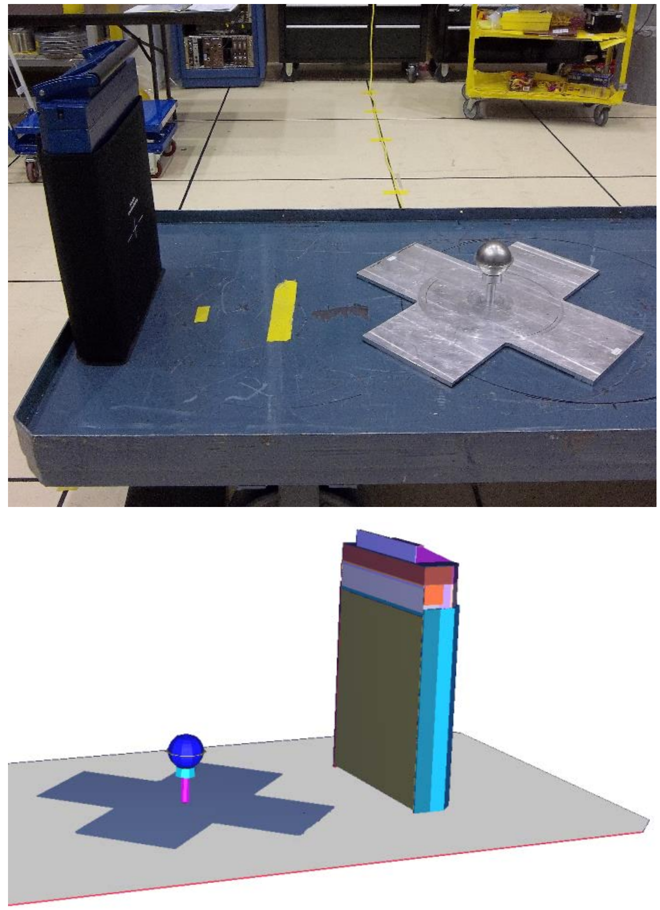

Fig. 1. The experimental setup (top) and a depiction of a section of the simulation model used (bottom, made with Visual Editor [11]).

the simulations to represent the five minute measurement time, and each distance case was modeled. A depiction of both the experimental and simulated setups can be seen in Fig. 1.

The output of MCNP used for this investigation is the Ptrac file, which was configured to store (among other things) the cell and time of each absorption in the active volume of the detector system. The information in this file is then manipulated using the mcnptools package to create a file that mimics the output of the MC-15, and can be processed in the same manner.

RESULTS

When the count rates and the resultant Sm_2 values are calculated for each of the separation distances, the overall

[1]MCNP and Monte Carlo N-Particle are registered trademarks owned by Los Alamos National Security, LLC, manager and operator of Los Alamos National Laboratory. Any third party use of such registered trademarks should be properly attributed to Los Alamos National Security, LLC, including the use of the designation as appropriate. For the purposes of visual clarity, the registered trademark symbol is assumed for all references to MCNP within the remainder of this paper.

TABLE I. The behavior of the lower moment count rates as a function of source-detector separation distance

	Measured Data		MCNP6 Results	
Distance (cm)	R_1	R_2	R_1	R_2
30	$1.6897 \pm 0.0010 \times 10^4$	$5.7258 \pm 0.0604 \times 10^3$	$1.7138 \pm 0.0010 \times 10^4$	$6.0444 \pm 0.0399 \times 10^3$
35	$1.3523 \pm 0.0009 \times 10^4$	$3.6730 \pm 0.0438 \times 10^3$	$1.4037 \pm 0.0009 \times 10^4$	$3.9823 \pm 0.0350 \times 10^3$
40	$1.1234 \pm 0.0008 \times 10^4$	$2.5490 \pm 0.0321 \times 10^3$	$1.1696 \pm 0.0008 \times 10^4$	$2.7828 \pm 0.0266 \times 10^3$
45	$9.6425 \pm 0.0070 \times 10^3$	$1.8660 \pm 0.0268 \times 10^3$	$9.8792 \pm 0.0072 \times 10^3$	$1.9730 \pm 0.0210 \times 10^3$
50	$8.5192 \pm 0.0046 \times 10^3$	$1.4406 \pm 0.0144 \times 10^3$	$8.4930 \pm 0.0065 \times 10^3$	$1.4785 \pm 0.0163 \times 10^3$
55	$7.3632 \pm 0.0042 \times 10^3$	$1.0914 \pm 0.0125 \times 10^3$	$7.3766 \pm 0.0060 \times 10^3$	$1.0974 \pm 0.0140 \times 10^3$
60	$6.4121 \pm 0.0039 \times 10^3$	$8.1818 \pm 0.0915 \times 10^2$	$6.4792 \pm 0.0055 \times 10^3$	$8.5136 \pm 0.0122 \times 10^2$
65	$5.8069 \pm 0.0036 \times 10^3$	$6.8165 \pm 0.1021 \times 10^2$	$5.7278 \pm 0.0051 \times 10^3$	$6.7011 \pm 0.1009 \times 10^2$
70	$5.1403 \pm 0.0034 \times 10^3$	$5.2424 \pm 0.0700 \times 10^2$	$5.1117 \pm 0.0048 \times 10^3$	$5.2068 \pm 0.0888 \times 10^2$
77.5	$4.4577 \pm 0.0031 \times 10^3$	$4.0300 \pm 0.0635 \times 10^2$	$4.3766 \pm 0.0044 \times 10^3$	$3.7505 \pm 0.0888 \times 10^2$

TABLE II. Comparison of measured and simulated Sm_2 values as a function of source detector separation distance

Distance (cm)	Measured Data ($\times 10^{-5}$)	MCNP6 Results ($\times 10^{-5}$)
30	2.005 ± 0.021	2.058 ± 0.014
35	2.009 ± 0.024	2.021 ± 0.018
40	2.020 ± 0.026	2.034 ± 0.020
45	2.007 ± 0.029	2.022 ± 0.022
50	1.985 ± 0.020	2.050 ± 0.023
55	2.013 ± 0.023	2.017 ± 0.026
60	1.990 ± 0.022	2.028 ± 0.029
65	2.022 ± 0.030	2.043 ± 0.031
70	1.984 ± 0.027	1.993 ± 0.034
77.5	2.028 ± 0.032	1.958 ± 0.046

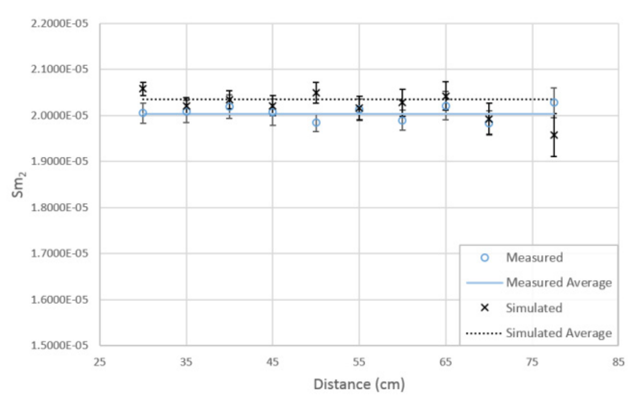

Fig. 2. The Sm_2 value as a function of source-detector separation distance for both measured and simulated data, plotted along with flat lines representing their average values.

trend can be seen in Fig. 2 for both simulated and measured data, and a more detailed look at the data is shown in Table I and Table II. From these it can be seen that the expected behavior, an independence of Sm_2 from detector absolute efficiency, is approximately upheld, as no measured value observed differs more than 1.2% from their weighted average of $2.004 \pm 0.008 \times 10^{-5}$, despite an exponential drop in the count rates themselves. This weighted average was calculated based on the uncertainties of the individual values, with those having a larger uncertainty having smaller weights and vice versa.

This measured average is very close (within 1.6%) to the simulated value of $2.036 \pm 0.007 \times 10^{-5}$. The simulated data also carries the expected trend in the Sm_2 value, as the ratio again remains mostly constant with distance. The table further shows that even as the observed count rates decrease due to a drop in the absolute efficiency of the detector, the parameter of interest is largely unaffected, as the leakage multiplication, source strength, and nuclear data have not changed.

CONCLUSIONS

When analyzing both experimental and measured data, the count rate ratio Sm_2 shows no dependence on detector response. Even though the count rates it relies on exponentially decrease with an increasing distance between the BeRP ball and the MC-15, the parameter held mostly constant over the range that was measured. Together with Smith-Nelson and Hutchinson's earlier report which demonstrated that this relationship can also be found in less detailed simulations, this means that when comparing a simulation model with an experiment that it is meant to represent, the position of detector is no longer a significant concern if the focus of the comparison is the nuclear material itself. In fact, since the formulas that compose the ratios only depend on the leakage multiplication and the factorial moments of the nuclear material, many other detector properties such as voltage bias and detection gas pressure can be ignored as well. This could have a significant impact on simulations, as it follows from this that any models of detectors can be significantly less detailed, or even omitted, as long as the simulation is still capable of producing the required count rate moments. Additionally, those constructing models of nuclear material can much more easily evaluate how well their model is representing their experimental setup, as any differences that could otherwise be potentially attributed to detector response, which can be quite complex or not very well understood for some systems, can now be squarely associated with inaccuracies of either the nuclear data or quantities that depend on how the material is modeled, such as leakage multiplication.

These observations do depend on a few assumptions, however. Since this analysis is based on the Hage-Cifarelli formalism, it is assumed that (among other effects), detector dead time is insignificant, any induced fissions occur at the same time as the emission of their inducing neutron, and point geometry of the source [1]. Furthermore, Eqs. (2), (3), and (4) assume that any source of (α,n) neutron emission is negligible. For some source-detector systems, these assumptions may not be applicable or accurate.

There are a few avenues down which this analysis can be naturally continued. If the detector response is no longer significant, than it follows that multiple types of multiplicity counters should be able to record the same result for a given sample of multiplying material. Therefore measurements and simulations can be carried out using many different types of detectors to verify this hypothesis. A simulation could even be performed without a detector, for example tracking particles crossing some arbitrary surface to calculate artificial count rates and therefore Sm_2. One of the assumptions previously mentioned was that the material in question is a negligible source of (α, n) neutron emission. However, following a similar procedure as the one used in this paper for the non-simplified Hage-Cifarelli equations should lead to a similar conclusion, so derivation of those equations and tests on sources that would be better fit by that model could also be performed.

REFERENCES

1. D.M. CIFARELLI, W. HAGE, "Models for a Three-Parameter Analysis of Neutron Signal Correction Measurements for Fissile Material Assay." *Nuclear Instruments and Methods in Physics Research Section A*, **252** 550-563 (1986).
2. A.T. SIMONE, et. al. "Characterizing the Oak Ridge Large Volume Active Well Coincidence Counter for Nuclear Safeguards Applications", Poster presented at: Nuclear Engineering Science Laboratory Synthesis Program (NESLS) Poster Competition; 2016 Aug; Oak Ridge National Laboratory.
3. M. A. SMITH-NELSON, J.D. HUTCHINSON, "The Sm2 Ratio for Evaluating Neutron Multiplicity Models." LA-UR-14-29047, Los Alamos National Laboratory, (2014).
4. J. HUTCHINSON, T. VALENTINE, "Subcritical Measurements of a Plutonium Sphere Reflected by Polyethylene and Acrylic." Nucl. Sci. Eng., 161, 357-362, 2009.
5. J. HUTCHINSON, D. LOAIZA, "Plutonium Sphere Reflected by Beryllium." PU-MET-FAST-038, International Handbook of Evaluated Criticality Safety Benchmark Experiments, NEA/NSC/DOC/(95)03, Nuclear Energy Agency, Organisation for Economic Co-operation and Development (Sep. 2007).
6. B. RICHARD, J. HUTCHINSON, "Nickel-Reflected Plutonium-Metal-Sphere Subcritical Measurements." FUND-NCERC-PU-HE3-MULT-001, International Handbook of Evaluated Criticality Safety Benchmark Experiments, NEA/NSC/DOC/(95)03, Nuclear Energy Agency, Organisation for Economic Co-operation and Development (Sep. 2014).
7. B. RICHARD, J. HUTCHINSON, "Tungsten-Reflected Plutonium-Metal-Sphere Subcritical Measurements." FUND-NCERC-PU-HE3-MULT-002, International Handbook of Evaluated Criticality Safety Benchmark Experiments, NEA/NSC/DOC/(95)03, Nuclear Energy Agency, Organisation for Economic Co-operation and Development (Sep. 2016).
8. M. SMITH-NELSON, "Momentum: version 0.36.3," LANL Software, March 29, 2015.
9. T. CULTER, M.A. SMITH-NELSON, J.D. HUTCHINSON "Deciphering the Binning Method Uncertainty in Neutron Multiplicity Measurements." LA-UR-14-23374, Los Alamos National Laboratory, (2014).
10. J.T. GOORLEY et. al., "Initial MCNP6 Release Overview," Nuclear Technology, 180, 298-315 (2012).
11. "The Visual Editor for MCNP". Retrieved from http://www.mcnpvised.com/visualeditor/visualeditor.html

PI: Sean Walston

Responsible Engineers: Eric Ruggiero
Tom Woehrle
Robert Ipong
Ron Kane

(U) MC-15 NEXT GENERATION MULTIPLICITY COUNTER TEST & EVALUATION REPORT

This work performed under the auspices of the U.S. Department of Energy by Lawrence Livermore National Laboratory under Contract DE-AC52-07NA27344.

Contents

BACKGROUND

The MC-15 Multiplicity Counter is a neutron multiplicity detector intended for field-use. This detector may need to be taken anywhere in the country on short notice. The environments to which the detector can be subject range from Death Valley in the summer to the summit of Mt. Rainier in the winter. Environmental testing has been performed to ensure that the MC-15 will survive and perform properly in any environment in which it is deployed or stored, during any method of transportation, and during any drops that may occur from handling the detector.

Neutron multiplicity counting is a method whereby neutrons from fissile materials are statistically distinguished from benign neutron sources. This technique can also estimate the mass and multiplication of any special nuclear materials (SNM) and can place qualitative bounds on the thickness of any hydrogenous materials surrounding the SNM.

Pictures of the detector and its case are shown below in Figures 1-4.

Figure 1. View of top and front of MC-15

Figure 2. View of external ports of MC-15

Figure 3. View of side of MC-15

Figure 4. MC-15 container

A ^{252}Cf neutron source was required to evaluate the MC-15 for seven of the eight tests. The source was ID 120228, had an activity of 4.9 μCi, and produced 9×10^3 neutrons per second when testing began. The encapsulation used to seal the source met ANSI Special Form Requirements, indicating that the encapsulation had been tested in temperatures ranging from -40°C to at least +400°C. Both of these extreme temperatures exceeded the maximum/minimum temperatures that the source was subjected to for these tests. The ^{252}Cf source was also placed in a small waterproof case to endure the extreme temperatures specified in this suite of tests as a means to provide secondary containment.

Before, after, and during some tests, neutron measurements were made with the MC-15 to ensure that it was still functioning correctly. For each test, the ^{252}Cf source was placed 6 inches as measured with a tape measure from the MC-15's front face and perpendicular to the '+' labelled on the detector. The count rate from the source was measured for 30 minutes for Tests 2-6, while neutron measurements were made continuously during Test 7 and for two minutes during Test 8. Test 1 required only the measurement of background neutrons and no source was required.

Discussion of Test Results

Per the MC-15 environmental testing plan, there were eight tests to be performed. The following sections contain information about each test, including what the original test plan called for, changes that had to be made to complete each test, the thermal/humidity/vibration data that has been collected to date, and any notable findings that occurred during testing. The results obtained through analysis of neutron data collected as a part of each test is summarized in the final section.

Test 1 – Background Neutron Count Rate Consistent Within 10% Over a Relative Humidity Range from 40% to 93%

The test plan stated backgrounds be continuously measured over a period of 26 hours, as shown in Figure 5.

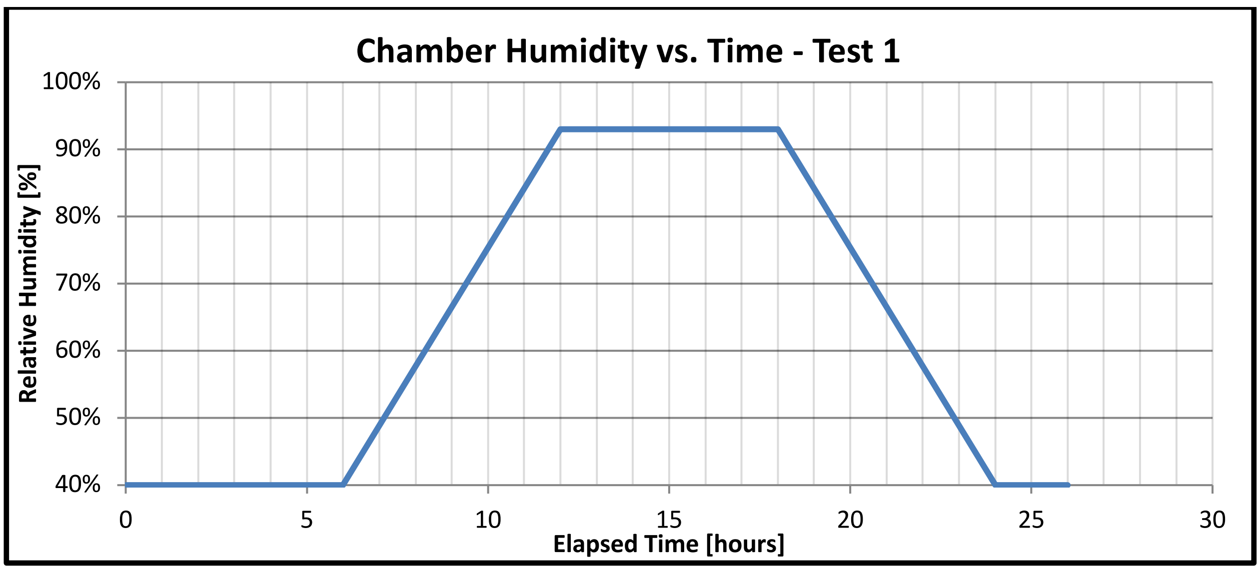

Figure 5. Initial planned humidity profile for Test 1

It was discovered after the test plan was written that the battery life of the detector was not long enough to run this test without requiring external charging, and externally powering the detector would cause electronic ports to be directly subject to humid conditions instead of being hermetically sealed. This test was broken down into two subtests. The first subtest captured background radiation data for 6 hours at 25°C and 40% RH. After this test, the detector was removed from the chamber and given a brief amount of time to charge. The second subtest captured background radiation data for 6 hours at 25°C and 93% RH. The conditions inside the chamber for both subtests are displayed in Figure 6 and Figure 7.

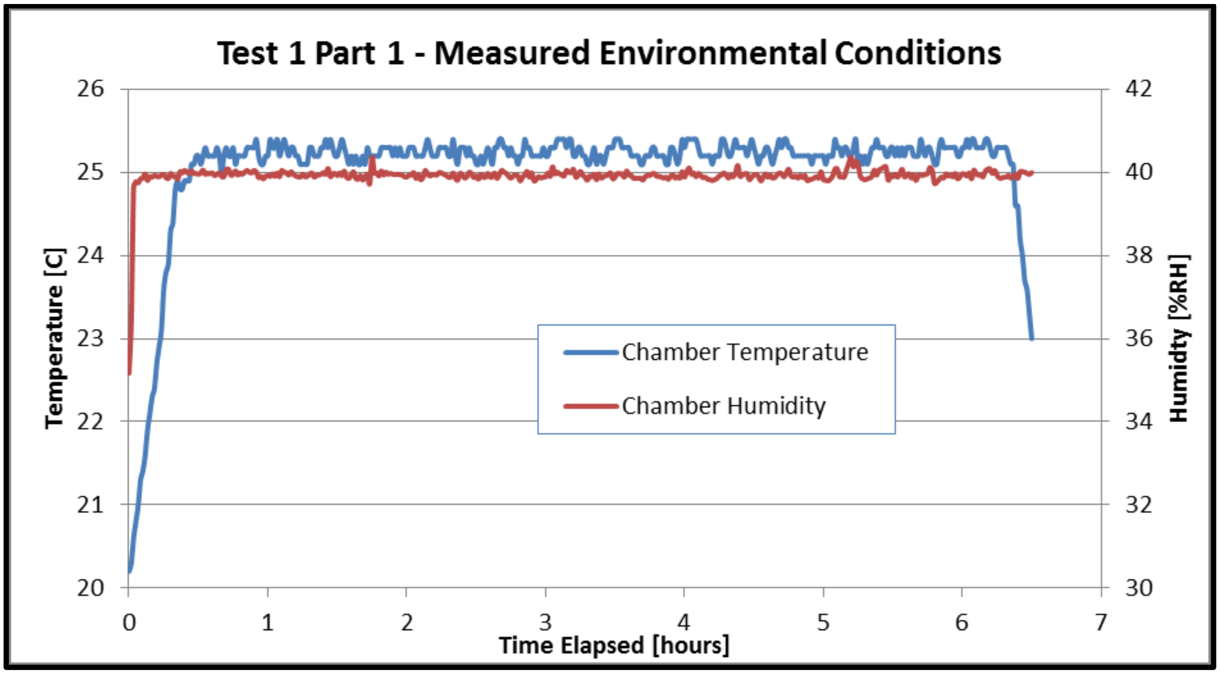

Figure 6. Measured environmental conditions for the first part of Test 1

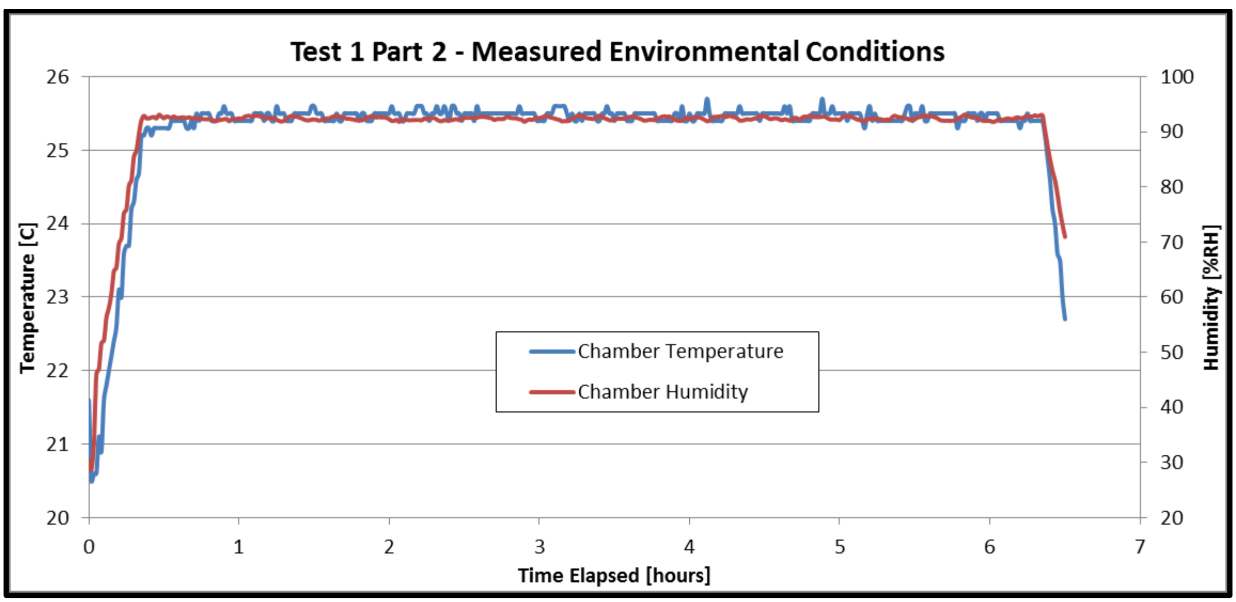

Figure 7. Measured environmental conditions for second part of Test 2

The data collected from both tests was analyzed and showed that the background neutron count remained consistent within 10% for the specified humidity conditions.

Test 2 – Capable of Surviving and Performing after Storage over the Temperature Range of -29°C to 60°C; Onboard Display Screen Readable Over Temperatures Ranging from 20°C to 50°C and under Light Conditions Ranging from Darkness to Bright Sunlight

The planned temperature profile, times when neutron measurements were conducted, and times lighting conditions were evaluated are shown in Figure 8.

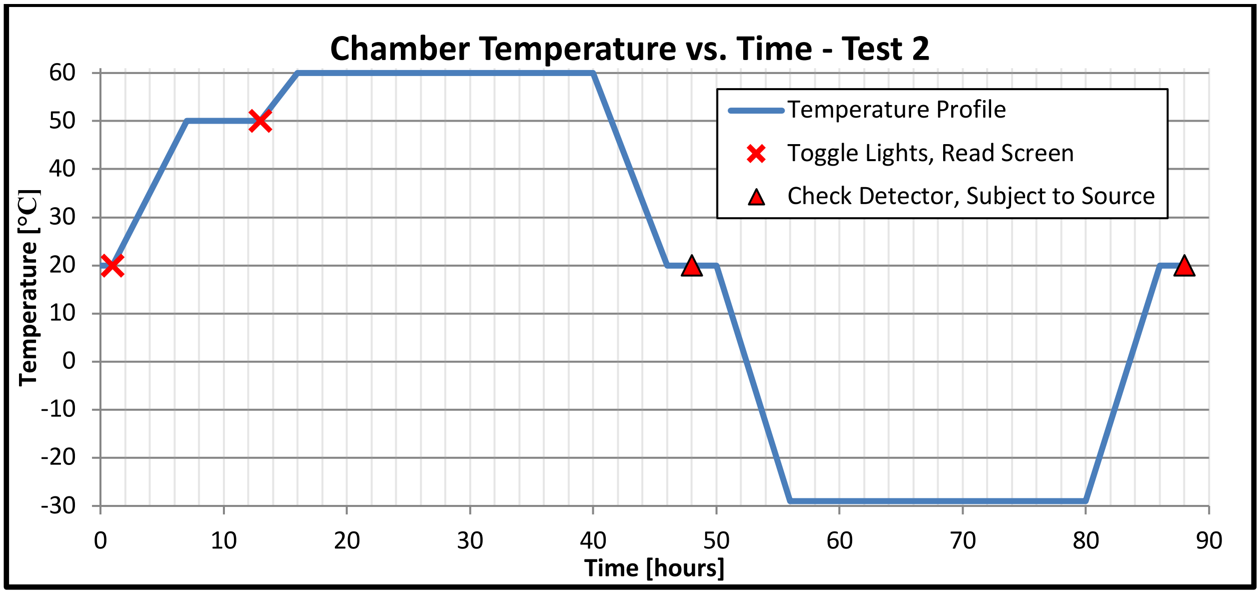

Figure 8. Plan for conducting Test 2

The first part of Test 2 was to determine if the MC-15 display screen was readable under a variety of temperature/lighting conditions. The detector remained outside of its case for the duration of the test. Two small changes were made to the planned profile: instead of holding the detector at 50°C for six hours before reading the screen in the different lighting conditions, the temperature was held at 50°C for one hour. It was deemed that soaking at 50°C for one hour was sufficient to examine temperature effects on reading the screen. Also, the detector was held at room temperature for longer than two hours before making a neutron measurement. The temperatures that were measured in the chamber during the tests can be found in Figure 9.

Four different lighting conditions were evaluated; no chamber light, dim ceiling light, bright, indirect halogen light, and direct halogen light. A meter was secured near the screen of the detector that measured the ambient brightness for each of the four conditions. The lighting conditions were initially performed at 20°C, and then performed at 50°C. The measured brightness for each lighting/temperature combination is shown in Table 1.

Table 1. Measured brightness for each temperature/lighting combination

	Brightness at Detector Screen (lux)	
	at 20°C	at 50°C
No Light	0	0
Dim Light	10	11
Indirect Halogen	671	665
Direct Halogen	5170	5330

There were no significant problems reading the screen for the examined temperature/lighting combinations. At 50°C with the direct halogen light shining on the screen, there was a glare that made the screen slightly more difficult to read, but it was still readable and may have been easier to read had a different viewing angle been possible.

The second part of the test involved soaking the detector for 24 hours at 60°C, ramping back to room temperature to perform a measurement with the detector, then soaking the detector at -29°C for 24 hours before ramping to room temperature to perform a neutron measurement. The temperature measured inside the chamber is shown in Figure 9.

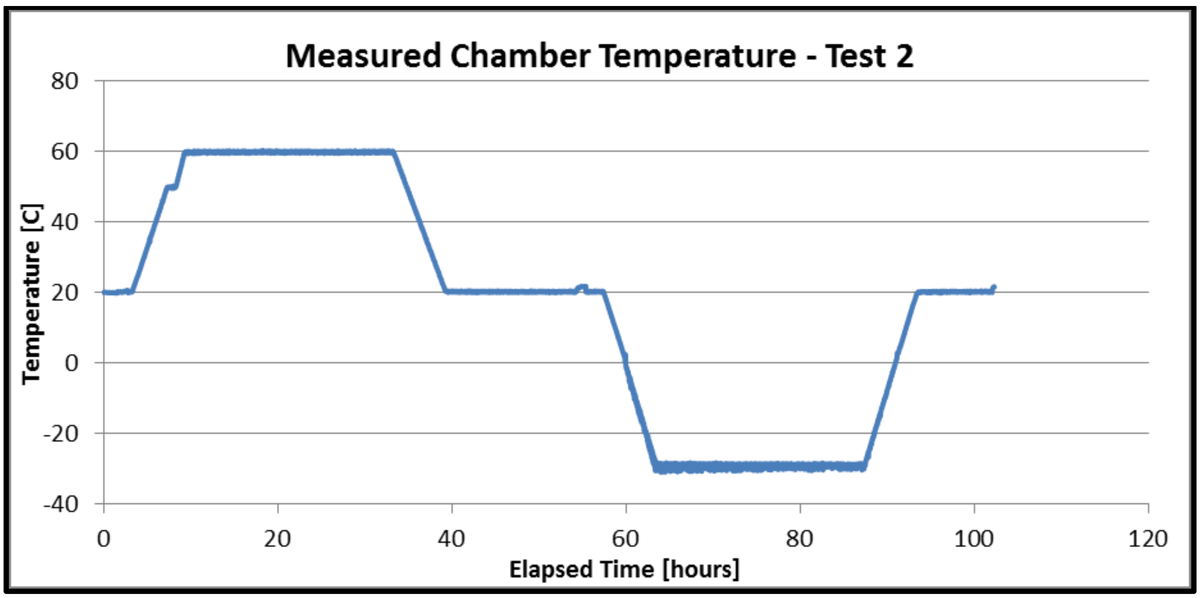

Figure 9. Temperature measured inside chamber while conducting Test 2

The data obtained from each neutron measurement was analyzed and compared to ensure that the detector consistently makes accurate measurements after exposure to both environmental conditions. The results are displayed and discussed in the data analysis section.

Test 3 – Capable of Surviving and Performing Properly after a Minimum of Five Thermal Cycles (Non-Operating, Unpowered, and in a Shipping Configuration) between -29°C to 66°C, from a Storage Temperature of 66°C to a Transportation Temperature of -29°C Measured at the Interior Surface of the Shipping Container

The test plan stated that the detector would be placed inside its shipping container and the temperature profile displayed in Figure 10 would be applied and controlled within the shipping container.

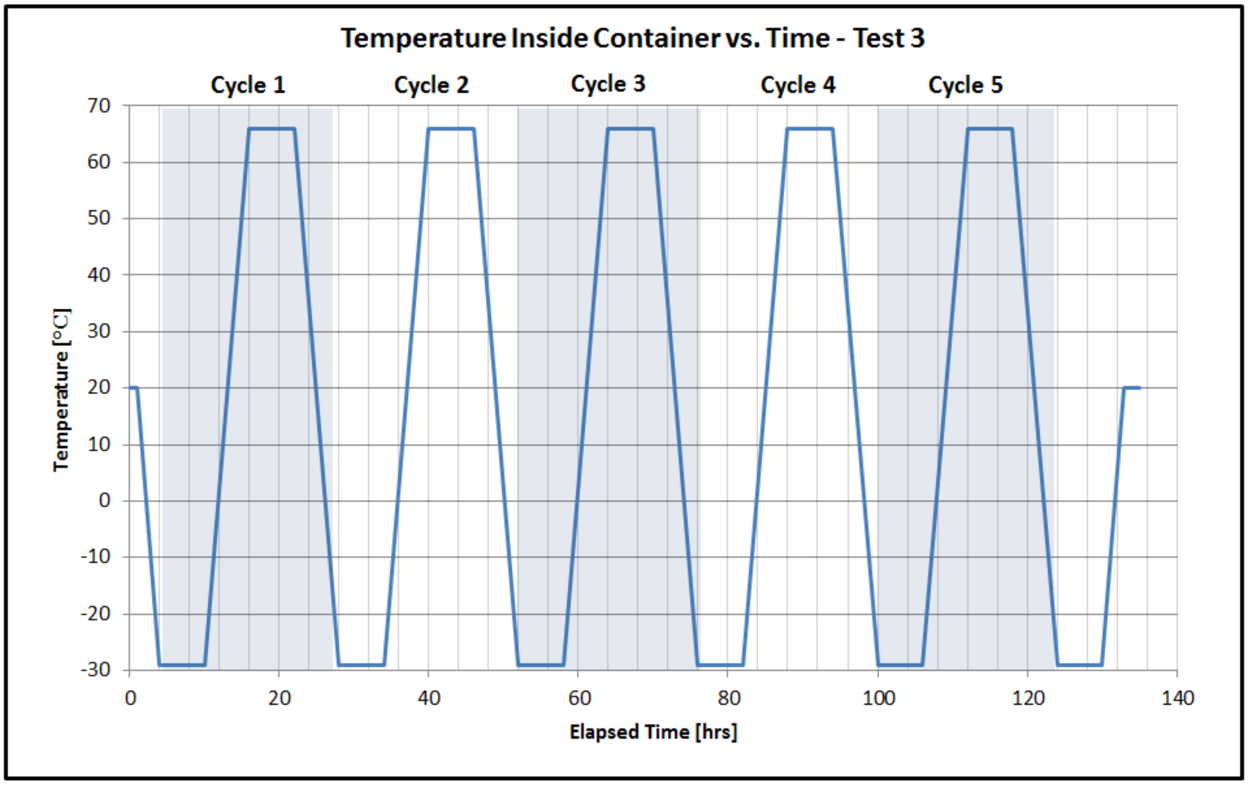

Figure 10. Planned temperature profile for Test 3

Because the container is very well-insulated, the chamber struggled to overdrive the temperature outside the case to control the temperature inside. To more accurately simulate the targeted conditions, the detector was removed from the case, and the temperature profile displayed was controlled using the sensors built into the chamber. This allowed the detector to experience the desired temperatures without any issues.

The temperature profile shown in Figure 10 also involves six cold temperature soaks when only five are necessary for completing five diurnal hot/cold temperature cycles. Because of this, after completing the fifth and final high-temperature soak, the temperature in the chamber was ramped down to 20°C for the post-test neutron measurement. The temperature that was measured inside the chamber during Test 3 is shown in Figure 11.

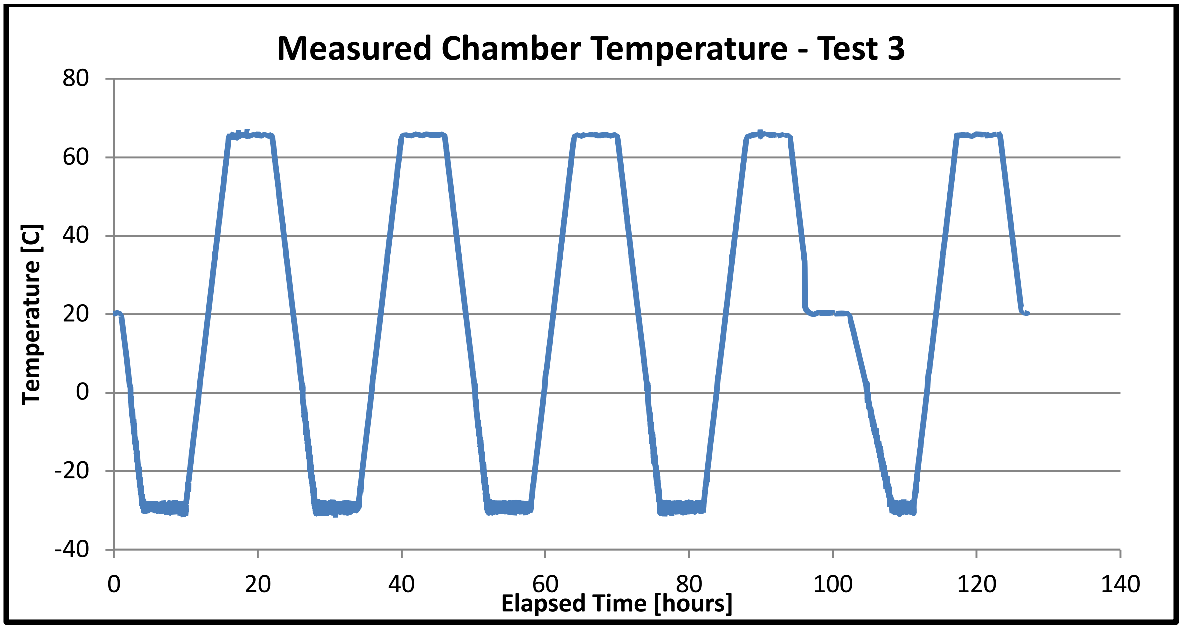

Figure 11. Chamber temperature measurement during Test 3

Figure 11 shows that the transition from the fourth high-temperature soak to the fifth low-temperature soak is not very smooth. This is because the chamber was inadvertently turned off while transitioning between the two temperatures. To avoid potential damage due to temperature shock, the temperature was held at 20°C for four hours before the fifth temperature cycle began.

The data obtained from each neutron measurement was analyzed and compared to ensure that the detector consistently makes accurate measurements after exposure to the specified environmental conditions. The results are displayed and discussed in the data analysis section.

TEST 4 – CAPABLE OF STORAGE IN EXTREME TEMPERATURE AND RELATIVE HUMIDITY ENVIRONMENTS: -29°C AT 10% RELATIVE HUMIDITY TO 38°C AT 95% RELATIVE HUMIDITY

The original temperature/humidity profile that was going to be used for Test 4 is displayed in Figure 12.

Figure 13 shows that the humidity in the chamber was not held at 10% during the cold and dry soak; the humidity in the chamber fluctuated between 40-50% during the duration of the -29°C soak. Work is currently being done to figure out why the low-humidity condition could not be controlled, and this part of the test will be redone in the future. The hot and humid soak produced conditions very close to those called out in the test specification. Measurements were performed before the cold soak, after the cold soak, before the hot soak, and after the hot soak. The analysis of the data collected from those tests is shown in data analysis section.

The detector remained inside its case for the entirety of this test. The only changes made to the temperature/humidity profile used for the actual test was to bring the chamber humidity to 0% when performing neutron counts. Also shown is the amount of time that the MC-15 sat at room temperature between cold and hot soaks for logistical reasons. The actual temperature/humidity measured in the chamber during Test 4 is shown in Figure 13.

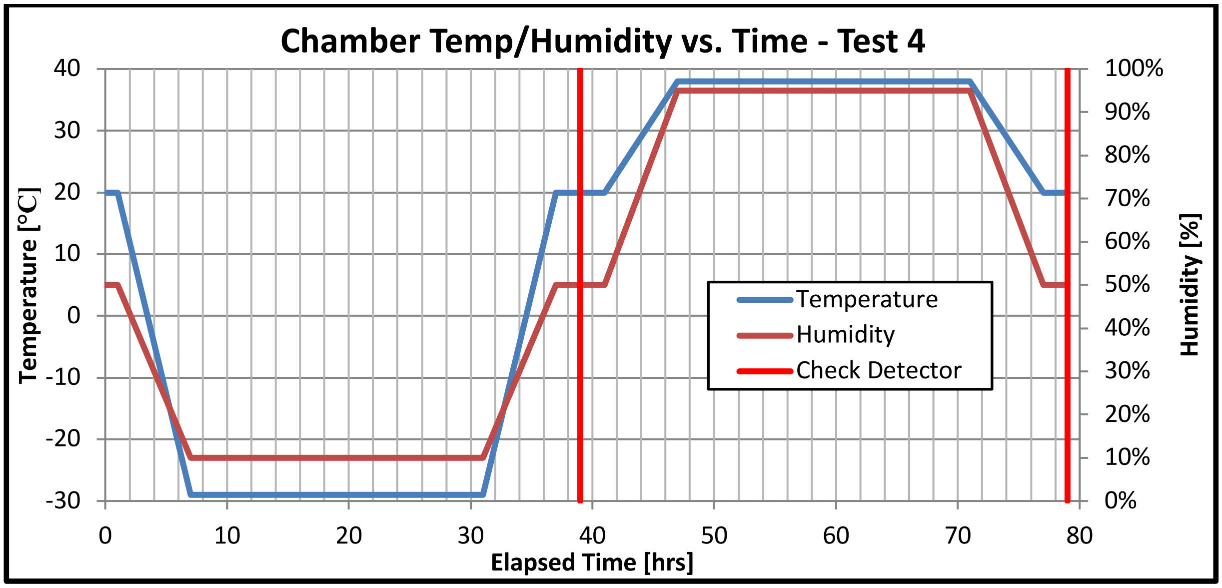

Figure 12. Plot of original temperature/humidity profile to be used for Test 4.

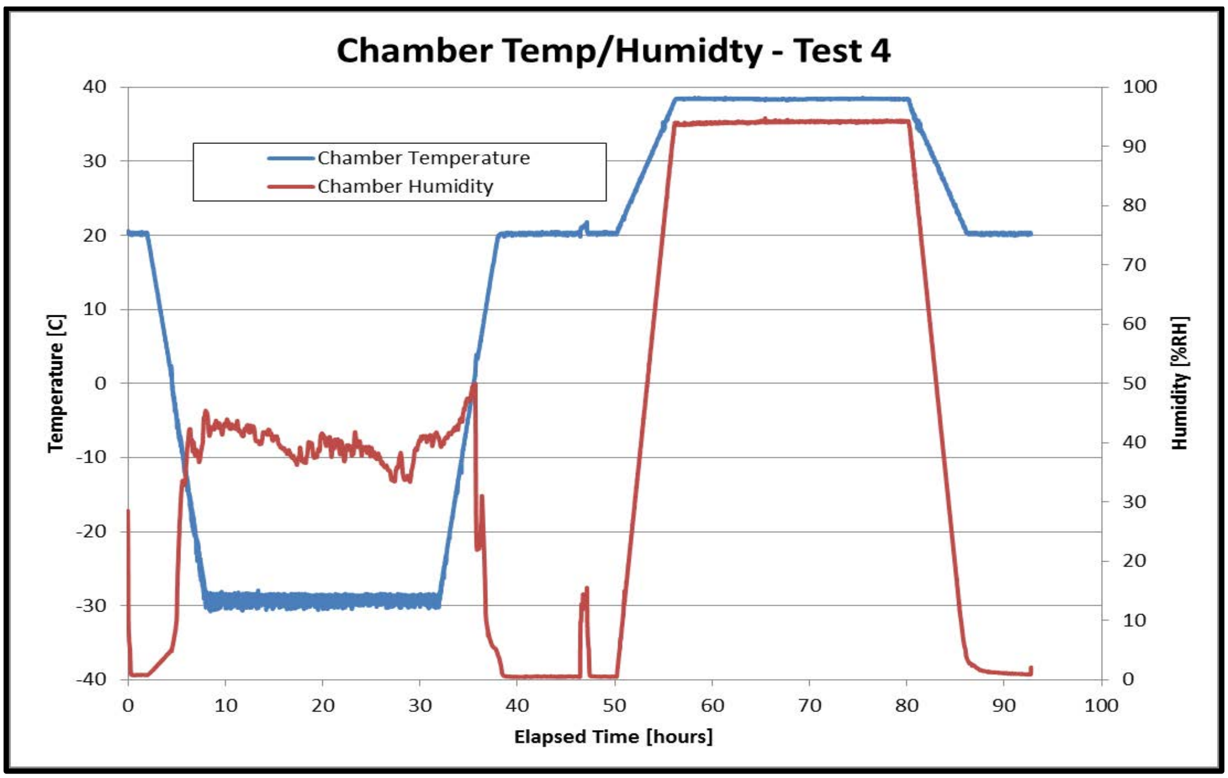

Figure 13. Actual temperature and humidity conditions created for Test 4.

Test 5 – Capable of Surviving and Performing Properly After Drops and Bumps in the Shipping Configuration

The plan for drop testing is as follows:

- Drop height must be 122 cm (48 in).
- Total of 26 drops must be performed:
    - Drop on each face; 6 drops;
    - Drop on each edge; 12 drops;
    - Drop on each corner; 8 drops.
- Floor receiving drop impact should consist of 2-in. thick plywood backed by concrete.

Before and after each drop, the MC-15 was subjected to the ^{252}Cf source.

Test 6 – Capable of Surviving and Performing Properly After Normal Vibrations Associated with Transportation

The test plan calls for simulating forklift, U.S. highway truck, helicopter, and jet aircraft transportation conditions. The detector is inside its case and non-operational while undergoing each vibration test. Before and after each vibration test, the detector was subjected to a ^{252}Cf source and a neutron measurement was made. The results from analyzing the collected neutron data are displayed and discussed in the data analysis section.

Test 6.1 – Forklift Handling

The forklift profiles shown in the test plan were created and run on the electrodynamic shaker. The vertical, transverse, and longitudinal shaker reference profiles and the actual shaker outputs can be viewed in Figure 14, Figure 15, and Figure 16, respectively.

The shaker was able to produce the specified profiles well. Because the amplitude of vibration was very low, there were occasional spikes in amplitude, but these did not have any significant effect on the RMS amplitude being applied to the detector as these spikes are on the order of 10^{-5} g of acceleration.

Test 6.2 – U.S. Highway Truck

The highway truck profiles shown in the test plan were created and run on the electrodynamic shaker. The vertical, transverse, and longitudinal shaker reference profiles and the actual shaker outputs can be viewed in Figure 17, Figure 18, and Figure 19, respectively.

The shaker was able to accurately produce the specified highway truck profiles.

Test 6.3 – UH60 (Blackhawk) Helicopter

The helicopter profile shown in the test plan was created, and the vertical test was run on the electrodynamic shaker. The shaker reference profiles and the actual shaker output can be viewed in Figure 20.

The shaker was able to accurately produce the specified helicopter profile. However, after the test was run, there were issues with operating the detector and the detector no longer recognized that the bottom battery was present, as shown in Figure 21 and Figure 22.

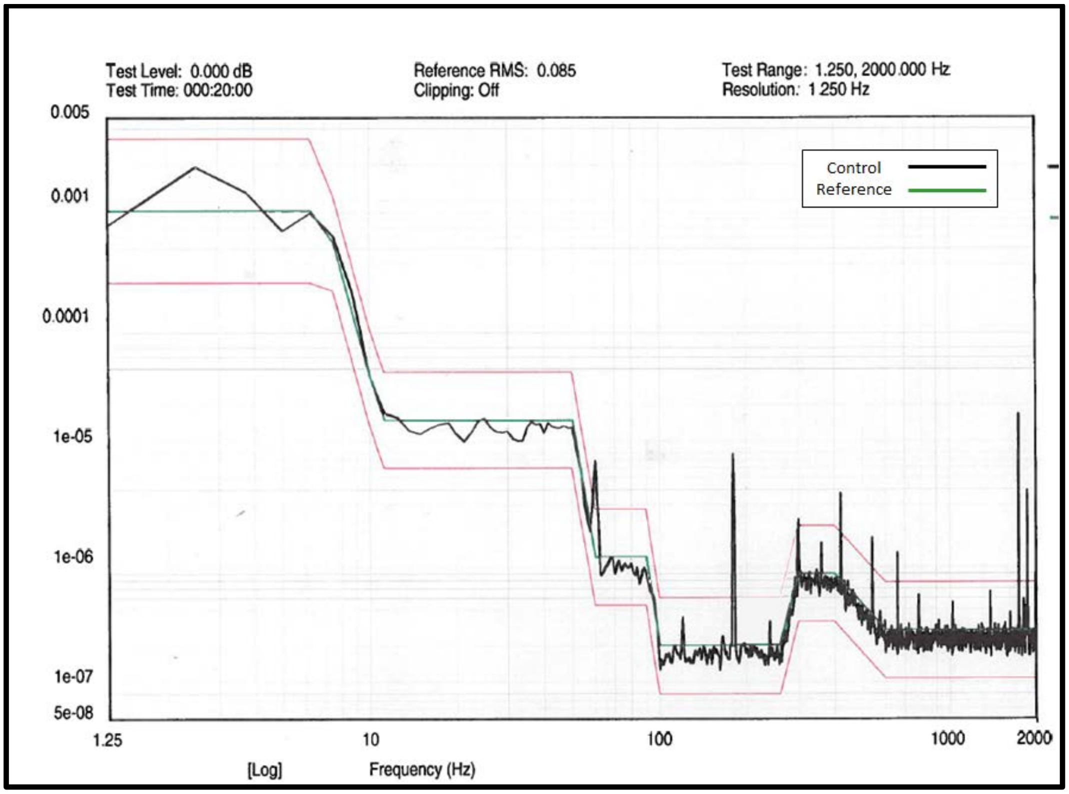

Figure 14. Vertical forklift control and reference profiles

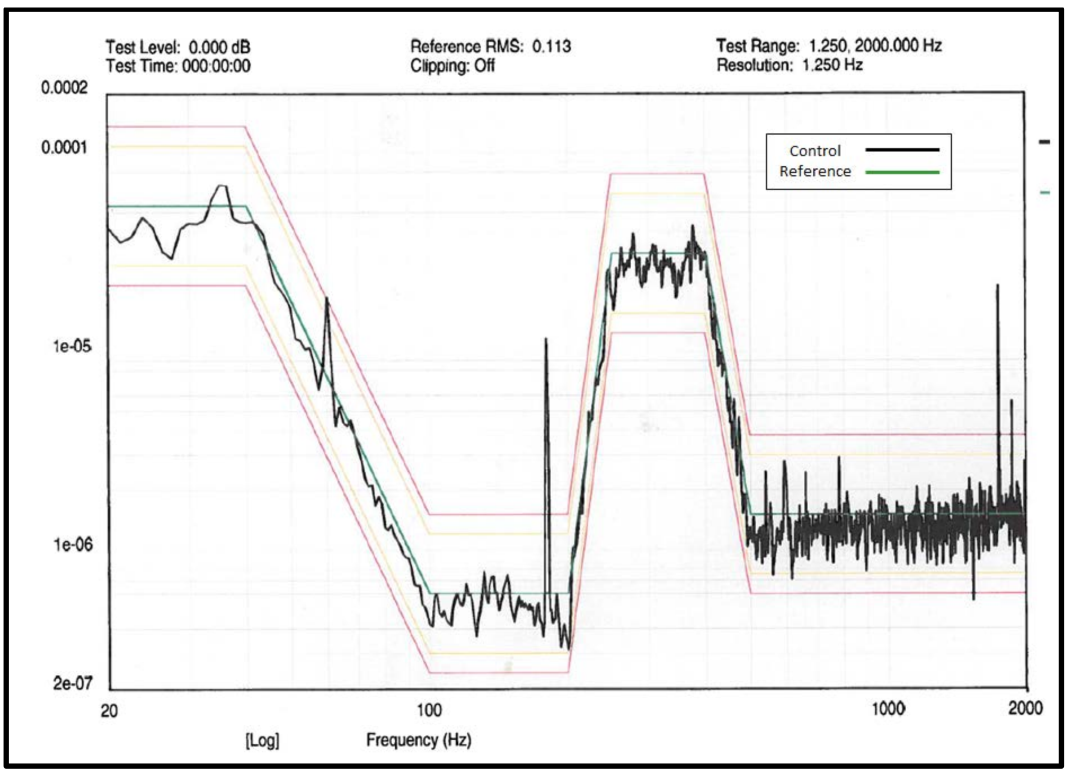

Figure 15. Transverse forklift control and reference profiles

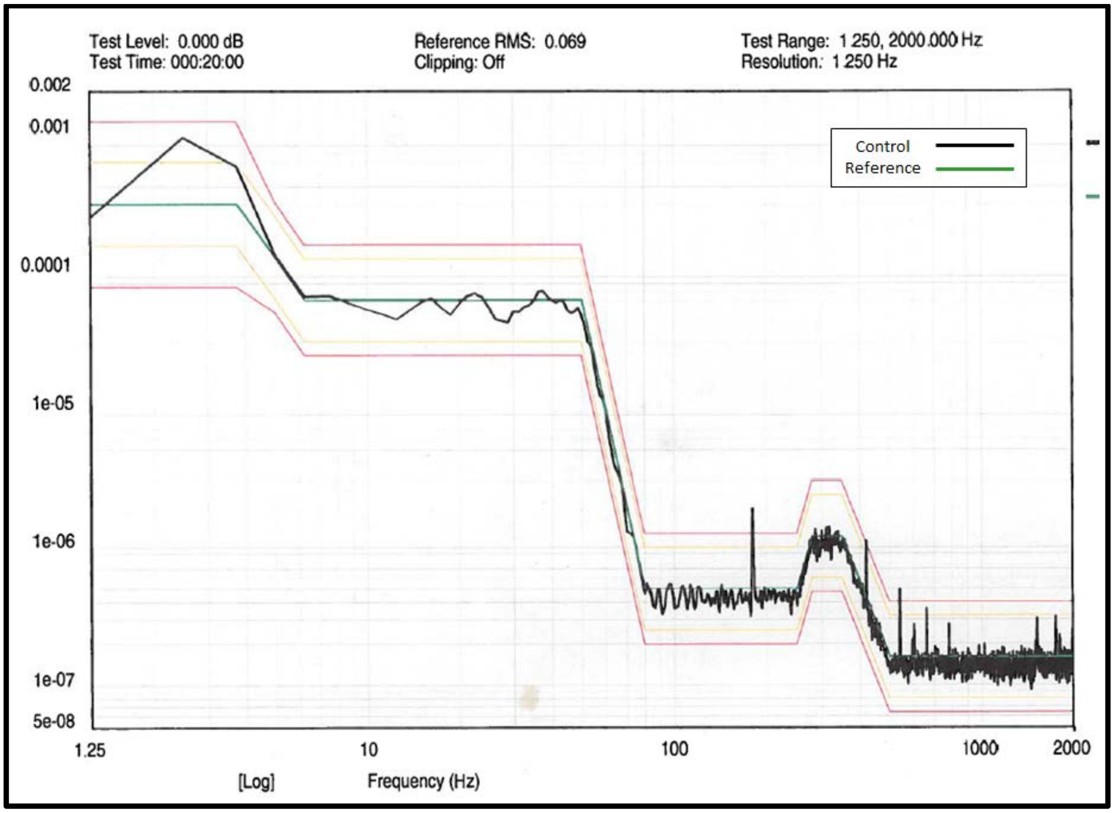

Figure 16. Longitudinal forklift control and reference profiles

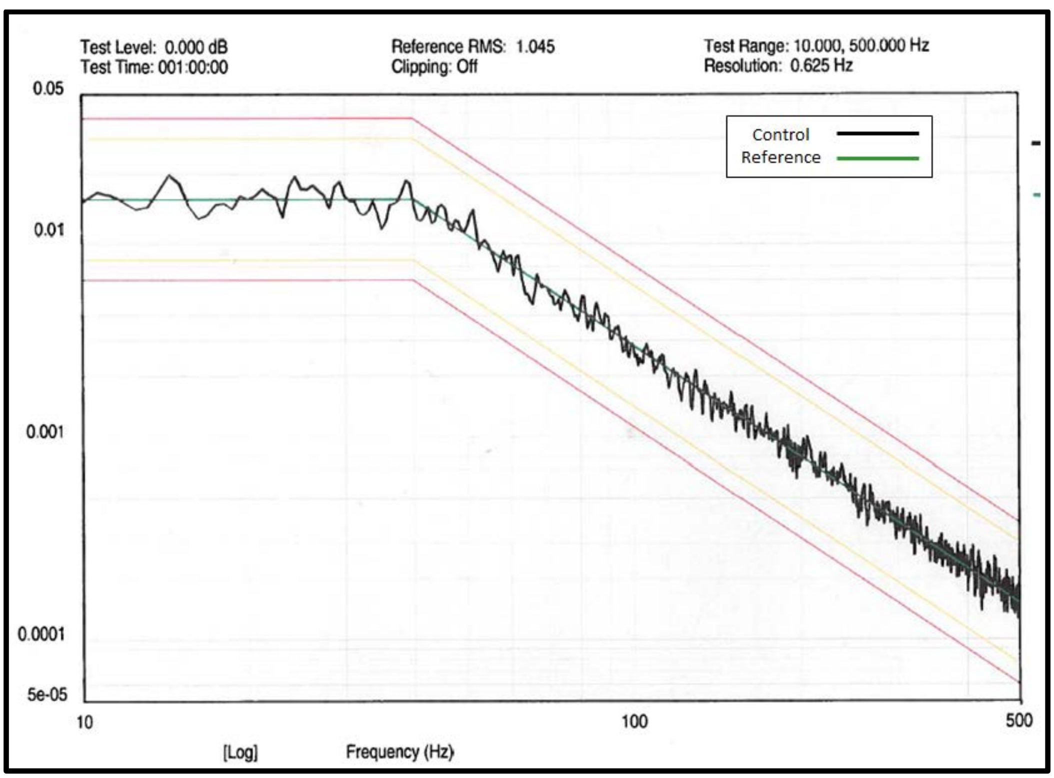

Figure 17. Vertical U.S. highway truck control and reference profiles

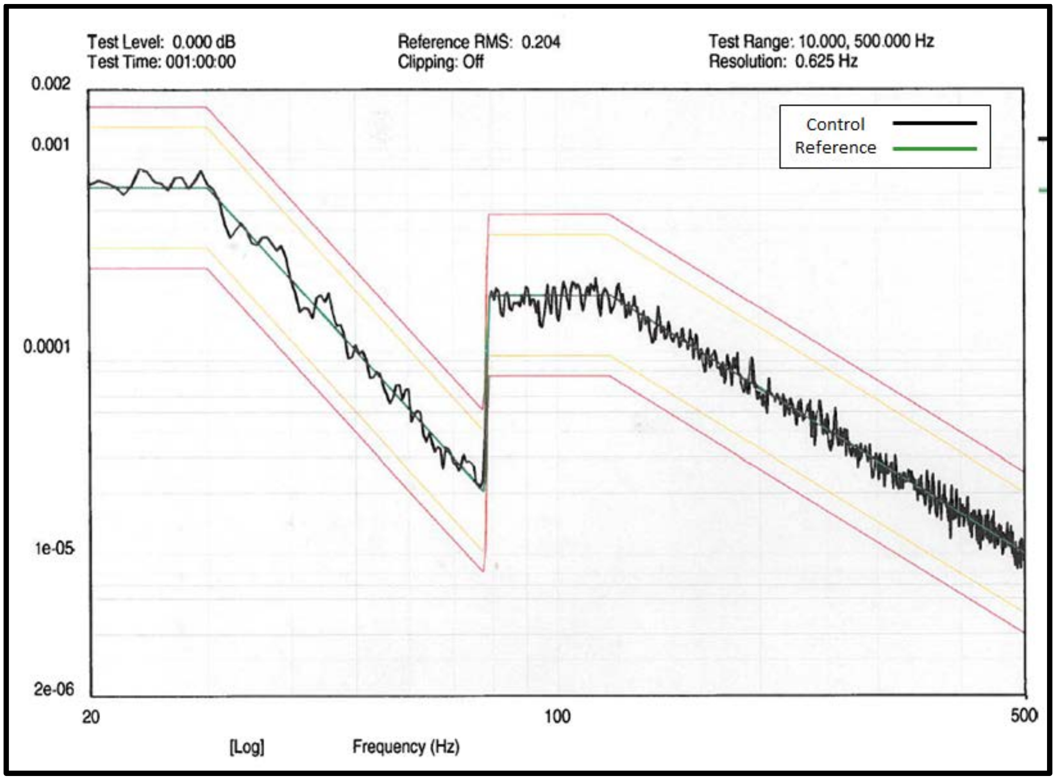

Figure 18. Transverse U.S. highway truck control and reference profiles

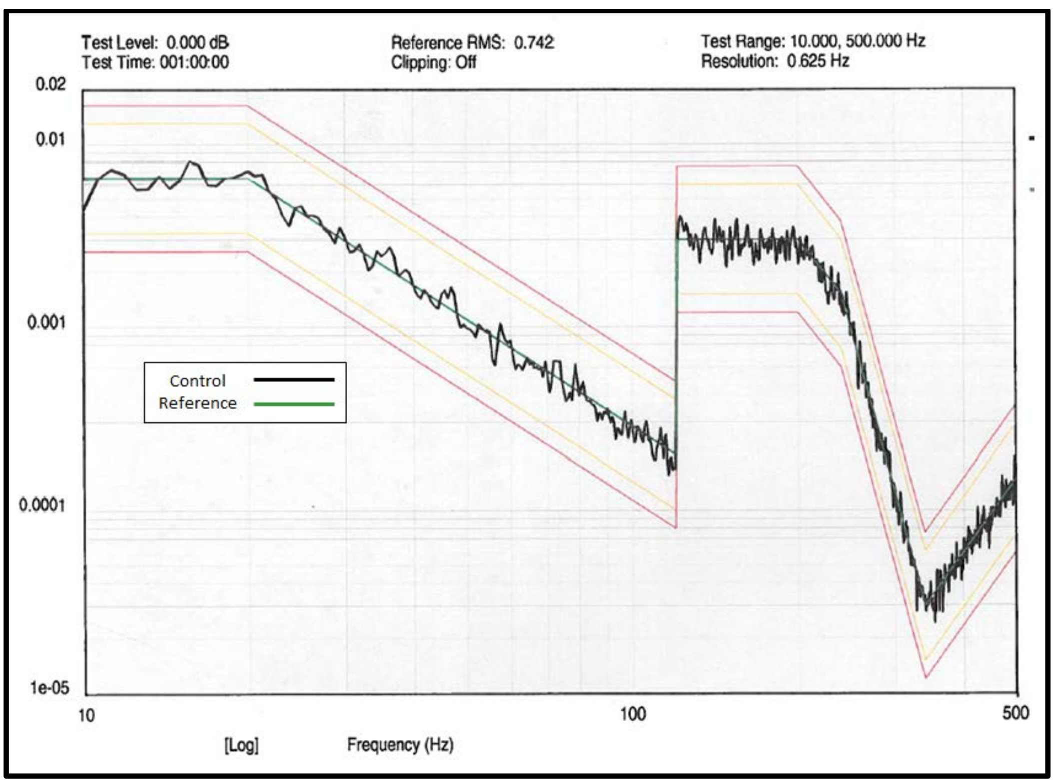

Figure 19. Longitudinal U.S. highway truck control and reference profiles

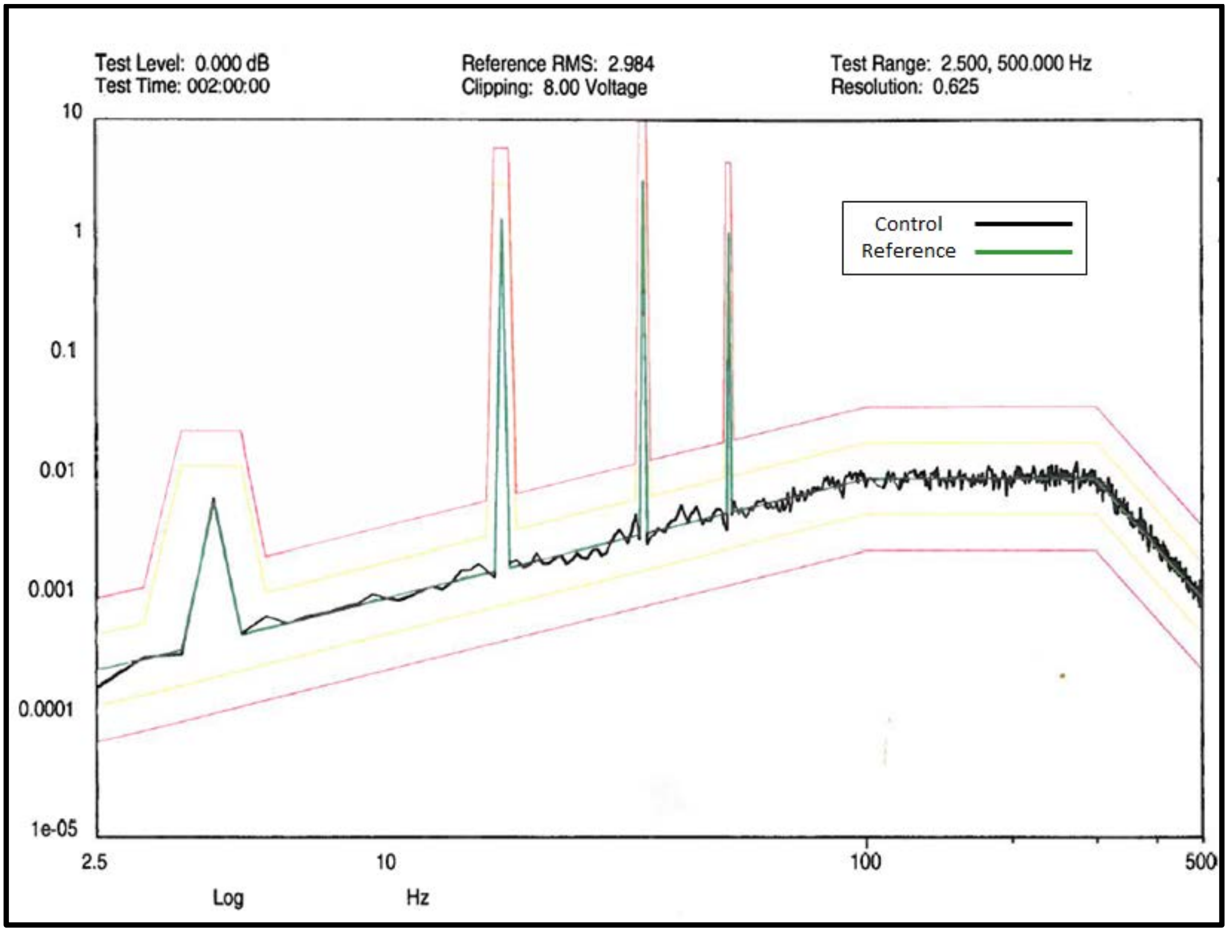

Figure 20. Vertical U.S. highway truck control and reference profiles

Figure 21. MC-15 main menu – bottom battery not present

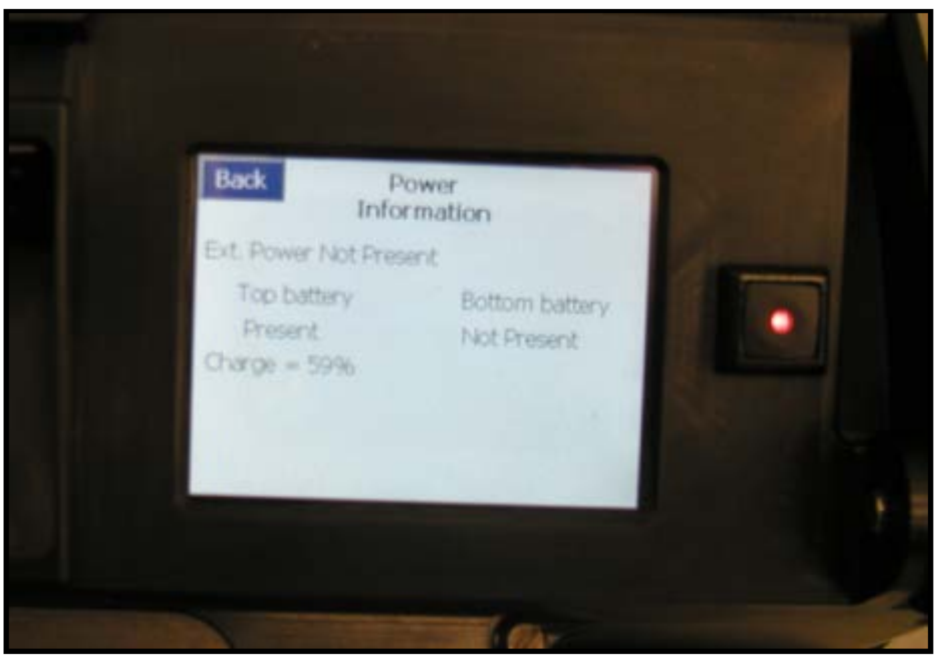

Figure 22. Power information display – bottom battery not present

The detector was still able to function using only the top battery, so a neutron measurement was able to be taken. During the count, all tubes appeared to be measuring data as they had for previous tests, so the only noticeable post-helicopter test problem was that the bottom battery stopped working. Analysis was performed on the collected data.

The bottom battery was removed from the detector and examined. The battery did not appear severely damaged, and the gage on the outside of the battery showed that the battery had a little more than half of its life remaining. To help diagnose the issue, the top battery was pulled out of its compartment and then placed in the bottom compartment, and the battery that had been in the bottom compartment was inserted into the top. The detector was turned on and recognized that both batteries were in place. A neutron measurement was made and the helicopter vibration test was re-run.

After the test, the detector was turned on and again exhibited problems with the recognizing the bottom battery and also had issues recognizing the top battery (which was causing problems when it was the bottom battery after the previous test). The detector was hooked up to external power and a neutron measurement was able to be performed, with all the tubes appearing to work properly. Analysis was performed on this data as well.

Rick Rothrock from LANL came out to perform additional diagnostic work for this battery problem. Two new batteries were placed in the detector. The detector was turned on and recognized that both batteries were present. For this test, the detector was turned on and connected to a computer through its data port prior to being placed in its case. This allowed Rick to observe if the batteries were functional during the test, and if the detector stops recognizing that one or both batteries are present mid-test. About 45-50 minutes into the two-hour test, the detector stopped recognizing the bottom battery while maintaining connection with the top battery. A neutron measurement was taken using power from the top battery, and analysis was again performed on the collected data.

The two batteries that were used for the first two helicopter tests and the two batteries that were used for the third helicopter test were sent to LANL for further inspection. He took the batteries apart and found that, for the batteries that were causing issues, the spades that create contact between the battery and the detector had broken off. This can be observed in Figure 23.

Figure 23. Spades broken off of one of examined batteries

Additional post-test analysis indicated that this failure was likely caused by an assembly error. There is a cushion (Part 12 in Figure 24), that was not included in the detector being tested. In addition, the cover (Part 15 in Figure 24) is made of a plastic material that is flexible enough to allow for battery motion within its compartment. A new cover was manufactured out of aluminum that was intended to be more rigid and restrict battery motion. Once the cover was received, the helicopter test was again performed to determine if the issue was resolved.

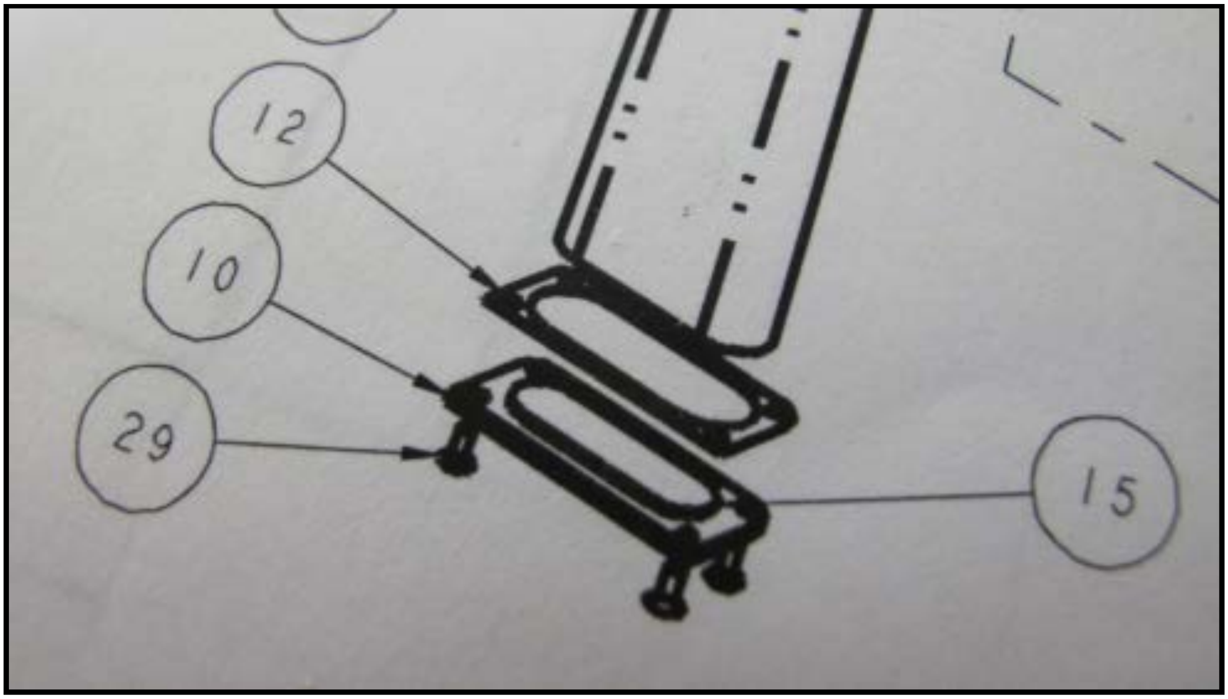

Figure 24. Portion of stack assembly drawing for MC-15

Test 6.4 – Jet Aircraft Cargo

The jet aircraft profile shown in the test plan was also run.

Test 7 – Remains Operational Over the Temperature Range of -23°C to 54°C

Test 7 involves placing the MC-15 in the thermal chamber and, running the temperature profile shown in Figure 25 while the detector was turned on, the neutron output from the ^{252}Cf source was measured.

This test was run almost exactly as described in the test plan. The detector had to be connected to external power to conduct a 75 hour measurement, but this was not an issue because there is no moisture in the chamber that can damage exposed electrical inputs. The temperature that was measured in the chamber during Test 7 is shown in Figure 26.

The temperature inside the chamber follows the profile specified in the test plan very closely. The neutron data collected during this test was analyzed, and the results are displayed and discussed in the data analysis section.

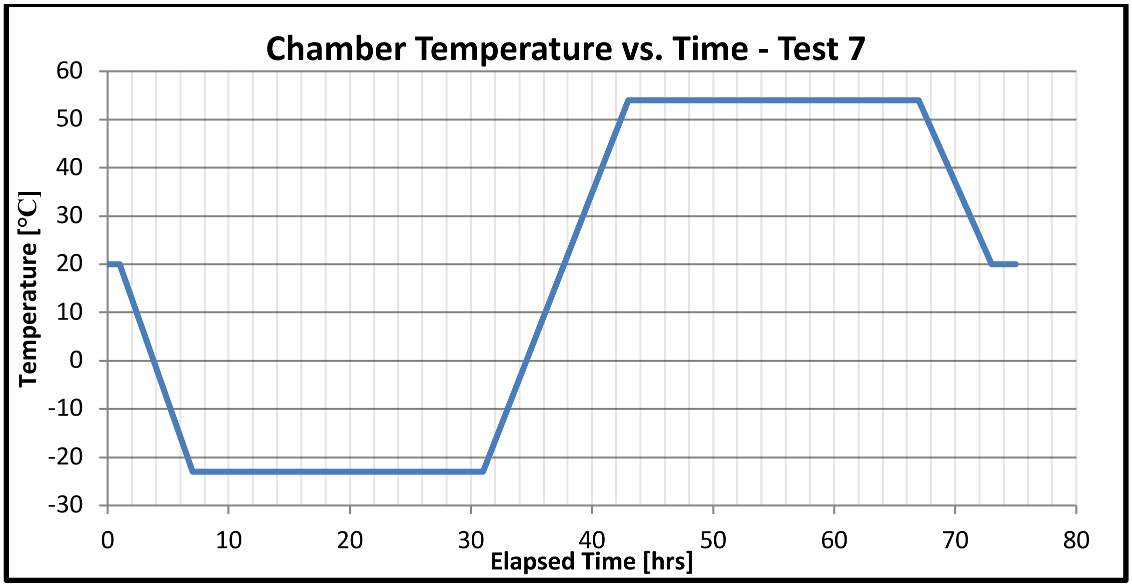

Figure 25. Planned temperature profile for Test 7

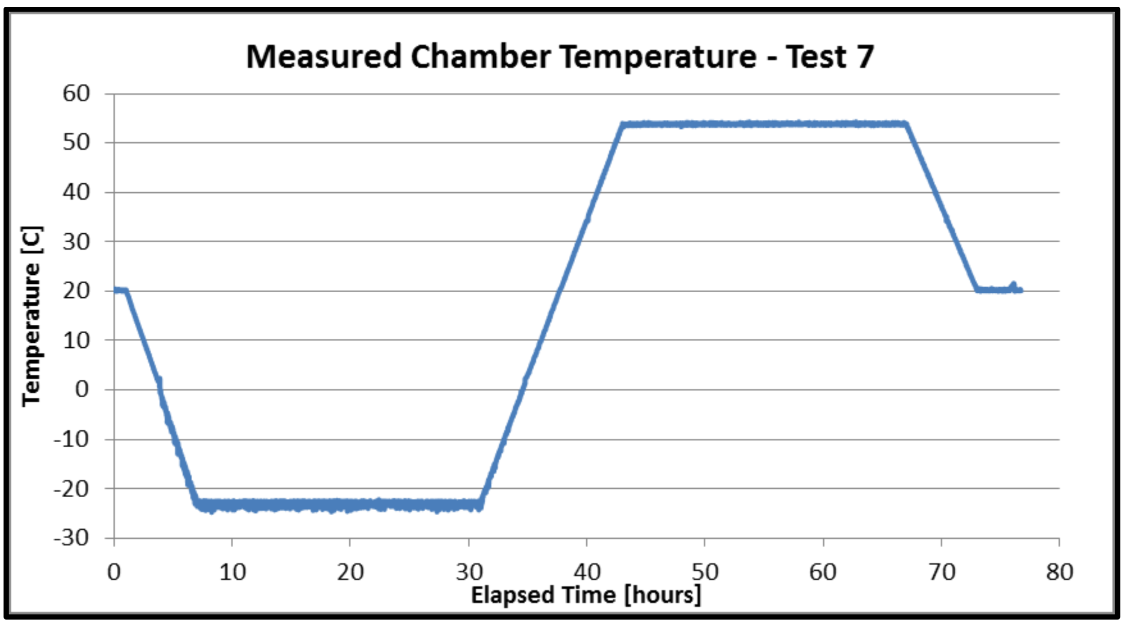

Figure 26. Temperature measured inside chamber while conducting Test 7

TEST 8 – REMAINS OPERATIONAL WITHOUT DEGRADATION IN SPECIFIED PERFORMANCE AND WITH NO PHYSICAL DAMAGE SUSTAINED DURING AND AFTER EXPOSURE FOR TWO MINUTES TO A FINE WATER SPRAY AT A FLOW RATE OF 4 LITERS/MINUTE WITH THE SPRAY NOZZLE TWO METERS FROM THE INSTRUMENT

Test 8 involves turning on the detector and placing it in the rain room in the presence of a ^{252}Cf neutron source. Six tests are to be performed; one test for each detector surface being directly impacted by the water, with each test lasting two minutes. This test has yet to be performed and will be conducted after all other tests are completed.

ANALYSIS OF DATA COLLECTED BY MC-15 BEFORE/DURING/AFTER ENVIRONMENTAL TESTING

The data that was collected from Tests 2, 3, 4, 5, 6, and 7 was analyzed. The detection efficiency and estimation of the ^{252}Cf mass are shown in Figure 27 and Figure 28, respectively.

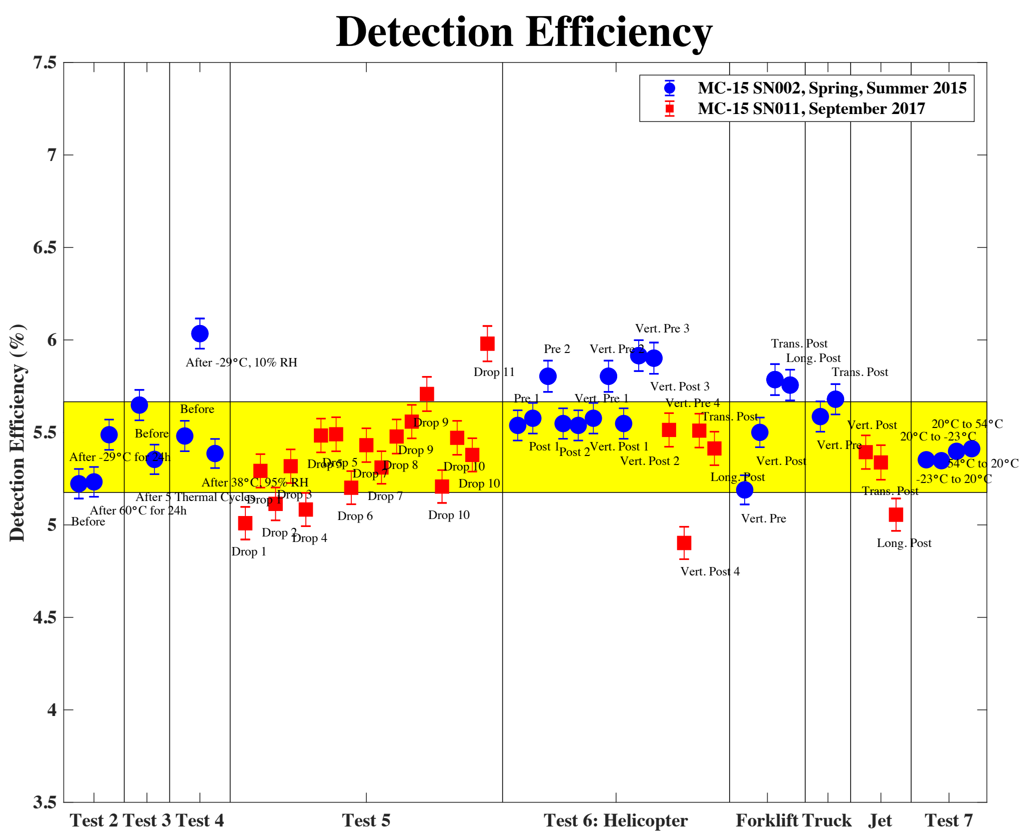

Figure 27. MC-15 detection efficiency. The yellow band is the combined result.

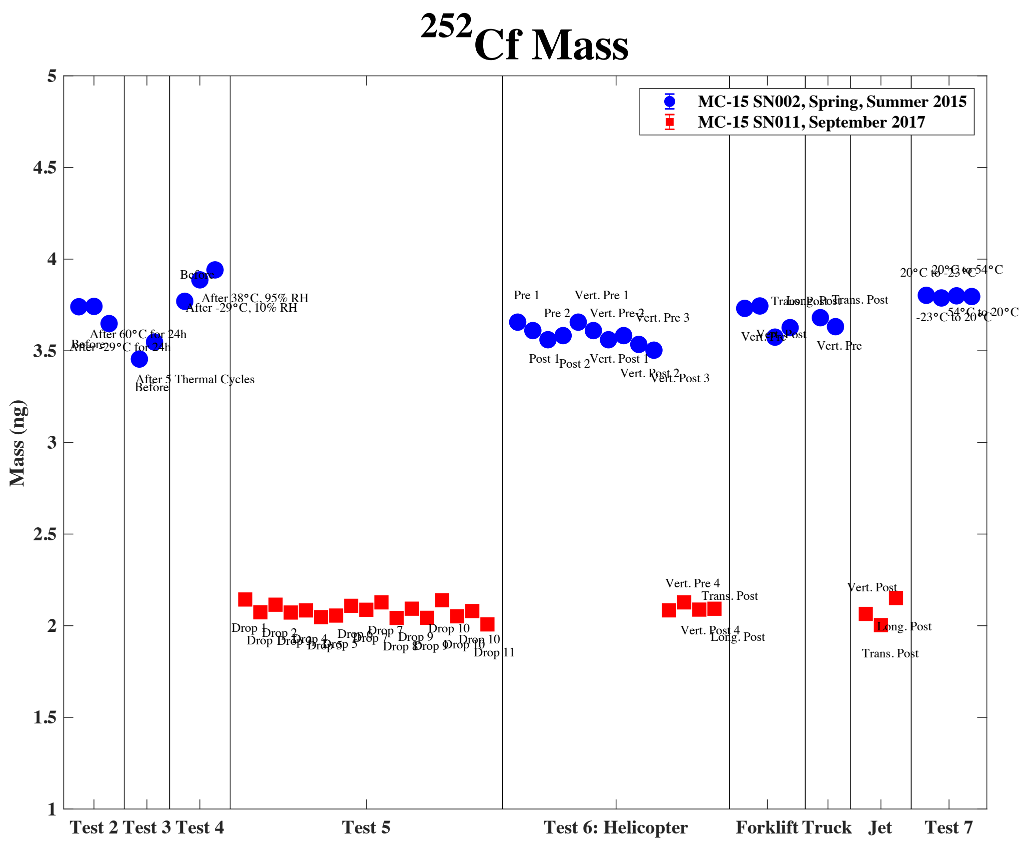

Figure 28. Estimation of ^{252}Cf mass from collected neutron data

Figure 27 shows that the detection efficiency of the MC-15 while in the presence of the ^{252}Cf has been very consistent. The efficiency from all tests has been within 5-6%, while the results from most tests are close to 5.5%. The slight differences in efficiency are considered acceptable, and might be due to having the ^{252}Cf source slightly more or less than six inches away from the detector while collecting data. The consistent detection efficiency shows that the detector is accurately capturing neutron data after being subjected to each tested environment.

Figure 28 shows the estimate of ^{252}Cf based on the collected neutron data from each test. The nominal mass of the source during the summer of 2015 was stated to be 3.9 ng, but the actual mass could have been up to 15% more or less than that amount. Also, because the source was not brand new, its neutron-producing mass was lower than it once was because of radioactive decay. By September 2017 when the tests of SN011 were conducted, a little less than a half-life had passed and the mass of ^{252}Cf was significantly less. This is borne out in the figure. Figure 28 shows that the mass estimates from each test are very consistent and are well within the +/- 15% range. The accuracy of the mass estimates shows that the detector is functioning very well after each tested environment.

The water spray tests, Fig. 29, also showed the detector to be robust.

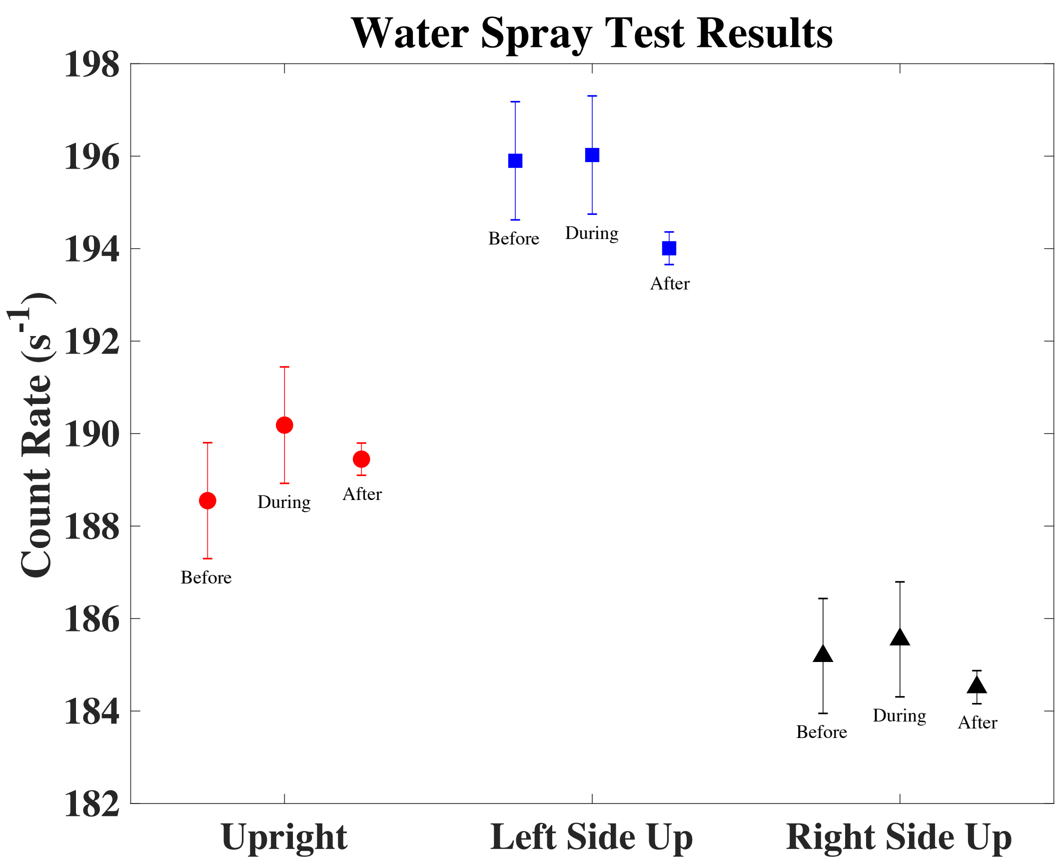

Figure 29. Count rates recorded for the water spray tests.

The MC-15 was set up to record 15 consecutive sets of data, each dataset containing two minutes' worth of data. The test operator would set up and start the test, exit the rain room and close it up, then turn on the water after two minutes had passed, and finally turn off the water after another two minutes had passed. The detector would then collect data for the remaining 26 minutes without water being sprayed.

This process was followed for the three tests conducted in the following orientations:

1. standing upright (Figure 30);
2. resting on right side (Figure 31);
3. resting on left side (Figure 32).

For each test, the neutron source was positioned approximately 6 inches from the front of the detector. Images from each test are shown below.

In addition to collecting data, the detector was checked after each test to determine if water had gotten through the seals used to protect electronic ports and the batteries. Water did not seem to get through any of the seals. However, caution should be used when opening up the covers. The rubber seal on the backs of the covers will protect the electronics during the test, but when the detector was still wet after the test and the covers were open, small amounts of moisture were able to get close to the electronics.

The touch screen appears to be less responsive than usual when it is wet. The touch screen is not always responsive even when it is dry, so this issue may not be exclusively due to the wet conditions.

The MC-15 appeared to operate normally in the raining environment. Further, it appeared to work well during the subsequent measurement campaign at the DAF. As noted, care should be taken when opening up covers when the detector is wet.

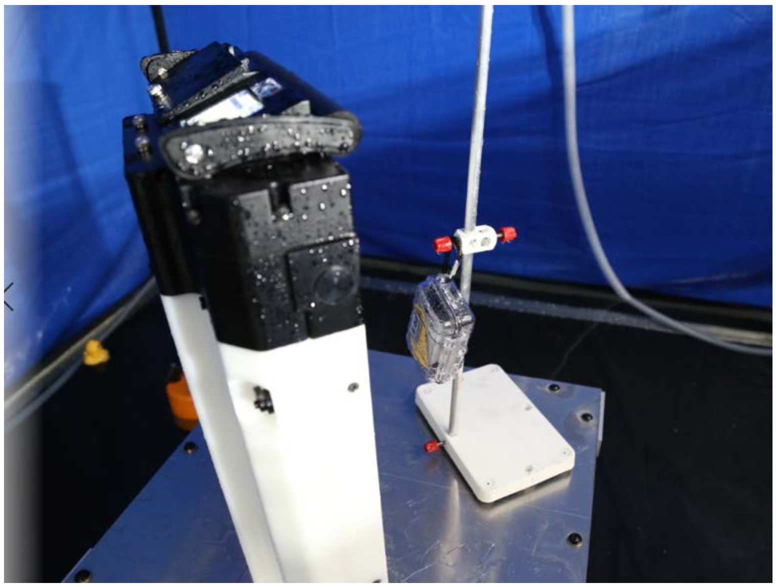

Figure 30. Detector standing upright (Test 1)

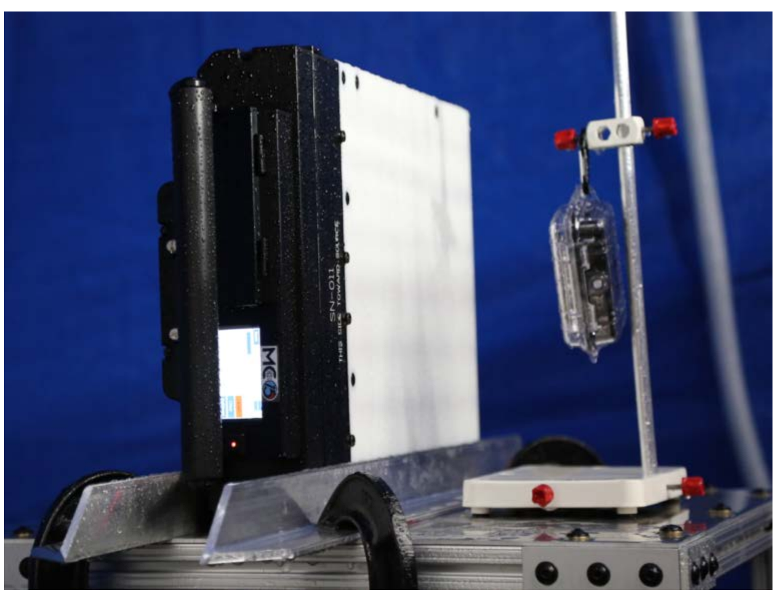

Figure 31. Detector resting on its right side (Test 2)

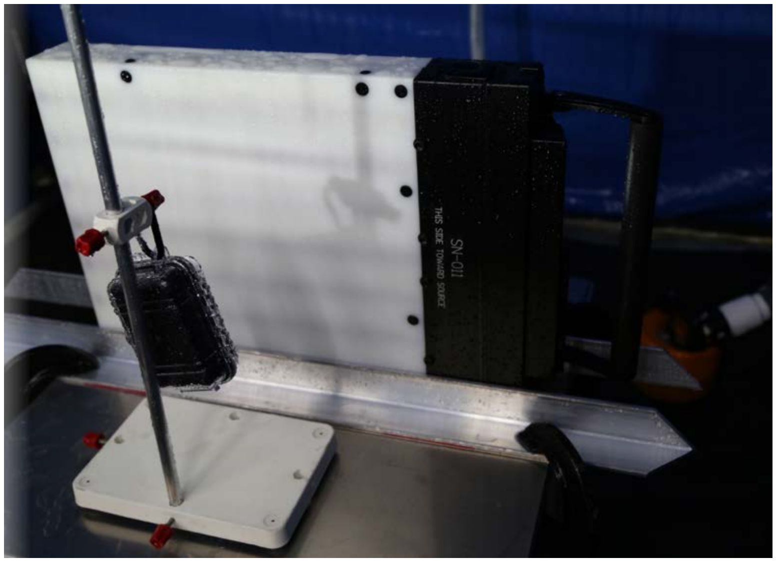

Figure 32. Detector resting on its left side (Test 3)

EM TESTS

Testing Conducted

- Operation with single-phase AC; 100 V to 240 V, 47 Hz to 63 Hz
- RF fields from 80 MHz to 2.5 GHz at 10 V/m
- 10 G DC magnetic fields in three orthogonal directions

Test Requirements and Procedures

See http://www.nist.gov/pml/div682/grp04/ansieeen42.cfm for the Protocol.

Testing and Evaluation Protocol for Portable Radiation Detection Instrumentation for Homeland Security T&E Protocol N42.33, 2013

Testing and Evaluation Protocol for Radiation Detection Portal Monitors for Use in Homeland Security T&E Protocol N42.35, 2013.

This protocol was applied to instrument operation with the AC power module using both the European and North American power and frequency standards.

Tests were performed in a space where neutron sources are allowed so instrument performance was evaluated using the average neutron background count as the performance indicator. Instrument count periods default to 1000s duration with background averages being 1.5-2 neutrons/s.

Operation using AC power with variations in voltage and frequency was accomplished using a leased power supply chassis. The power module was first tested using a resistive load with a moderate current draw to ensure that its operation under 'abnormal' conditions would not damage the neutron instrument. The instrument uses internal batteries for operation but testing included performance with charged and partially drained batteries.

Results Summary

No abnormal responses were noted in the neutron background count during any of the tests. Individual test record sheets are attached with description and instrument readings list.

NIST	TEST AND EVALUATION PROTOCOL	TEP NO. N42.35	PREPARED BY: DIV682	
	TITLE: Radiation Detection Portal Monitors for Homeland Security	EFF. DATE 2013-05-30	REV. 3.00	PAGE 1 of 1
	Software version used for V&V of Spreadsheets: Microsoft Excel 2010 (compatibility mode)			

Section 8.3 AC Line Voltage Operation
Test Data and Report

Manufacturer: LANL Neutron Coincidence Instrument

Model: MC-15 **Serial Number:** 2

Requirement: For those monitors capable of operating from 120/240 volts power, the requirement is: AC lines with a supply voltage that is within ±12 % of the nominal voltage and within ±3 % frequency.

Note: The instrument is portable but also uses a modular power supply for recharging internal batteries or operating for extended periods, nominal operation is marked as 100-240V 50/60 Hz.

Ambient Conditions: 23 °C ________ %RH ________ mmHg

Gamma Source Data: No gamma source used

Neutron Source Data: Background neutron count used, 1000s counting period

Test Data

	Nominal Voltage	
	condition	Neutron
Readings		
1	120 @ 60	1.92
2	100 @ 47	2
3	100 @ 63	1.93
4	240 @ 50	1.94
5	240 @ 47	1.96
6	240 @ 63	2.02
7	248 @ 47	1.81
8	248 @ 63	1.87
9	Bkgn 1	1.92
10	Bkgn 2	1.81
Mean		1.92
STD		0.07
COV		3.69%

Condition shows the voltage and frequency used for each test. Background measurements used the internal battery.

Acceptance Range - Neutron

1.63 (-15%) to 2.21 (+15%) (add units)

	100V @ 47 Hz		100V @ 63Hz		248V @ 47Hz		248V @ 63Hz	
	PS V/I	Neutron	PS V/I	Neutron	PS V/I	Neutron	PS V/I	Neutron
Readings								
1	23.35 / 0.2333	2 n/s	23.34 / /0.2333	1.93	23.32 / 0.2331	1.81	23.32 / 0.2332	1.87
2								
3								
4								
5								
6								
7								
8								
9								
10								
Mean	#DIV/0!	#DIV/0!	#DIV/0!	1.93	#DIV/0!	1.81	#DIV/0!	1.87

Are Results Within Range?		
	Yes	no
Voltage +12%	Yes	
Voltage -12%	Yes	
47 Hz	Yes	
63 Hz	Yes	

Measurements were made using a variable voltage and frequency power supply over the range of the power supply module. A fixed load resistor was used for the voltage / current measurements prior to full instrument testing to ensure that the instrument would not be damaged.

Comments: ____________________

Completed by: Emer Baluyot **Date:** 12/15/2015

Reviewed by: Ron Kane **Date:** 12/15/2015

Raw data are listed below, data were acquired 12/10/15 and 12/15/15

The following table lists measurements for the power supply module operating with a fixed resistive load prior ro testing with the Neutron Instrument.

Frequency	47 Hz		50 Hz		55 Hz		60 Hz		63 Hz		
Voltage	V	A	V	A	V	A	V	A	V	A	
100 V	23.35	0.2333	23.34	0.2333	23.34	0.2333	23.34	0.2333	23.34	0.2333	Measured 12/10/15
120 V	23.33	0.2332	23.33	0.2332	23.33	0.2333	23.33	0.2333	23.33	0.2333	Measured 12/10/15
240 V	23.33	0.2332	23.33	0.2332	23.33	0.2332	23.32	0.2332	23.32	0.2332	Measured 12/10/15
248 V	23.32	0.2331	23.32	0.2331	23.32	0.2332	23.32	0.2332	23.32	0.2332	Measured 12/15/15

Note: 0.7 V Voltage drop in Current Meter
Load is 100 Ohms (5x500 Ohms in Parallel)

Neutron background counts over a period of 1000 s were recorded as the power supply input voltage and frequency were adjusted to the listed

		Spurious Indicator		Instrument Alarm		
Voltage, Frequency	Average Rate	Yes	No	Yes	No	
Background (Batt)	1.92 n/s		X		X	Measured 12/10/15
120 V, 60 Hz	1.97 n/s		X		X	Measured 12/10/15
100 V, 47 Hz	2 n/s		X		X	Measured 12/10/15
100 V, 63 Hz	1.93 n/s		X		X	Measured 12/10/15
240 V, 50 Hz	1.94 n/s		X		X	Measured 12/10/15
240 V, 47 Hz	1.96 n/s		X		X	Measured 12/10/15
240 V, 63 Hz	2.02 n/s		X		X	Measured 12/10/15
Background (P/S)	1.81 n/s		X		X	Measured 12/15/15
248 V, 47 Hz	1.81 n/s		X		X	Measured 12/15/15
248 V, 63 Hz	1.87 n/s		X		X	Measured 12/15/15

	TEST AND EVALUATION PROTOCOL	TEP NO. N42.33	PREPARED BY: DIV682	
NIST	TITLE: Portable Radiation Detection Instrumentation for Homeland Security	EFF. DATE 2013-05-30	REV. 3.00	PAGE 1 of 1
	Software version used for V&V of Spreadsheets: Microsoft Excel 2010 (compatibility mode)			

Sections 8.3 - Magnetic Fields
Test Data and Report

Manufacturer: LANL Neutron Multiplicity Counter
Model: MC-15 **Serial Number:** 002

Requirements: The instrument should be fully functional when exposed to a constant DC magnetic field in three mutually orthogonal orientations relative to a 10 Gauss magnetic field.

Note: Comments are required when a test requirement is not verified.

Ambient Conditions: 23 °C ____ %RH ____ mmHg
Test Equipment Used: Helmholtz Coil, HP DC Power Supply 6002A, Gauss/Tesla Meter 5080
Source Data:

Measurement Results Without Sources

	Orientation					
	Initial		Second		Third	
	Yes	No	Yes	No	Yes	No
Did the instrument alarm during the test?		X		X		X
Did the instrument display spurious indications?		X		X		X

Observations: Counts are recorded using background events in Neutrons/s over a 1000 s counting period

Measurement Results (No Neutron Source)

Coil V/A	12.6V, 5.8A		14.9V, 6.8A		13.3V, 6.1A		
	Initial Orientation		Second Orientation		Third Orientation		
	Nominal Zero Intensity	10 Gauss (DC)	Nominal Zero Intensity	10 Gauss (DC)	Nominal Zero Intensity	10 Gauss (DC)	
P/S 1	1.81	1.84	1.88	1.9	1.86	1.95	Neutrons/s over 1000 s count interval
P/S 2	1.82	1.81	1.89	1.83	1.85	1.94	
P/S 3	1.89	1.82	1.81	1.9	1.84	1.96	
Batt 4	1.74	1.83	1.81	1.87	1.81	1.83	
Batt 5	1.78	1.81	1.82	1.74	1.93	1.81	
Batt 6	1.88	1.86	1.92	1.86	1.91	1.88	
7							
8							
9							
10							
Mean	**1.82**	**1.83**	**1.86**	**1.85**	**1.87**	**1.90**	
STD	**0.06**	**0.02**	**0.05**	**0.06**	**0.05**	**0.06**	
COV%	**3.17%**	**1.06%**	**2.57%**	**3.24%**	**2.41%**	**3.42%**	

Acceptance Range

Initial Orientation:	**1.55**	to	**2.09**	
Second Orientation:	**1.58**	to	**2.13**	
Third Orientation:	**1.59**	to	**2.15**	
	low -15%		high +15%	

Comments: The instrument is fairly large for the 1-m Helmholtz coil set, a portable gaussmeter was used to measure the field at the extremes to ensure a minimum of 10 G, the center peak was approximately 12 G.

Completed by: Emer Baluyot **Date:** 12/14/2015

Reviewed by: Ron Kane **Date:** 12/14/2015

	TEST AND EVALUATION PROTOCOL	TEP NO. N42.33	PREPARED BY: DIV682	
NIST	TITLE: Portable Radiation Detection Instrumentation for Homeland Security	EFF. DATE 2013-05-30	REV. 3.00	PAGE 1 of 1
	Software version used for V&V of Spreadsheets: Microsoft Excel 2010 (compatibility mode)			

Section 8.2 Radio Frequency Susceptibility Test Data and Report

Manufacturer: LANL Neutron Coincidence Instrument

Model: MC-15 **Serial Number:** 2

Requirements: The instrument shall not be affected by radio frequency (RF) fields over the frequency range of 80 MHz to 2.5 GHz at an intensity of 10 volts per meter (V/m). No alarms shall occur as a result of the RF radiation alone.

Note: Comments are required when a test requirement is not verified.

Ambient Conditions: 23 °C ______ %RH ______ mmHg

Test Equipment Used: Various antennas and amplifier combinations were used in this evaluation. No radiation source was used, only neutron background counts were observed.

Source Data: No source, background only

Frequency:80 MHz-200 MHz 10V/m
Sweep Time:5 Seconds, Amplifier Pin:-10 dBm
Equipment:HP 8665A, AR 25W1000M7, EMCO 3104 SN 2875, ETS HI-6105

	1000 Sec Count	Instrument Alarm		Spurious Indicator	
	Average Count	Yes	No	Yes	No
Background	1.80 n/s		X		X
1st Orientation	1.80 n/s		X		X
2nd Orientation	1.81 n/s		X		X
3rd Orientation	1.75 n/s		X		X

Frequency:200 MHz-1 GHz 10V/m
Sweep Time:5 Seconds, Amplifier Pin:-10 dBm
Equipment:HP 8665A, AR 25W1000M7, EMCO 3106 SN 2336, ETS HI-6105

	1000 Sec Count	Instrument Alarm		Spurious Indicator	
	Average Count	Yes	No	Yes	No
Background	1.74 n/s		X		X
1st Orientation	1.73 n/s		X		X
2nd Orientation	1.83 n/s		X		X
3rd Orientation	1.75 n/s		X		X

Frequency:1 GHz-2 GHz 10V/m
Sweep Time:5 Seconds, Amplifier Pin:-9 dBm
Equipment:HP 8665A, SM0520-36H SN 10826, AR AT4002A SN 0328239, ETS HI-6105

	1000 Sec Count	Instrument Alarm		Spurious Indicator	
	Average Count	Yes	No	Yes	No
Background	1.73 n/s		X		X
1st Orientation	1.74 n/s		X		X
2nd Orientation	1.72 n/s		X		X
3rd Orientation	1.73 n/s		X		X

Frequency:2 GHz-2.5 GHz 10V/m
Sweep Time:5 Seconds, Amplifier Pin:-27 dBm
Equipment:HP 8665A, EM Power 2122 SN 1001, AR AT4002A SN 0328239, ETS HI-6105

	1000 Sec Count	Instrument Alarm		Spurious Indicator	
	Average Count	Yes	No	Yes	No
Background	1.78 n/s		X		X
1st Orientation	1.75 n/s		X		X
2nd Orientation	1.75 n/s		X		X
3rd Orientation	1.68 n/s		X		X

Comments: **The instrument showed no interference effects due to illuminatoin by RF energy.**

Completed by: Emer Baluyot **Date:** 12/16/2015

Reviewed by: Ron Kane **Date:** 12/16/2015

* Note that observations shall include a list of all frequencies for which there was an unexpected alarm or a spurious indication. The alarm type and/or spurious indication observed shall be recorded for each frequency or range of frequencies.

SUMMARY

All tests have been completed. Test 1 shows that humidity does not have any significant effects on background neutron measurements. Tests 2, 3, 4, 5, 6, and 7 show that the detector can withstand/operate properly during or after all specified thermal/humidity conditions, vibrations, and drops. Test 8 shows that the MC-15 is impervious to water spray.

For the EM tests, no abnormal responses were noted during any of the tests.

With respect to Test 6, the helicopter transportation profile caused damage to the bottom battery of the detector. This was because a cushion meant to decrease the amount of space in the bottom battery compartment was not included, and because the bottom battery compartment cover was made of a plastic material that was not as rigid as the aluminum cover used for the top battery compartment. New aluminum covers for the bottom battery compartment were manufactured and transportation vibration testing then showed that, with the new cover in place, the batteries are robust.

NUCLEAR CRITICALITY SAFETY PROGRAM
U.S. DEPARTMENT OF ENERGY

Hands-On Training Courses

Managers Course	Apr 8 - 12, 2019
Managers Course	Jun 3-7, 2019
CSE Course	Aug 12 - 23, 2019
CSE Course	Jan 27 - Feb 7, 2020

Find out more

Focus Areas

Program Management
Integral Experiments
Nuclear Data
Analytic Methods
Information Preservation & Dissemination
Training and Education

Latest News

- What's New?
- NCSP Newsletters
- NCSP Calendar
- NCSP Five Year Execution Plan
- IE Section of the NCSP Five Year Execution Plan
- NCSP Mission & Vision
- Annual NCSP Technical Program Review
  - Previous Years' Presentation

Our Services

- Enroll in registry of criticality safety professionals
- Enroll in NCSP hands-on training courses
- Explore self-study criticality safety training modules
- Explore criticality safety key references and handbooks
- Submit a Nuclear Data Request
- Acquire NCSP criticality safety codes

Our Groups

- NCSP Organization
- NCSP Management Team
- NCSP Task Managers
- Criticality Safety Support Group (CSSG)
- Nuclear Data Advisory Group (NDAG)
- DOE Criticality Safety Coordinating Team (CSCT)
- NCSP Partners

National Criticality Experiments Research Center

Welcome to the National Criticality Experiments Research Center (NCERC), home to some of the most highly trained individuals and specialized capabilities on Earth.

September 5, 2018

Communications Office
(505) 667-7000

NCERC has long been part of the Laboratory's iconic history and its unique science will continue to drive the art of the possible– Evelyn Mullen, Associate Director for Threat Identification and Response

Imagine a resource so unique and specialized that there is only one in the country which services needs from around the world. Welcome to the National Criticality Experiments Research Center (NCERC), home to some of the most highly trained individuals and specialized capabilities on Earth. As Los Alamos National Laboratory celebrates 75 years of scientific excellence and nuclear expertise, it is fitting to recognize this essential capability focused on assuring the safety and security of operations involving nuclear materials throughout the United States and the world.

NCERC's foundation began in Los Alamos at the Laboratory's Technical Area-2 in 1943, but moved to TA-18 in 1946, where it remained until 2010. "NCERC has long been part of the Laboratory's iconic history and its unique science will continue to drive the art of the possible," said Evelyn Mullen, Associate Director for Threat Identification and Response. "The contributions of this important facility will be felt far into the future supporting key mission areas of the Laboratory. These include the nuclear weapons enterprise, global security, space exploration and clean energy solutions for our national security partners in addition to successfully executing its core mission in the Nuclear Criticality Safety Program." After a complex transition from Los Alamos to the Device Assembly Facility (DAF) at the Nevada National Security Site (NNSS), the facility restarted critical experiment operations in 2011. Operated by Los Alamos National Laboratory for the DOE National Nuclear Security Administration (NNSA), NCERC maintains an essential skill base of nuclear material handling and criticality safety expertise based on experimental capability. Funded through the Nuclear Critical Safety Program (NCSP), it remains the nation's only general-purpose critical experiments facility. NCERC's mission is to conduct experiments and training with critical assemblies and fissionable material, at or near the critical state, in order to explore reactivity phenomena. Criticality experiments are generally low power operations with fissile materials, such as plutonium or enriched uranium, conducted to bring these materials to the critical point. This is the point at which the fission process becomes self-sustaining. This fission process must be inherently understood and controlled to ensure the safety, security, and reliability of both the nation's nuclear weapons stockpile and future reactor designs.

The safe handling of large quantities of plutonium and uranium is heavily dependent on the data generated over past decades at NCERC and its predecessor facility. Many of these unique experiments are part of the Nuclear Criticality Safety Program (NCSP), an essential program to the nuclear community. The program is designed to protect nuclear operations personnel, the public and the environment from the consequences of a criticality incident using formality of operations, written operating procedures, criticality safety evaluations, criticality safety controls (engineered features & administrative features), training and other programmatic features. The criticality safety discipline is enhanced by the training of specialists nationwide by NCERC personnel using the facility's unique nuclear materials and capabilities.

What began in the 1970s as a two-day hands-on course for fissionable material operators has evolved to include one-week courses for managers and process supervisors, and a two-week course for criticality safety analysts. During the courses held year-round, personnel from DOE, other government agencies, the commercial nuclear community and the military are provided a rare opportunity to witness criticality demonstrations while attending the training. Supported out of DOE NA-50, Infrastructure and Environment, the program demonstrates how varying the properties of a fissionable material system can affect criticality. The first part of training is a classroom discussion of historical criticality accidents and their impact on how operations are performed today. During the second half of training, students take part in hands-on demonstrations with fissionable material in sub-critical configurations and then have the opportunity to observe critical demonstrations conducted remotely. These trainings are now core requirements for criticality safety analysts, and support fissionable material operations across the DOE complex.

One very illuminating demonstration uses a general purpose, lightduty vertical lift assembly machine named Planet to assemble a configuration of plastic plates and uranium foils. A container with 26 foils of uranium is opened and the foils are removed and layered between plastic plates that mimic water. Students monitor the increasing neutron count rate as the layers are added--ten layers on the moveable lower portion and twelve on the top stationary platform. The students and NCERC staff then move to the remote control room and bring the two halves together. They observe the system reach criticality, graphically illustrating that 22 foils can form a critical system when a neutron moderator such as plastic (or water) is present, whereas 26 foils can be in a single container with no moderator present and remain in a subcritical state. This demonstration allows criticality safety personnel to observe a vivid example of the importance of moderators as related to establishing criticality safety limits.

The data generated and analyzed from the experiments conducted at NCERC significantly reduces the margins of uncertainty for criticality safety evaluations by determining the exact point where a given system will attain the critical state. Without this facility's capability, the confidence in the U.S. nuclear stockpile assessment would decrease, the accuracy with which analysts provide criticality safety guidance to those working with fissile materials in production and R&D facilities nationwide would diminish, and operating costs would increase.

Additionally, the research, design and development of new nuclear reactor designs must include experimentation and today NCERC is the only place critical experiments can be conducted to prototype new reactors. Nuclear energy is considered by many to hold future benefits for clean, environmentally safe energy, power grid resilience, national security and deep space exploration. One of the most novel technologies to recently be tested at NCERC is the Kilopower Reactor Using Stirling Technology experiment. A joint project with NASA, Kilopower is a power system that can operate in extremely harsh environments and is efficient, reliable, safe, low cost, and compact. The experiment demonstrated the efficiency of fission power for lunar and planetary exploration. It is anticipated this new nuclear power system could enable long-duration crewed missions to the Moon, Mars and destinations beyond.

Beyond the support NCERC provides to the Nuclear Criticality Safety

Program, NCERC performs experiments to validate nuclear data and computer codes. This work is essential because the United States and its allies no longer test nuclear weapons and as a result the nuclear community at large relies on complex experiments and computer analyses to predict how nuclear weapons will perform. "NCERC is a capability that provides a vital underpinning to the entire mission of the Department of Energy," said Robert Margevicius, Program Director for Strategic Materials and Infrastructure at the Lab. "I think of NCERC in terms of the Navy's fleet of submarines: performing its function largely out of view, but with accomplishments that help enable the military's overarching success." He continued, "And this happens organically through the highly dedicated team of Lab personnel at the core of NCERC's functionality."

The experiments, demonstrations, and training conducted at NCERC also support the Laboratory's nuclear weapons capability in the handling and processing of nuclear materials. This is achieved through scientific and engineering expertise in concert with highly advanced, state-of-the-art equipment often also developed at the Lab. Throughout the years many critical assembly machines have been developed, four of which are in operation today. These machines, and the experiments conducted using them, are essential to understanding the phenomenology of criticality accidents.

Criticality accidents are situations where fissile material unintentionally exceeds the critical state. In over 75 years of processing and handling of nuclear materials worldwide, there have been 22 known criticality accidents in processing facilities around the globe. Of these, seven have occurred in the United States, the most recent over 40 years ago. This track record of safety has been in no small part due to the tireless work conducted at NCERC. Throughout the DOE complex, criticality safety evaluations are performed before any operations with fissile material begin. The evaluations determine that controls are in place such that the entire process will remain subcritical under both normal and credible abnormal process conditions. In contrast, the experiments at NCERC intentionally take fissile material to and above the critical state but only under extremely well controlled conditions. These experiments provide the data required which allows operations with fissionable material throughout the DOE complex to proceed. The Godiva critical assembly at NCERC can be used to simulate a criticality accident under controlled conditions with no personnel present.

As concerns have grown that rogue states and organizations might obtain and use nuclear materials to disrupt democracies, this specialized discipline has become part of the comprehensive training that nuclear incident response personnel receive. NCERC is the only place in the United States nuclear incident responders can train and hone their diagnostic skills with nuclear material in quantities and configurations that they could encounter in realistic scenarios. In addition to Criticality Safety and Nuclear Emergency Response, NCERC also supports Arms Control, Nuclear Nonproliferation and National Technical Nuclear Forensics.

Because of the uniqueness of NCERC capabilities, Los Alamos National Laboratory collaborates with the French, British, Japanese and others on integral critical experiments. These collaborations provide invaluable information and data to the nuclear community for the continued development and maintenance of global nuclear safeguards. The International Criticality Safety Benchmark Evaluation Project (ICSBEP) organized by the Nuclear Energy Agency, provides a link between experiments and the world's nuclear data libraries. Critical experiments are essential to the continued refinement of these libraries maintained by the United States, Japan and Europe.

The National Criticality Experiments Research Center is an asset to our country, national security programs, and the nuclear energy community at large. NCERC is a vital component to maintaining and advancing the capability (people, techniques, analytical methods, materials, and equipment) to conduct fissionable material operations. From the early days of the Manhattan Project to the safety and security of nuclear material operations, clean energy, and the future of space travel, NCERC is an integral part of it all.

List of sites and organizations where the MC-15 Neutron Multiplicity Detector has been tested or used

- Walthausen Critical Reactor Facility at Rensselauer Polytechnic Institute
- Nevada National Security Site
- National Criticality Experiments Research Center (NCERC)
- Los Alamos National Laboratory
- Lawrence Livermore National Laboratory
- Sandia National Laboratories